UNIVERSITY OF SOUTHAMPTON

Analysis and Modelling of Boundary-Layer Flashback Processes for Hydrogen-Rich Gas-Turbine Combustion

by

James R. Bailey

ORCID: 0000-0002-8784-4008

A thesis submitted for the degree of
Doctor of Philosophy

in the
Faculty of Engineering and Physical Sciences
Aeronautical and Astronautical Engineering

July 2021

UNIVERSITY OF SOUTHAMPTON

ABSTRACT

FACULTY OF ENGINEERING AND PHYSICAL SCIENCES
AERONAUTICAL AND ASTRONAUTICAL ENGINEERING

Doctor of Philosophy

ANALYSIS AND MODELLING OF BOUNDARY-LAYER FLASHBACK PROCESSES FOR HYDROGEN-RICH GAS-TURBINE COMBUSTION

by James R. Bailey

This thesis presents analysis and modelling of boundary-layer flashback processes for hydrogen-rich gas-turbine combustion. The future use of industrial gas turbines will be dependent on lowering their carbon intensity, thus requiring flexible use of alternative fuels, such as those rich in hydrogen. Hydrogen has significantly different properties to traditional fuels, for example hydrogen shows an increased risk of flashback, where the flame propagates upstream from the combustion chamber into the premixing section of the gas turbine. Flashback is a significant safety concern which causes plant shutdowns and damage to equipment. The risk of flashback for hydrogen fuels, with their significantly higher flame speed, is particularly high in the case of boundary-layer flashback. Boundary-layer flashback has also been shown to be caused by an increase in swirl, which is particularly important for gas turbines where swirl is commonly used for flame stabilisation. To enable the use of hydrogen-rich fuels in gas turbines it is therefore important to understand the physical mechanisms underlying boundary-layer flashback in swirling flows and to predict the effect of swirl on flashback speeds.

This thesis describes models of flashback in channels and annuli using a Froude number to describe the effect of swirl. The predictions of flashback speed, and physical mechanisms underlying them, are validated using both two-dimensional laminar simulations and three-dimensional turbulent simulations in planar channels and annuli. In non-swirling flows, boundary-layer flashback is dominated by flame propagation that is enhanced by volumetric expansion through the flame. In swirling flows, it is shown that the radial pressure gradient, resulting from centripetal acceleration, causes flow diversion around the flame and results in pressure-driven flashback. These two physical mechanisms are described by models using a momentum balance over the flame, and an additive model that combines a flame-propagation and a pressure-driven term. The trend in flashback speed with swirl is validated using the laminar simulations and experimental data from previous investigations. Finally, the laminar simulations are used to investigate and develop empirical models for the effect of bulk velocity, channel height and boundary-layer development on flashback speed.

Contents

List of Figures

List of Tables

List of Accompanying Material

All data supporting this study are openly available from the University of Southampton repository at https://doi.org/10.5258/SOTON/D1615.

List of Publications Arising from this Thesis

J.R. Bailey and E.S. Richardson, DNS analysis of boundary layer flashback in turbulent flow with wall-normal pressure gradient, Proceedings of the Combustion Institute, https://doi.org/10.1016/j.proci.2020.06.004.

Declaration of Authorship

I, James R. Bailey, declare that this thesis entitled Analysis and Modelling of Boundary-Layer Flashback Processes for Hydrogen-Rich Gas-Turbine Combustion and the work presented in it are my own and has been generated by me as the result of my own original research.

I confirm that:

1. This work was done wholly or mainly while in candidature for a research degree at this University;
2. Where any part of this thesis has previously been submitted for a degree or any other qualification at this University or any other institution, this has been clearly stated;
3. Where I have consulted the published work of others, this is always clearly attributed;
4. Where I have quoted from the work of others, the source is always given. With the exception of such quotations, this thesis is entirely my own work;
5. I have acknowledged all main sources of help;
6. Where the thesis is based on work done by myself jointly with others, I have made clear exactly what was done by others and what I have contributed myself;
7. Parts of this work have been published as: J.R. Bailey and E.S. Richardson, DNS analysis of boundary layer flashback in turbulent flow with wall-normal pressure gradient, Proceedings of the Combustion Institute, https://doi.org/10.1016/j.proci.2020.06.004..

Signed:

Date:

Acknowledgements

I would firstly like to acknowledge the financial support for my PhD from the EPSRC Centre for Doctoral Training in Next Generation Computational Modelling grant EP/L015382/1, the IRIDIS High Performance Computing Facility at the University of Southampton and the UK Consortium on Turbulent Reacting Flows grant EP/K024876/1 who awarded me funding for the use of the ARCHER UK National Supercomputing Service (http://www.archer.ac.uk).

I would like to thank NGCM for their efforts in providing invaluable training, an environment in which to learn more widely about computational modelling, the opportunities to be a part of public engagement as well as supporting us during our time in Southampton.

I would like to thank all of my colleagues along the way, from NGCM, Energy Technology, Building 25, and aero and astro. I have enjoyed sharing the experience with you, discussing our projects, having some fun, and supporting and helping each other along the way.

To my supervisor, Ed, you have been a great help, from initially helping get my PhD on track, to giving your input on where we could take the work and providing innumerable insights during our discussions about the work. I feel you have always offered up your time if I needed to discuss things and helped keep things progressing, even if it has not been the smoothest experience with the Covid-19 pandemic! I feel I have learnt so much from you about how to approach problems, how to break them down and think about them and present them to someone else, and I will take that with me into the future.

To Clare and Jeff, many thanks for your help, your support and advice through the ups and the downs and for your time spent proof-reading, it was very useful to spot things I may never have seen!

To my family, thank you for all of your love and support in getting me to this point, your belief in me and your kind and reassuring words have always helped me. You have also always listened patiently as I told you about moving from cuboids to cylinders, and why my work in making it happen was worthwhile!

To my wife, Catherine, you have always stood up for me and helped me keep going, helped me maintain a sense of perspective, made welcome suggestions for a break, or a tasty meal or cake, as well as so many laughs and good times together. Thank you for everything, and I look forward to our future adventures together.

Acronyms

IGTs Industrial gas turbines. 3, 4, 7

NO_x nitrogen oxides. 3, 4

CCS carbon capture and storage. 4

CIVB combustion-induced vortex breakdown. 5, 35

DNS Direct Numerical Simulations. 13, 25, 27, 32, 33, 44, 45, 53

LES Large-Eddy Simulations. 26, 27, 44

ILES implicit LES. 26

NSCBC Navier-Stokes characteristic boundary conditions. 51, 53

Nomenclature

A'	Ratio of flame surface area to the cross-sectional area of the flow
B	Constant in logarithmic velocity profile
D	Density ratio, ρ_u/ρ_b
D_i	Mixture-averaged diffusion coefficient of species i
D_i^T	Thermal diffusion coefficient of species i
Da	Damköhler number
Da_c	Critical Damköhler number
Da_w	Wall-scale Damköhler number
$\overline{E}$	Kinetic energy of the mean flow
Fr	Froude number, $Fr = S_L/u_b$
Fr_b	Gravity-current Froude number, $Fr_b = u_f/u_b$
Gr	Grashof number
H	Full channel height
H'	Confinement ratio
I_0	Intensification factor
K	Karlovitz number or non-dimensional wall velocity gradient
K_0	Relative wall velocity gradient
$K_{p,\alpha}$	Non-dimensional pressure gradient in direction α
Ka	Karlovitz number
Ka^{ch}	Channel Karlovitz number
Ka_c	Critical Karlovitz number
Ka_s	Non-dimensional tangential strain rate
Ka_δ	Reaction-zone Karlovitz number

L	Domain length
L_{11}	Integral length scale
Le	Lewis number
Le_F	Fuel Lewis number
Le_O	Oxidiser Lewis number
Le_Z	Intermediate-species Lewis number
M_k	Symbol of species k
Ma	Markstein number
N	Number of grid points
P	Production rate of turbulent kinetic energy
P^+	Non-dimensional pressure, $P/(\rho_u u_\tau^2)$
P_{tw}	Pressure on the top wall of the channel
Pe	Peclet number
Pe_Q	Quenching Peclet number
Q_j	Progress rate of reaction j
R^*	Radius ratio, R_1/R_0
R^2	Coefficient of determination
R_0	Inner radius
R_1	Outer radius
Re	Bulk-flow Reynolds number
Re_0	Centre-line Reynolds number
Re_g	Gravity-current Reynolds number
Re_τ	Friction-velocity Reynolds number
Ro	Rotation number
Ro_τ	Friction-velocity Rotation number
S	Ratio of background to mean-shear vorticity
S_L	Laminar flame speed
S_L^0	Unstretched laminar flame speed
S_T	Turbulent flame speed
S_c	Consumption speed

S_d Displacement speed

S_d^* Density-weighted displacement speed

S_f Flame propagation velocity

Sw Swirl number

T Temperature

U_{FB} Bulk-flow flashback limit

U_{bulk} Bulk velocity

$(U_{bulk} - V_f)$ Flashback speed

$(U_{bulk} - V_f)^*$ Relative flashback speed, $(U_{bulk} - V_f)/S_L$

V' Linear wall velocity gradient

V_f Lab-frame flame propagation velocity

V_{scan} Speed, moving frame-of-reference

$\mathbf{V}_{\alpha i}$ Diffusion velocity of species i in direction α

V_θ Circumferential velocity

W Mean molecular weight

W_i Molecular weight of species i

X Mole fraction

$[X]$ Molar concentration

Y Mass fraction

a Cylinder inner radius

a^+ $a/\delta_n u$

a_T Tangential strain rate

b Wall heat transfer parameter, $(\lambda_w/\lambda_g)(\delta_T/h_w)$

$\overline{\nabla c}$ Flame surface density

c Progress variable

c_p Heat capacity

e_0 Specific total energy

$f_{\alpha i}$ Body force in direction α acting on species i

g Gravity

g' Densiometric body force

g_c	Critical velocity gradient
h	Total enthalpy (sensible plus chemical)
h_0	Convective heat transfer coefficient
h_f	Gravity-current front height
h_{rf}	Height of reversed-flow region
k	Turbulent kinetic energy
k'	Wall heat transfer parameter
l_t	Large-eddy length scale
l_F	Flame radius of curvature
m	Mass
$\nabla \cdot \mathbf{n}$	Curvature
$\vec{n}$	Flame normal
n_i	Number of moles of species i
p	Pressure
$\mathbf{q}$	Heat-flux vector
r_{ij}	Correlation coefficient
s	Entropy
s_{ij}	Fluctuating rate of strain
t_v	Friction-velocity time scale
u	x-velocity
u'	Velocity fluctuation
u^*	Non-dimensional bulk velocity, U_{bulk}/S_L
u^+	u/u_τ
u_b	Buoyancy velocity, $u_b = \sqrt{g'\delta}$
u_c	Centre-line velocity
u_f	Gravity-current front speed
u_g	Buoyancy velocity
u_m	Mean velocity
u_τ	Friction velocity
v	y- or radial velocity

w	z- or circumferential velocity
x_f^*	Flame position in x-direction
y^+	$y/\delta_n u$
y^*	Non-dimensional y, y/δ_L
Φ_w	Non-dimensional wall heat flux
Ω	Angular velocity
α	Thermal diffusivity
γ	Non-dimensional cylinder inner radius
δ	Channel half-height
δ^*	Non-dimensional channel or annulus half-height, δ/δ_L
δ_1'	Height ratio
δ_L	Thermal flame thickness
δ_T	Diffusive flame thickness
δ_{ij}	Kroenecker delta
δ_p	Penetration distance
δ_q	Quenching distance
δ_r	Reaction-zone thickness
δ_ν	Friction-velocity length scale
ϵ	Dissipation rate of turbulent kinetic energy
η	Kolmogorov length scale
θ'	Non-dimensional temperature
θ_f	Flame angle relative to that opposing the mean oncoming flow
κ	Stretch rate
κ'	von Karman constant
λ	Thermal conductivity
λ_w	Wall thermal conductivity
μ	Dynamic viscosity
ν	Kinematic viscosity
ν_{kj}'	Molar stoichiometric coefficients of the forward reaction for species k in reaction j
ν_{kj}''	Molar stoichiometric coefficients of the backward reaction for species k in reaction j

ρ	Density
τ_w	Wall shear stress
ϕ	Equivalence ratio
$\dot{\omega}_F$	Mass rate of reaction of fuel

Part I

Introduction

Chapter 1

Introduction

Industrial gas turbines (IGTs) are an important part of the power-generation system. Their power output can be rapidly increased or decreased to match fluctuating demand for power. IGTs have been developed to have high efficiency, relatively low cost and low emissions of nitrogen oxides (NO_x) (Richards et al., 2001; Taamallah et al., 2015). NO_x are linked to smog and acid rain, which, in turn, cause respiratory illness and environmental damage (Lieuwen and C. Yang, 2013). IGTs therefore represent one of the best options to move towards the provision of low-carbon power, supporting the grid by smoothing out the power supply from potentially intermittent renewable power sources. However, IGTs are currently designed and optimised to use natural gas, and their future use will be dependent on lowering their carbon intensity (Richards et al., 2001; Taamallah et al., 2015).

Lowering the carbon intensity of IGTs requires the use of alternative fuels, such as those rich in hydrogen. These fuels could be derived from various sources, for example the gasification of biomass, which produces low net-carbon synthesis gas (syngas), a mixture of hydrogen and carbon monoxide. Low-carbon energy sources could also be provided by the gasification of other solid fuels combined with carbon capture and storage (CCS) or the recycling of industrial hydrogen by-products. These alternative fuels could all be used to retain the advantages of IGTs, whilst addressing the need to lower their carbon intensity (Richards et al., 2001; Taamallah et al., 2015).

In an IGT, a flow of air enters the turbine and is compressed; in a premixed system this air flow is then mixed with the fuel prior to entry into the combustion chamber. Here the flame is stabilised,

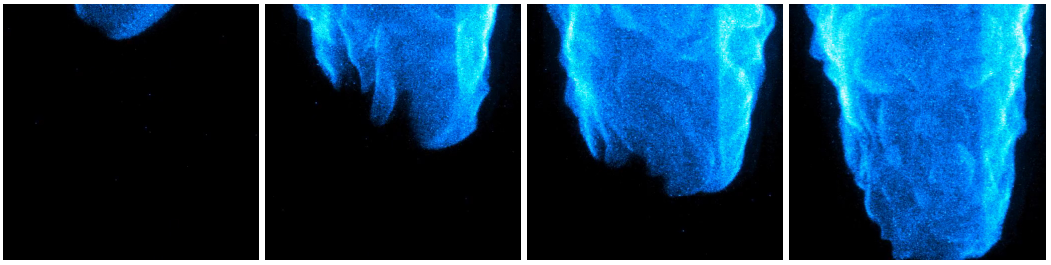

Figure 1.1: Images of flashback of a CH_4-air flame within a swirling flow through the mixing tube shown in Figure 1.2 (where the flow is from bottom to top) (Ebi and Clemens, 2016) (available under the CC BY 4.0 License).

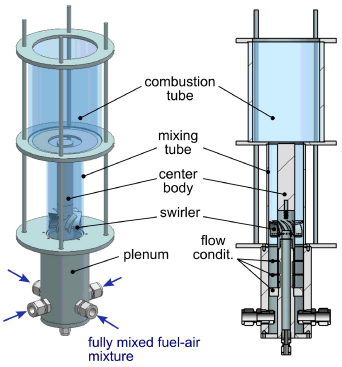

Figure 1.2: Diagram of the combustor used by Ebi and Clemens (2016).

commonly by swirling the incoming flow of fuel and air, and the fuel is burned. On leaving the combustion chamber the hot, pressurised gases then pass through a turbine to generate mechanical power which both powers the compressor and is used to generate electricity. The efficiency of this process is dependent on the increase in pressure given by the compressor and the turbine inlet temperature. The maximum turbine inlet temperature is limited by the temperatures which the turbine blades can withstand. Through improved compressor design, improved turbine-blade cooling and progress in material engineering, higher efficiencies have been achieved. However, higher temperatures lead to higher NO_x emissions, which necessitates the lowering of flame temperatures. To achieve these lower flame temperatures, lean, premixed combustion is used: the fuel and air are premixed prior to entry into the combustion chamber and a lower fuel-to-air ratio is used. This reduces the generation of NO_x but also means that a combustible mixture of fuel and air is present upstream of the desired flame location where the risk of this mixture being ignited is a safety concern.

The move from using natural gas to alternative fuels within this system presents significant technical challenges (Richards et al., 2001; Taamallah et al., 2015). Syngas has a lower volumetric energy density than natural gas which means that achieving the same power output will require an increase in the volumetric flow rate through the system. The properties of hydrogen and hydrogen-rich fuels also differ significantly in terms of their combustion behaviour. Hydrogen is more reactive and diffusive, resulting in a flame speed which could be five times higher than methane. This means the flame is less likely to be pushed out of the combustion chamber by high oncoming flow, reducing the likelihood of a situation known as blow-off, but increases the risk of the flame propagating upstream into the premixing section, which is not designed to cope with the high temperatures of the combustion chamber. This process is known as flashback and is a serious safety concern, resulting in damage to equipment and shutdowns.

Figure 1.1 demonstrates flashback occurring within an experimental combustor (Figure 1.2) where the flame has propagated upstream from the combustion chamber and into the premixing section. In the experiment, a swirling flow is used to create zones where the hot burned gases recirculate and heat up the incoming unburned mixture, initiating the burning process and stabilising the position of the flame within the combustion tube. A perturbation in conditions is then applied which allows the flame to move upstream and into the mixing tube. Propagation then continues down the mixing tube, despite the oncoming flow being faster than the propagation speed of the flame.

The properties of syngas, like volumetric energy density and flame speed, are also sensitive to the process conditions and fuel source used to generate the syngas. Even small changes in the

proportion of hydrogen within a syngas mixture can give significantly different fuel properties (Dam et al., 2011). Fuel-flexible burners must handle these changing properties as well as the different properties of hydrogen-rich fuels, such as in the risk of flashback (Taamallah et al., 2015), where flashback will be the focus of the work in this thesis.

Flashback can be caused by four different physical mechanisms, as described below, whereby the flame is able to propagate faster than the oncoming flow and move upstream (Lieuwen et al., 2008; Kalantari and McDonell, 2017):

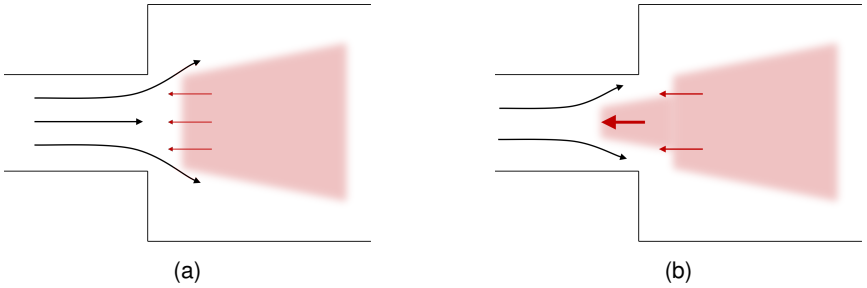

Figure 1.3: Flashback in the core flow. The red shaded area indicates the region of burned gases, red arrows correspond to flame propagation and black arrows to the flow. Black lines indicate acoustic waves. The size of the arrow is drawn relative to the speed (flow or flame).

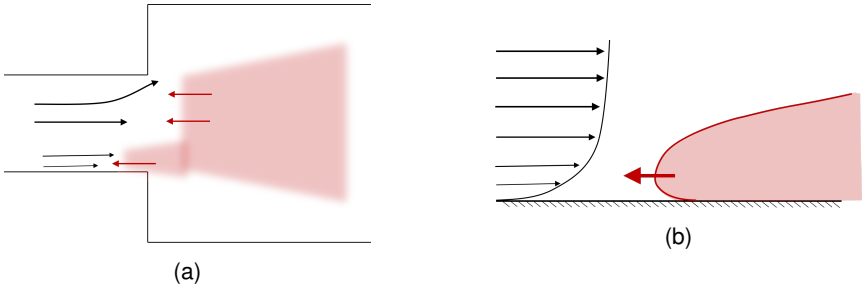

Figure 1.4: Boundary-layer flashback. The shading and arrows are the same as in Figure 1.3.

- **Flashback in the core** and in **the boundary layer** (Kalantari and McDonell, 2017) are shown in Figures 1.3 and 1.4. In both cases, the flame is stabilised by a balance between the oncoming flow (causing the flame to recede) and the flame propagating upstream to maintain its position (Figure 1.3a). If the flame is able to propagate faster than the oncoming flow then the flame moves upstream and flashback can occur. The presence of the flame may also cause local flow reversal which accelerates flashback. In swirling flows, the core of the swirling flow is a region with lower pressure in which flashback may occur (Lieuwen et al., 2008), as shown in Figure 1.3b. In boundary-layer flashback, the flow is lower in the vicinity of the wall and therefore this is a region where flashback may occur (Lieuwen et al., 2008; Kalantari and McDonell, 2017). Figure 1.4a shows this occurring against the outer wall of the premixing section while Figure 1.4b demonstrates the local balance between the flame speed and the speed of the oncoming flow. Both boundary-layer and core-flow flashback are a greater risk for fuels with higher flame speeds, such as those rich in hydrogen (Kalantari and McDonell, 2017).

- **Combustion-induced vortex breakdown (CIVB)** (Leibovich, 1978; Dam et al., 2011; Kröner et al., 2003; Fritz et al., 2004) is shown in Figure 1.5. Swirling flows are widely used in IGT

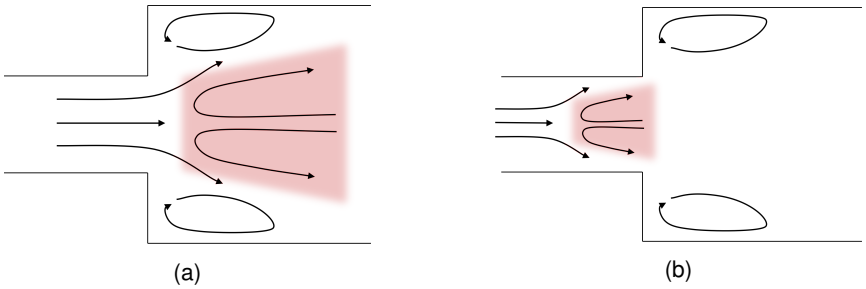

Figure 1.5: Flashback - combustion-induced vortex breakdown (CIVB). Reproduced from Lieuwen et al. (2008). The flow enters from the mixing tube on the left into the combustion chamber. The shading and arrows are the same as in Figure 1.3.

combustion chambers for flame stabilisation. Figure 1.5a shows an oncoming swirling flow and zones where the flow recirculates (Lieuwen et al., 2008). The recirculating flow of burned gases heats up the oncoming flow and initiates the combustion process, thereby maintaining the position of the flame (Richards et al., 2001). However, the combustion process itself can induce breakdown of the vortices in the oncoming swirling flow (Lieuwen et al., 2008) (Figure 1.5b). Combustion causes heat-release and thermal expansion through the flame front which gives a density gradient perpendicular to the pressure gradient, which is from the outside to the inside of the swirling flows. This misalignment of density and pressure gradient generates baroclinic torque which generates a region of lower oncoming flow velocity and allows the flame to move upstream (Lieuwen et al., 2008; Kalantari and McDonell, 2017). This region of lower oncoming flow velocity and the flame then move upstream together, resulting in flashback (Leibovich, 1978; Dam et al., 2011).

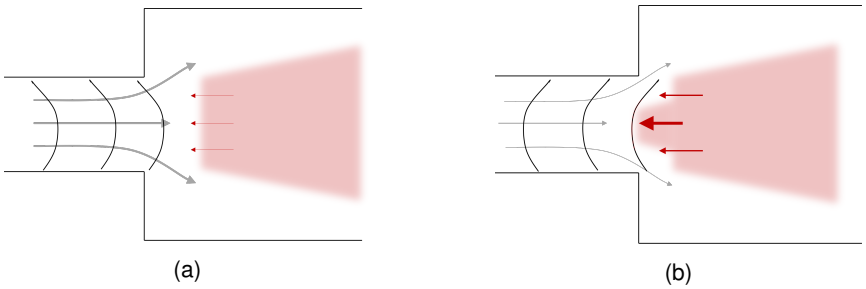

Figure 1.6: Flashback - combustion instability-induced. The shading and arrows are the same as in Figure 1.3.

- **Combustion instability-induced flashback** (Thibaut and Candel, 1998; Lapeyre et al., 2017; Hoferichter et al., 2014; Hoferichter and Sattelmayer, 2017) (Figure 1.6). Fluctuations in flame speed generate pressure or acoustic waves. These acoustic waves travel through the combustion chamber and can be reflected back towards the flame. If these fluctuations in flame speed and pressure (due to the returning acoustic wave) combine constructively, these fluctuations grow even larger. If the fluctuations grow sufficiently large, increases in flame speed potentially combine with the slowing of the oncoming flow to allow the flame to propagate upstream (Lieuwen et al., 2008).

Of the four flashback mechanisms, combustion-induced vortex breakdown and flashback through the core flow both require a swirling flow whereas boundary-layer flashback can occur in either

a non-swirling or swirling flow. Of these flashback scenarios, boundary-layer flashback within a swirling flow is the least studied, with the dominant mechanism causing flashback currently unclear: previous investigations have linked flashback to either CIVB, to the mechanisms seen in non-swirling boundary-layer flashback or to the density gradient across the flame front causing a rise in static pressure (Ebi et al., 2018). Given the common use of swirling flows for flame stabilisation in IGTs and that an increase in swirl has been shown to cause flashback (Heeger et al., 2010), it is important to understand and predict the effect of swirl on flashback.

For boundary-layer flashback, many investigations have been conducted on flashback from the combustion chamber into the premixing section (termed unconfined configurations)(see Kalantari and McDonell (2017) for a review) and recent work (Eichler and Sattelmayer, 2011; Eichler et al., 2012; Eichler and Sattelmayer, 2012; Gruber et al., 2012) has extended this to situations where the flame is already present inside the premixing section (confined configurations). However, this understanding for confined configurations has yet to be extended to flows which are not fully developed (Kalantari and McDonell, 2017). It is important to understand the effect of a developing boundary layer to design flashback-resistant combustion systems. The velocity profile of a developing boundary layer is also closer to that of a turbulent flow and so the effect of a developing boundary layer can be extended to describe some of the effects of a turbulent flow which is present in an IGT.

1.1 Thesis Overview

In this thesis I present an investigation of boundary-layer flashback of swirling and non-swirling flows, focussing on the impact of swirl on flashback. I elucidate the mechanisms of boundary-layer flashback in swirling flows and develop models which predict the effect of swirl on flashback speed. I extend this to also describe the effect of a developing boundary layer and the wall velocity gradient on flashback speeds. My investigations will use two-dimensional laminar simulations in annular sections and three-dimensional turbulent simulations in planar channels and annuli, as well as the development of analytical models.

1.1.1 Aims

In this work I aim to:

- investigate boundary-layer flashback of hydrogen and hydrogen-rich fuels as relevant to the swirling flows of industrial gas turbines

1.1.2 Objectives

The objectives of this work are to:

- understand the mechanisms of boundary-layer flashback in swirling flows
- understand how the physical aspects of a swirling flow affect flashback speed
- develop models describing the effect of swirl on flashback speed

1.1.3 Contributions

The key contributions arising from this thesis are:

- Analytical models describing the effect of swirl, density ratio and confinement on flashback speeds in planar channels and annuli. An additive model which predicts flashback speeds as a combination of flame-propagation and pressure-driven terms.
- An investigation into the effect of swirl, bulk velocity and a developing boundary layer in two-dimensional laminar annular sections. This investigation verifies the trends predicted by the analytical and additive models and is used to develop empirical models for the effect of bulk velocity and a developing boundary layer on flashback speeds at different levels of swirl.
- An investigation into the effect of wall-normal pressure gradient or swirl in three-dimensional turbulent planar channels and annuli, respectively. These investigations verify the dominating physical mechanisms causing boundary-layer flashback in swirling flows and describe how the other physical aspects of a swirling flow impact flashback speed.

1.1.4 Organisation

The remaining chapters of this thesis are organised as follows:

- **Part I**:

  Chapter 2 presents the background to boundary-layer flashback and a review of existing literature.

  Chapter 3 presents the formulation for how this problem will be investigated.

- **Part II**:

  Chapter 4 presents the formulation of momentum-balance and additive models for predicting flashback speeds.

  Chapter 5 presents two-dimensional laminar simulations of flashback in annular sections investigating the effect of swirl, bulk velocity and a developing boundary layer.

- **Part III**:

  Chapter 6 presents three-dimensional turbulent simulations of flashback in planar channels investigating the effect of a wall-normal pressure gradient and change in flow orientation.

  Chapter 7 presents three-dimensional turbulent simulations of non-reacting swirling flow and flashback in annular sections, investigating the effect of swirl.

  Chapter 8 presents an evaluation of the momentum-balance models of Chapter 4 using turbulent experimental data and previous models of boundary-layer flashback.

  Chapter 9 presents a summary of the work, conclusions and suggestions for future work.

Chapter 2

Background

2.1 Introduction to Boundary-Layer Flashback

In this section, I will expand the physical description of boundary-layer flashback, the relevant background information for the understanding of the physical processes and the latest investigations into boundary-layer flashback.

Figure 2.1 shows a schematic of boundary-layer flashback, where the oncoming boundary-layer flow is from the left. When the flame is far from the wall, the wall has minimal local effects on the flame and so the flame is freely propagating. When then flame is near the wall then the flame and wall interact and there is heat loss to the wall that impacts flame propagation. In boundary-layer flashback the flame near the wall is able to propagate upstream against the oncoming flow, giving flame propagation led within the near-wall region. The trailing flame is able to freely propagate into the oncoming flow, where the local flow velocity can be higher than the local flame propagation speed.

To understand boundary-layer flashback it is necessary to understand each of these physical processes so in the following sections I present the relevant background information for each.

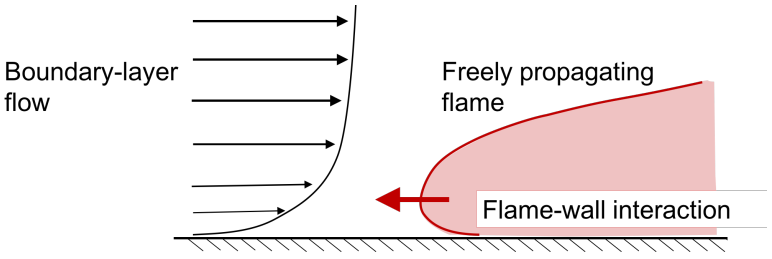

Figure 2.1: Schematic diagram representing boundary-layer flashback. On the left is a boundary-layer velocity profile (black) and on the right a flame during boundary-layer flashback (red).

2.1.1 Turbulent Boundary Layers

Free-stream turbulence is characterised by an energy cascade where energy is transferred from the larger, energy-containing scales to the smaller scales where viscosity becomes dominant and the turbulent kinetic energy is dissipated as heat (Jiménez, 2012). In wall-bounded turbulent flows we gain an additional parameter: the distance from the wall (Jimenez, 2013). Firstly, this adds a momentum cascade to the energy cascade - the momentum at the centre-line of the flow, where the velocity is highest, is transferred to the wall, where it is lost to the wall (Jiménez, 2012). Secondly, the range of turbulent scales also changes with distance from the wall: for example, the presence of the wall restricts the size of the large eddies in the near-wall region, giving a smaller range of length scales (Jimenez, 2013). Different effects are also seen, for example in the importance of viscosity, where the slower flows nearer the wall mean the importance of viscosity becomes greater (Jimenez and Moser, 2007).

I will start this section by defining some of the important parameters for turbulence in general, before moving on to turbulent boundary layers specifically.

In a turbulent flow, the kinetic energy can be separated into the kinetic energy from the mean flow, $\overline{E}$, and that from turbulent fluctuations, k, which is given by:

$$k = \frac{1}{2}\left\langle u'^2 + v'^2 + w'^2 \right\rangle \tag{2.1}$$

where u', v' and w' represent the velocity fluctuation in each spatial dimension and $\langle\rangle$ represents ensemble averaging. The turbulent kinetic energy is produced from the kinetic energy of the mean flow:

$$P \equiv -\left\langle u_i' u_j' \right\rangle \frac{\partial \left\langle \overline{u_i} \right\rangle}{\partial x_j} \tag{2.2}$$

where P is the production of turbulent kinetic energy, and i and j represent spatial directions. This equation contains the Reynolds stress term, $\left\langle u_i' u_j' \right\rangle$, which represents the additional momentum transport resulting from the fluctuating velocities in a turbulent flow field. The produced turbulent kinetic energy passes through the energy cascade to be dissipated as heat. This dissipation of turbulent kinetic energy, ϵ, is a function of the fluctuating rate of strain, s_{ij}:

$$\epsilon = 2\nu \left\langle s_{ij} s_{ij} \right\rangle \tag{2.3}$$

$$s_{ij} = \frac{1}{2}\left(\frac{\partial u_i'}{\partial x_j} + \frac{\partial u_j'}{\partial x_i}\right) \tag{2.4}$$

where ν is the kinematic viscosity.

These terms can then be used to characterise the length scales of the largest and smallest eddies in the energy cascade. The Kolmogorov scale, η, represents the smallest eddies in the flow and is given by $(\nu/\epsilon)^{3/4}$. The largest scales can be represented by the large-eddy length scale, $l_t = k^{3/2}/\epsilon$, or by the integral length scale, L_{11}, which is calculated from the velocity field using two-point correlations:

$$L_{11}(x,t) = \frac{1}{R_{11}(0,x,t)} \int_0^\infty R_{11}(r,x,t)dr \tag{2.5}$$

$$R_{ij}(r,x,t) = \left\langle u_i(x,t) u_j(x+r,t) \right\rangle \tag{2.6}$$

where R is the two-point correlation, which is a function of: x, a spatial position; t, time; and r, a separation from x.

Within a turbulent channel flow, we can now define the structure of the flow as it varies with distance from the wall. Across the channel, shear stress is composed of viscous transfer and Reynolds stresses, which vary in importance with wall distance. In the near-wall region, viscosity is important and properties are scaled using ν and the friction velocity, u_τ:

$$u_\tau = \sqrt{\frac{\tau_w}{\rho}} \tag{2.7}$$

$$\tau_w = \mu \frac{\partial u}{\partial y}\bigg|_{wall} \tag{2.8}$$

where τ_w is the wall shear stress, μ the dynamic viscosity and ρ the density. This gives a length scale, $\delta_\nu = \nu/u_\tau$, and a time scale, $t_\nu = \nu/u_\tau^2$. Properties scaled using these are termed wall units and are denoted by a superscript $+$. Far from the wall, viscosity is no longer important and properties are scaled using outer units, the channel half-width, δ, and centre-line velocity, u_0. The friction-velocity Reynolds number, Re_τ, defines the scale separation between the inner and outer scales and is defined by:

$$Re_\tau = \frac{\delta}{\delta_\nu} = \frac{u_\tau \delta}{\nu} \tag{2.9}$$

Reynolds numbers can also be defined based on the bulk flow, $\overline{u}$, and centreline velocity, u_0:

$$Re = \frac{2\delta\overline{u}}{\nu} \tag{2.10}$$

$$Re_0 = \frac{u_0\delta}{\nu} \tag{2.11}$$

Moving from the wall to the central part of the flow, a number of regions can be defined. The region closest to the wall is the viscous sub-layer where Reynolds stresses are negligible and viscosity is dominant. This region extends up to $y^+ = 5$ (Jimenez and Moser, 2007). The velocity in this region is found to follow a linear scaling $u^+ = y^+$ (Prandtl, 1925). The turbulent structures in this region are made of stream-wise velocity streaks and quasi-stream-wise vortices, which together form a cycle which maintains the turbulence in the entire flow (Jiménez and Pinelli, 1999). The streaks alternate low and high velocity and are long ($x^+ = 1000$ to 10000) with average span-wise spacings of 100 wall units. The quasi-stream-wise vortices are slightly tilted away from the wall and advect the mean velocity gradient to form the streaks (Jiménez and Pinelli, 1999).

Momentum transport also occurs through ejection and sweeps events. Ejection events occur when the low-velocity streaks decelerate and fluid is ejected from out from the wall. The ejection events are then followed by sweep events, where the fluid moves toward the wall from above. These events contribute a significant amount of the Reynolds stresses ($u'v'$). To evaluate the contributions of ejections and sweeps, quadrant analysis was developed. This analysis separates the fluctuations into four groups: quadrant 1 (positive u' and v'), quadrant 2 (negative u', positive v'), quadrant 3 (negative u' and v') and quadrant 4 (positive u', negative v'), where quadrant 2 and 4 correspond to sweeps and ejections, respectively, and which were shown to make the largest contributions to the Reynolds shear stress (Wallace, 2016).

Between the viscous sub-layer and the outermost layer is a buffer layer which extends from $y^+ = 5$ to 100. Here Reynolds stresses are no longer negligible but viscosity remains dominant. The outermost layer is the overlap or logarithmic layer which extends from $y^+ = 100$ to $y/\delta = 0.2$. The velocity profile in this region follows a logarithmic profile (von Karman, 1930):

$$u^+ = \frac{1}{\kappa'} \ln y^+ + B \tag{2.12}$$

where κ' is the von Kármán constant and B is a constant. Due to the bounds on the region, many low-Reynolds-number flows do not contain an overlap layer.

Effect of Curvature and Span-wise Rotation

Flashback within swirling flows in an annulus no longer occurs against the flat wall of a planar channel but along a wall showing transverse curvature, in the case of axial-only flow, or in a flow with stream-wise curvature, in the case of a swirling flow. Previous investigations of flashback, which are described below, have shown the importance of the interaction between the turbulence and the flame. It is therefore important to understand the effect of curvature and spanwise rotation on boundary-layer flow.

The effects of transverse curvature have been studied using a minimal flow unit where only the inner-wall boundary layer is represented (Neves et al., 1994) and through the simulation of annular flow (Chung et al., 2002).

To characterise curvature (Neves et al., 1994), the cylinder inner radius, a, is described relative to the two flow length-scales: δ and δ_ν. This gives:

$$\gamma = \frac{\delta}{a} \tag{2.13}$$

$$a^+ = \frac{a}{\delta_\nu} \tag{2.14}$$

The effect of curvature on the boundary-layer flow is dependent on curvature (Neves et al., 1994). When γ is small, the boundary-layer flow is similar to that of a planar boundary-layer. As γ increases then the effects of curvature increase. For large γ, if a^+ is large then curvature only affects the outer boundary-layer flow whereas for smaller a^+ curvature affects both the inner and outer parts of the flow. A curvature-dependent law of the wall (Reid and Wilson, 1963; Rao, 1964) has also been derived to describe these effects:

$$u^+ = a^+ \ln\left(1 + \frac{y^+}{a^+}\right) \tag{2.15}$$

To second-order this becomes:

$$u^+ = y^+ \left(1 + \frac{y^+}{2a^+}\right) \tag{2.16}$$

In the log region if γ is large then the slope of the log region remains the same as in the planar case. As γ increases and a^+ decreases then the slope of the log region decreases and for sufficiently large γ and small a^+ the log region becomes negatively curved. Chung et al. (2002) also showed that positions of zero shear stress and maximum velocity no longer coincide when transverse curvature

is present. The position of zero shear stress was shown to be closer to the inner wall than that of maximum velocity.

The velocity fluctuations and Reynolds shear stress also decrease with increasing curvature (Neves et al., 1994). This decrease is larger for the normal and azimuthal fluctuations. This was linked to the decreasing pressure-strain term in the budget of axial-velocity intensity that is responsible for the energy transfer from the streamwise to the normal and azimuthal components. The smaller turbulent kinetic energy was not linked to the wall being a less efficient source of turbulent kinetic energy but instead to the smaller wall surface area relative to the volume of the flow. The Reynolds shear stress contributions from each quadrant were shown to have similar fractional contributions from each, and similar cross-over point in the magnitude of second-quadrant and fourth-quadrant events, when compared to a planar channel flow.

Transverse curvature was also shown to affect the boundary-layer structures (Neves et al., 1994). Increasing curvature meant the low-speed streaks had longer streamwise length, and the mean span-wise spacing of the streaks decreased below 100 wall units. This spacing was proportional to r and increased to more than 100 further from the wall.

The effects of spanwise rotation have been studied using experiments and Direct Numerical Simulations (DNS) through the addition of a Coriolis force term to simulate spanwise rotation of angular velocity, Ω (Kristoffersen and Andersson, 1993). In this way, the authors have isolated the effect of rotation from that of curvature, so, while not simulating the effect of swirl in an annulus, these results will be used to help interpret the effect of swirl on the non-reacting flow.

The rotation is characterised using a rotation number:

$$Ro = \frac{2|\Omega|\delta}{\overline{u}} \tag{2.17}$$

or:

$$Ro_\tau = \frac{2\Omega\delta}{u_\tau} \tag{2.18}$$

The effect of the rotation on the flow is characterised using a ratio of background vorticity to mean-shear vorticity:

$$S = \frac{-2\Omega}{\partial u/\partial y} \tag{2.19}$$

The background and shear vorticity are of the same sign when $S > 0$. The background and shear vorticity are of different signs when $S < 0$, and the effect of rotation destabilises the flow when $-1 < S < 0$.

The mean velocity profile is shown to become increasingly asymmetric with increasing rotation (Kristoffersen and Andersson, 1993). In wall co-ordinates this gives a pressure side where the velocity decreases relative to that of planar channel flow and a suction side where the velocity increases. There is also shown to be a region in the velocity profile where $\partial u/\partial y = 2\Omega$.

The stabilisation and destabilisation of the flow impacts the turbulence on the suction and pressure sides, respectively (Kristoffersen and Andersson, 1993). On the suction side the turbulent Reynolds stresses decrease with increasing rotation, with the turbulence quenched at higher rotation rate ($Ro = 0.50$). On the pressure side the turbulence intensities and Reynolds shear stress increase with rotation at moderate rotation rate but restabilise at higher rotation rate.

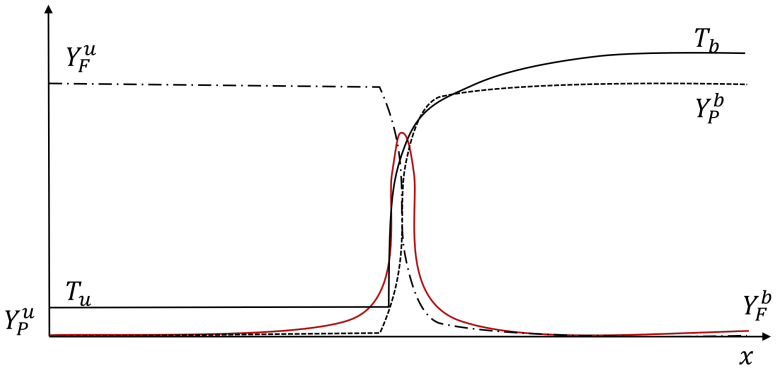

Figure 2.2: Schematic of one-dimensional laminar flame. The graph shows the temperature (T, solid black), fuel mass fraction (Y_F, dot-dashed black), product mass fraction (Y_P, dashed black) and heat-release rate (red line) from unburned (^{u}) to burned conditions (^{b}) through the flame (denoted x).

In addition to these effects, large-scale Taylor-Görtler-like vortices also form (Kristoffersen and Andersson, 1993). These are stream-wise rotating and transport fluid from the pressure side of the flow into the centre of the channel, enhancing the turbulence here. The rotating flow is subject to the centrifugal instability (Alfredsson and Persson, 1989) which results in these vortices. This is the same mechanism behind Taylor, Dean and Taylor-Görtler vortices, which occur respectively for: tangential flow between rotating cylinders; curved channel flow; and boundary-layer flow over a concave surface (Saric, 1994).

The Taylor-Görtler-like vortices are near-circular, with their size dependent on the rotation rate. As the rotation rate increases, the size of the laminarised wall layer on the suction side increases, reducing the wall-normal and therefore span-wise extent of the vortices. This increases the number of pairs of vortices found in a given domain width. Where the domain width matches the preferred scale of the vortices, the position of the vortices remains steady, allowing the contributions of the vortices to the Reynolds stress components to be evaluated. For $Ro = 0.15$, the vortices were found to contribute around 25% of the turbulent kinetic energy in v and w. Where the domain does not match the preferred scale of the vortices, their position was found to remain steady but their shape, size and strength changed gradually (Kristoffersen and Andersson, 1993).

2.1.2 Freely propagating Flames

The structure of a laminar flame is shown in Figure 2.2: on the right are the hot, burned gases containing the combustion products; in the centre is a reaction zone where fuel and air react releasing heat and to the left of this reaction zone is the pre-heat zone where the unburned gases are heated until they begin to react. The transition from unburned to burned gases is represented by a progress variable, c, which goes from 0 in the unburned to 1 in the burned gases. In this work the progress variable is calculated using the mass fraction of a given species, H_2:

$$c = \frac{Y^u_{H_2} - Y_{H_2}}{Y^u_{H_2} - Y^b_{H_2}} \tag{2.20}$$

where u represents unburned and b burned conditions.

Representing the structure of the flame using one dimension, the flame can be characterised in terms of its speed and thickness. The displacement speed, S_L, gives the speed of the flame relative to the flow while the consumption speed, S_c, is given by the rate of consumption of reactants:

$$S_c = \frac{-1}{\rho_u Y_F^u} \int_{-\infty}^{+\infty} \dot{\omega}_F dx \tag{2.21}$$

where ρ_u is the density of the unburned mixture, Y_F^u the mass fraction of fuel in the unburned mixture and $\dot{\omega}_F$ the mass rate of reaction of the fuel. The flame thickness can be described using a thermal thickness: $\delta_L = (T_2 - T_1)/max(|\partial T/\partial x|)$; diffusive thickness, $\delta_T = \lambda_u / \left(\rho_u c_p S_L\right) = \alpha_u / S_L$ (where λ_u is the thermal conductivity of the unburned mixture, c_p the heat capacity of the unburned mixture and α_u the thermal diffusivity of the unburned mixture $= \lambda_u/(c_p \rho_u)$), or a reaction-zone thickness, δ_r calculated from the width of the peak in heat-release rate at half the maximum height of the peak. A density ratio, $D = \rho_u/\rho_b$, can also be used to describe the volumetric expansion through the flame.

These flame properties are dependent on the temperature of the unburned mixture and the fuel-air mixture being burned. We can characterise the fuel-air mixture using an equivalence ratio, ϕ, which equals: 1 when the fuel and oxidiser are in stoichiometric proportions; is less than 1 when the fuel is below stoichiometric proportions (fuel-lean) and is greater than 1 when the fuel is above stoichiometric proportions (fuel-rich):

$$\phi = \frac{(n_H/n_O)}{(n_H/n_O)_{st}} = \frac{(m_H/m_O)}{(m_H/m_O)_{st}} \tag{2.22}$$

where n is the number of moles of a given element and m the mass, and the subscript st indicates stoichiometric conditions.

2.1.3 Freely propagating Turbulent Flames

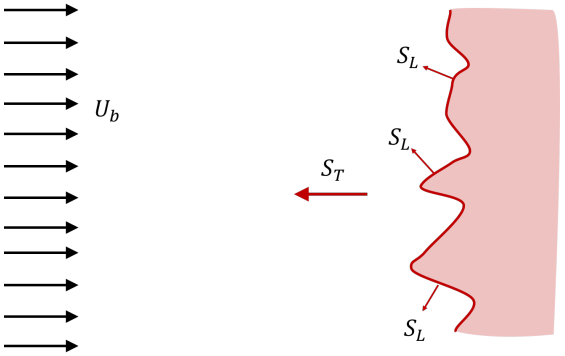

Figure 2.3: Flamelet description of turbulent flame propagation. The flame front is shown in red propagating from right to left against the oncoming flow which has bulk velocity U_b. Locally the flamelets are laminar and propagate at the laminar burning velocity, S_L, but globally the flame, which has been wrinkled by the turbulence, propagates at the turbulent burning velocity, S_T. The region of burned gases is shaded red.

The effect of turbulence on flames can be described using flamelets: flamelets are locally laminar regions of flame which may be affected by the turbulence present in the flow (see Figure 2.3). Turbulent fluctuations can increase the flame surface area above that of a laminar flame. Locally the

flame front is still propagating as a laminar flame with laminar flame speed, S_L, but the turbulence increases surface area such that the turbulent propagation speed, S_T, is now given by:

$$S_T \sim S_L A' \tag{2.23}$$

where A' is the ratio of the flame surface area and cross-sectional area of the flow.

Turbulent fluctuations can also alter the structure of the flame locally, giving a local flame speed which is larger than the laminar flame speed. In this case the turbulent propagation speed is given by:

$$S_T \sim S_L A' I_0 \tag{2.24}$$

where I_0 is an intensification factor, representing the ratio of the local flame propagation speed to that of the laminar flame speed. This intensification factor results from the effect of stretch on the flame. Stretch, κ, is a fractional rate-of-change of flame area and is described by a combination of strain and curvature (Chen and Im, 1998):

$$\kappa = a_T + S_d \nabla \cdot \vec{n} \tag{2.25}$$

where $a_T = \nabla_t \cdot \vec{u}$ is the tangential strain rate and $\nabla \cdot \vec{n}$ represents curvature, where n is the vector normal to the flame surface. When the flame is stretched the flame surface area increases, the flame becomes thinner and the gradients of mass fraction and temperature increase, increasing the provision of unburned gases but increasing heat loss. If the increased provision of reactants outweighs the increased loss of heat then the flame speed increases, but if the loss of heat outweighs the increased provision of reactants then flame speed decreases. The relative diffusivity of heat and the reactant are described by the Lewis number:

$$Le = \frac{\alpha}{D_m} \tag{2.26}$$

where α is the thermal diffusivity of the mixture and D_m is the mass diffusivity of the limiting reactant. Lean hydrogen flames have a Lewis number less than 1 such that flame speed increases with stretch. The effect of stretch on flame speed is given by:

$$\frac{S_c}{S_L^0} = 1 - Ma \frac{\kappa \delta_T}{S_L^0} \tag{2.27}$$

where S_c is the consumption speed, S_L^0 the unstretched laminar flame speed and Ma the Markstein number, which is a function of Le.

The interaction between turbulence and the flame is described using a number of regimes, which are shown in Figure 2.4. The situation where the turbulent eddies are able to wrinkle the flame but the flame locally propagates like a laminar flame is described as a wrinkled or corrugated flamelet. This is present when the smallest turbulent eddies, at the Kolmogorov scale, are much larger than the flame thickness. The turbulent eddies do not enter the pre-heat or reaction zones but can globally wrinkle the flame. We can represent this using a ratio of a chemical time scale, t_l, to a turbulence time scale, t_η, in the Karlovitz number, Ka. Here the $t_\eta = (\nu/\epsilon)^{1/2}$ and $t_l = \delta_l / S_L$. For $u'/S_L > 0$, the flamelets are corrugated while for $u'/S_L < 0$ they are termed wrinkled.

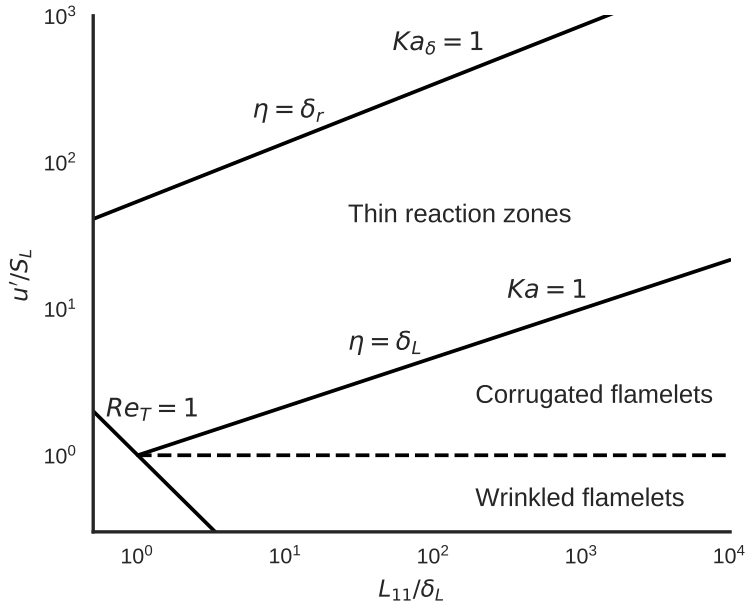

Figure 2.4: Regime diagram of premixed turbulent combustion. Labelled are each of the regimes and the lines separating those regimes. (Peters, 1999)

As the turbulent eddies become smaller, and quicker, they are able to enter the pre-heat zone and thicken the flame. This regime is called the thin reaction zones regime and occurs when the turbulence time scales are equal to the chemical time scales, i.e. $Ka = 1$. As the turbulent eddies become even smaller they are now able to enter the reaction zone of the flame and thicken the reaction zone, giving the broken reaction zones regime, the uppermost regime in Figure 2.4. This occurs when the turbulence time scales are equal to the chemical time scales, as represented by the reaction zone thickness. We define this Karlovitz number, Ka_δ, as:

$$Ka_\delta = \frac{\delta_r / S_L}{(\nu/\epsilon)^{1/2}} \tag{2.28}$$

These relationships are represented using a regime diagram (Figure 2.4). This diagram also includes the separation between laminar and turbulent flames given by the turbulent Reynolds number, $Re_T = u' L_{11} / S_L \delta_L$.

As well as turbulence, the flame surface area is also affected by instabilities such as the thermo-diffusive and Darrieus-Landau hydrodynamic instabilities. The thermo-diffusive instability (see Figure 2.5) results from the differential diffusion of heat and the deficient species. In this case we are interested in the deficient species because it is this species which will limit the rate of reaction. Figure 2.5 shows a perturbed flame front with bulges and cusps. At the bulges there is a large surface area, relative to the volume of burned gases, for the flame to lose heat (orange arrows in the diagram) and gain species (blue arrows). At the cusps the opposite is true. When $Le = 1$ the relative diffusivity of heat and deficient species is the same; for the bulges the increase in flame propagation speed provided by the additional supply of deficient species is offset by the additional loss of heat, and vice versa for the cusps. When $Le > 1$, the bulges lose heat more quickly relative to the gain of deficient species, and propagate more slowly relative to the cusps, meaning that the flame front is thermo-diffusively stable. However, when $Le < 1$, the bulges gain species quickly relative to the loss

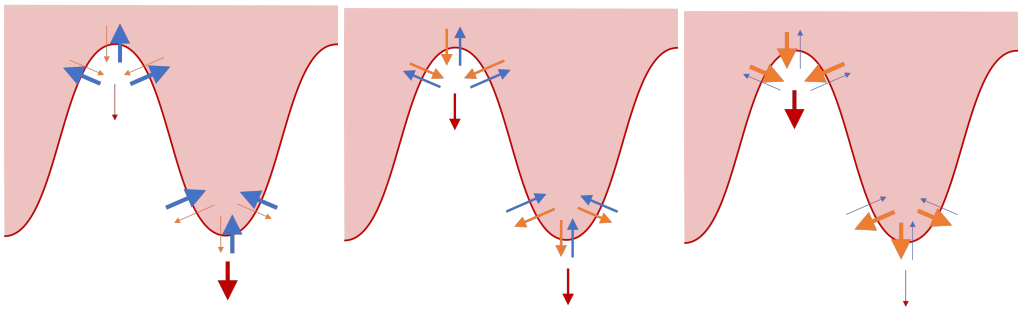

(a) $Le < 1$ (b) $Le = 1$ (c) $Le > 1$

Figure 2.5: Schematic diagrams of the effect of Lewis number and the thermo-diffusive instability. The red line represents the flame front, the shaded red the region of burned mixture and red arrows flame propagation. Orange arrows show the diffusion of heat while blue arrows show the diffusion of species. The size of the arrows are related to the rate of diffusion/flame propagation.

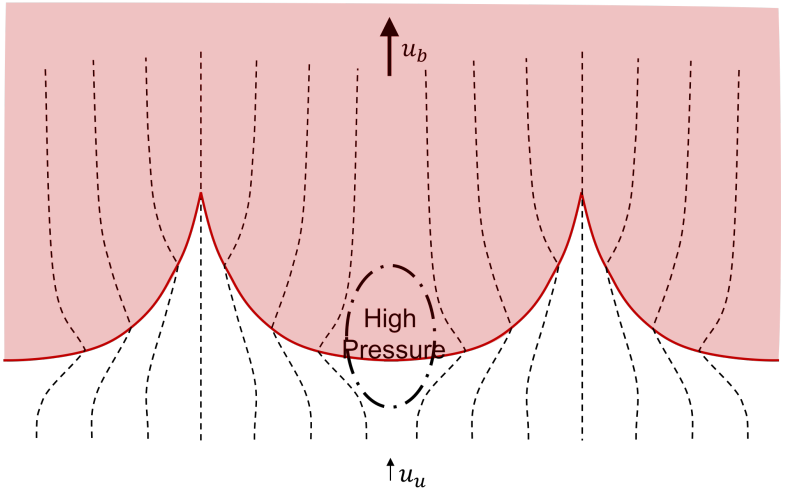

Figure 2.6: Schematic of Darrieus-Landau hydrodynamic instability (adapted from the presentation by Lipatnikov and Chomiak (2010)). Shown are the flame front (solid red), the region of burned gases (shaded red), streamlines of the flow passing through the flame front (dashed black), a region of high pressure (dot-dashed black) and the flow velocities in the unburned (u_u) and burned (u_b) regions.

of heat, propagate more quickly than the cusps, meaning that the flame front is thermo-diffusively unstable and the flame surface area will increase.

The Darrieus-Landau hydrodynamic instability (see Figure 2.6) results from the flow being diverted around leading points of the flame, increasing pressure in these regions and creating an adverse pressure gradient for the oncoming flow. The leading points of the flame are therefore subject to a lower oncoming flow than the trailing points, which results in the growth of the perturbations in the flame shape.

2.1.4 Flame-Wall Interaction

Flame-wall interaction (Dreizler and Böhm, 2015) occurs due to heat transfer between a flame and a relatively cold wall, and is significant because of the effects on flame propagation. The magnitude of the heat transfer increases as the flame approaches the wall more closely, with the heat-loss eventually becoming so great that the flame cannot propagate and is quenched.

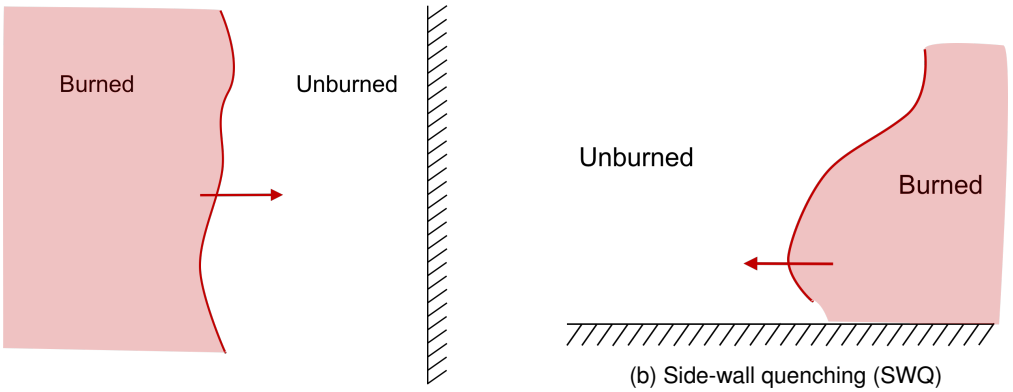

(a) Head-on quenching (HOQ)

(b) Side-wall quenching (SWQ)

Figure 2.7: Diagram of the two configurations studied in flame-wall interactions - head-on quenching (HOQ) and side-wall quenching (SWQ). Flame fronts are shown in red with an arrow indicating the direction of propagation. The burned region is shown in shaded red.

Flame-wall interaction studies have been characterised with reference to two configurations: head-on quenching (HOQ) and side-wall quenching (SWQ) (Dreizler and Böhm, 2015)(see Figure 2.7). In HOQ the flame propagates perpendicularly to the wall and approaches it directly. In SWQ the flame propagates parallel to the wall, moving along the wall. The physical processes occurring are similar and I will describe them for HOQ. In HOQ (Poinsot et al., 1993), the flame initially propagates freely, with no effect of the wall. When the flame is close enough the quenching process begins: wall heat flux increases and the flame's consumption speed drops because of this heat loss to the wall. At a given wall distance, termed the quenching distance, the wall heat flux peaks and flame propagation stops. At this point, the rate of reaction between radicals and fuel is low, and the heat release from the flame is dominated by the recombination of radicals (Popp et al., 1996; Popp and Baum, 1997; Dabireau et al., 2003; Owston et al., 2007; Gruber et al., 2010). This gives a flame structure which is different to that of a freely propagating flame (Dabireau et al., 2003; Gruber et al., 2010) and a potentially altered combustion regime (Gruber et al., 2010). The final stage of HOQ is that the unburned fuel and any intermediate species diffuse back towards the hot, burned products and react, reducing their concentration near the wall (Poinsot et al., 1993).

Flame-wall interaction is characterised by a non-dimensional distance and wall heat flux. Flame-wall distances are normalised using the flame thickness, variously the thermal or diffusive thickness, to give a Peclet number, Pe, which for the quenching distance is the quenching Peclet number, Pe_Q. The wall heat flux is normalised using a flame power, $\rho_u Y_{Fuel} S_L \Delta H = \rho_u S_L c_p \left(T_b - T_u\right)$, to give the non-dimensional wall heat flux, Φ_w.

The non-dimensional parameters Pe_Q and Φ_w have been shown to be affected by: pressure (Owston et al., 2007); equivalence ratio (Hasse et al., 2000; Owston et al., 2007); wall temperature (Popp and Baum, 1997; Hasse et al., 2000; Owston et al., 2007), fuel (Popp et al., 1996; Hasse et al., 2000; Dabireau et al., 2003; Gruber et al., 2010), Le (Lai and Chakraborty, 2016a,b; Sellmann et al., 2017; Konstantinou et al., 2021), turbulence intensity (Lai and Chakraborty, 2016a,b; Sellmann et al., 2017; Ahmed et al., 2018; Zhao et al., 2018, 2019; Konstantinou et al., 2021) and thermal expansion (Zhao et al., 2018, 2019). In particular for fuel, it has been shown (Dabireau et al., 2003; Gruber et al., 2010) that hydrogen has a significantly smaller quenching distance compared to hydrocarbon flames. For HOQ, hydrocarbon fuels have a Pe_Q around 3.5 while hydrogen has a Pe_Q around 1.7. Φ_w was also shown to be around 0.13 for hydrogen compared to around 0.33 for hydrocarbon fuels.

The interaction between turbulence, flame and wall has also been shown to significantly affect local quenching and wall heat flux. The quasi-stream-wise vortices present in the turbulent boundary layer have been shown (Bruneaux et al., 1996; Alshaalan and Rutland, 2002; Gruber et al., 2010) to push and pull material towards and away from the wall, significantly decreasing quenching distances and increasing wall heat flux.

2.2 Flashback

In this section I will present the latest investigations of boundary-layer flashback. The first two sections review numerical and experimental investigations of flashback, looking at non-swirling and swirling flows, respectively. In the final section I review the models which have been developed to predict flashback limits (the flow conditions and flame properties at the onset of flashback), flashback speed and flame shape during flashback. Before proceeding, I introduce some essential concepts in boundary-layer flashback.

Critical-Velocity-Gradient Model

The critical-velocity-gradient model (Lewis and von Elbe, 1943) has been widely used in investigating laminar boundary-layer flashback (Kalantari and McDonell, 2017) and combines the concepts from boundary-layer theory, flame propagation and flame-wall interaction to begin to understand the flashback processes occurring and predict flashback limits.

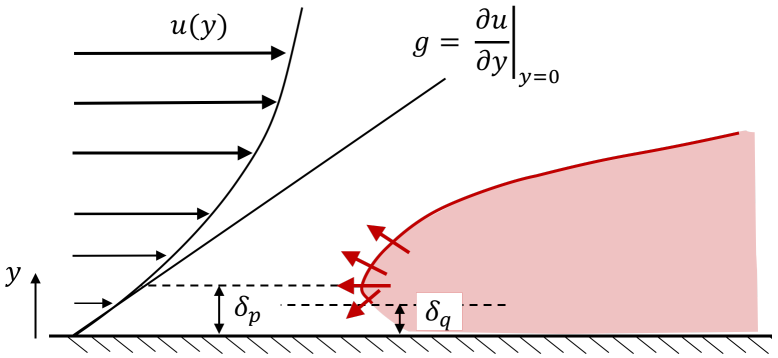

Figure 2.8: Schematic of the model of Lewis and von Elbe (1943). On the left is a laminar velocity profile (black) and on the right a flame with the flame front (red line), region of burned gases (red shaded) and flame propagation (red arrows). Diagram adapted from that in Kalantari and McDonell (2017).

Figure 2.8 shows a schematic of the critical-velocity-gradient model of Lewis and von Elbe (1943) where the flame is stationary i.e. at the onset of flashback. There is assumed to be a balance between the flame propagation and the oncoming flow velocity where, if the flame propagation speed exceeds the flow velocity at a given wall distance, then flashback will occur. The flame is assumed to propagate at a velocity $S_f(y)$ which decreases close to the wall due to heat loss before decaying to zero when the flame is quenched at the quenching distance, δ_q (as described by investigations of flame-wall interaction). There is also assumed to be a penetration distance, δ_p, at which the flame speed equals the oncoming flow velocity. For a laminar flow the flow velocity increases with y through

the boundary layer. Lewis and von Elbe (1943) assume that there is no effect of the flame on the oncoming flow. The rate of increase of flow velocity with wall distance is represented as a velocity gradient, g:

$$g = \left| \frac{\partial u}{\partial y} \right| \tag{2.29}$$

At the penetration distance, the flow velocity equals the flame speed, which is assumed to be the laminar flame speed, S_L:

$$u|_{y=\delta_p} = \delta_p g_c = S_L \tag{2.30}$$

where g_c is the critical velocity gradient at the onset of flashback and can now be given by:

$$g_c = \frac{S_L}{\delta_p} \tag{2.31}$$

Depending on the flow configuration, g_c can then be converted to a flashback limit: the flow velocity at the onset of flashback.

The model therefore combines the understanding of flame propagation, and how flame-wall interaction affects this, with the understanding of the velocity profile in a laminar boundary layer to describe the boundary-layer flashback process.

Flow Confinement

In this thesis and the investigations which are described below, the focus is maintained on the configuration with the highest flashback limits. In this section, the unconfined and confined configurations are described, and the focus on the confined configurations motivated. This section also describes the limits of the critical-velocity-gradient model of Lewis and von Elbe (1943).

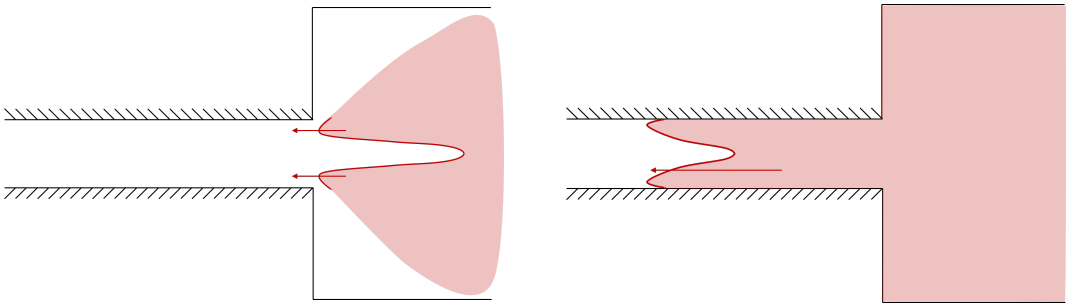

(a) Unconfined (b) Confined

Figure 2.9: Diagram showing the definition of unconfined and confined configurations as defined by Eichler and Sattelmayer (2011). The red arrows indicate flame propagation, red lines the flame front and shaded red the region of burned gases.

Eichler and Sattelmayer (2011), Eichler et al. (2012) and Eichler and Sattelmayer (2012) conducted experimental investigations, supplemented by numerical simulation, to evaluate flashback limits in unconfined and confined configurations, and to understand the effect of the flame backpressure on the different flashback limits in these configurations.

The unconfined and confined configurations are shown in Figure 2.9. In the unconfined configuration, the flame is initially stabilised within the combustion chamber and is not interacting with the wall. The

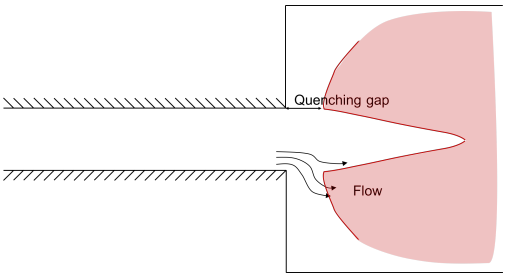

Figure 2.10: Diagram of unconfined configuration showing the quenching gap between the channel exit and the flame, and the diversion of the flow around this flame leading point. The red lines indicate the flame front, the shaded red the region of burned gases and the black arrows the oncoming flow.

flashback limit is the point at which the flame propagates upstream and is able to enter the premixing channel. In the confined configuration, the flame is already present inside the premixing channel and flashback occurs when the flame is able to propagate upstream.

Eichler and Sattelmayer (2011) and Eichler et al. (2012) investigated different confined and unconfined burner configurations and evaluated flashback limits for each. The authors showed that the flashback limits for the confined flames were significantly higher than those for the unconfined flame. The authors linked this to the flame backpressure, where the flow diversion around the leading point of the flame generates an adverse pressure gradient acting on the oncoming flow (as seen in the Darrieus-Landau hydrodynamic instability). This gives flow separation, and a region of reversed flow ahead of the flame leading point. In the unconfined case, the cold tube tip quenches the flame giving a flame that is stabilised at a distance away from the tip, termed a quenching gap (as shown in Figure 2.10). This means the flow exiting the tube diverges around the leading point of the flame, reducing the backpressure of the flame on the boundary layer and reducing the likelihood of causing reversed flow compared to the confined case.

This result is significant for two reasons: firstly, it means that flashback limits are higher for confined flames, where the flame is already present in the premixing section, and, secondly, it means that the flame and flow cannot be assumed to be independent in the confined configuration, as assumed in the model of Lewis and von Elbe (1943).

The focus of this work will be on the configurations with the highest flashback limits, the confined configuration. The following sections therefore focus on confined boundary-layer flashback in non-swirling and swirling flows.

2.2.1 Physics of Confined Boundary-Layer Flashback in Non-Swirling Flows

Laminar Flows

In this section, the propagation of flames in laminar non-swirling flows within confined configurations is reviewed. The propagation speed of these flames is then relevant to the evaluation of flashback limits. Investigations of flame propagation in both planar channels and circular tubes have been conducted. The domains investigated have mostly been two-dimensional, although some studies have extended this to three dimensions. The studies have investigated the flame shape and propagation speed of the resulting flames. Most investigations have focussed on the flame shape in the

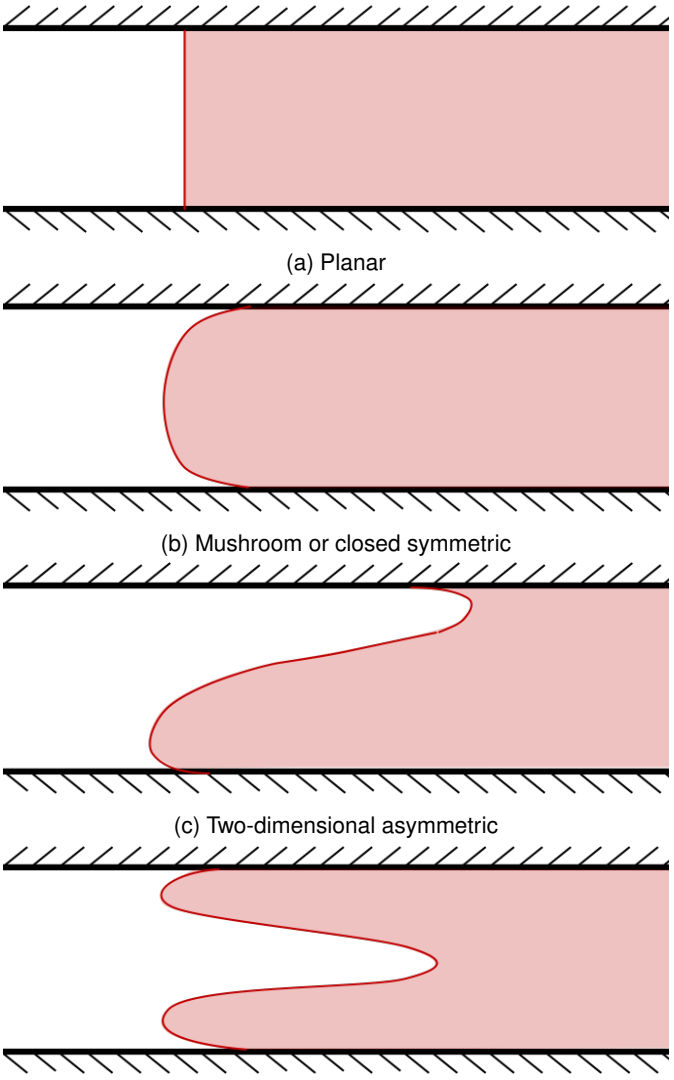

Figure 2.11: Schematics of general flame shapes. Red lines represent the flame front while the red shaded area represents the region of burned gases.

wall-normal direction but some have also investigated the growth of perturbations along the flame front. In the wall-normal direction, four flame shapes have generally been found, which are shown in Figure 2.11. The flame shapes result from the flame instabilities: thermo-diffusive, Darrieus-Landau hydrodynamic, Saffman-Taylor (resulting from differences in viscosity) and Rayleigh-Taylor. The investigations have looked into the effect of: Lewis number, incoming flow rate, channel height, wall heat-loss, wall heat transfer (along the length of the channel), and gravity on flame shape.

Kurdyumov et al. (2007) conducted experimental investigations of flame propagation in circular tubes and compared them to numerical simulations of flame propagation along a wall subject to a linear velocity gradient, with open upper boundary. These were used to determine critical conditions for flashback, where the flashback limit was found in terms of a critical Damköhler number, Da_c. Da_c is the inverse of the critical Karlovitz number, K_c, which was introduced in an earlier study (Kurdyumov et al., 2000). For a flame moving at speed, V_f, the linear velocity gradient at the wall, V', curves the flame front such that it has a radius of curvature, $l_F = S_L/V'$. K, a non-dimensional wall velocity

gradient, determines how the flame propagation speed differs from S_L. K is defined from the ratio of the diffusive thickness to the radius of curvature, which can be written in a number of forms:

$$K = \frac{\delta_T}{l_F} = \frac{V'\alpha}{S_L^2} = \frac{V'\delta_T}{S_L} = \left(\frac{U_N}{S_L}\right)^2 \tag{2.32}$$

where $U_N = \sqrt{\alpha V'}$. Defined in this way, the Karlovitz number is similar to a non-dimensional critical velocity gradient like that in Lewis and von Elbe (1943), $g_c\delta_p/S_L$, with the penetration distance, δ_p, replaced by the diffusive flame thickness, δ_T. For K_c, higher values of K_c mean a higher wall velocity gradient is required to prevent flashback, while the opposite is true for Da_c.

The simulations in this work used a variable-density flow, with power-law relations for transport properties, solving the low-Mach number conservation equations. Wall boundary conditions were also treated using a wall heat-loss parameter, k, such that the wall temperature boundary condition becomes:

$$\frac{\partial\theta'}{\partial y} + \frac{k'}{\mu}\theta' = 0 \tag{2.33}$$

where θ' is the non-dimensional temperature $(T - T_0)/(T_1 - T_0)$, based on the unburned temperature, T_0, and the adiabatic flame temperature, T_1. $k' = 0$ therefore gives adiabatic walls and $k' = \infty$ isothermal. The authors showed that: Da_c decreases with decreasing Le; that Da_c is not sensitive to changes in thermal expansion; and that Da_c varies strongly with wall heat transfer, with isothermal walls giving higher Da_c than adiabatic walls. These findings matched those of Kurdyumov et al. (2000) who conducted numerical simulations of two-dimensional planar channels, symmetric at the mid-plane of the channel, in this case using the thermo-diffusive approximation, giving a constant density flow, and a one-step overall reaction.

Tsai (2008) investigated the flame shape for flames propagating in planar channels and circular ducts with isothermal walls. DNS of methane-air flames ($\phi = 1$) were conducted, solving the complete Navier-Stokes equations using one-step chemistry. Thermal conductivity and viscosity were assumed to be linear functions of temperature, while heat capacity was assumed to be constant. Two-dimensional simulations of planar channels were conducted, simulating either half the channel with a symmetry condition at the mid-plane or the whole channel, with no symmetry condition. Simulations in circular ducts were also conducted, comparing an assumption of axi-symmetry with a three-dimensional simulation. In both of these cases, there is a critical channel height for a change in flame shape from the mushroom-shaped flame found at small channel height ($\delta = 50\delta_T$ for channels and $R = 60\delta_T$ for circular ducts). With the symmetry condition, tulip-shaped flames form, while without it, asymmetric flames form. The asymmetric flame was shown to be the stable form and to have a significantly higher relative flashback speed, $(U_{bulk} - V_f)/S_L$, where V_f is the lab-frame propagation speed. This would also give significantly higher flashback limits. In general, flashback speed is shown to increase with increasing channel height, although the increase becomes more significant above the limit of symmetry.

Kurdyumov and Fernández-Tarrazo (2002) also conducted numerical simulations in two and three dimensions of circular adiabatic, rather than isothermal, tubes, using the thermo-diffusive approximation and one-step chemistry. They also showed a critical radius for symmetry, where the flame was found to be planar below the critical radius. The authors showed that the quenching radius varies from around 1 δ_T at $Le = 0.3$ to around 16 δ_T at $Le = 1.5$, significantly smaller than the $60\delta_T$ found by Tsai (2008) for isothermal walls.

Tsai (2008) also showed that there is a critical flow rate for asymmetry, where the mushroom-shaped forms for $U_{bulk} < 0.3S_L$, with flashback speed decreasing with increasing bulk velocity. For $U_{bulk} > 0.3S_L$ the asymmetric flame forms and a v-shaped profile of flashback speed with increasing bulk velocity forms: initially increasing with increasing bulk velocity before reaching a peak and then decreasing with increasing bulk velocity.

Jiménez et al. (2015) used DNS to investigate the propagation of lean ($\phi = 0.4$) hydrogen-air flames in narrow adiabatic channels, using detailed chemistry and transport but without the Soret effect. There was again shown to be a critical flow rate and critical channel height for an asymmetric flame to form. The authors showed that, when both symmetric and asymmetric solutions were possible, the symmetric solutions were only possible when a symmetry condition was imposed and that removing this condition led to the flame becoming asymmetric. The critical channel height, above which only asymmetric solutions are stable for oncoming flows, was shown to be around 4 δ_T. The asymmetric flames again had higher propagation speeds than the symmetric, giving higher flashback limits. The Soret effect was also investigated and shown to increase the flame propagation speed at large flow rates due to the increased hydrogen transport. These overall trends of a critical flow rate and channel height for asymmetry, with the asymmetric flame having a higher flashback limits was also shown by the earlier studies of Kurdyumov (2011) who used numerical simulations with the thermo-diffusive approximation, also for planar channels with adiabatic walls, supplemented by linear stability analysis of the two-dimensional steady-state flames.

Jiménez and Kurdyumov (2017) extended the work of Jiménez et al. (2015) to include the effect of heat losses, using the same wall treatment as Kurdyumov and Jiménez (2014). The authors confirmed the findings of Kurdyumov and Jiménez (2014) that, for a flame with a Lewis number less than 1, the heat-loss to the wall gives a range of flow rates within which flame propagation is not possible. Jiménez and Kurdyumov (2017) extended this to show that increasing heat-loss gives an increasing range of flow rates. The authors again showed that the asymmetric flames have a higher burning rate than the symmetric, also showing that this results in a smaller range of flow rates where flame propagation is not possible.

Dejoan and Kurdyumov (2019) conducted variable-density two-dimensional simulations and three-dimensional DNS of the zero-Mach number Navier-Stokes equations, with one-step chemistry. This investigation simulated narrow, circular, adiabatic tubes, focussing on $Le < 1$. The two-dimensional axi-symmetric simulations showed that for negative inflow velocities both convex and concave flame shapes are possible, with the convex having a higher flame speed at larger negative flow rates. For positive flow velocities, only the concave solutions were found. The two-dimensional axi-symmetric simulations also showed the effect of the variable-density compared to the constant-density approach: firstly, there was a greater range of flow rates where two flame solutions were possible; and, secondly, the variable-density flame solutions showed higher flame propagation speeds than the constant density. The effect on flame propagation speeds contrasts with the earlier findings of Kurdyumov et al. (2007) who showed thermal expansion to have little impact.

Dejoan and Kurdyumov (2019) also conducted three-dimensional DNS and showed that the concave flame was unstable, while the convex flame was only stable for large negative flow rates, with the non-axisymmetric flame being dominant. These simulations also showed that the non-axisymmetric flames propagate faster than the axi-symmetric, giving higher flashback limits. These three-dimensional simulations were conducted for $d = (R/\delta_T)^2 = 10$ ($R = 3.2\delta_T$).

Dejoan et al. (2019) used the same simulation setup as Dejoan and Kurdyumov (2019) to investigate the propagation and asymmetry of isobaric premixed flames in planar channels. Heat losses to the wall were also included, using the same treatment as Kurdyumov and Jiménez (2014). The effect of thermal expansion, Le and heat losses were investigated. In general, asymmetric flames were shown to be stable while symmetric ones were not. Two sets of initial conditions were used: the first set initialised an asymmetric flame and the second initialised a symmetric flame with weak perturbations. For some conditions only symmetric flames form, and the asymmetric flame converges to the symmetric one. For a large set of conditions the asymmetric flame is more stable and the symmetric flame converges to the asymmetric one. For some conditions both flame types were stable and propagated at different speeds. It was also shown that, for sufficiently small Le, two flashback conditions were found: one for the symmetric and one for the asymmetric. The conditions for asymmetric flames are given by critical channel widths and flow rates above which the adiabatic flames are asymmetric. This was shown even for flames where $Le = 1$, in contrast to the constant-density results of Kurdyumov and Jiménez (2014) where the flame was always symmetric. From the point of an infinite critical flow rate with no thermal expansion, as thermal expansion increases, the critical flow rate for asymmetric flames to form decreases. Heat losses were shown to increase the stability of the symmetric flames, with the critical flow rate for asymmetric flames to form increasing with increasing heat losses. The critical channel width for asymmetric flames also decreases with decreasing Le, so that, for sufficiently small Le, the two flashback conditions are possible.

Bioche et al. (2019) investigated the effect of gravity in the wall-normal direction on flashback by comparing experimental results from flame propagation in a tube to the numerical simulations of methane-air flames in the same narrow channels. The experimental results all showed that the flame shape is asymmetric and slanted, with propagation being led at the top of the channel. The simulations included the effect of gravity and showed how baroclinic torque acts to tilt the flame. This tilting is then increased by heat conduction through the walls preheating the unburned mixture.

As well as investigating flame shape in the wall-normal direction, Fernández-Galisteo et al. (2018); Fernández-Galisteo and Kurdyumov (2019) have investigated the influence of flame instabilities on perturbations along the flame front using numerical simulation and linear stability analysis. Fernández-Galisteo et al. (2018) investigated flame shape and propagation speed within Hele-Shaw cells, which consist of two parallel plates with a very narrow gap in between where the flame propagates from an open to a closed end of the cell. To simulate this configuration, the authors conducted numerical simulations of a two-dimensional domain where fluid properties were averaged in the wall-normal direction. The simulations used one-step chemistry, constant heat capacity, variable transport coefficients with the low-Mach-number approximation. The effect of flame instabilities on the flame shape were investigated, covering: thermal expansion, buoyancy, viscosity and differential diffusion. Viscosity changes were shown to induce additional wrinkling, increasing the flame surface area and propagation speed. Thermo-diffusive instabilities promote small-scale wrinkling on the large-scale hydrodynamic structures. Thermal expansion was shown to increase flame speed with increasing density ratio, ρ_u/ρ_b. Buoyancy effects were represented using G, an inverse Froude number;

$$G = \left(\frac{\delta}{\delta_T}\right)^2 |g| \delta_T \frac{\sin\alpha}{12 Pr S_L^2} \tag{2.34}$$

where α is the cell angle. A positive value of α is used to denote flames propagating with the less dense, burned gases above the denser, unburned gases (Rayleigh-Taylor stable). The surface area

and propagation speed were shown to be linearly inversely proportional to G and, at sufficiently high G, buoyancy effects stabilise the effects of the hydrodynamic and viscous instabilities.

Summary

The investigations reviewed in this section have shown the importance of asymmetric flame shapes (in both two and three dimensions). Asymmetric flames have been shown to have higher propagation speeds than a symmetric flame for the same conditions and to generally be more stable. Critical flow rates and channel heights have been found, below which only symmetric flames can form. There critical flow rates and channel heights are strongly affected by wall heat loss and thermal expansion. Thermal expansion has also been shown to strongly affect flashback speed. Gravity acting in the wall-normal direction has been shown to give tilted, asymmetric flame shapes due to the influence of baroclinic torque.

Turbulent Flows

Eichler and Sattelmayer (2012) investigated the different confined and unconfined configurations mentioned earlier. They also further investigated the configuration of a flame stabilised on a hot, ceramic tile, which had been found to give the most stringent flashback limits. They investigated the flashback process for laminar and turbulent flames using $\mu - PIV$ and used numerical simulation to investigate the effect of the flame backpressure on the approaching flow. During the turbulent flashback process, the flame was shown to propagate as a series of bulges and cusps. These bulges can propagate upstream, remain in the same stream-wise position or be moved downstream. Each bulge is shown, after a few milliseconds, to change shape by widening laterally. In around half of cases, this widened bulge then separates into new bulges which begin the cycle again.

Eichler and Sattelmayer (2012) also used numerical simulations of laminar flames, again stabilised against a hot wall in a region of the domain. They solved the compressible Navier-Stokes equations with chemical reactions handled using an assumption of a perfectly stirred reactor for each cell, with a reduced chemical scheme for H_2-O_2. The pressure rise and region of boundary-layer separation upstream of the flame, both strongly linked to the flashback process, were investigated. It was shown that even for a hot wall with no reaction, there is a pressure rise upstream of the flame.The region of boundary-layer separation was also shown to exist even before flashback occurs, such that boundary-layer separation is not uniquely linked to flashback. It was also shown that a one-dimensional momentum balance between a point just ahead and just behind the flame front, used in later models of flashback, did not predict the pressure rise ahead of the flame.

Gruber et al. (2012) used three-dimensional, turbulent-channel-flow DNS to investigate flame flashback. The simulations solved the fully compressible Navier-Stokes equations using a detailed chemistry mechanism for hydrogen-air. Two reacting-flow simulations were conducted at 1 and 2 atm using realistic, time-varying turbulence, generated using an auxiliary, non-reacting simulation to feed data into the reacting domain. The simulations were conducted at rich conditions ($\phi = 1.5$) at $Re_\tau = 180$. Gruber et al. (2012) characterised the channel using a Damköhler number defined using the wall

time-scales, originally defined in Gruber et al. (2010):

$$Da_w = \frac{t_w}{t_l} = \frac{\nu / u_\tau^2}{\delta_l / S_L} \tag{2.35}$$

where t_w and t_l are wall and flame time scales. By this definition, the channel-flow simulations were conducted at $Da_w \approx 1.2$. The simulations were initialised as a planar flame, with a progress-variable mapping converting the one-dimensional flame profile onto the three-dimensional domain.

Gruber et al. (2012) demonstrated the transient flame propagation where the flame propagates upstream as a series of bulges and cusps across the span-wise direction. The leading points of the flame are in the near-wall region giving a v-shape wall-normally as the flames propagating against each wall meet in the centre of the channel. Gruber et al. (2012) showed that the initial wrinkling of the flame front to form these bulges and cusps is due to the low- and high-velocity streaks, where the passage of a low-velocity streak initiates a bulge and a high-velocity streak a cusp. There were also shown to be pockets of reversed flow ahead of the flame front, larger than the quenching distance from the wall, caused by the increased pressure ahead of the flame front generating an adverse pressure gradient. The flashback velocity of the flame was shown to be enhanced by the hydrodynamic instability and these reversed-flow regions.

Valiev et al. (2015) used two-dimensional simulations to investigate the influence of the hydrodynamic instability and turbulence-flame interaction on flashback velocity, by simulating two-dimensional flames propagating in a periodic shear flow. The amplitude and wavelength of the periodic flow were varied to investigate the turbulence-flame interaction using a similar configuration to Gruber et al. (2012) but in two dimensions. The fully compressible Navier-Stokes equations were solved, with chemistry represented by the same detailed mechanism for hydrogen-air. The flame was again initialised using a progress variable mapping and with the periodic inflow. Here the pressure was maintained at 1 atm, for a stoichiometric hydrogen-air flame with an unburned temperature of 298 K.

The simulations showed that there were two stages in the flame propagation. The first where the flame shape was defined by the initial shear flow and the second developing over time to be defined by the Darrieus-Landau instability. The simulations showed that the velocities at both stages of propagation were affected by the amplitude and wavelength of the periodic shear inflow.

Endres and Sattelmayer (2018) investigated the flashback of premixed hydrogen-air confined flames using Large-Eddy Simulations (LES). Their aim was to check whether experimental flashback limits could be reproduced using LES and to investigate boundary-layer separation at different points during flashback.

A non-reacting simulation was again used to feed turbulent flow into the reacting simulation. Both simulations used the Smagorinsky turbulence model with van Driest damping, with the reactive simulations using implicit LES (ILES) to calculate reaction rates from the filtered temperature and species distributions. The reactive LES simulated a channel with isothermal walls. One section of the wall was adiabatic to act as a flame holder, maintaining the flame in the domain. Flashback limits were then investigated by increasing the equivalence ratio of the incoming flow. The flashback limits were defined by the point at which flame tongues were able to propagate upstream for a substantial distance before being quenched by the isothermal walls.

The investigation showed: that flashback limits can be predicted using LES; that, for a flame stabilised on a hot wall, boundary-layer separation occurs before flashback; and that flashback only occurs when the size of the region of boundary-layer separation is larger than the quenching distance. This matches the findings of Eichler and Sattelmayer (2012) who conducted the same analysis using LES for laminar flames. Endres and Sattelmayer (2018) also showed that even when the flame is being moved downstream, after a period propagating upstream, boundary-layer separation still occurs.

Endres and Sattelmayer (2019) used the same setup of numerical simulations to study the effect of pressure on flashback limits. This investigation used detailed as well as finite-rate chemical kinetics to simulate flashback at pressures of 0.5 to 3 bar. Overall Endres and Sattelmayer (2019) found that flashback propensity increases with increasing pressure and that to predict flashback it is necessary to understand the effect of pressure on flame propagation speed, flame thickness, quenching distance and separation tendency of the approaching flow. For increasing pressure: the flame thickness decreases and the flame front becomes more wrinkled along the flame front; the turbulent flame speed decreases; and the average flame angle to the wall and flame tip radius decrease, leading to a reduction in average flow deflection. As well as these changes, quenching distance and separation-zone size also decrease with increasing pressure, with these opposing effects shown not to cancel out. Endres and Sattelmayer (2019) showed that in the majority of cases flashback occurs within the separation zone upstream of the flame front but there is no constant relation between the separation-zone size and quenching distance, and also that for the cases at low pressure, and therefore high equivalence ratio, the flame speeds were large enough that propagation upstream occurred outside of the separation zones.

Ahmed et al. (2019) and Ahmed et al. (2020) investigated turbulent boundary-layer flashback to evaluate how turbulent kinetic transport is affected during flashback Ahmed et al. (2019); and the evolution of the surface density function (SDF, $|\nabla c|$) and the influence of strain rates Ahmed et al. (2020). Their data came from a DNS of the flashback of a rich hydrogen-air mixture ($\phi = 1.5$) at $Re_\tau = 120$. For the turbulent kinetic energy transport equation during flashback, pressure dilatation and turbulent transport due to pressure were shown to be the dominant terms (Ahmed et al., 2019). The effect of strain on the SDF is shown to depend on wall distance. ∇c is expected to preferentially align with the most extensive principal strain rate when the strain rate from heat-release dominates that of turbulence, and to align with the most compressive principle strain rate in the opposite case. Ahmed et al. (2020) found that alignment with the most extensive principle strain rate strengthens as the distance from the wall increases. This is linked to a weakening of the dilatation rate in the near-wall region due to the cold wall. In addition, some of the SDF statistics were shown to qualitatively, and in some cases quantitatively, depend on the choice of species for defining the progress variable.

Summary

Investigations of non-swirling, confined boundary-layer flashback within channel flow have investigated the initiation of flashback and the propagation of the flames. During flashback the flame front is at the downstream end of a flow-separation region. Both flame front and the flow-separation region move upstream as flashback occurs. The flow-separation region results from volumetric expansion through the flame front and its confinement by the wall generating an adverse pressure gradient. Some investigations have linked the onset of flashback to boundary-layer separation or a region of

boundary-layer separation larger than the quenching distance. However, later investigations have shown that boundary-layer separation can be present upstream for a stable or receding flame, and that flashback can occur outside of a region of boundary-layer separation. In a turbulent flow, the high- and low-velocity streaks generate a bulge and cusp structure along the flame front. The bulges, initiated in the low-velocity streaks, lead the flashback process. These bulges were shown to move downstream for a period before widening laterally and sometimes breaking up into a new series of bulges.

2.2.2 Physics of Flashback in Swirling Flows

This section reviews the experimental investigations of flashback against the centre-body of a mixing tube in swirling flows. Given the small number of investigations into swirling flow, both confined and unconfined configurations are included in this section.

Nauert et al. (2007) experimentally investigated unconfined flashback within a swirling flow for a burner with centre-body. Flashback limits, in terms of a critical swirl number, were evaluated for a range of equivalence ratio and Reynolds number. Here an increase in swirl number was shown to precipitate flashback from the combustion chamber into the mixing tube. The flashback process was also captured: at low swirl, the flame was stabilised in the combustion chamber above the bluff body; at higher swirl, the flame stabilised next to the bluff body (which was extended outside of the mixing tube) and precessed around it; a small increase in swirl number from this point caused the flame to enter the mixing tube and flashback rapidly. The estimated burning velocity was found to be much smaller than the flashback speed, which the authors link to reverse flow resulting from azimuthal vorticity.

Heeger et al. (2010) used the same burner as Nauert et al. (2007) to investigate flashback, finding flashback limits for different Reynolds numbers in terms of critical equivalence ratios. Heeger et al. (2010) showed that the flashback process is associated with negative axial velocities ahead of the flame tip. The authors describe a mechanism for these negative axial velocities where the radial pressure gradient and density drop in the burned gases combine to cause an increase in static pressure in the burned gases which opposes the oncoming flow and causes the negative axial velocities.

Karimi et al. (2015) conducted an experimental and theoretical investigation into flame flashback in swirling flows against the centre-body of the burner. This investigated the mechanism of flame propagation described by Heeger et al. (2010) where the radial pressure gradient causes an increase in pressure in the burned region. Experimental measurements of pressure were made on the burner centre-body and then an existing approach used to describe flame propagation in the core of a vortex (Ishizuka et al., 1998) was adapted to this configuration to predict flashback speed and the pressure change. Karimi et al. (2015) found the pressure rise to be between 20 and 30 Pa, which matched that predicted by the previous work (Ishizuka et al., 1998; Ishizuka, 2002) on flame propagation in a vortex core:

$$\Delta P = \rho_u V_{\theta max}^2 \left[1 - \left(\frac{\rho_b}{\rho_u} \right)^2 \right] \tag{2.36}$$

where V_θ is the circumferential velocity. The analytical analysis conducted by Karimi et al. (2015) will be covered in the next section, on flashback models.

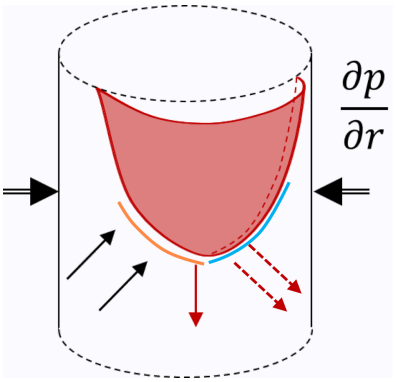

Figure 2.12: Schematic of swirling-flow flashback in an annulus. The solid black arrows show the local flow direction, the solid red arrow the mean direction of flame propagation, the dashed red arrows the local direction of flame propagation and the double-lined black arrows represent the radial pressure gradient. The blue line highlights the leading and the orange line the trailing side of the flame, as described by Ebi and Clemens (2016).

Ebi and Clemens (2014), Ebi and Clemens (2015), Ebi and Clemens (2016), Ebi et al. (2018) and Ranjan et al. (2019) investigated flashback for a swirl combustor for mixtures of methane, and hydrogen and methane in air. Each investigation developed the measurements taken within the flame and flow, with the latest investigation (Ebi et al., 2018) measuring velocity fields in the unburned and burned gases and processing these to give the velocity fields in the frame of reference of the leading point of the flame.

This set of investigations showed that there are some fundamental differences in the mechanism by which propagation occurs in these swirling flames compared to those in non-swirling channel flow. In channel flow, flashback occurs from small-scale bulges in the flame front propagating upstream through the low-velocity streaks of the boundary layer. In a swirling flow it was shown that propagation occurs through a larger-scale flame tongue with one leading point moving upstream. This flame tongue (Figure 2.12) moves, on average, down the centre-body while also precessing around the centre-body with the swirling flow. Ebi and Clemens (2016) define the flame tongues as being different to the bulges by their size. The flame tongues have a characteristic size of the order of the diameter of the mixing tube (20 - 30 mm) whereas the bulges have a characteristic size of the order of 2 - 3mm, more similar to the size of the turbulent structures in the flow. Small-scale bulges are formed on the flame tongue which can sometimes propagate upstream for a distance but ultimately are pushed back by the oncoming flow. These small-scale bulges show the same propagation mechanism as in channel flow where a region of reversed flow is created ahead of the flame front into which the flame propagates. However, the flame tongue does not flashback by this mechanism.

Ebi et al. (2018) developed the description of the structure of the flame tongue (Figure 2.12). The leading point of the flame, the flame base, is defined as the most upstream point of the flame. Downstream of this, facing the oncoming swirling flow, is a trailing side (highlighted in orange in Figure 2.12) which is identified as being the wake from the leading side. This trailing side was shown to be wedge shaped in the wall-normal direction. The leading side (highlighted in blue) is downstream of the flame base but facing away from the oncoming flow. This leading side was shown to be a typical premixed flame front with a convex shape to the reactants in the wall-normal direction.

Ebi and Clemens (2016) also contrasted the behaviour of methane-air and hydrogen-methane-air flames. The hydrogen-methane-air flames showed more frequent occurrence of small-scale bulges

than the methane-air, that these bulges were smaller in size and had a greater ability to propagate upstream for short distances than the methane-air flames. This was linked to the smaller quenching distance and larger flame speeds of hydrogen-air flames. Overall this difference was not linked to the upstream propagation of the flame with hydrogen-methane-air flames showing the same mechanism of upstream propagation, through the formation of flame tongues.

Ranjan et al. (2019) used the experimental data to construct a steady flame shape and velocity field in the frame-of-reference of the flame. This allowed the construction of quasi-streamlines and an analysis of the velocity components and forces acting on the flow along this quasi-streamline. The lab-frame speed of the flame front as well as its shape are nearly constant during propagation. This allowed the flame-front profiles and velocity fields from a series of points in time to be combined to produce the steady velocity field and flame shape. Ranjan et al. (2019) then showed how the flow approaching the flame is deflected radially around the leading point of the flame because of the blockage effect from volumetric expansion and, additionally for the swirling flow, due to the centrifugal force acting. This radial deflection will reduce the speed of the oncoming flow, increasing the likelihood of flashback. The centrifugal force is proportional to the angular velocity of the flame tongue and so the reduction in speed of the oncoming flow will increase with swirl.

Ranjan et al. (2019) also showed that the Coriolis force impacts the streamline. In the burned gases, the Coriolis force acts to divert the flow closer to the centre body, reducing its radial position. The authors describe this as a possible explanation for the increase in pressure in the burned gases, as measured by Karimi et al. (2015).

Ebi et al. (2020) investigated flashback for a swirl combustor for mixtures of methane and hydrogen, and air at elevated pressure (2.5 bar). The effect of the proportion of hydrogen on flashback limits was measured and compared to the predictions of the critical velocity gradient model, a model based on boundary-layer separation (Hoferichter et al., 2016) and a scaling using the extinction stretch rate.

Ebi et al. (2020) showed that flashback limits, in terms of equivalence ratio, become smaller with increased proportions of hydrogen. The investigation also showed a different flashback mechanism for the swirling flow compared to that seen in the previous investigations (Ebi and Clemens, 2014, 2015, 2016; Ebi et al., 2018). In this second mechanism, the flame propagated more similarly to flame propagation in non-swirling channel flows: the flame propagates locally against the oncoming flow (lead by the orange side in Figure 2.12) with small-scale bulges forming along the flame front, also facing this oncoming flow. This is in contrast to the previous investigations which showed the small-scale bulges not leading flame propagation and the flame moving locally with the swirl rather than directly upstream.

Ebi et al. (2020) suggest that propagation of the side facing the oncoming flow is linked to quenching due to stretch and therefore derived flashback limits for the point at which the extinction stretch rate matched that stretch rate within the turbulent boundary layer. This was used to derive a flashback Karlovitz number:

$$Ka^{FB} = \frac{\kappa_{shear}}{\kappa_{ext}} \tag{2.37}$$

where κ_{ext} is the extinction stretch rate and κ_{shear} represents the stretch rate of the turbulent boundary layer, given by:

$$\kappa_{shear} \sim \theta \frac{\partial u}{\partial r} \sim \frac{S^u_{d,crit}}{u} \frac{\partial u}{\partial r} \tag{2.38}$$

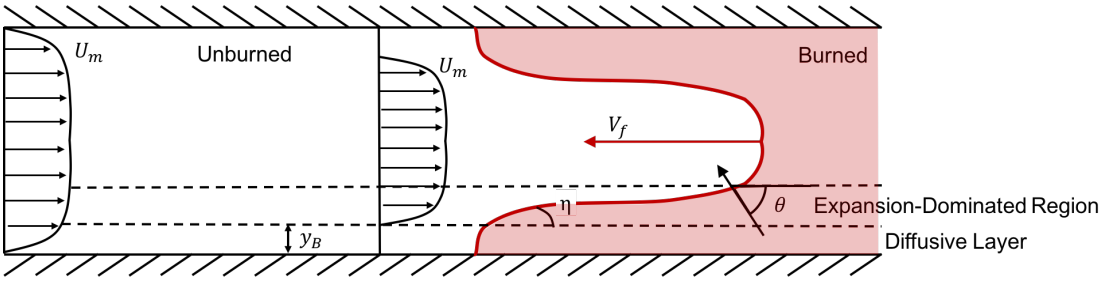

Figure 2.13: Schematic for the model of mean flame shape (Gruber et al., 2015). The flame front is represented by the red line, with the shaded red the burned region, while the black arrows represent the oncoming flow. The diagram shows a flame propagating from right to left against the oncoming flow.

where $\partial u/\partial r$ is the velocity gradient evaluated at twice the stretched laminar flame thickness, $S^u_{d,crit}$ is the stretched flame speed evaluated on the unburned side of the flame front.

Summary

For swirling flows, investigations have been conducted of flashback within a swirling flow against the centre-body of a mixing-tube. These investigations have shown that an increase in swirl can precipitate flashback and that the pressure in the burned gases increases for a swirling flow. The flashback process is also different to that of non-swirling flows. A flame tongue forms which propagates upstream. In some cases, the side of the tongue facing the oncoming flow propagates upstream as a series of bulges and cusps, similar to flashback in non-swirling flows. In other investigations the side facing the oncoming flow is just a wake from the side of the tongue not facing the oncoming flow, and it this other side which leads flame propagation upstream.

2.2.3 Flashback Models

This section reviews models of flashback that have predicted flashback limits, flashback speed and flame shape during flashback. For this section, models for unconfined and confined configurations have been included to show the range of approaches used. The different approaches have been broken down into: kinematic, bulk-momentum, empirical and boundary-layer-separation, each of which is covered in the following sections.

Kinematic

Gruber et al. (2015) derived a model of the mean flame shape during confined flashback in turbulent boundary layers. The model (Figure 2.13) separates the flow and flame into different regions and derives relationships for the flame angle in each. This is combined with models for the lab-frame propagation speed, V_f, to predict a mean flame shape. The results are then evaluated using two of the authors' DNS of flame flashback.

Figure 2.13 shows a schematic of the mean-flame-shape model. The flame shape is assumed to be stationary and to move with a lab-frame velocity, V_f. The position of the flame front is described by

a balance between the local mean flow, $\overline{u}(y)$, and the turbulent propagation speed, S_T of the flame front, which is at an angle of θ from being wall-parallel. Writing this at a given point along the flame front and at the channel centre-line gives:

$$V_f = U_m(h) - S_T(h) = U_m(y) - S_T(y)/\cos\theta(y) \tag{2.39}$$

where h is the channel half-height. At the wall, S_T will become zero such that θ approaches $\pi/2$ i.e. it is a thin wedge propagating upstream. However, in the near-wall region volumetric expansion will have an effect. In a planar flame the thermal expansion across the flame front, resulting from the lower density of the burned mixture compared to the unburned, causes an acceleration of the burned mixture. However, for a v-shaped flame in a channel, the wall constrains expansion in this direction, resulting in expansion away from the wall. This will tilt the flame front away from being parallel to the wall and cause the flame front to propagate faster by a factor of the density ratio, $D = \rho_u/\rho_b$. This gives a wall-normal flame propagation speed of DS_L and wall-parallel propagation speed of V_f meaning that in the expansion-dominated region the flame-front angle obeys $\tan\eta = DS_L/V_f$, where η is the flame angle to the wall in the expansion-dominated region (shown in Figure 2.13). The second effect of the volumetric expansion is to cause an increase in pressure, generating an adverse pressure gradient which opposes the oncoming flow and deflects the oncoming flow around the flame front. This blockage effect is characterised as occurring in a blockage height given by the wall distance separating the region where diffusive effects dominate and the expansion-dominated region. The region of diffusive effects are described using a wall-normal diffusive spreading of a scalar controlling flame advancement. The distance from the wall is then described using $y \sim (\kappa x/S_L)^{1/2}$. The wall distance at which this flame angle matches that given for the expansion-dominated region then defines the blockage height. DNS-derived mean velocity and velocity-fluctuation profiles are then compressed into the region between the blockage distances from each wall.

Using this approach it then remains to use the lab-frame flashback velocity and turbulent burning velocity to calculate the flame angle. The lab-frame flashback velocity is calculated based on an analysis of curved flames in channel flows Bychkov et al. (1999) using:

$$V_f \sim -aS_L \tag{2.40}$$

$$a = 1 + \frac{D(D-1)^2}{D^3 + D^2 + 3D - 1} \tag{2.41}$$

where D is the density ratio ρ_u/ρ_b, while the turbulent burning velocity is assumed to follow:

$$S_T = ((Bu')^2 + (aS_L)^2)^{1/2} \tag{2.42}$$

where the parameter B describing the effect of velocity fluctuations on the turbulent burning velocity is calculated using existing DNS databases. This gives $S_T(y)$ which, with the relations for the diffusive layer and expansion-dominated region, and the velocity profile $U_m(y)$ allows a solution for $\theta(y)$ to be found.

Gruber et al. (2015) used two DNS of flame flashback to evaluate their model of mean flame shape. For the case with a larger statistical sample, where the authors believe the turbulent fluctuations will have been averaged out more, the model aligns well with the mean flame shape in the main part of the flow. The model also gives good predictions for the leading point of the flame, lending validity to the blockage height model given. However, the prediction of the flame angle is poor in the near-wall

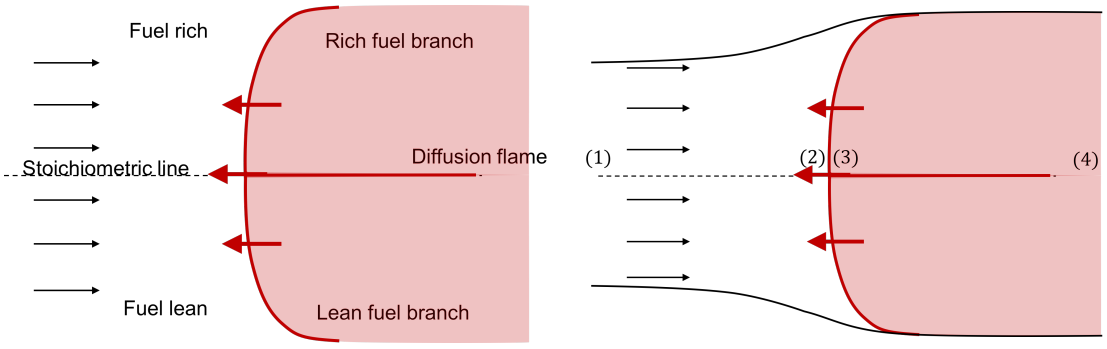

(a) Structure of a triple flame.

(b) Model configuration.

Figure 2.14: Diagrams of the structure of a triple flame (a) and the model configuration of Ruetsch et al. (1995) (b). Points (1) to (4) are on the stoichiometric line and represent: far upstream, immediately before the flame, immediately behind the flame and far downstream.

region where the model assumes a constant flame angle (given by $\cos\theta = S_L/V_f = 1/A$) but the DNS results show a highly curved flame front where, moving away from the wall, the flame normal initially points towards the wall, before becoming parallel to the wall and then facing away from the wall. Given that this point on the flame front leads the propagation of the flame upstream it would be beneficial if the model could predict the flame shape in this region. Overall, the model is only evaluated using two DNS cases, with different Damköhler and Lewis numbers, and further validation of its predictions is required.

Bulk Momentum

Ruetsch et al. (1995) investigated triple flames and developed a model for the increase in flame speed due to the effects of heat release (shown in Figure 2.14). A momentum balance was conducted in a control volume between two streamlines which just touched the outside edge of the flame. Four points along the line of stoichiometry were then considered: far upstream (1) and far downstream (4), and points either side of the flame front (2) and (3). By applying the Rankine-Hugoniot equations and a mass balance over the whole control volume, an equation for the velocity ratio between points 1 and 2 was derived, where the velocity at point 2 was assumed to be the laminar burning velocity, S_L. Solving the momentum balance gave an equation for the height ratio δ_1/δ_4. Given the unconfined configuration, the pressures everywhere were assumed to be equal. Solving the equations for the velocity and height ratios gave a velocity ratio, $u_1/S_L = \sqrt{\rho_u/\rho_b}$. This approach showed that the heat release across the flame front causes an increase in flame speed for a curved flame. The volumetric expansion through the flame front causes a diversion of the flow around the leading point of the flame. The flame is therefore effectively propagating into a slower oncoming flow, giving a propagation speed faster than the laminar flame speed.

Karimi et al. (2015) conducted a theoretical analysis of flame flashback in swirling flows against the centre-body of the burner, using a bulk-momentum approach with experimental data for validation. This investigated a mechanism of flame propagation caused by the rise of pressure behind the flame front resulting from the centripetal acceleration acting on the lower density burned products.

The derived model is based on an analysis of flame propagation along a vortex core conducted by Ishizuka et al. (2000); Ishizuka (2002). The derivation applies a momentum balance to control

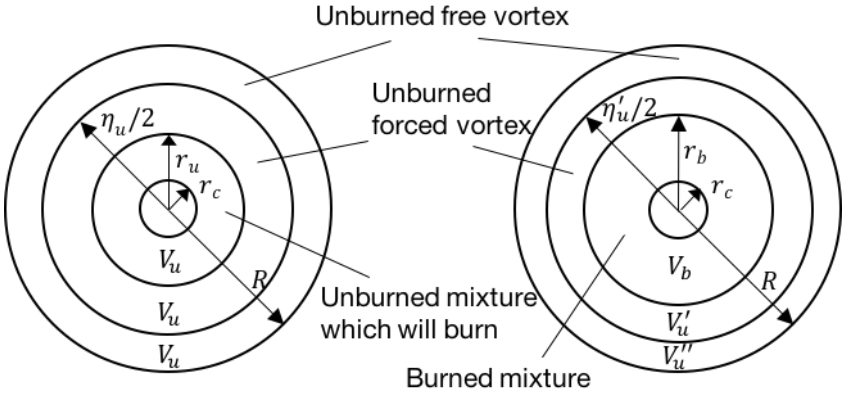

Figure 2.15: Diagram of the basis for the model of Karimi et al. (2015).

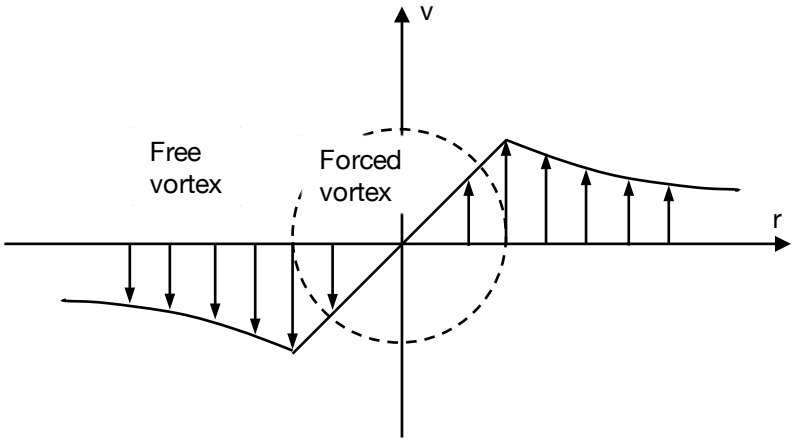

Figure 2.16: Velocity distribution within the assumed Rankine vortex.

volumes separating the flow into three regions (see Figure 2.15). Firstly, the swirling flow is assumed to be a Rankine vortex containing a forced vortex inner and free vortex outer (Figure 2.16). The forced vortex is then separated into two regions based on the flow downstream of the flame leading point: the first region contains the mixture burned and the second remains unburned. For the flow upstream of the flame leading point, this gives a region which will burn and a region which will not. The axial velocity is assumed to be uniform while the radial velocity is zero. This approach also assumes the flow is axi-symmetric, laminar and inviscid, the flame is laminar and premixed with a constant flame speed and that momentum is conserved during combustion. The flow within the burned and unburned regions is assumed to be of constant density. The model then applies the conservation of mass, and linear and angular momentum, with the radial momentum equation to predict both the pressure rise and increase in flame speed caused by flame propagation along the centre-body of the burner. The model was able to match the measured pressure rise from the small set of experimental data and predicts an increase in flame speed, although this was not measured in the experiment. This approach contains a number of large assumptions such as a constant axial velocity, with no boundary layer, and the assumption that the flow against the centre-body is sufficiently one-dimensional not to account for the volumetric expansion of the stream tube through the flame front. The model also requires the specification of the relative radii of the different regions of the flow and the ratio of the flame surface area to the cross-sectional area of the flow,

which are not evaluated by the model. However, the model is able to predict the pressure rise and increase in flame speed for this swirling-flow configuration.

Boundary-layer separation model

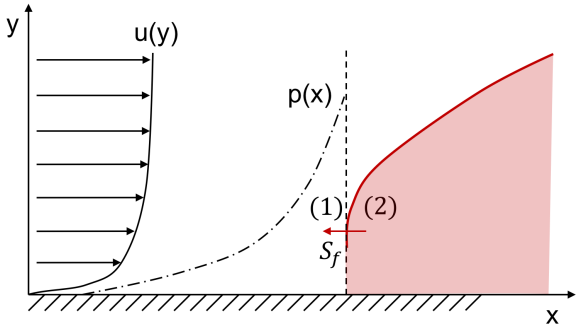

Figure 2.17: Diagram illustrating the basis of the boundary-layer-separation model (Hoferichter et al., 2016). The flame front (shown in red) is propagating from right to left against the oncoming flow. The pressure distribution, $p(x)$, follows a parabolic profile ahead of the flame front. Also marked are the two points ((1) and (2)) between which the mass and momentum balances are conducted to derive the expected pressure rise ahead of the flame tip.

Hoferichter et al. (2016) derived semi-analytical flashback limits for confined flames in channel flow based on boundary-layer separation theory (shown in Figure 2.17). The model is based on the observation from experiments and simulation that during flashback the flame moves upstream with a pocket of reversed flow ahead of it. This model therefore uses Stratford's criterion for boundary-layer separation combined with an empirical pressure distribution and turbulent burning velocity to predict the occurrence of boundary-layer separation and therefore flashback.

Stratford's criterion for boundary-layer separation is (Hoferichter et al., 2016):

$$C_p \left(x \frac{dC_p}{dx} \right)^{\frac{1}{2}} = 0.39 \left(10^{-6} Re_x \right)^a \tag{2.43}$$

where C_p is the pressure coefficient $C_p(x) = (p(x) - p(x=0))/(1/2\rho u^2)$, Re_x is a position-of-separation-based Reynolds number, $Re_x = ux/\nu$, with x being the position of separation and the suggested value for the exponent a is 0.1. Hoferichter et al. (2016) assume a quadratic pressure distribution ahead of the flame based on empirical observations:

$$p(x) = p(x=0) + \frac{\Delta p}{x_f^2} x^2 \tag{2.44}$$

where Δp is the pressure rise across of the flame. This can be differentiated and combined with Stratford's criterion (2.43) to give a relation for the free-stream velocity U_{FB} at the onset of flashback:

$$\sqrt{2} \left(\frac{2\Delta p}{\rho_u U_{FB}^2} \right)^{\frac{1}{2}} = 0.39 \left(10^{-6} \frac{U_{FB} x_f}{\nu_u} \right)^a \tag{2.45}$$

To make the result independent of the flame-tip position, the exponent a is set to zero, which the authors test the effect of and show to have little influence. To model the pressure rise upstream of the flame front, mass and momentum conservation are applied either side of the flame front assuming one-dimensional flow and are combined to give:

$$\Delta p = p_u - p_b = \rho_u S_t^2 \left(\frac{\rho_u}{\rho_b} - 1 \right) \tag{2.46}$$

The authors then use established models for the turbulent burning velocity, S_t. These models account for the laminar, unstretched burning flame speed, $S_{L,0}$, the flame stretch rate and effect of flame stretch through the Markstein length, and the level of velocity fluctuations in the channel and the effect of those velocity fluctuations on the overall flame speed. Flashback is assumed to occur where the turbulent burning velocity is at its maximum. This corresponds to the wall distance with the highest velocity fluctuations, $y^+ = 16.4$.

The derived model is compared to experimental results for flashback limits and seems to predict very similar values. As well as channel flow, the model is used for tube flow where the near-wall normalised velocity fluctuations are described as being similar and the overall model gives predictions in good agreement with experiments. However, this derivation is based on flashback occurring when boundary-layer separation occurs. Eichler and Sattelmayer (2012) noted that boundary-layer separation can occur for flames which are not undergoing flashback, while Endres and Sattelmayer (2019) noted flashback occurring outside of the region of boundary-layer separation. Eichler and Sattelmayer (2012); Endres and Sattelmayer (2019) also showed how the pressure rise upstream of the flame is overestimated by the one-dimensional relation used. This relation also gives the pressure drop resulting from volumetric expansion through the flame rather than the pressure rise ahead of the flame, which is the input required. Endres and Sattelmayer (2019) also showed that the boundary-layer separation criterion underestimates the flow separation probability. Flashback is assumed to occur at the point of maximum turbulent burning velocity, where the velocity fluctuations are the highest. However, this does not account for the distribution of the mean flow and therefore the relative velocity of the flame and flow. Gruber et al. (2015) found that flashback occurs in the region where low-velocity streaks are present, with the flame propagating upstream through these streaks. Depending on the particular velocity and velocity-fluctuation distribution, flashback may be more likely to occur at other wall distances.

Björnsson et al. (2020) modified and extended the boundary-layer-separation model of Hoferichter et al. (2017). Björnsson et al. (2020) describe the original model as working well at room temperatures but deviating significantly at low Lewis numbers and at higher pre-heat temperatures. Björnsson et al. (2020) aim to extend the model for application to diffusers as well as planar channels and pipes while improving the prediction of the back-pressure, which Endres and Sattelmayer (2019) showed to be over-predicted by the model. The model of Björnsson et al. (2020) makes the following modifications: a generalised version of the boundary-layer stability criterion is used, as opposed to one for a flat plate; the outer-layer boundary-layer velocity profile is assumed to follow a power-law, which is fitted for each geometry, so that the approach can be applied to other geometries; the adverse pressure gradient is now a combination of the flame-generated back-pressure, as originally used by Hoferichter et al. (2017), and a local-flow adverse pressure gradient; and the Markstein-length correction used in the calculation of turbulent flame speed is replaced by a Lewis-number correction to improve predictions at low Lewis number. The generalised Stratford criterion used is

now:

$$C_p^{\frac{1}{4}(n-2)} \left(\delta \frac{dC_p}{dx}\right)^{\frac{1}{2}} = \left(\frac{3\,(0.41\beta)^4}{(n+1)n^2}\right)^{\frac{1}{4}} \left(1 - \frac{3}{n+1}\right)^{\frac{1}{4}(n-2)} \tag{2.47}$$

where β is an empirical coefficient equal to 0.73, δ is the boundary-layer thickness and n is a constant, assumed to equal 6. Overall these modifications do give better predictions at higher pre-heat temperatures, with significantly improved predictions of the pressure rise over the flame front. Endres and Sattelmayer (2019) investigated diffusers with angles of 2° and 4°. Björnsson et al. (2020) show that their model gives reasonable predictions for a diffuser angle of 2° but there are still discrepancies for the 4° diffuser, even with the adjustment of the parameter C in the Damköhler correlation:

$$\frac{S_t}{S_L} = 1 + C\left(\frac{u'}{S_L}\right)^{0.5} \tag{2.48}$$

The model also still requires the assumption for the stream-wise extent of the flame back-pressure profile (equal to 1 cm).

Summary

In the previous section I have presented a number of models which variously aim to predict flashback limits and speeds, and flame shapes. Gruber et al. (2015) predicts mean flame shape during channel-flow flashback using models for the flashback velocity and turbulent burning velocity, and the properties of the fuel and a turbulent channel flow. Hoferichter et al. (2016) (extended by Björnsson et al. (2020)) predicted flashback limits for channel-flow flashback based on a predicted pressure rise upstream of the flame and a model for the turbulent burning velocity using boundary-layer-separation theory. Karimi et al. (2015) predicted the pressure rise and flashback velocity based on a momentum balance in swirling flows, based on previous work which applied the analysis to flame propagation along a vortex core. The final model requires inputs of the fuel and flow properties: density ratio and swirl number; and the areas of each part of the vortex in the unburned and burned regions. Ruetsch et al. (1995) predicted the flame-speed enhancement due to heat release in a triple flame. Their final model predicts the flame speed as a function of the laminar flame speed and the density ratio.

2.3 Gravity Currents

The situation where the radial pressure gradient of a swirling flow causes an increase in pressure in the burned gases, as described by Heeger et al. (2010), is loosely analogous to the situation in gravity currents where two fluids of different densities flow relative to one another due to gravity. In comparison to boundary-layer flashback, gravity currents are relatively well characterised and a number of simple models for the propagation speed of gravity currents have been developed. The analogy between density-driven flow in gravity currents and boundary-layer flashback may suggest approaches that can be applied in order to model flashback phenomena.

A gravity current is the flow of one fluid within another driven by differences in hydrostatic pressure resulting from the density difference between the two fluids (Simpson, 1982; Härtel et al., 2000b). This density difference can be a result of dissolved material or temperature differences between the

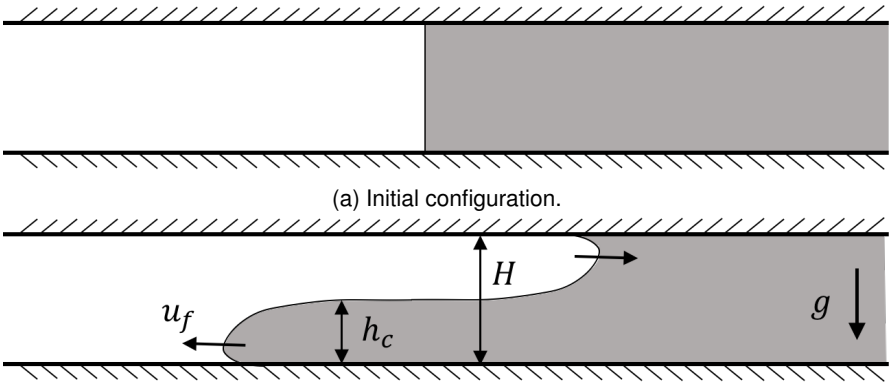

(a) Initial configuration.

(b) Propagation of fluid front.

Figure 2.18: Schematic diagrams of gravity currents in lock-exchange flow. The shaded grey area shows a fluid of higher density than the white area. The black arrows indicate pressure-driven flow. The overlain axes represent the pressure distribution at the given axial position.

fluids (Simpson, 1982) and occurs naturally in: sea breezes, which are the flow of relatively cold, dense air within the atmosphere, and pyroclastic flows from volcanic eruptions, as well as industrially in the flow of molten glass to make sheet glass (Huppert, 2006).

Gravity currents are commonly studied in lock-exchange flows (Härtel et al., 2000b)(shown in Figure 2.18), where two fluids of different densities are initially separated by a vertical gate within a planar channel. The gate is removed and the fluids flow into one another. After an initial transient, the fronts propagate at a steady speed. The speed of the front is denoted u_f for a height of the fully developed gravity current, h_c. The configuration is scaled using: the channel half-height, δ; average density of the two fluids, ρ_a; and buoyancy velocity, u_b:

$$u_b = \sqrt{g'\delta} \tag{2.49}$$

where g' is the densiometric gravity:

$$g' = g\frac{(\rho_{max} - \rho_{min})}{\rho_a} \tag{2.50}$$

A number of non-dimensional numbers are defined from these. The Grashof number, Gr, defines the ratio of buoyancy and viscous forces:

$$Gr = \left(\frac{u_b\delta}{\nu}\right)^2 \tag{2.51}$$

A Reynolds number for the fully developed front, Re_g, is defined:

$$Re_g = \frac{u_f h_c}{\nu} \tag{2.52}$$

The Froude number is defined either using the ratio of the front velocity and either $g'h_c$ or $g'H$:

$$Fr_b = \frac{u_f}{\sqrt{g'h_c}} \tag{2.53}$$

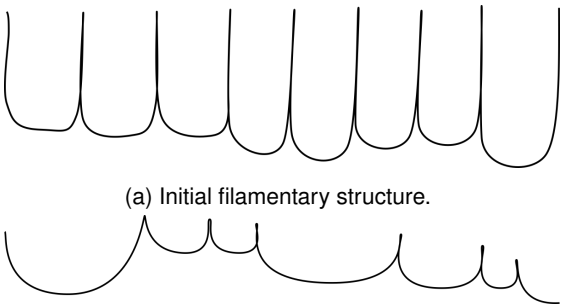

(a) Initial filamentary structure.

(b) Lobe-and-cleft pattern.

Figure 2.19: Pattern of the lobe-and-cleft instability along the fluid front on a plane parallel to the wall (Härtel et al., 2000a).

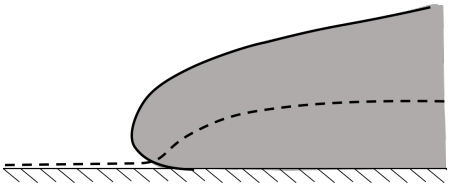

Figure 2.20: Schematic diagram of the lobe-and-cleft gravitational instability (Härtel et al., 2000a). The shaded grey area shows a fluid of higher density than the surrounding white area. The dashed black line shows a stagnation streamline.

$$Fr_H = \frac{u_f}{\sqrt{g'H}} \tag{2.54}$$

Models have been developed which predict Fr_b. Von Kármán (1940) applied the Bernoulli condition along the interface of the two fluids and showed that $Fr_b = \sqrt{2}$. This is invalid in deep water because of the dissipation along the interface (Simpson, 1982). Benjamin (1968) instead used a momentum integral and showed that Fr_b is dependent on the overall height of the fluids, H: varying from $\sqrt{2}$ for $h_c/H = 0$ (matching the result of Von Kármán (1940)) to $1/\sqrt{2}$ for $h_c/H = 0.5$, based on the following equation:

$$Fr_b = \sqrt{\left(2 - \frac{h_c}{H}\right)\left(\frac{1 - h_c/H}{1 + h_c/H}\right)} \tag{2.55}$$

Shin et al. (2004) added the exchange between the front of the gravity wave and the backward-propagating disturbance to give Fr_H in terms of the initial depth of release, δ_i (Cantero et al., 2007):

$$Fr_H = \frac{1}{2}\left[\frac{\delta_i}{H}\left(2 - \frac{\delta_i}{H}\right)\right] \tag{2.56}$$

This gives values of $1/\sqrt{2}$ at $h_c/H = 0$ and 1 at $h_c/H = 0$, compared to the $1/\sqrt{2}$ and $\sqrt{2}$ of Benjamin (1968) (Cantero et al., 2007).

Three-dimensional gravity currents have been shown to develop a lobe-and-cleft structure along the fluid front due to a gravitational instability (Härtel et al., 2000a). The development of the lobe-and-cleft instability begins with a filamentary structure (Figure 2.19a) which develops into the lobe-and-cleft pattern shown in Figure 2.19b. The structure develops from the gravitational instability shown in Figure 2.20: a stagnation streamline passes underneath the leading point of the front, giving an unstable region, where the denser fluid is above the less-dense fluid, and resulting in a lobe-and-cleft structure along the fluid front. In addition to the lobe-and-cleft instability, Kelvin-Hemholtz vortices

can form at the fluid front downstream of the leading edge, at sufficiently high Gr (Härtel et al., 2000b).

2.4 Proposed Approach

Following the review above, a number of practical research questions are defined which will be investigated in this thesis:

- As relevant to the use of hydrogen and hydrogen-rich fuels within industrial gas turbines:
  - what is the physical mechanism for boundary-layer flashback within swirling flows?
  - how does a wall-normal pressure gradient affect flashback speed?
  - how does an oblique flow orientation affect flashback?
  - how does the annular geometry affect flashback in non-swirling and swirling flows?
  - how does a developing boundary layer affect flashback speeds?

An increase in swirl has been shown to initiate flashback (Nauert et al., 2007) but the mechanisms driving this swirling boundary-layer flashback have not so far been determined. The question remains how the swirling flow, and the generation of a radial pressure gradient or additional baroclinic torque, influence flashback. Swirling boundary-layer flashback has been linked to both combustion-induced vortex breakdown, where flashback is described as being caused by baroclinic torque generated by the radial pressure gradient (Kiesewetter et al., 2007), and the mechanisms seen in the confined boundary-layer flashback of non-swirling flows, where volumetric expansion and flow diversion around the leading point of the flame create an adverse pressure gradient and reverse flow which accelerate flashback (Eichler, 2011; Eichler and Sattelmayer, 2011; Eichler et al., 2012; Eichler and Sattelmayer, 2012; Gruber et al., 2012). Heeger et al. (2010) also describe the effect of the radial pressure gradient increasing the pressure through the flame, increasing the pressure in the burned mixture, and driving flame propagation. Given these different possible explanations, the first research question is therefore what is the physical mechanism for boundary-layer flashback within swirling flows. The second question then aims to quantify the effect of the wall-normal or radial pressure gradient on flashback speed.

The boundary-layer flashback of turbulent swirling flows has also been shown experimentally to be different to that of non-swirling flows (Ebi and Clemens, 2014, 2015, 2016; Ebi et al., 2018). Rather than a series of bulges and cusps forming which propagate upstream (as seen for non-swirling

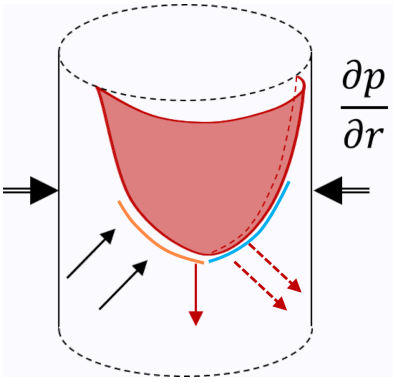

Figure 2.21: Schematic of swirling-flow flashback in an annulus. The solid black arrows show the local flow direction, the solid red arrow the direction of mean propagation and the double-lined black arrows represent the radial pressure gradient.

flows), a flame tongue is formed (shown in Figure 2.21) which locally propagates (dashed red arrows) upstream from a leading side of the flame tongue (highlighted in blue). This gives a misalignment between the oncoming flow and the direction of flame propagation. Ebi et al. (2020) has shown that in some cases this process is more similar to non-swirling boundary-layer flashback, with the flame propagating directly opposing the oncoming flow (the orange side leading). In addition to this flow misalignment, the annular geometry means that there is the presence of curvature in the walls of the annulus. Depending on the level of swirl, this curvature could be transverse (for no swirl) or streamwise to the flow (for a swirling flow). The presence of transverse curvature or spanwise rotation, which has similarities to an azimuthal flow in an annulus, has been shown to affect the structure of the turbulent flow, which, given the strong interaction between turbulence and non-swirling boundary-layer flashback, means that curvature could impact the flashback process. These two points motivate the next two research questions of how the oblique flow orientation and the annular geometry affect flashback.

In addition to the effects outlined above, the effect of a developing boundary layer has also been identified as important and currently unevaluated (Kalantari and McDonell, 2017). A developing boundary layer will increase the wall velocity gradient for the same bulk velocity and channel height, which has been shown to be important in boundary-layer flashback, such as in the model of Lewis and von Elbe (1943). The wall velocity gradient is also changed by the bulk velocity and channel height. The effect of bulk velocity and channel height are important for evaluating flashback limits. The final research question therefore aims to answer how a developing boundary layer affects flashback speeds.

These research questions will be investigated using a combination of analytical modelling and numerical simulation. An analytical model will be developed to describe the effect of a wall-normal pressure gradient to: predict different flashback behaviours and to test alternative phenomenological explanations for flashback. Models predicting flashback limits which account for fuel and flow properties can also aid in the design of combustion devices. The development of fuel-flexible burners means combustion devices must prevent flashback for fuels and flow conditions with widely varying properties. Models which account for these differences will support the design process. The ability of the developed models to describe the trends in flashback speed with swirl will be investigated and evaluated using data from previous experimental investigations and DNS.

Numerical simulation is widely used to study combustion characteristics of stationary and motive engines for present-day power-generation and transport applications, where it is able to represent the time- and space-varying quantities within the system (Poinsot and Veynante, 2005). The three general approaches to numerical simulation are: Reynolds-averaged Navier-Stokes (RANS), LES and DNS. In RANS, the time-averaged governing equations are solved. Models must be introduced for the effect of turbulence and for the rate of reaction, which are inherently time-varying. In LES, time-varying governing equations are solved for scales larger than the grid. Here models are needed for the effect of the sub-grid-scale turbulence and rate of reaction. In DNS, all of the scales of flow, turbulence and chemistry are represented. This makes DNS significantly more computationally expensive but suited to the study of the fundamental processes occurring. It is often referred to as a numerical experiment which can supplement physical experimentation (Poinsot et al., 1996).

DNS have been used in previous investigations, such as those presented in this chapter, to complement the outcomes from experimental and theoretical work. Physical experiments can be said to be the whole truth, partially revealed: a real system is being studied and so the whole truth is present

but, given the very small flow and flame length scales and the physical difficulties in measuring at those levels, the whole is only partially revealed. DNS can be said to give the partial truth but wholly revealed: due to the computational expense of DNS only small-scale systems can be simulated and these may not reveal the whole truth of a realistic system, but DNS resolves all of the flow and flame scales without closure models and therefore reveals the whole truth at these scales.

In this work, two- and three-dimensional DNS of annular sections, planar channels and annuli will be used to isolate the competing contributions of:

- wall-normal pressure gradient and swirl
- turbulence
- flow orientation
- surface curvature
- boundary-layer development

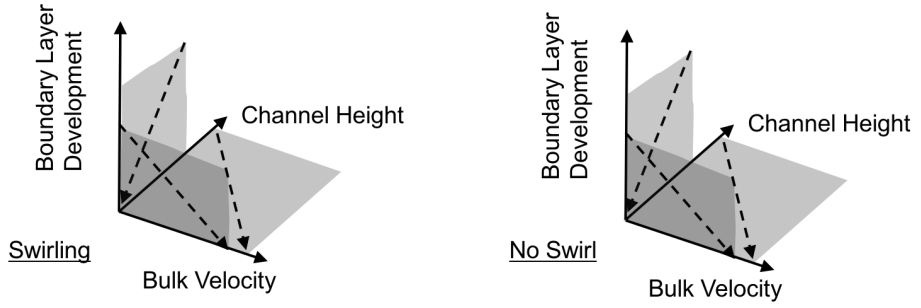

Figure 2.22: Diagram of parametric investigation to be undertaken using two-dimensional laminar simulations. The two diagrams represent investigations for a swirling flow and a flow with no swirl. The dashed black arrows represent the change in wall velocity gradient on each of the planes represented by the grey shaded area.

Two-dimensional laminar simulations will be used to evaluate the effect of swirl on flashback speeds and test the predictions of the models, as well as to investigate the effect of a developing boundary layer, bulk velocity and channel height, for both a swirling and non-swirling flow. Figure 2.22 shows this schematically, and shows how the wall velocity gradient (dashed arrows) changes on each plane.

Using two-dimensional simulations allows the evaluation of the physical mechanisms behind boundary-layer flashback in swirling flows without the additional effects present in a turbulent flow. It will also allow a larger range of parameters to be investigated to evaluate the effect of swirl, a developing boundary layer, bulk velocity and channel height.

Table 2.1: Set of cases to be investigated using three-dimensional DNS of reacting turbulent channel flow.

Case	Wall-normal pressure gradient	Flow Orientation
1	None	Normal
2	None	Oblique
3	Present	Normal

Table 2.2: Set of cases to be investigated using three-dimensional DNS of reacting turbulent annular flow.

Case	Flow	Wall-normal pressure gradient	Flow Orientation	Curvature
1	Axial-only	None	Normal	Transverse
2	Swirling	Present	Oblique	Stream-wise

Three-dimensional turbulent simulations in planar channels and annuli will be used to: validate that the mechanisms seen in two dimensions also apply to turbulent flow; evaluate how an oblique flow orientation impacts flashback; and evaluate how the curved wall of an annulus affects flashback. Table 2.1 shows how a planar channel flow will be used to independently investigate the effects of a wall-normal pressure gradient and of the oblique flow orientation. Table 2.2 then shows how the annular flow will be used to investigate the combined effect of the wall-normal pressure gradient and oblique flow orientation, as well as the effect of curvature.

The use of DNS will allow evaluation of the local flame propagation speeds and the factors affecting it. The flame structure here may differ from that in freely propagating flames, so using DNS will allow this local evaluation of flame propagation to be achieved without the need for combustion models, which were developed for freely propagating flames. This can then be used to validate the mechanisms controlling flashback speed.

In the next chapter I will move on to describe the formulation of these numerical simulations.

Chapter 3

Formulation

This chapter describes the set of common conditions used in the simulations conducted in this work. Further specific conditions or variations on this will be described within the subsequent chapters.

The aim of this formulation is to simulate the key physical phenomena responsible for flashback in practical burners. In these burners, flame flashback occurs between the walls of the premixing section. This premixing section could be in various configurations such as a conical flame holder or one of multiple channels in a swirler (see Figure 3.1).

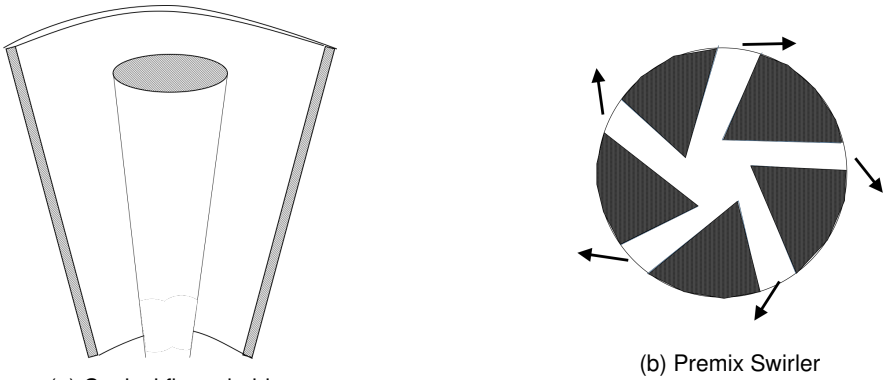

(a) Conical flame holder

(b) Premix Swirler

Figure 3.1: Example of premixing sections and flame holders. Flame flashback occurs into the channels in these premixing sections.

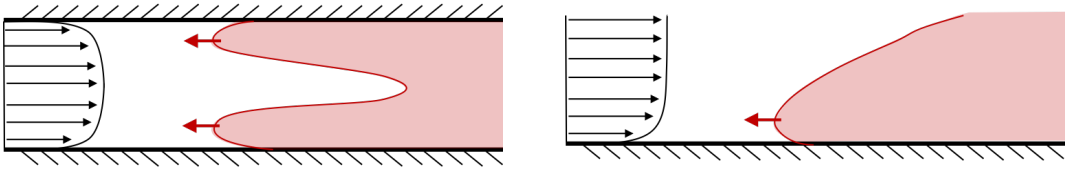

(a) Channel flow

(b) Flat-plate boundary layer

Figure 3.2: Canonical simulation configurations which could represent boundary-layer flashback.

3.1 Numerical Formulation

This section will describe the governing equations of Direct Numerical Simulation which will be used to conduct the simulations in this work.

Co-ordinate systems

In this section I will define governing equations in Cartesian and cylindrical coordinates. For the Cartesian coordinates I will use x, y and z for the three dimensions and u, v and w to indicate the velocity in each direction. This work considers the flow between walls - either in a rectangular channel or cylindrical annulus. x, y and z will correspond to the stream-wise, wall-normal and cross-stream-wise directions. The governing equations will be written using the following notation:

$$\nabla_i \cdot (\rho u_i u_j) = \frac{\partial(\rho u_i u)}{\partial x} + \frac{\partial(\rho u_i v)}{\partial y} + \frac{\partial(\rho u_i w)}{\partial z} \tag{3.1}$$

For the cylindrical coordinates x will define the axial direction, θ the circumferential and r the radial direction. The corresponding velocities in each direction will be u, v, w respectively.

3.1.1 Fully Compressible Reacting-Flow Equations - Cartesian Co-ordinates

The following are the governing equations for a fully compressible, reacting flow (Chen et al., 2009) solving for the mass, momentum, energy and species:

$$\frac{\partial \rho}{\partial t} = -\nabla \cdot (\rho \boldsymbol{u}) \tag{3.2}$$

$$\frac{\partial(\rho u_i)}{\partial t} = -\nabla_j \cdot (\rho u_i u_j) + \nabla_j \cdot \tau_{ji} - \frac{\partial p}{\partial x_i} + \rho \sum_{k=1}^{N_s} Y_k f_{ik} \tag{3.3}$$

where ρ is the mixture density, u_i the velocity in direction i, τ_{ji} the ji-th component of the stress tensor, p pressure, Y_k the mass fraction of species k, f_{ik} the body force on species k in direction i and N_s the number of species present. The form of the energy equation used in this work solves for specific total energy, e_0, which is the internal energy plus kinetic energy. The Dufour effect is neglected.

$$e_0 = \frac{u_i u_j}{2} - \frac{p}{\rho} + h \tag{3.4}$$

$$\frac{\partial(\rho e_0)}{\partial t} = -\nabla_j \cdot \left[u_j (\rho e_0 + p)\right] + \nabla_j \cdot (\tau_{ij} \cdot u_i) - \nabla_j \cdot q_j + \rho \sum_{k=1}^{N_s} Y_k f_{ik} \cdot (V_{ik} + u_i) \tag{3.5}$$

$$\frac{\partial(\rho Y_k)}{\partial t} = -\nabla_j \cdot (\rho Y_k u_j) - \nabla_j \cdot \left(\rho Y_k V_{jk}\right) + W_k \dot{\omega}_k \tag{3.6}$$

where h is the total enthalpy (sensible plus chemical), q_j is the j-component of the heat flux vector, V_{jk} the mass diffusion velocity of species k in direction j and W_k is the molecular weight of species k.

The stress tensor, neglecting bulk viscosity, is given by (Chen et al., 2009):

$$\tau_{ij} = \tau_{ji} = \mu \left(\frac{\partial u_i}{\partial x_j} + \frac{\partial u_j}{\partial x_i} - \frac{2}{3}\delta_{ij} \nabla \cdot \mathbf{u} \right) \tag{3.7}$$

where δ_{ij} is the Kroenecker delta.

The mixture-averaged transport model has been used to calculate the diffusion velocities of the species (Chen et al., 2009):

$$V_{ik} = -D_k \frac{\nabla_i X_k}{X_k} \tag{3.8}$$

where V_{ik} is the diffusion velocity of species k in direction i, X_k is the mole fraction of species k and D_k the diffusion coefficient for species k .

Additionally, the Soret effect is included:

$$V_{ik}^T = -\frac{D_k^T}{\rho Y_k} \frac{\partial}{\partial x_i} \ln T \tag{3.9}$$

where D_k^T is the thermal diffusion coefficient and V_k^T is the diffusion velocity from thermal diffusion which is added to the diffusion velocity above:

$$V_{ik} = -\frac{D_k}{X_k} \frac{\partial X_k}{\partial x_i} - \frac{D_k^T}{\rho Y_k} \frac{\partial}{\partial x_i} \ln T \tag{3.10}$$

The heat flux vector is given by:

$$q_i = -\lambda \frac{\partial T}{\partial x_i} + \sum_{k=1}^{N_s} h_k \rho Y_k V_{ik} \tag{3.11}$$

representing the the heat flux due to temperature gradients and the diffusion of heat due to mass diffusion.

3.1.2 Fully Compressible Reacting-Flow Equations - Cylindrical Co-ordinates

The following sets of equations set out the fully compressible reacting-flow equations in cylindrical co-ordinates. The equations for mass, momentum, energy and species in cylindrical co-ordinates are given by (Sandberg, 2007; Yoo, 2019):

$$\frac{\partial \rho}{\partial t} = -\left(\frac{\partial}{\partial x}(\rho u) + \frac{1}{r}\frac{\partial}{\partial r}(r\rho v) + \frac{1}{r}\frac{\partial}{\partial \theta}(\rho w) \right) \tag{3.12}$$

$$\frac{\partial}{\partial t}(\rho u) = -\left(\frac{\partial}{\partial x}(\rho uu - \tau_{xx}) + \frac{1}{r}\frac{\partial}{\partial r}(r(\rho uv - \tau_{rx})) + \frac{1}{r}\frac{\partial}{\partial \theta}(\rho uw - \tau_{\theta x}) + \frac{\partial p}{\partial x} \right) \tag{3.13}$$

$$\begin{aligned} \frac{\partial}{\partial t}(\rho v) = -\Bigg(& \frac{\partial}{\partial x}(\rho uv - \tau_{rx}) + \frac{1}{r}\frac{\partial}{\partial r}(r(\rho vv - \tau_{rr})) + \frac{1}{r}\frac{\partial}{\partial \theta}(\rho vw - \tau_{\theta r}) \\ & + \frac{(-\rho w^2 + \tau_{\theta\theta})}{r} + \frac{\partial p}{\partial r} \Bigg) \end{aligned} \tag{3.14}$$

$$\frac{\partial}{\partial t}(\rho w) = -\left(\frac{\partial}{\partial x}(\rho u w - \tau_{\theta x}) + \frac{1}{r}\frac{\partial}{\partial r}(r(\rho v w - \tau_{\theta r})) + \frac{1}{r}\frac{\partial}{\partial \theta}(\rho w w - \tau_{\theta\theta}) - \frac{\tau_{\theta r}}{r} + \frac{1}{r}\frac{\partial p}{\partial \theta}\right) \tag{3.15}$$

Here, as above, the Dufour effect is neglected.

$$\begin{aligned}&\frac{\partial}{\partial t}(\rho e_0) + \frac{\partial}{\partial x}(u(\rho e_0 + p)) - \frac{\partial}{\partial x}(u\tau_{xx} + v\tau_{rx} + w\tau_{\theta x}) + \frac{\partial q_x}{\partial x} + \\ &\frac{1}{r}\frac{\partial}{\partial r}(vr(\rho e_0 + p)) - \frac{1}{r}\frac{\partial}{\partial r}(ur\tau_{xr} + vr\tau_{rr} + wr\tau_{\theta r}) + \frac{1}{r}\frac{\partial (rq_r)}{\partial r} + \\ &\frac{1}{r}\frac{\partial}{\partial \theta}(w(\rho e_0 + p)) - \frac{1}{r}\frac{\partial}{\partial \theta}(u\tau_{x\theta} + v\tau_{r\theta} + w\tau_{\theta\theta}) + \frac{1}{r}\frac{\partial q_\theta}{\partial \theta} = 0\end{aligned} \tag{3.16}$$

The species equation is then given by (Kee et al., 2003; Yoo, 2019):

$$\begin{aligned}&\frac{\partial}{\partial t}(\rho Y_i) + \frac{\partial}{\partial x}(\rho u Y_i) + \frac{1}{r}\frac{\partial}{\partial r}(r\rho v Y_i) + \frac{1}{r}\frac{\partial}{\partial \theta}(\rho w Y_i) \\ &+ \frac{\partial}{\partial x}(\rho Y_i V_{i,x}) + \frac{1}{r}\frac{\partial}{\partial r}(r\rho Y_i V_{i,r}) + \frac{1}{r}\frac{\partial}{\partial \theta}(\rho Y_i V_{i,\theta}) + \dot{\omega}_i W_i = 0\end{aligned} \tag{3.17}$$

The components of the stress tensor are given below (Sandberg, 2007; Yoo, 2019):

$$\tau_{xx} = \frac{2\mu}{3}\left[2\frac{\partial u}{\partial x} - \frac{1}{r}\frac{\partial}{\partial r}(rv) - \frac{1}{r}\frac{\partial w}{\partial \theta}\right] \tag{3.18}$$

$$\tau_{rr} = \frac{2\mu}{3}\left[-\frac{\partial u}{\partial x} + 2\frac{1}{r}\frac{\partial}{\partial r}(rv) - \frac{1}{r}\frac{\partial w}{\partial \theta}\right] \tag{3.19}$$

$$\tau_{\theta\theta} = \frac{2\mu}{3}\left[-\frac{\partial u}{\partial x} - \frac{1}{r}\frac{\partial}{\partial r}(rv) + \left(\frac{2}{r}\frac{\partial w}{\partial \theta} + \frac{3v}{r}\right)\right] \tag{3.20}$$

$$\tau_{rx} = \mu\left[\frac{\partial u}{\partial r} + \frac{\partial v}{\partial x}\right] \tag{3.21}$$

$$\tau_{\theta x} = \mu\left[\frac{\partial w}{\partial x} + \frac{1}{r}\frac{\partial u}{\partial \theta}\right] \tag{3.22}$$

$$\tau_{\theta r} = \mu\left[\frac{1}{r}\left(\frac{\partial v}{\partial \theta} - w\right) + \frac{\partial w}{\partial r}\right] \tag{3.23}$$

The components of the heat-flux vector are given by (Yoo, 2019):

$$q_x = -\lambda\frac{\partial T}{\partial x} + \sum_{i=1}^{N_s} h_i \rho Y_i V_{xi} \tag{3.24}$$

$$q_r = -\lambda\frac{\partial T}{\partial r} + \sum_{i=1}^{N_s} h_i \rho Y_i V_{ri} \tag{3.25}$$

$$q_\theta = -\lambda\frac{1}{r}\frac{\partial T}{\partial \theta} + \sum_{i=1}^{N_s} h_i \rho Y_i V_{\theta i} \tag{3.26}$$

The components of the diffusion velocity are given below, with the Soret effect again included (Yoo, 2019).

$$V_{xi} = -\frac{D_i}{X_i}\frac{\partial X_i}{\partial x} - \frac{D_i^T}{\rho Y_i}\frac{\partial \ln T}{\partial x} \tag{3.27}$$

$$V_{ri} = -\frac{D_i}{X_i}\frac{\partial X_i}{\partial r} - \frac{D_i^T}{\rho Y_i}\frac{\partial \ln T}{\partial r} \tag{3.28}$$

$$V_{\theta i} = -\frac{D_i}{rX_i}\frac{\partial X_i}{\partial \theta} - \frac{D_i^T}{\rho Y_i r}\frac{\partial \ln T}{\partial \theta} \tag{3.29}$$

The Navier-Stokes characteristic boundary conditions (NSCBC) for the x-direction in cylindrical coordinates are given in Appendix B.

3.1.3 Equation of State

The ideal gas law is used for the equation of state:

$$\rho = \frac{pW}{RT} \tag{3.30}$$

where R is the ideal gas constant and W the mean molecular weight of the mixture.

3.1.4 Fluid Properties

Thermodynamic and transport properties are calculated based on two sets of properties for each species Kee et al. (1980, 1986). These thermodynamic property models give the heat capacity, enthalpy and entropy for the species. The transport property models give the dynamic viscosity, thermal conductivity and diffusion coefficients for each species.

Thermodynamic Properties

The thermodynamic property model is based on a seven coefficient polynomial parametrisation (Kee et al., 1980):

$$\frac{c_p^0(T)}{R} = a_0 + a_1 T + a_2 T^2 + a_3 T^3 + a_4 T^4 \tag{3.31}$$

$$\frac{h^0(T)}{RT} = a_0 + \frac{a_1}{2}T + \frac{a_2}{3}T^2 + \frac{a_3}{4}T^3 + \frac{a_4}{5}T^4 + \frac{a_5}{T} \tag{3.32}$$

$$\frac{s^0(T)}{R} = a_0 \ln(T) + a_1 T + \frac{a_2}{2}T^2 + \frac{a_3}{3}T^3 + \frac{a_4}{4}T^4 + a_6 \tag{3.33}$$

where a_0 to a_6 are coefficients for each species and R is the universal gas constant. Commonly these coefficients are specified for two contiguous temperature ranges.

Transport Properties

The calculation of the pure-species viscosities, binary diffusion coefficients and thermal conductivities are achieved using a polynomial fit for the temperature-dependent parts of the full pure-species property expressions that are given in Section A (Kee et al., 1986):

$$\ln \mu_k = \sum_{n-1}^{N} a_{n,k} (\ln T)^{n-1} \tag{3.34}$$

$$\ln \lambda_k = \sum_{n-1}^{N} b_{n,k} (\ln T)^{n-1} \tag{3.35}$$

$$\ln D_{jk} = \sum_{n-1}^{N} d_{n,jk} (\ln T)^{n-1} \tag{3.36}$$

where, by default, $n = 4$, and a, b and c are the coefficients of the polynomial fits.

The mixture-averaged properties are then given by the semi-empirical Wilke formula for viscosity:

$$\mu = \sum_{k=1}^{K} \frac{X_k \mu_k}{\sum_{j=1}^{K} X_j \Phi_{kj}} \tag{3.37}$$

where:

$$\Phi_{kj} = \frac{1}{\sqrt{8}} \left(1 + \frac{M_k}{M_j}\right)^{-\frac{1}{2}} \left(1 + \sqrt{\frac{\mu_k}{\mu_j}} \left(\frac{W_j}{W_k}\right)^{\frac{1}{4}}\right) \tag{3.38}$$

The mixture-averaged thermal conductivity is given by:

$$\lambda = \frac{1}{2} \left(\sum_{k=1}^{K} X_k \lambda_k + \frac{1}{\sum_{k=1}^{K} X_k \lambda_k} \right) \tag{3.39}$$

and the mixture-averaged diffusion coefficient, D_k, by:

$$D_k = \frac{\sum_{k \neq j}^{K} X_j W_j}{W \sum_{k \neq k}^{K} X_j / D_{jk}} \tag{3.40}$$

Using this form, with a numerically insignificant (10^{-12}) amount of each species also retained, prevents numerical issues when the pure-species condition is approached.

3.1.5 Chemistry

To represent the chemical reactions occurring we first define a set of chemical reactions (Poinsot and Veynante, 2005):

$$\sum_{j=1}^{N} \nu'_{kj} M_k <=> \sum_{j=1}^{N} \nu''_{kj} M_k \tag{3.41}$$

where M_k is the symbol for species k, ν'_{kj} and ν''_{kj} are the molar stoichiometric coefficients of the forward and backward reactions of species k in reaction j and N is the number of species.

We can then define a progress rate of, Q_j, for reaction j:

$$Q_j = K_{fj}\Phi_{k=1}^{N}\left[X_k\right]^{v'_{kj}} - K_{rj}\Phi_{k=1}^{N}\left[X_k\right]^{v''_{kj}} \tag{3.42}$$

where K_{fj} and K_{rj} are the forward and reverse rates of reaction j and $[X_k]$ is the molar concentration of species k.

The rates of reaction are modelled using the Arrhenius Law:

$$K_{fj} = A_{fj}T^{\beta_j}\exp\left(\frac{-E_{a,j}}{RT}\right) \tag{3.43}$$

where A_{fj} is the pre-exponential constant for the forward reaction of reaction j, β_j is the temperature exponent for reaction j, $E_{a,j}$ is the activation energy and R is the universal gas constant.

We can then define the rate of reaction, or rate of change of mass, per unit volume:

$$\dot{\omega}_{kj} = Q_j W_k \nu_{kj} \tag{3.44}$$

where $\dot{\omega}_{kj}$ is the rate of reaction of species k in reaction j and $\nu_{kj} = \nu''_{kj} - \nu'_{kj}$.

Summing over all reactions gives the total rate of reaction for species k:

$$\dot{\omega}_k = \sum_{j=1}^{M}\dot{\omega}_{kj} \tag{3.45}$$

Chemical schemes are then defined which give the required Arrhenius constants for a set of reactions.

3.1.6 Software

Fully Compressible - S3D

For the fully compressible simulations the DNS code S3D will be used (Chen et al., 2009). S3D integrates the governing equations using a fourth-order six-stage explicit Runge-Kutta scheme. Spatial derivatives are calculated using an eighth-order central finite difference dropping to third-order at the boundaries. S3D also uses a tenth-order explicit spatial filter to remove high-frequency noise and reduce aliasing error (Chen et al., 2009; Gruber et al., 2010). Parallelisation is achieved using three-dimensional domain decomposition with MPI for inter-process communication. Reaction rates, and mixture and transport rates are calculated using the CHEMKIN and TRANSPORT libraries. NSCBC are implemented to prescribe boundary conditions (Chen et al., 2009).

S3D has been widely used for a range of studies, including investigations of flame-wall interactions Gruber et al. (2010) and boundary-layer flashback Gruber et al. (2012).

As part of this work S3D has been extended to solve the cylindrical Navier-Stokes, including cylindrical NSCBC; to apply a wall-normal body force; and to include a moving frame-of-reference. For both the cylindrical solutions and the applied body force the target pressure at the boundary conditions is updated to reflect the hydrostatic pressure. The updates are described in Section 3.1.7.

1D Flame Speeds - Cosilab

For the calculation of one-dimensional laminar flame speeds Cosilab will be used. Cosilab aims to find a steady solution to the one-dimensional flame propagation. An Euler numerical scheme is used for unsteady time-advancement while a Newton scheme is used to iterate the steady solution. Adaptive gridding is also used to adjust the set of points to the solution. When both the steady Newton solution and adaptive grid are within the tolerances defined a steady solution has been found from which the one-dimensional laminar flame speed is extracted.

3.1.7 Software Development

This section describes the major aspects of software development of S3D undertaken as part of this work.

Moving Frame-of-Reference

Two modes of moving frame-of-reference have been implemented: the first uses an adaptive scan velocity, V_{scan}, updated using a proportional-integral controller to maintain the flame position; and the second uses a fixed scan velocity which is used for the turbulent feed data. The adaptive moving frame-of-reference is described here and the moving frame-of-reference for turbulent feed data is described below.

A moving frame-of-reference is used in simulations of moving flames in order to keep the flame at a set position within the computational domain. The speed of this moving frame-of-reference is updated periodically by applying a Galilean transformation, updating the axial velocity and wall boundary conditions throughout the domain.

The flame front is defined using a value of 0.7 for the progress variable based on H_2 mass fraction. The axial flame position is defined as the most upstream point on the flame front. A first-order accurate calculation of the lab-frame flashback speed, V_f, is evaluated from the change in flame position (a positive speed is a positive change in axial position) and the update period of the moving frame-of-reference. A proportional-integral controller then updates the velocity of the moving frame-of-reference, V_{scan}:

$$V_{scan} = (V_f + V_{scan}) - K_p \frac{e(t)}{\Delta T_c} - K_i \sum_0^t e(t) \tag{3.46}$$

where K_p and K_i are the proportional and integral coefficients (set to 1.05 and 1.0, respectively), $e(t)$ is the position error and ΔT_c the time period for controller updates (set to 1×10^{-5}). The axial velocity in the entire domain is then updated by the change in V_{scan} and the velocity setpoint of the wall boundary conditions updated to the new V_{scan}.

This method of applying a moving frame-of-reference is used in Chapter 5, for the two-dimensional laminar simulations.

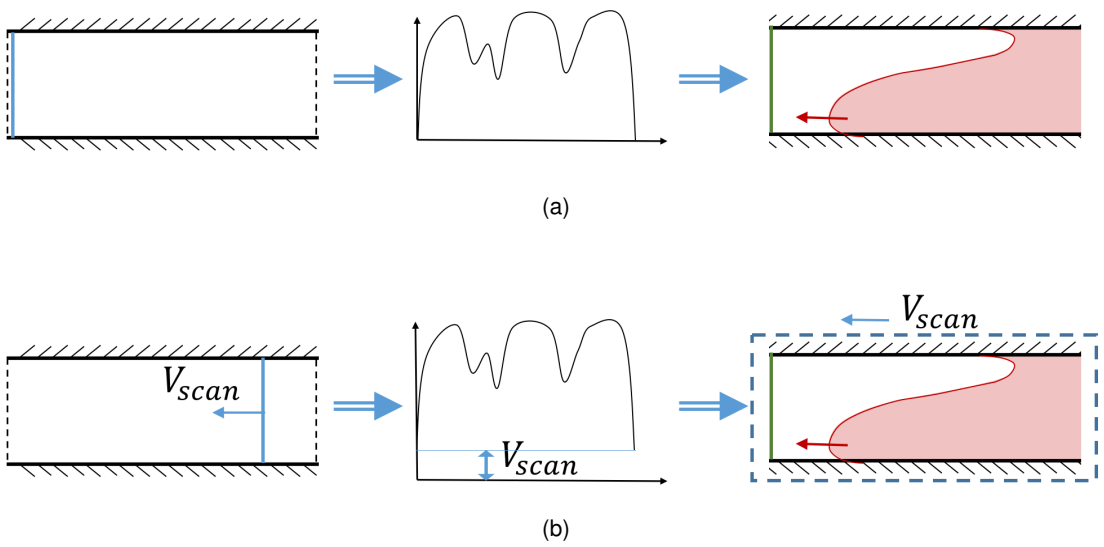

Figure 3.3: Diagram of implementation of saving and reading of turbulent feed data, including extension to use a moving frame-of-reference with scan velocity, V_{scan}. The solid blue line shows the plane where velocity data is saved, the double-lined blue arrows show the movement of data, the solid green line the inputting of the velocity data, the solid blue arrow the moving frame-of-reference and the red arrow the flame propagation.

Moving Frame-of-Reference for Turbulent Feed Data

A moving frame-of-reference for the turbulent feed data was also implemented. S3D was already set up for the saving of turbulent feed data from an auxiliary, non-reacting flow simulation (as shown in Figure 3.3a). The software saves the velocity data at the inlet plane to the domain at a given frequency. When running a reacting-flow simulation it is then possible to read this saved data, interpolating in time and space, to feed the turbulent velocity field into the inlet of the reacting simulation. A time and velocity scaling also adjusts for any difference in scales between the non-reacting and reacting simulations.

To conduct a reacting-flow simulation with a moving frame-of-reference and turbulent feed data (Figure 3.3b), the saving of the velocity data also accounts for the moving frame-of-reference. Within the non-reacting flow simulation, a specified V_{scan} was used to move the plane at which velocity data was saved, interpolating in space between grid points. V_{scan} was added to the saved velocity data, which could then be read into the reacting-flow simulation, as already implemented. When fed into the reacting-flow simulation the velocity data therefore already includes the turbulent velocity field and V_{scan} so that the flame evolves within the realistic, time-evolving turbulence but the simulation also includes a moving frame-of-reference to help maintain the position of the flame.

This method of applying a moving frame-of-reference is used in Chapter 7, for the turbulent, annular simulations.

Boundary-Condition Pressure Target

The wall-normal pressure is given for the applied body force and for a swirling flow, respectively, by:

$$\frac{\partial P(y)}{\partial y} = \rho(y)g(y) \tag{3.47}$$

$$\frac{\partial P(x,r,\theta)}{\partial r} = \rho(r)\frac{V_\theta(x,r,\theta)^2}{r} \tag{3.48}$$

In planar coordinates without the applied body force a uniform pressure target is used for the boundary conditions. With the applied body force or a swirling flow the pressure is no longer uniform in the wall-normal direction. The equations above are integrated from the original target pressure, P_0, at the top wall to give the hydrostatic pressure. Where a three-dimensional domain is used the density field at a given plane is averaged in z or θ; in swirling annular flow the swirl velocity, V_θ, is also plane-averaged; these one-dimensional time-varying fields are then used in the integration. This pressure profile is used to initialise the pressure field and as the target pressure in the outlet boundary conditions.

Applied Body Force

Planar DNS, presented in Chapter 6 of this thesis, use an applied wall-normal body force to simulate the effects of the radial pressure resulting from centripetal acceleration in swirling flows. In a swirling flow the swirl velocity, and therefore radial pressure gradient, decay to zero at the walls. The applied wall-normal pressure gradient reflects this by using the following y-dependent body force:

$$g_y(y) = g\left(1 - \left(1 - \frac{y}{\delta}\right)^4\right) \tag{3.49}$$

This body force distribution decays to zero at the walls and corresponds approximately to the distribution of circumferential velocity in the low-Reynolds number annular flashback case of Ebi and Clemens (2016).

In Chapter 7 an annular configuration is used where the swirl velocity and radial pressure gradient which result from it are resolved. This applied body force is therefore not used for these simulations. The swirl velocity profile for the annular simulations results from the application of a uniform azimuthal pressure gradient as described in Section 3.1.8.

Cylindrical Co-ordinates

The cylindrical Navier-Stokes and cylindrical NSCBC described above have been implemented in S3D as part of this work. This implementation will be verified in Section 3.2.2.

3.1.8 Simulation Setup

The simulations conducted in this work follow a common setup - with some differences between the two-dimensional laminar simulations and the three-dimensional turbulent simulations. In this

section I give the details of how these simulations are set up which, in general, follow the setup used by Gruber et al. (2010, 2012) for their investigations of flame-wall interactions and flashback respectively.

Reacting

All of the reacting-flow simulations use the same configuration with an inlet and outlet in x, walls in y and periodic boundary conditions in z/θ. Mean flame propagation is in x, opposing the oncoming flow. The walls are no-slip and isothermal, with a temperature equal to the inlet temperature of the flow. The flames flash back faster than the wall temperature responds and so an isothermal wall is assumed. The wall velocity is equal to the velocity of the moving frame-of-reference. The flame is allowed to freely propagate within the domain with the moving frame-of-reference used to control the position of the flame.

The flame is initialised using a progress-variable mapping. The position of the flame front as a function of y is specified - the laminar simulations use a planar flame front at a given x-position; the turbulent simulations use a wedge-shaped flame at an angle to the bottom wall. The progress variable across the flame front is specified using a hyperbolic tangent function from the position of the flame front, x_0, and a width of the profile, δ_x, taken to be the thermal flame thickness:

$$f(x,y) = 0.5(1 + \tanh((x - x_0(y))/\delta_x)) \tag{3.50}$$

The specified progress variable is then mapped into a temperature and mass fraction for each species using a one-dimensional flame solution. A one-dimensional, steady flame solution is found and characterised using a progress variable based on the H_2O mass fraction. From the specified progress variable at each point in the domain the temperature and each species' mass fraction are calculated by linearly interpolating within the one-dimensional solution.

This progress-variable mapping gives temperatures in the burned region at the wall which are significantly higher than the wall temperature. To remove these temperature gradients the hyperbolic tangent function is used to smooth the near-wall temperature profile from the wall temperature at the wall to the originally specified temperature away from the wall leaving the species profiles unchanged. This smoothing is again applied with a central position and thickness. Here this central position was 0.004 of the full channel height with the thickness set to half of this value, 0.002 of the full channel height. These values were chosen to approximate the temperature profile found from two-dimensional simulations of flame flashback.

All of the simulations are to be conducted at atmospheric pressure. Where no wall-normal pressure gradient is present the pressure is initialised to 1 atm. Where a wall-normal pressure gradient is present the pressure on the top (higher-pressure) wall is specified to be 1 atm. From the top wall the pressure gradient profile given by Equation 3.47 or 3.48 is integrated across the domain and used to initialise the pressure.

The velocity profile for the laminar simulations is initialised using the inlet velocity profile. For the turbulent simulations the auxiliary non-reacting turbulent-flow simulation is used to give an initial velocity field. The initial axial unburned velocity profile is scaled by the density ratio between the unburned

mixture and the conditions at each point based on the temperature and mixture composition to account for mass conservation. The flame front is initially assumed not to be moving and the velocities in the domain are adjusted using:

$$u(x,y,z) = \frac{\rho_0 u(0,y,z)}{\rho(x,y,z)} \tag{3.51}$$

where ρ_0 is the density of the unburned mixture, $u(0,y,z)$ the inlet velocity at the given y,z position and $\rho(x,y,z)$ is the density at each location in the domain based on that position's temperature and mixture composition.

For the turbulent simulations the inlet velocity is updated using the auxiliary non-reacting turbulent flow data. This simulation uses a doubly periodic flow between walls which is run until Re_τ converges to around $Re_\tau = 180$. Samples of the velocity data are taken (10 every mean flow-through time of a cell, $\Delta x/\overline{u}/10$) and these are linearly interpolated in space and time to define the inlet velocity in the reacting-flow simulation. For the annular set of simulations in Chapter 7 the simulations also included a moving frame-of-reference with the turbulent feed data, as described in Section 3.1.7.

For the reacting laminar simulations the aim is to find a converged flame solution. Convergence is assessed using the flame shape and flashback speed. The simulations are continued until the flame solution converges. This converged solution is then used for analysis.

For the turbulent simulations the solution is time-dependent as the flame evolves within the time-varying turbulent flow field. An initial settling period of 0.4 ms is used to allow any pressure oscillations generated during initialisation to decay. For the turbulent planar simulations samples will then be taken every 2 wall time units over the course of the simulation. For the turbulent annular simulations, this was increased to every 0.5 wall time units.

The resolution used will maintain 10 grid points within a thermal flame thickness (Poinsot et al., 1996) and sufficient grid points in y to represent the wall-normal velocity profile. For the laminar simulations a grid convergence study will be conducted to check the required grid resolution.

Chemical reactions will be represented using the chemical scheme involving 9 species and 21 reactions shown in Table 3.1.

Table 3.1: The H_2 chemical scheme (Li et al., 2004) used to conduct the reacting simulations. A is the pre-exponential factor, b the temperature exponent and E_a the activation energy giving an Arrhenius rate constant from: $k = AT^b exp(-E_a/RT)$.
[a] for these reactions, the overall reaction rate is given by the sum of the two reaction rates.

Equation	Rate Constant	A	b	E_a
H + O2 <=> O + OH		3.55e+12	-0.41	6.95e+07
H2 + O <=> H + OH		5.08e+01	2.67	2.63e+07
H2 + OH <=> H + H2O		2.16e+05	1.51	1.44e+07
H2O + O <=> 2 OH		2.97e+03	2.02	5.61e+07
H2 + M <=> 2 H + M		4.58e+16	-1.40	4.37e+08
2 O + M <=> O2 + M		6.16e+09	-0.50	0.00e+00
H + O + M <=> OH + M		4.71e+12	-1.00	0.00e+00
H + OH + M <=> H2O + M		3.80e+16	-2.00	0.00e+00
H + O2 (+M) <=> HO2 (+M)	k_0	6.37e+14	-1.72	2.20e+06
	k_∞	1.48e+09	0.60	0.00e+00
H + HO2 <=> H2 + O2		1.66e+10	0.00	3.44e+06
H + HO2 <=> 2 OH		7.08e+10	0.00	1.23e+06
HO2 + O <=> O2 + OH		3.25e+10	0.00	0.00e+00
HO2 + OH <=> H2O + O2		2.89e+10	0.00	-2.08e+06
2 HO2 <=> H2O2 + O2[a]		4.20e+11	0.00	5.01e+07
2 HO2 <=> H2O2 + O2[a]		1.30e+08	0.00	-6.82e+06
H2O2 (+M) <=> 2 OH (+M)	k_0	1.20e+14	0.00	1.90e+08
	k_∞	2.95e+14	0.00	2.03e+08
H + H2O2 <=> H2O + OH		2.41e+10	0.00	1.66e+07
H + H2O2 <=> H2 + HO2		4.82e+10	0.00	3.33e+07
H2O2 + O <=> HO2 + OH		9.55e+03	2.00	1.66e+07
H2O2 + OH <=> H2O + HO2[a]		1.00e+09	0.00	0.00e+00
H2O2 + OH <=> H2O + HO2[a]		5.80e+11	0.00	4.00e+07

Non-Reacting

The non-reacting simulations use doubly periodic boundary conditions, in x and z/θ, retaining the wall direction in y. The simulation is initialised using a turbulence spectrum with the turbulent fluctuations superimposed on an initial turbulent velocity profile:

$$u(y) = \sqrt{-\frac{\partial p}{\partial x}\frac{2}{\rho_0}\frac{\delta}{c_f}}\left(1 - \left(\frac{\delta - y}{\delta}\right)^{10}\right) \tag{3.52}$$

where c_f is the friction factor and ρ_0 the density of the unburned mixture. The initialisation used gives a turbulent Reynolds number of around 50. The simulation then uses an applied pressure gradient to maintain the flow and allow the turbulence to develop. In all cases the pressure gradient is applied uniformly across y; this applies to the planar cases for pressure gradients in x, or x and z, and to the annular cases for pressure gradients in x or x and θ.

3.2 Verification

3.2.1 Planar, Turbulent, Non-Reacting Channel Flow

The flashback simulations are conducted with realistic time-evolving turbulence fed by an auxiliary non-reacting turbulent channel flow. The simulation setup follows that used by Gruber et al. (2012) in their investigations of boundary-layer flashback. The turbulent channel flow simulations are verified in this section against the data of Moser et al. (1999).

Two simulations were conducted using two different flow angles. The first simulation used a typical flow in x only with flow angle of 0°. In the second the flow angle is 45°; this is to allow the effect of oblique flow on flame flashback to be investigated. The simulation parameters for each case are given in Table 3.2. Table 3.3 then gives the mean-flow parameters for each case, including the non-dimensional pressure gradients, $K_{p,i}$ Chung et al. (2002):

$$K_{p,i} = \frac{\nu}{\rho u_\tau^3} \frac{\partial p}{\partial x_i} \tag{3.53}$$

Table 3.3 shows that an Re_τ of around 180 was achieved in each case.

Table 3.2: Simulation parameters for the planar, non-reacting cases.

Case	1	2
Flow Angle	0°	45°
$\delta(m)$	1.0×10^{-2}	1.6×10^{-3}
$L_x \times L_y \times L_z$	$15\delta \times 2\delta \times 3\delta$	$10\delta \times 2\delta \times 3\delta$
L_x^+	2644	1781
L_z^+	529	534
$N_x \times N_y \times N_z$	$380 \times 400 \times 150$	$250 \times 400 \times 150$
Δx^+	7.0	7.2
Δy^+	1.5	1.5
Δz^+	3.5	3.6

Table 3.3: Mean flow parameters for the planar, non-reacting cases. For the oblique case, u is taken to be the velocity magnitude $(u^2 + w^2)^{\frac{1}{2}}$.

Case	1	2
Flow Angle	0°	45°
Re	5400	5490
Re_0	3170	3210
Re_τ	176	178
$-K_{p,x}$	0.00490	0.00270
$-K_{p,z}$	0	0.00270
U_c/u_τ	18.0	18.0
U_m/u_τ	15.3	15.4
M	0.040	0.177

Figures 3.4 and 3.5 show the two-point correlation coefficients for each case. They show the two-point correlation for each velocity component decaying to zero within half the length and width of the domain, demonstrating that the domain is of sufficient size.

Figures 3.6, 3.7, 3.8 and 3.9 show the mean velocity profiles for each case. The velocity profiles are shown with the data of Moser et al. (1999) and the velocity profiles $u^+ = y^+$ and $u^+ = 5.5 +$

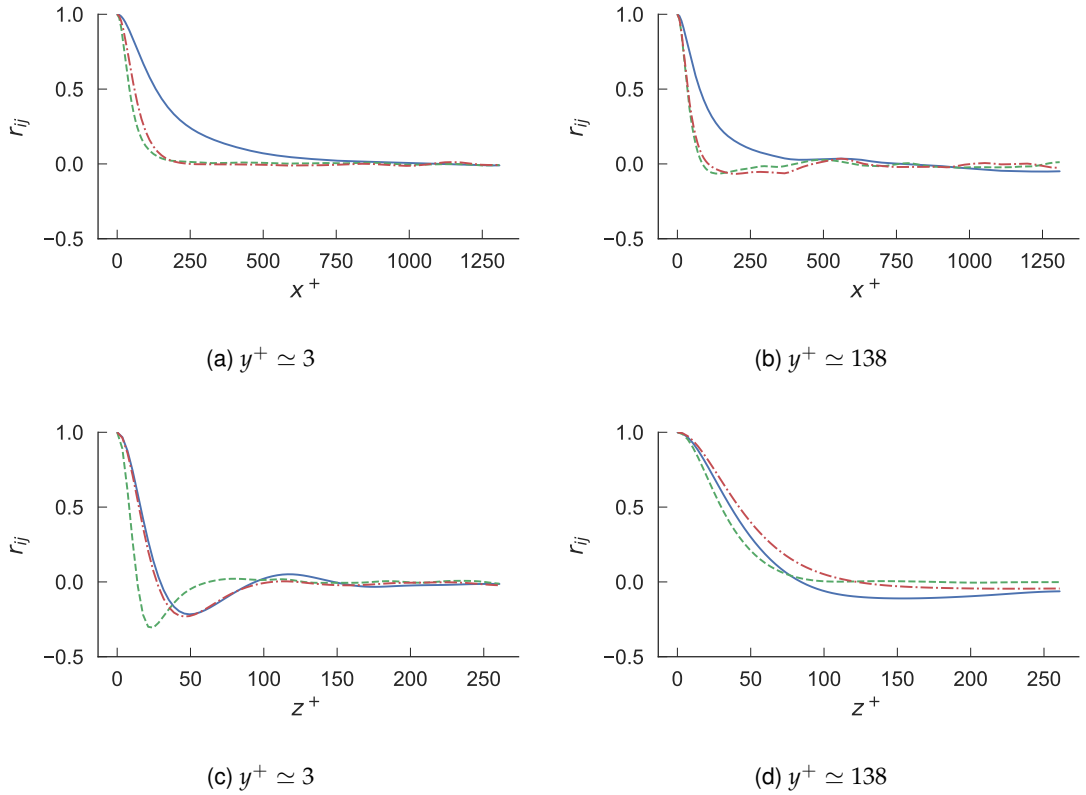

(a) $y^+ \simeq 3$ (b) $y^+ \simeq 138$

(c) $y^+ \simeq 3$ (d) $y^+ \simeq 138$

Figure 3.4: Two-point correlation coefficients in x and z for Case 1 for the three velocity components: u (solid blue), v (dashed orange), w (dot-dashed green).

$2.5 \ln y^+$. For Case 2, u is the velocity in the mean stream-wise direction. The Figures show a good agreement between the simulation data and the verification data of Moser et al. (1999).

Figure 3.10 shows the rms velocities and Reynolds stress for Case 1, again with the data of Moser et al. (1999). They show good agreement between the simulation data and the verification data of Moser et al. (1999).

Overall sufficient agreement is shown between the simulation data and the verification data of Moser et al. (1999) for the data to be used in providing the time-varying turbulent inlet flow to the reacting simulations.

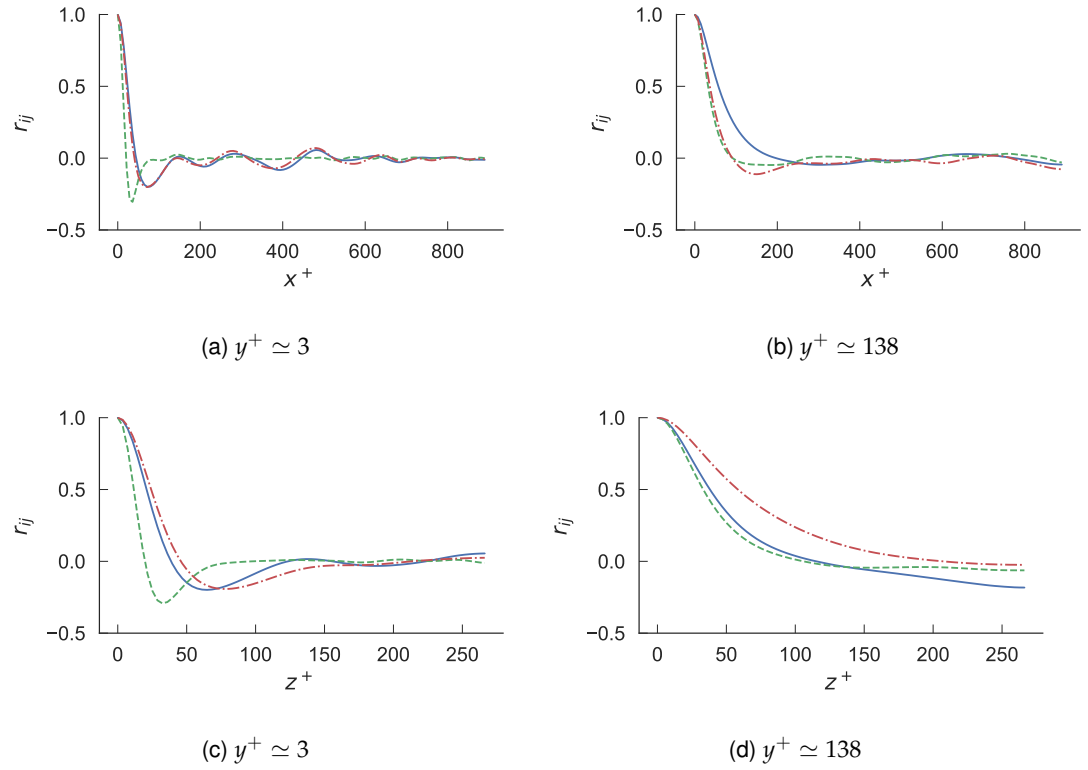

(a) $y^+ \simeq 3$ (b) $y^+ \simeq 138$

(c) $y^+ \simeq 3$ (d) $y^+ \simeq 138$

Figure 3.5: Two-point correlation coefficients in x and z for Case 2 for the three velocity components: u (solid blue), v (dashed orange), w (dot-dashed green).

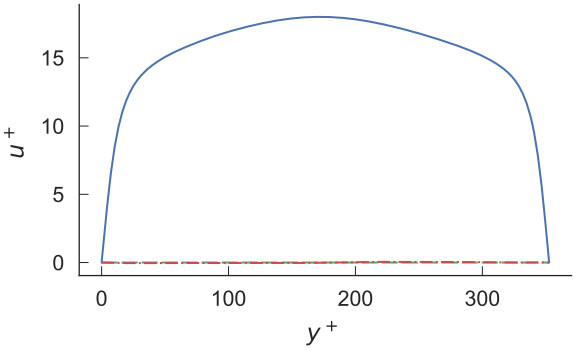

Figure 3.6: Average velocity profile for the turbulent channel flow Case 1. The three velocity components are shown: u (solid blue), v (orange dotted), w (green dot-dashed).

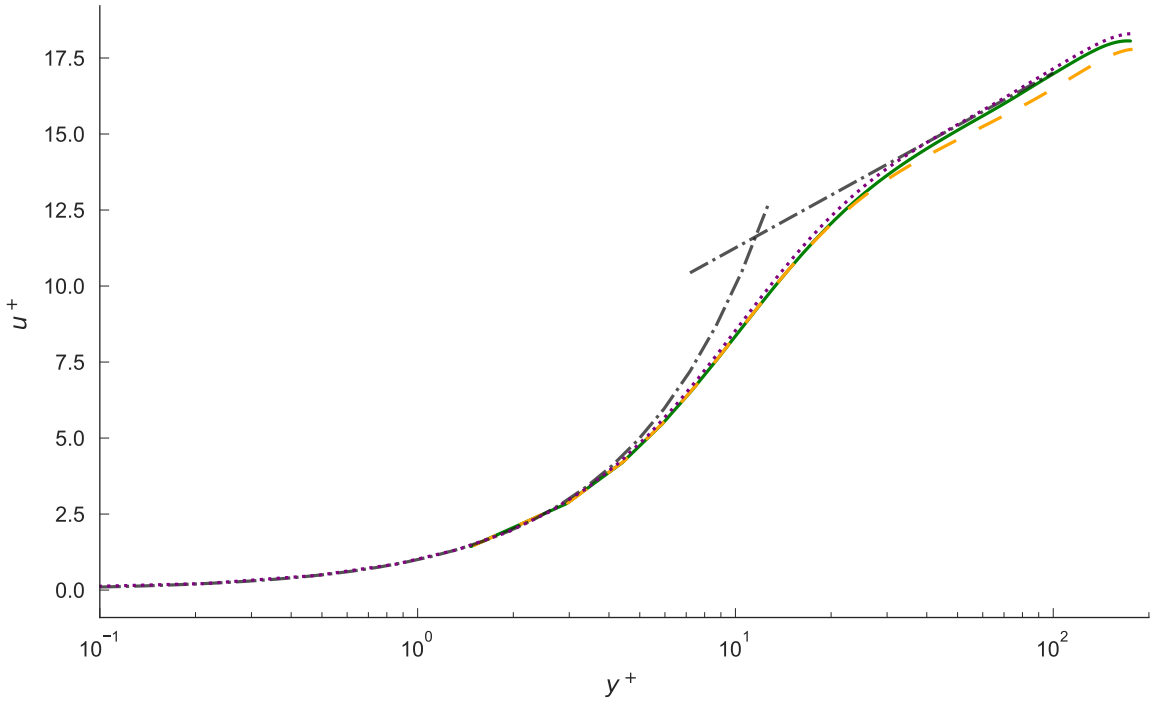

Figure 3.7: Average profile of u for the turbulent channel flow Case 1 in comparison to the data of Moser et al. (1999) (red crosses). The inner (solid blue) and outer (dashed green) profiles of u are shown, and the profiles $u^+ = y^+$ and $u^+ = 5.5 + 2.5 \ln y^+$ (black dot-dashed).

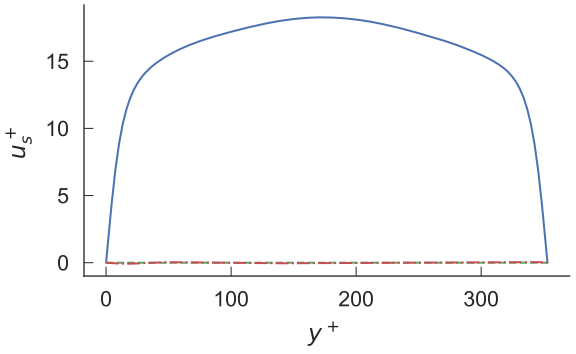

Figure 3.8: Average velocity profile for the turbulent channel flow Case 2. The three velocity components are shown: u (solid blue), v (orange dotted), w (green dot-dashed), where u and w refer to the stream-wise and cross-stream-wise velocity components in this case.

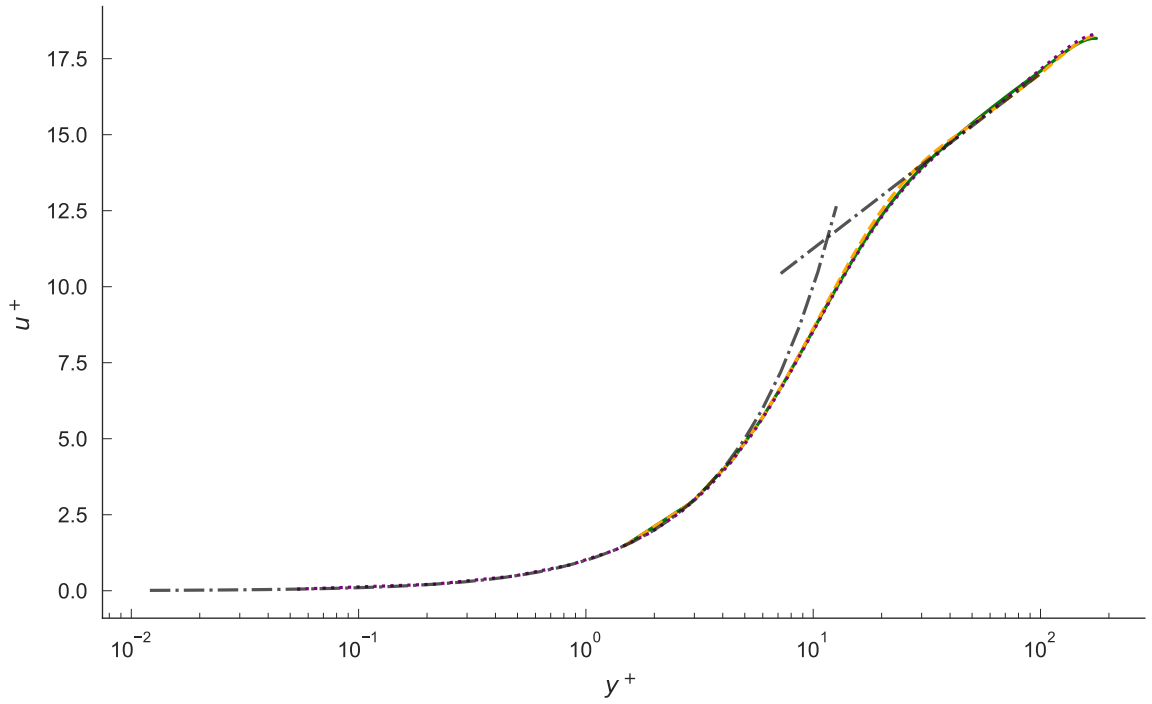

Figure 3.9: Average profile of u for the turbulent channel flow Case 2 in comparison to the data of Moser et al. (1999) (red crosses). The inner (solid blue) and outer (dashed green) profiles of u are shown, and the profiles $u^+ = y^+$ and $u^+ = 5.5 + 2.5 \ln y^+$ (black dot-dashed). u refers to the stream-wise velocity component in this case.

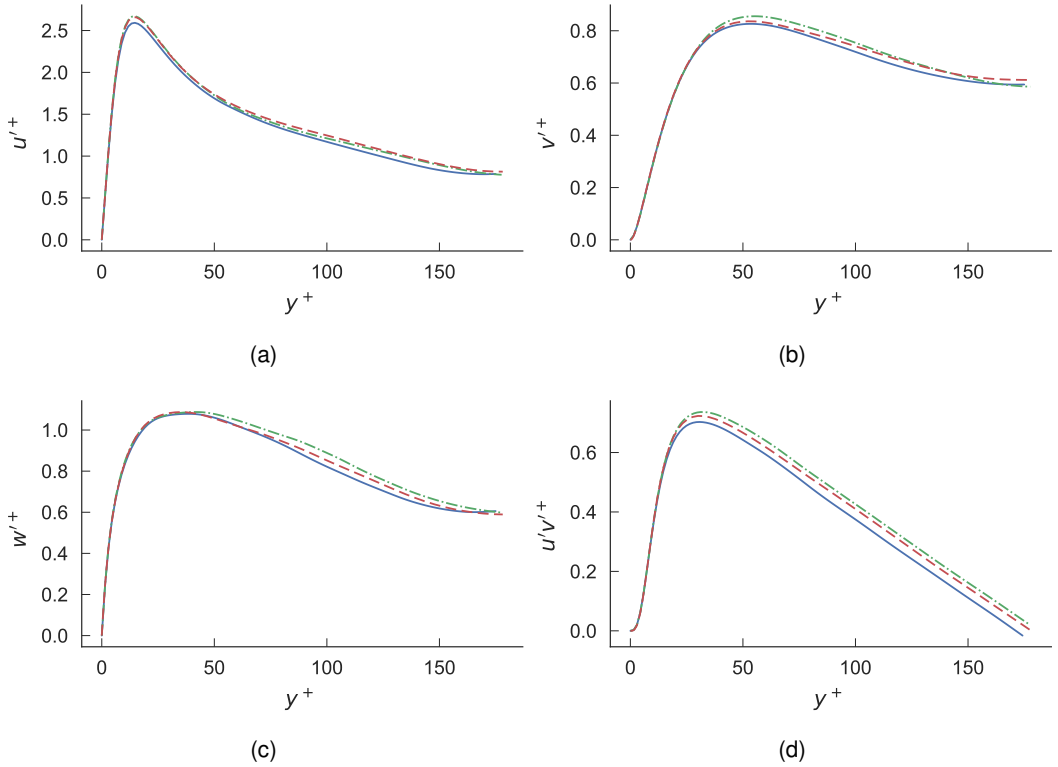

Figure 3.10: Profiles of rms velocities and Reynolds stress for turbulent channel flow Case 1. The profiles for the inner (solid blue) and outer (dashed green) walls are shown in comparison to the results of Moser et al. (1999) (red dot-dashed).

3.2.2 Cylindrical coordinates and boundary conditions

To verify the implementation of the cylindrical coordinates, a laminar annular flow with periodic boundary conditions in x and θ was run. Starting from zero velocity but with an applied pressure gradient in x and θ the converged solution for the velocity profile was checked against the analytical results for u (Chen and Chang, 1992) and w (Dou et al., 2005):

$$u(r) = -\frac{1}{4\mu}\frac{\partial p}{\partial x}\left[(R_0^2 - r^2) + (R_1^2 - R_0^2)\frac{\ln(r/R_0)}{\ln(R_1/R_0)}\right] \tag{3.54}$$

$$\begin{aligned} a &= \left(\frac{R_1}{R_1^2 - R_0^2}\right)\left(\frac{R_0^2}{R_1}\ln R_0 - R_1 \ln R_1\right) \\ w(r) &= -\frac{1}{2\mu}\frac{\partial p}{\partial \theta}\left[ar - R_0^2(a + \ln R_0)\frac{1}{r} + r\ln r\right] \end{aligned} \tag{3.55}$$

where μ is the dynamic viscosity, and $\partial p/\partial x$, $\partial p/\partial \theta$ the axial and azimuthal pressure gradients, respectively, R_1 the outer radius and R_0 the inner radius.

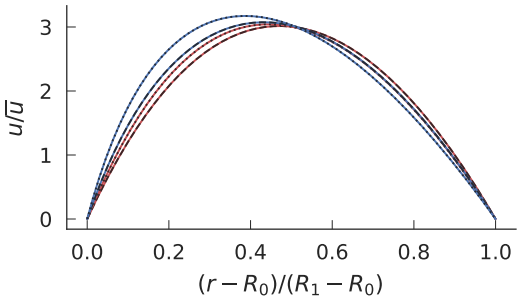

Figure 3.11: Laminar, annular velocity profiles. The simulation results are red lines at $R_1/R_0 = 2$ and the blue at $R_1/R_0 = 4$. The black lines are the analytical profiles for the axial (dashed) and circumferential (dotted) velocities.

Figure 3.11 shows the simulated velocity profiles for a laminar annulus in comparison to the analytical solutions at two radius ratios. The results show the simulated profiles in very good agreement with the analytical solutions.

3.2.3 Moving Frame-of-Reference

To verify the independence of the solutions from the moving frame-of-reference, three simulations were run (listed in Table 3.4: the first simulation was run with the flame initialised towards the outlet of the domain and allowed to propagate with constant scan velocity, $V_{scan} = 4$ m/s, such that no control was applied to the moving frame-of-reference and the flame propagated upstream slowly; a second simulation was run without the moving frame-of-reference applied, where the flame was allowed to propagate until it reached the inlet of the domain; and the third simulation used the moving frame-of-reference control. The flashback speed and flame shape for simulations one and two were then compared to the converged results from simulation three.

Table 3.4: Setup of simulations for verification of moving frame-of-reference.

Case	Mode	Speed (m/s)
1	Fixed	4
2	N/A	0
3	Control	Adaptive

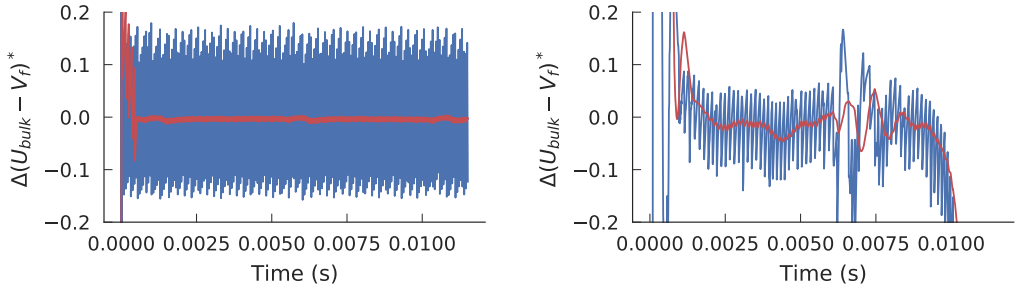

Figure 3.12: Difference in flashback speed ($\Delta(U_{bulk} - V_f)^*$) between the converged result using moving frame-of-reference control (Case 3) and Cases 1 and 2, with: fixed moving frame-of-reference ($V_{scan} = 4$) (a) and no moving frame-of-reference (b). The plots show the instantaneous (blue) and moving average (red line, averaging over 0.5 ms, 50 data points).

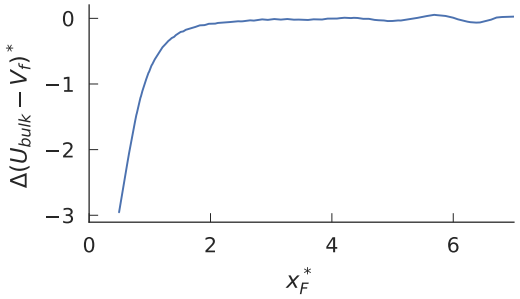

Figure 3.13: Difference in flashback speed ($\Delta(U_{bulk} - V_f)^*$) between Case 2 with no moving frame-of-reference and the converged result using moving frame-of-reference control (Case 3), against flame position, $x_F^* = x_F/\delta$. The plot shows the moving average speed (0.5 ms, averaging 50 points).

Figure 3.12 shows the Cases 1 and 2 and the change in flashback speed between each simulation and the converged result using the moving frame-of-reference control (Case 3):

$$\Delta(U_{bulk} - V_f)^* = \frac{1}{S_L}\left[\left(U_{bulk} - V_f\right) - \left(U_{bulk} - V_f\right)_0\right] \tag{3.56}$$

where the subscript 0 refers to Case 3. Both plots show that, when the flame is moving, the flashback speed oscillates but the deviation from the converged result with moving frame-of-reference control remains small (less than 0.1 S_L) and, when the moving average is applied, the flashback speed becomes steady and shows an even smaller difference from the converged result. For Figure 3.12b the flashback speed drops towards the end of the simulation as the flame reaches the inlet of the domain. Figure 3.13 shows the moving-average difference in flashback speed as a function of flame position, showing that the flashback speed begins to reduce significantly at around $x_F^* = x_F/\delta = 2$.

Figure 3.14 shows the flame shape and region of reversed flow for each of the simulations. It shows

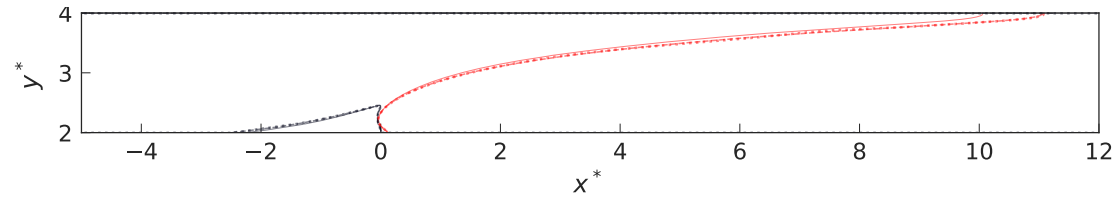

(a)

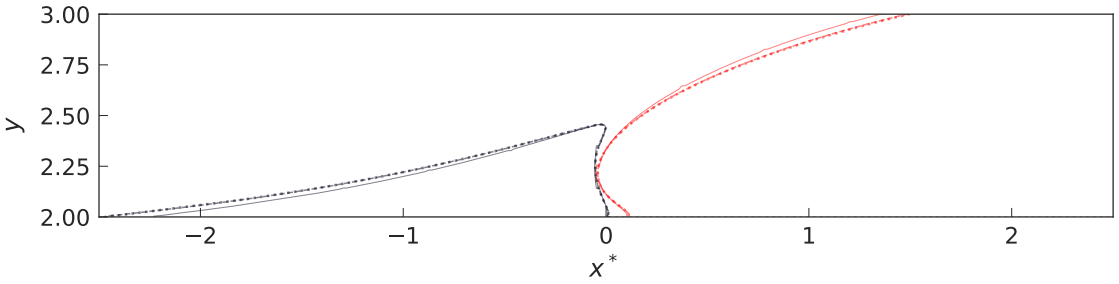

(b)

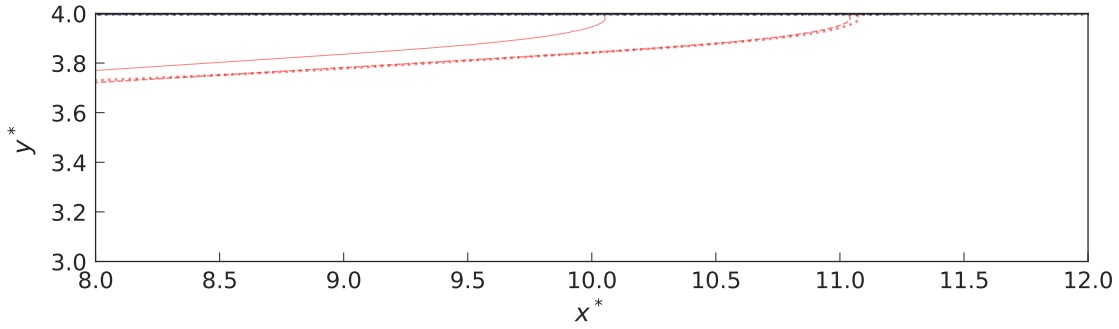

(c)

Figure 3.14: Flame shape (red lines) and region of reversed flow (black lines) for the three cases: with moving frame-of-reference control (solid); fixed moving frame-of-reference ($V_{scan} = 4$, dashed) and no moving frame-of-reference (dotted). (b) and (c) show close-ups of the leading and trailing points of the flame, respectively.

that there are small differences in the flame shape and region of reversed flow for the simulation without moving frame-of-reference compared to those with the moving frame-of-reference and with the moving-frame-of-reference control. However, the leading point of the flame remains very similar, and the differences found do not affect the flashback speed.

3.2.4 Two-dimensional Independence Studies for Grid Resolution, Domain Size and Flame Position

Independence studies have been used to verify that none of: the grid resolution, domain size or flame position affect the results of the simulations in terms of the flashback speed and flame shape.

If the flame is positioned too close to the inlet of the domain then the inlet boundary conditions can impact the flame and the flow upstream of the flame, affecting the flashback speed and flame shape.

Flame positions from the inlet, x_f, at $x_f/\delta = 3, 4, 5$ and 6 will be used to check the independence of the results from flame position.

The grid resolution will also be checked to ensure the independence of the results. The base resolution will give 10 grid points within a thermal flame thickness in x and use 240 grid points in y, to represent the channel flow. Resolutions at 0.66, 1.5 and 2 times the original will be checked on representative cases.

The domain size will be checked to ensure that the outlet boundary conditions do not impact the flame or flow downstream. The initial domain length will be increased by 5 δ to ensure there is no change in flashback speed and flame shape. This will be checked for a flame with low Fr, which is longer in size than a flame at high Fr.

Grid Resolution

Table 3.5: Relative flashback speeds, $(U_{bulk} - V_f)/S_L$, for different grid resolutions at high Fr ($Fr = \infty$).

Case	$\delta_L/\Delta x$	N_y	$(U_{bulk} - V_f)/S_L$
1	7	160	5.52
2	10	240	5.25
3	15	368	5.16
4	20	480	5.15

Table 3.6: Relative flashback speeds, $(U_{bulk} - V_f)/S_L$, for different grid resolutions at low Fr ($Fr = 0.1$).

Case	$\delta_L/\Delta x$	N_y	$(U_{bulk} - V_f)/S_L$
1	7	160	12.01
2	10	240	11.94
3	15	368	11.91
4	20	480	11.90

Tables 3.5 and 3.6, and Figures 3.15 and 3.16 show the flashback speeds and flame shapes at high and low Fr respectively. They show that there are only small differences in the measured flashback speeds for cases 2, 3 and 4. Figure 3.15 also shows that at each resolution the flame shape at the flame leading point is very similar. There are differences at the trailing end of the flame, reflecting the accumulation of small errors along the length of the flame, but these differences do not affect the flashback speed significantly.

Domain Size

Table 3.7: Relative flashback speeds $(U_{bulk} - V_f)/S_L$ for different domain sizes, L_x/δ.

Fr	L_x/δ	$(U_{bulk} - V_f)/S_L$
0.1	8	11.93
0.1	20	11.94
0.1	25	11.94
0.06	30	19.60
0.06	40	19.57

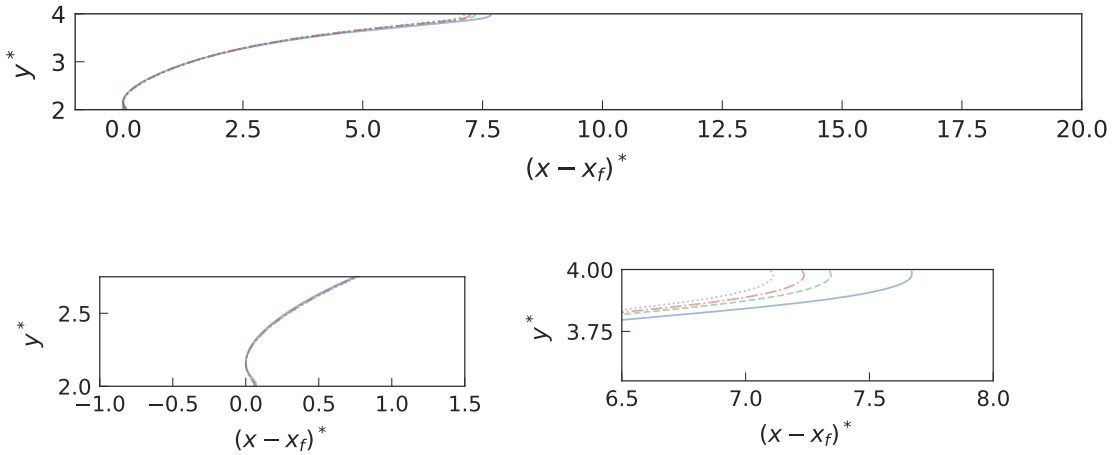

Figure 3.15: Converged flame shape at high Fr for different grid resolutions. As described in Table 3.5: Case 1 (blue solid), Case 2 (green dashed), Case 3 (red dot-dashed) and Case 4 (purple dotted).

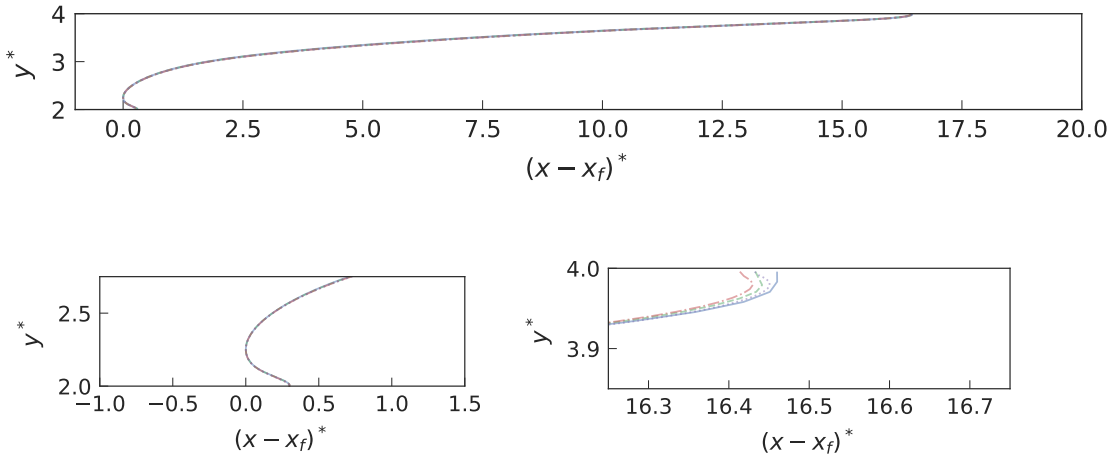

Figure 3.16: Converged flame shape at low Fr for different grid resolutions. As described in Table 3.6: Case 1 (blue solid), Case 2 (green dashed), Case 3 (red dot-dashed) and Case 4 (purple dotted).

Table 3.7, and Figures 3.17 and 3.18 show the flashback speeds and flame shapes for $Fr = 0.1$ and $Fr = 0.06$ at different domain sizes. In the longest simulation the flame front is completely contained within the domain, whereas in the shorter simulations the flame front crosses the outlet of the domain. Table 3.7 shows that this does not make a significant difference to the flashback speeds, even for a significantly shortened domain, while Figures 3.17 and 3.18 also show that the flame shape is unaffected. This shows that, provided the leading point of the flame is sufficiently far from the solution domain boundaries, the simulated flashback speed and flame shape are independent of the domain size. In the investigations to be conducted the simulations will be conducted with sufficient domain size to contain the whole of the flame front. The independence of the solutions

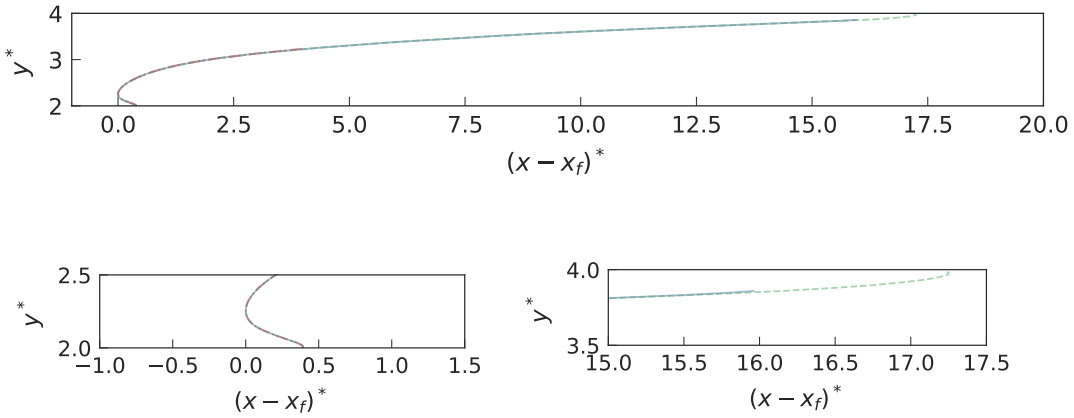

Figure 3.17: Converged flame shape at $Fr = 0.1$ for different domain sizes: $L_x/\delta = 8$ (red dot-dashed), $L_x/\delta = 20$ (blue solid) and $L_x/\delta = 25$ (green dashed).

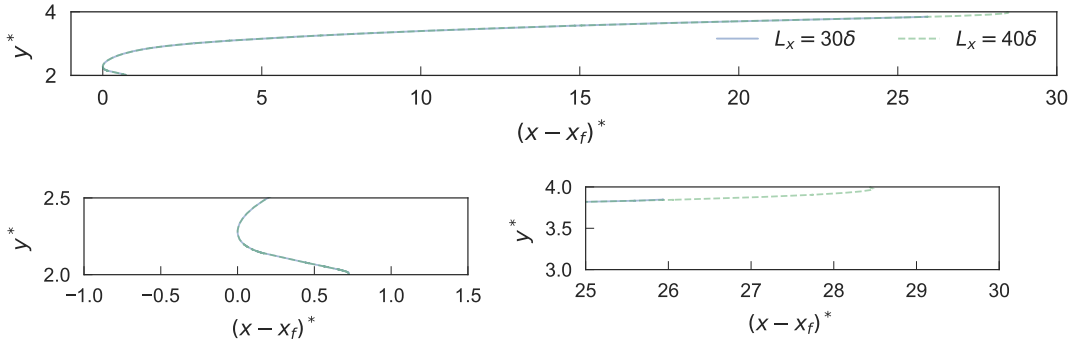

Figure 3.18: Converged flame shape at $Fr = 0.06$ for different domain sizes: $L_x/\delta = 30$ (blue solid) and $L_x/\delta = 40$ (green dashed).

with the boundary conditions affecting the flame front also verifies the implementation of the outlet boundary conditions as matching that of the equations solved in the domain.

Flame Position

Table 3.8 and Figure 3.19 show the flashback speed and flame shape at different flame positions at $Fr = 0.06$, where the extent of the reversed flow region and possible interaction with the inlet boundary conditions is greatest. Table 3.8 shows that between $x_f^* = x_f/\delta$ =3 and 6 there is little change in the simulated flashback speed. The change is larger between $x_f^* = 3$ and 4 but still not significant. This matches the results shown in Figure 3.13, where a flame was allowed to propagate upstream until it reached the inlet to the domain and the flashback speed was shown to drop significantly from around $x_f^* = 2$. Figure 3.19 shows that for the majority of the flame there is little change in the flame shape, particularly at the leading point of the flame. The trailing parts of the flame front do meet the upper wall at different locations as the flame position is changed. However, this does not affect the flashback speed significantly and the shape of the leading point remains the

same throughout. This shows that, even in the case with the largest region of reversed flow, using a flame position of $x_f^* = 4$ means the results are independent of the flame position.

Table 3.8: Relative flashback speeds ($(U_{bulk} - V_f)/S_L$) for different locations of the flame leading point ($x_f^* = x_f/\delta$) at $Fr = 0.06$.

x_f^*	$(U_{bulk} - V_f)/S_L$
3	7.93
4	8.03
5	8.07
6	8.08

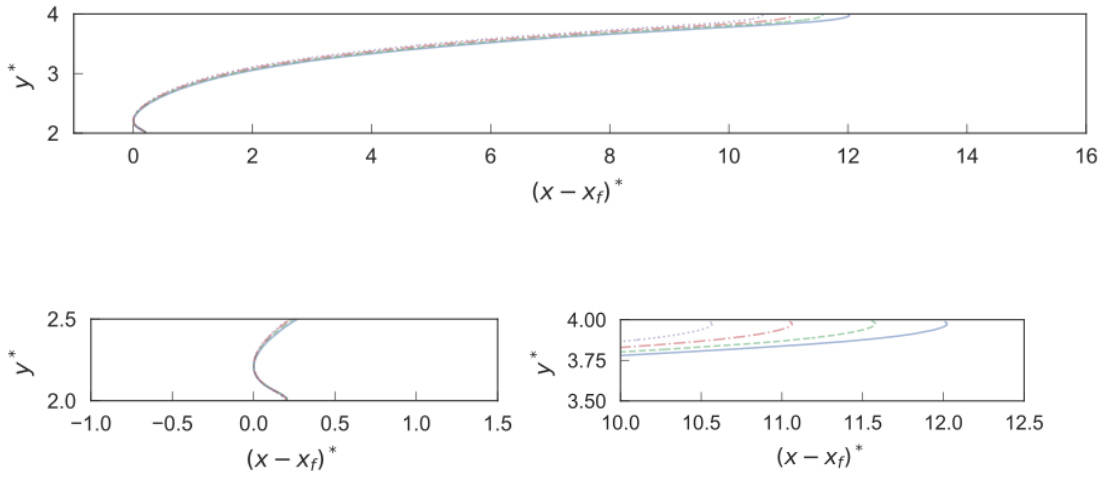

Figure 3.19: Converged flame shape for different locations of the flame leading point at $Fr = 0.06$: $x_f^* = x_f/\delta = 3$ (blue solid), $x_f^* = 4$ (green dashed), $x_f^* = 5$ (red dot-dashed) and $x_f^* = 6$ (purple dashed).

Part II

Model Formulation and Laminar Flows

Chapter 4

Flashback-Speed Models

In this chapter analytical models are developed which predict the effect of swirl on flashback speed. The models develop previous models of flame speed and extend them to account for the effect of swirl and the confinement resulting from flashback in a channel.

Analytical models are desired because they are helpful in providing estimates of flashback speeds without the cost of setting up and running time-dependent Computational Fluid Dynamics (CFD) simulations or experiments. They contain clear assumptions and show explicitly how flashback speed is affected by the included parameters. This helps understand and explain the trends to expect and those observed in simulations or in practice. The theoretically derived model of Lewis and von Elbe (1943), for example, has formed the basis for flashback-limit predictions and provides a very good basis for predictions in unconfined configurations (Kalantari and McDonell, 2017). The models derived here will be used to analyse the trends in flashback speed seen later in this thesis and to understand the mechanisms which control these trends.

The basis for the analytical modelling developed is a momentum balance around the flame, similar to that used previously in models of gravity currents (Benjamin, 1968), for flashback (Karimi et al., 2015) and in triple-flame velocity models (Ruetsch et al., 1995). Triple flames (Figure 4.1a) are an example of a partially premixed configuration where there is a gradient in mixture-fraction from rich

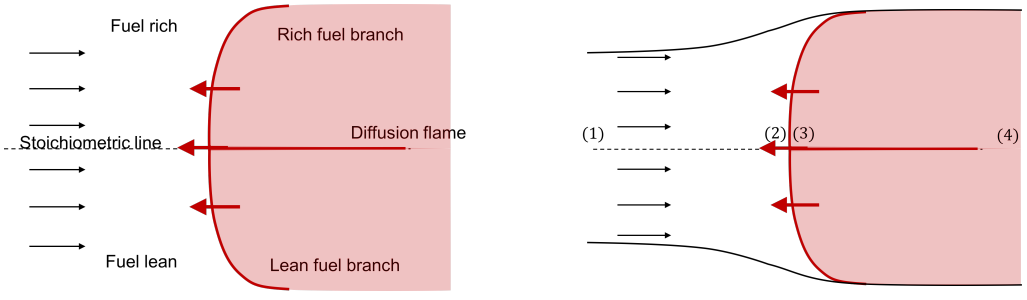

(a) Structure of a triple flame.

(b) Model configuration.

Figure 4.1: Diagrams of the structure of a triple flame (A) and the model configuration of Ruetsch et al. (1995) (B). Points (1) to (4) are on the stoichiometric line and represent: far upstream, immediately before the flame, immediately behind the flame and far downstream.

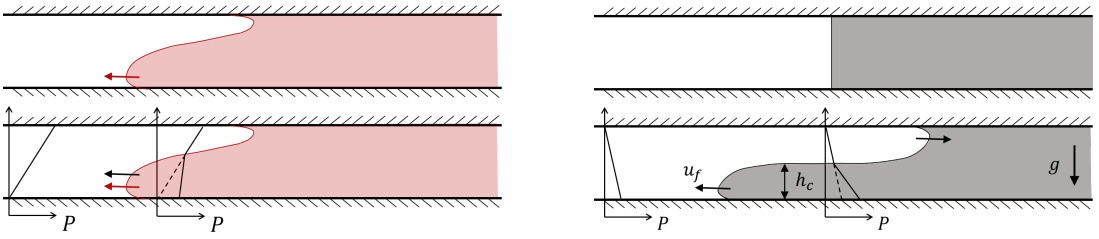

(a) (b)

Figure 4.2: Schematics of flame propagation (a) and gravity currents (b). For the flame propagation, the shaded red area indicates burned gases and the red arrow flame propagation. For the gravity current, the shaded grey area shows a fluid of higher density than the white area. The black arrows indicate pressure-driven flow. The overlain axes represent the pressure distribution at the given axial position.

to lean. Two of the branches of the triple flame are the rich and lean flames on each side of the stoichiometric line. From these branches, excess fuel and air, respectively, create a diffusion flame.

Figure 4.2a shows a schematic of boundary-layer flashback. Making the assumption that this flashback process can be treated as quasi-steady state then there is a balance between momentum fluxes, pressure forces and viscous forces in the control volume around the flame. This momentum balance is affected by inertia, acceleration through the flame front (due to the heat release and thermal expansion) and, where present, any body forces acting on the domain. Making additional assumptions that the flow is inviscid and the wall is adiabatic mean the flashback configuration shown in Figure 4.2a becomes analogous to the triple-flame configuration shown in Figure 4.1. According to this analogy, the streamline passing through the leading point of the flame corresponds to the wall, in the case of flashback, and to the stoichiometric iso-surface, in the case of the triple flame.

In the presence of wall-normal acceleration or body forces, the flashback configuration can also be considered analogous to that of a gravity current. Figure 4.2b shows a schematic of a lock-exchange flow, where two fluids of different densities are initially separated. When this separation is removed, the two fluids flow relative to one another, with the heavier fluid (grey) flowing underneath the lighter fluid (white). Figure 4.2b also shows the pressure distribution in the domain where the pressure gradient in the heavier fluid increases compared to that in the lighter fluid. This can be compared to the situation in boundary-layer flashback 4.2a, where the top diagram shows boundary-layer flashback in a non-swirling flow with flame propagation only (red arrow). The bottom diagram shows a swirling flow where the radial pressure gradient resulting from centripetal acceleration means that the pressure increases with radial distance. The lower density of the burned gases means the pressure gradient is lower here than in the unburned gases. This can result in a pressure increase with axial distance which drives the flow of the burned gases relative to the unburned in addition to flame propagation. The pressure increase with axial distance was hypothesised by Heeger et al. (2010) as a possible mechanism of boundary-layer flashback in a swirling flow. Here the analogy is made with a gravity current in the limit of no flame propagation. Developing a model based on this pressure-driven flow will allow testing of whether this physical mechanism can describe the trends for the effect of swirl on flashback speeds.

The approach taken here begins by adapting the triple-flame model of Ruetsch et al. (1995) shown in Figure 4.1 for application to flashback, and extending it to account for flow confinement in channels and for wall normal body forces or acceleration. The model of Ruetsch et al. (1995) defines

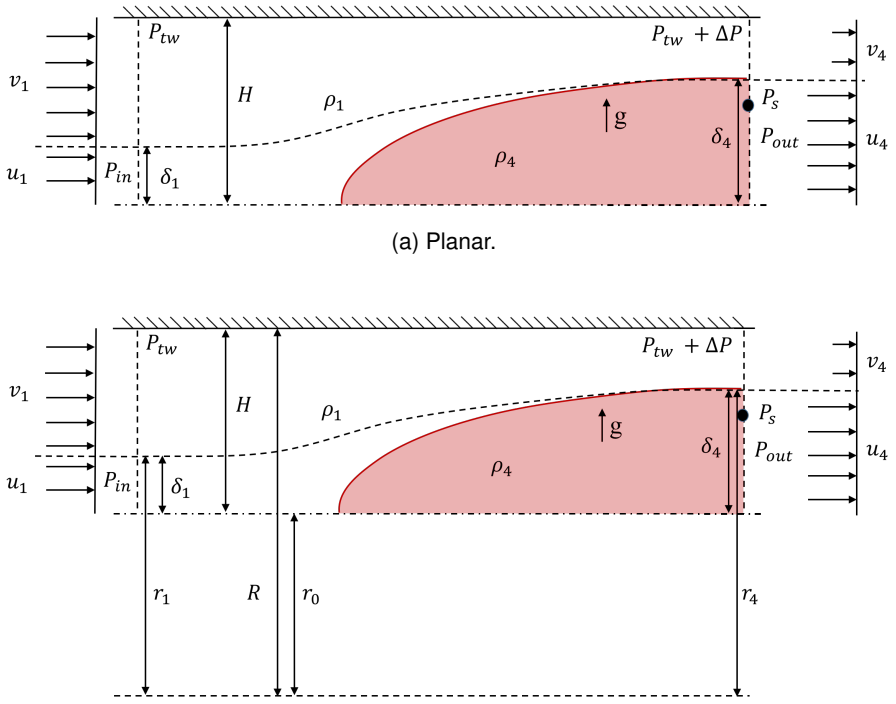

(a) Planar.

(b) Annular.

Figure 4.3: Diagrams of the control-volume geometries used in the planar and annular momentum-balance models of flashback speed. All variables are defined in Table 4.1.

a control volume bounded by the two streamlines which meet the outer edges of the rich and lean flame branches. Four points along the streamline through the flame leading point, which in this case are along the stoichiometric line, are then defined: far upstream (1), immediately upstream of the flame front (2), immediately downstream of the flame front (3) and far downstream (4). Assuming the densities in the unburned and burned regions are uniform, the Rankine-Hugoniot relations are applied between points (2) and (3), and mass and momentum conservation is applied betweens points (1) and (2), (3) and (4), and over the whole control volume. Given the unconfined configuration, the pressure everywhere on the control-volume boundaries is assumed to be constant which gives relations defining the expansion of the streamlines (height-ratio between points (1) and (4), $\delta_1/\delta_4 = \rho_4/\rho_1$) and the propagation speed of the triple flame (velocity-ratio between points (1) and (2), $u_1/u_2 = \sqrt{\rho_1/\rho_4}$, where u_2 is assumed to equal S_L).

Figure 4.3 shows the geometry of the control volume to be used. The upper surface of the control volume is defined by a streamsurface sufficiently far from the wall such that it intersects with the flame in a region where the flame can be approximated as being parallel to the wall. In a premixed flow, the flame speed is finite everywhere in the fluid, so a stationary flame front would never strictly be parallel to the flow, however, provided the flashback speed (relative to the bulk flow) is around an order of magnitude greater than the laminar or turbulent flame speeds (which is typically the case), it is a reasonable approximation to treat the flame surface as being parallel to the wall.

To account for the wall-normal pressure gradient, a body force, g, has been added to the model of Ruetsch et al. (1995) and this means that the pressures in the domain are calculated by integrating from the pressure on the top wall of the channel and P_{in} and P_{out} are average pressures acting on

the inlet and outlet of the control volume. The body force is used to create a densiometric Froude number, similar to that used in gravity currents:

$$Fr = \frac{u_2}{u_g} = \frac{u_2}{\sqrt{\delta_4 g \frac{(\rho_1 - \rho_4)}{\rho_1}}} \tag{4.1}$$

where u_g is the buoyancy velocity. The limit of Fr$\rightarrow 0$ corresponds to a buoyancy velocity much greater than the flame propagation speed, such that the flame surface is driven like the interface in a pure gravity current. The model would then be expected to recover the predicted speed of gravity currents in unconfined configurations: $u_1/u_g = \sqrt{2}$ (Benjamin, 1968). In the limit of infinite Fr, flame propagation is dominant, leading to the recovery of the result of Ruetsch et al. (1995): $u_1/S_L = \sqrt{\rho_1/\rho_4}$.

The effect of confinement is accounted for by the pressure change along the top wall of the channel, ΔP, which is calculated by conducting a mass and momentum balance over the region of unburned flow above the streamline. This chapter describes the derivation and solution of this model in planar and annular co-ordinates.

The momentum-balance models will be derived in planar and annular co-ordinates. In both these geometries the assumptions and derivation process remain the same but the method of calculating the cross-sectional areas of each region are changed to fit the geometry being investigated.

In addition to the momentum-balance models, to be derived in planar and annular co-ordinates, an additive model is also developed. This model is motivated by the limiting cases of Ruetsch et al. (1995) at infinite Fr and gravity currents at zero Fr. The additive model combines $u_1/u_g = \sqrt{2}$ and $u_1/S_L = \sqrt{\rho_1/\rho_4}$, and is shown to be a simplification of the planar momentum-balance model.

The next section gives the nomenclature used in the models before the planar and annular momentum-balance, and then additive models are derived.

4.1 Nomenclature

Table 4.1: Nomenclature used in the models of flashback speed.

Dimensional variables:	
ρ_i	Density at points 1 to 4
u_i	Velocity in control volume 1 at points 1 to 4
v_i	Velocity in control volume 2 at points 1 to 4
δ_1	Streamline height at inlet to control volume
δ_4	Streamline height at outlet of control volume
P_{in}	Average pressure acting on inlet to control volume
P_{out}	Average pressure acting on outlet of control volume
P_{tw}	Pressure on top wall of channel at inlet to control volume
$P_{tw} + \Delta P$	Pressure on top wall of channel at outlet of control volume
g	Body force
H	Channel height
P_s	Streamline pressure at the upper surface of the control volume
r_0	Inner radius of annulus (annular model only)
R	Outer radius of annulus (annular model only)
r_1	Radial height of streamline at inlet to control volume $= r_0 + \delta_1$ (annular model only)
r_4	Radial height of streamline at outlet of control volume $= r_0 + \delta_4$ (annular model only)
Non-Dimensional variables:	
τ	Thermal expansion ratio $= (\rho_u - \rho_b)/\rho_u = 1 - 1/D$
u_i'	Velocity ratios $= u_i/u_2$
r_i'	Radius ratio $= r_i/r_4$ (annular model only)
r_0'	Inner radius ratio $= r_0/r_4$ (annular model only)
R'	Outer radius ratio $= R/r_4$ (annular model only)
σ, m_1, m_2, n_1, n_2	Model constants defining the streamline pressure used in the momentum equations
Independent variables:	
Fr	Froude number $= u_2/\sqrt{\delta_4 g \tau}$
D	Density ratio $= \rho_1/\rho_4$
H'	Confinement ratio $=H/\delta_4$
R^*	Annulus radius ratio $= R/r_0$ (annular model only)
Dependent variables:	
u_1'	Velocity ratio $= u_1/u_2$
δ_1'	Height ratio $= \delta_1/\delta_4$ (planar model only)
r_1'	Height ratio $= r_1/r_4$ (annular model only)
$\Delta P'$	Non-dimensional pressure drop $= \Delta P/(\frac{1}{2}\rho_1 u_1^2)$

4.2 Planar Model with Uniform Body Force

4.2.1 Derivation of Height-Ratio Equation

The basis for this derivation is the mass and momentum balance over the control volume containing the region of burned gases:

$$\rho_1 u_1 \delta_1 = \rho_4 u_4 \delta_4 \tag{4.2}$$

$$\rho_1 u_1^2 \delta_1 + \delta_1 P_{in} + (\delta_4 - \delta_1) P_s = \rho_4 u_4^2 \delta_4 + \delta_4 P_{out} \tag{4.3}$$

On the top wall of the channel at the left-hand end of the control volume, the pressure is set to P_{tw}. P_{in} can then be calculated as the average pressure acting over the inlet to the control volume from P_{tw} and the pressure gradient ρg:

$$P_{in} = P_{tw} - \rho_1 g(H - \delta_1) - \rho_1 g \frac{\delta_1}{2} \tag{4.4}$$

For P_{out} the pressure is again calculated from the pressure on the top wall and the pressure gradient. If the system is unconfined then this pressure is assumed to also be P_{tw}. However, if the system is confined then as the height of the streamtube changes, the fluid in the unburned region of the channel must occupy a smaller space and accelerate to conserve mass. This acceleration and the pressure force acting on the streamline separating the regions will cause a drop in pressure in this unburned region. The pressure on the top wall at the outlet of the control volume will therefore change. We denote this ΔP so that P_{out} is given by:

$$P_{out} = P_{tw} + \Delta P - \rho_1 g(H - \delta_4) - \rho_4 g \frac{\delta_4}{2} \tag{4.5}$$

All that remains now is to evaluate the pressure acting on the streamline. This choice of pressure may affect the results from the model and so a general equation is defined for this pressure, which is again based on calculating a change in pressure from the top wall of the channel, P_{tw}. It is assumed that P_s is a constant value and this value is somewhere between the upstream and downstream pressures, based on an average between δ_1 and δ_4. A parameter σ is used to denote how close this pressure is set to the upstream or downstream pressures ($\sigma = 1$ being taken at the upstream, and $\sigma = 0$ at the upstream), while m_1, m_2, n_1, n_2 denote the location where the average pressure is taken.

$$\begin{aligned} P_s &= P_{tw} - \rho_1 g(H - \delta_4) - \sigma \rho_1 g \left(m_1' \delta_1 + m_2' \delta_4\right) + (1 - \sigma)(\Delta P + \rho_4 g \left(n_1' \delta_4 + n_2' \delta_1\right)) \\ &= P_{tw} - \rho_1 g(H - \delta_4) - \rho_1 g \left(m_1 \delta_1 + m_2 \delta_4\right) + (1 - \sigma)\Delta P - \rho_4 g \left(n_1 \delta_4 + n_2 \delta_1\right) \end{aligned} \tag{4.6}$$

m_1', m_2', n_1' and n_2' are constants where $m_1' \sigma = m_1$, $m_2' \sigma = m_2$, $n_1'(1 - \sigma) = n_1$, $n_2'(1 - \sigma) = n_2$.

Using these expressions to eliminate P_{in}, P_{out}, P_s and u_4 from the conservation of momentum and introducing the non-dimensional variables $D = \rho_1 / \rho_4$, $\delta_1' = \delta_1 / \delta_4$, $Fr = u_2 / \sqrt{\delta_4 g \tau}$, $u_1' = u_1 / u_2$, $\Delta P' = \Delta P / (1/2 \rho_1 u_1^2)$ gives the following expression for the height-ratio (a more detailed derivation

of these steps is given in Appendix C.1):

$$\begin{aligned} 0 =& \delta_1'^2 \left[-D(D-1)u_1'^2 Fr^2 + D\left(m_1 + \frac{1}{2}\right) + n_2 \right] + \\ & \delta_1' \left[(D-1)Fr^2 u_1'^2 - D(m_1 + 1 - m_2) + n_1 - n_2 - (1-\sigma)\frac{1}{2}\Delta P' D u_1'^2 Fr^2 \right] + \\ & \left[\frac{1}{2} - n_1 - Dm_2 - \sigma\frac{1}{2}\Delta P' D u_1'^2 Fr^2 \right] \end{aligned} \tag{4.7}$$

As Fr tends to ∞ and $\Delta P'$ tends to 0 then the model of Ruetsch et al. (1995) is recovered:

$$\delta_1' = \frac{1}{D} = \frac{\rho_4}{\rho_1} \tag{4.8}$$

Taking the pressure on the streamline as equal to the outlet pressure at $((\delta_4 + \delta_1)/2)$ gives:

$$\delta_1' = \frac{Fr^2 u_1'^2 - 1 - \Delta P' Fr^2/D}{D u_1'^2 Fr^2 + 1/2} \tag{4.9}$$

4.2.2 Derivation of Velocity-Ratio Equation

The derivation of the velocity-ratio equation starts from Ruetsch et al. (1995) Equation 6:

$$u_1'^2 = \frac{\rho_1/\rho_4 - 1}{(P_1 - P_4)/(\frac{1}{2}\rho_1 u_1^2) + 1 - (\rho_1/\rho_4)(\delta_1/\delta_4)^2} \tag{4.10}$$

or in the non-dimensional variables defined here:

$$u_1'^2 = \frac{D-1}{(P_1 - P_4)/(\frac{1}{2}\rho_1 u_1^2) + 1 - \delta_1'^2 D} \tag{4.11}$$

In Ruetsch et al. (1995) the domain was unconfined so that the pressures throughout the domain were assumed to be equal, P_1 was therefore assumed to equal P_4 and the term $(P_1 - P_4)/(\frac{1}{2}\rho_1 u_1^2)$ disappears. In this case, the body force means that the pressure along the bottom wall will change along the line of symmetry. In addition, confinement by the top wall means that there will be a pressure drop down the channel which will affect P_4 and is given by Equation 4.19.

P_1 and P_4 are evaluated using the hydrostatic pressures at these points:

$$P_4 = P_{tw} + \Delta P - \delta_4 \rho_4 g \tag{4.12}$$

$$P_1 = P_{tw} - \delta_4 \rho_1 g \tag{4.13}$$

Substituting in these values and non-dimensionalising using Fr gives:

$$u_1'^2 = \frac{D - 1 + \frac{2}{Fr^2}}{1 - (\delta_1'^2/D) - \Delta P'} \tag{4.14}$$

The result of Ruetsch et al. (1995) can be recovered as Fr tends to infinity, $\Delta P'$ to 0, and substituting in $\delta_1' = 1/D$ from the original expression for the height-ratio.

$$u_1'^2 = D \tag{4.15}$$

4.2.3 Derivation of Pressure-Drop Equation

The final derivation is that of the pressure drop between the upstream and downstream ends of the control volume. This derivation follows the same procedure as above for the height ratio, but with the mass and momentum balance applied in the upper region that does not burn.

Mass and momentum balance for the control volume, with the velocity in this region denoted by v and the height of the channel given by H:

$$\rho_1 v_1 (H - \delta_1) = \rho_1 v_4 (H - \delta_4) \tag{4.16}$$

$$\begin{aligned} &\rho_1 v_1^2 (H - \delta_1) + \left(P_{tw} - \frac{(H - \delta_1)}{2} \rho_1 g \right) (H - \delta_1) = \\ &\rho_1 v_4^2 (H - \delta_4) + (\delta_4 - \delta_1) P_s + \left(P_{tw} + \Delta P - \frac{(H - \delta_4)}{2} \rho_1 g \right) (H - \delta_4) \end{aligned} \tag{4.17}$$

The same procedure is used here as for the height-ratio equation, but re-arranging for $\Delta P'$, with the same set of non-dimensional variables, plus the confinement ratio, $H' = H/\delta_4$ (a more detailed derivation of these steps is given in Section C.4).

$$\begin{aligned} &\frac{\Delta P'}{2} u_1'^2 D \left(\sigma(1 - \delta_1') - (H' - \delta_1') \right) = D u_1'^2 (H' - \delta_1') \left(\frac{(H' - \delta_1')}{(H' - 1)} - 1 \right) + \\ &\frac{(\delta_1' - 1)}{2\tau Fr^2} \left[D \left((\delta_1' - 1) + 2m_1 \delta_1' + 2m_2 \right) + 2(n_1 + n_2 \delta_1') \right] \end{aligned} \tag{4.18}$$

Again, taking the pressure on the streamline as equal to the outlet pressure at $((\delta_4 - \delta_1)/2)$ gives:

$$\Delta P' = -2 \frac{(1 - \delta_1')}{(H' - 1)} - \frac{(\delta_1' - 1)^2}{u_1'^2 Fr^2 (H' - \delta_1')} \tag{4.19}$$

As H' tends to ∞, this term will tend to zero, consistent with the unconfined model.

4.2.4 Summary: Confined Model

Using the current choice of streamline pressure gives three equations for the three dependent variables: the height-ratio (δ_1'), velocity-ratio (u_1') and pressure drop $(\Delta P')$ based on the independent variables of the Froude number (Fr), density ratio (D) and confinement ratio (H'):

$$\delta_1' = \frac{Fr^2 u_1'^2 - 1 - \Delta P' Fr^2 / D}{D u_1'^2 Fr^2 + 1/2} \tag{4.20a}$$

$$u_1'^2 = \frac{D - 1 + \frac{2}{Fr^2}}{1 - (\rho_1/\rho_4)(\delta_1/\delta_4)^2 - \Delta P'} \tag{4.20b}$$

$$\Delta P' = -2\frac{(1-\delta_1')}{(H'-1)} - \frac{(\delta_1'-1)^2}{u_1'^2 Fr^2 (H'-\delta_1')} \tag{4.20c}$$

4.2.5 Special Case: Unconfined Model

The unconfined model is generated by assuming that the pressure drop is zero. This removes the pressure drop equation and allows the height-ratio and velocity-ratio equations to be simplified to:

$$\delta_1' = \frac{Fr^2 u_1'^2 - 1}{D u_1'^2 Fr^2 + 1/2} \tag{4.21a}$$

$$u_1'^2 = \frac{D - 1 + \frac{2}{Fr^2}}{1 - (\rho_1/\rho_4)(\delta_1/\delta_4)^2} \tag{4.21b}$$

4.3 Annular Model with Uniform Body Force

In this section, the unconfined model of the previous section is re-derived using cylindrical co-ordinates, but again with a uniform body force, g. This means that the pressure distributions are still linear functions of r but the cross-sectional areas become functions of r^2. δ is retained as referring to heights from the bottom wall of the channel, while r is measured from the axis of the annulus. The relevant height for the buoyancy velocity is still δ_4, so this is retained in the definition of Fr. The two scales are related using r_0:

$$\delta_4 = r_4 - r_0 \tag{4.22}$$

which in non-dimensional co-ordinates becomes:

$$\delta_4' = 1 - r_0' \tag{4.23}$$

This allows Fr to be defined using r_4:

$$Fr = \frac{u_2}{\sqrt{g\tau\delta_4}} = \frac{u_2}{\sqrt{g\tau r_4}} \frac{1}{\sqrt{1-r_0'}} \tag{4.24}$$

Other than these differences, the same procedure used for the planar model is used here to give a final set of equations for: the height-ratio (δ_1') and velocity-ratio (u_1') based on the independent variables of the Froude number (Fr), density ratio (D) and, additionally, the annulus radius ratio (R/r_0).

4.3.1 Derivation of Height-Ratio Equation

As in the planar model the derivation of the height-ratio equation uses the mass and momentum balance over the control volume containing the burned flow:

$$\pi(r_1^2 - r_0^2)\rho_1 u_1 = \pi(r_4^2 - r_0^2)\rho_4 u_4 \tag{4.25}$$

$$\pi\left(r_4^2 - r_1^2\right)P_s + \pi\left(r_1^2 - r_0^2\right)\left(P_{in} + \rho_1 u_1^2\right) = \pi\left(r_4^2 - r_0^2\right)\left(P_{out} + \rho_4 u_4^2\right) \tag{4.26}$$

P_{in}, P_{out} and P_s are described using radial co-ordinates:

$$P_{in} = P_{tw} - \rho_1 g\left(R - r_1\right) - \rho_1 g\left(\frac{r_1}{2} - \frac{r_0}{2}\right) \tag{4.27}$$

$$P_{out} = P_{tw} - \rho_1 g\left(R - r_4\right) - \rho_1 g\left(\frac{r_4}{2} - \frac{r_0}{2}\right) \tag{4.28}$$

$$P_s = P_{tw} - \rho_1 g\left(R - r_4\right) - \rho_4 g\left(r_4 - r_1\right) \tag{4.29}$$

The conservation of mass is used to eliminate u_4 from the conservation of momentum. The momentum equation and the equations for each of the pressures are then non-dimensionalised by dividing through by $\rho_4 u_2^2 r_4^2$ and substituting in the non-dimensional variables ($D = \rho_1/\rho_4$, $r_1' = r_1/r_4$, $r_0' = r_0/r_4$, $Fr = u_2/\sqrt{\delta_4 g\tau}$, $u_1' = u_1/u_2$, $P_{tw}' = P_{tw}/(1/2\rho_1 u_2^2)$):

$$\begin{aligned} &-\frac{D^2 u_1'^2\left(r_1'^2 - r_0'^2\right)^2}{1 - r_0'^2} + D u_1'^2\left(r_1'^2 - r_0'^2\right) + \\ &\frac{P_s}{\rho_4 u_2^2}\left(1 - r_1'^2\right) + \frac{P_{in}}{\rho_4 u_2^2}\left(r_1'^2 - r_0'^2\right) - \frac{P_{out}}{\rho_4 u_2^2}\left(1 - r_0'^2\right) = 0 \end{aligned} \tag{4.30}$$

$$\frac{P_{in}}{\rho_4 u_2^2} = \frac{DP_{tw}'}{2} - \frac{D^2\left(R' - r_1'\right)}{Fr^2\left(D-1\right)\left(1 - r_0'\right)} - \frac{D^2\left(r_1' - r_0'\right)}{2Fr^2\left(D-1\right)\left(1 - r_0'\right)} \tag{4.31}$$

$$\frac{P_{out}}{\rho_4 u_2^2} = \frac{DP_{tw}'}{2} - \frac{D^2\left(R' - 1\right)}{Fr^2\left(D-1\right)\left(1 - r_0'\right)} - \frac{D^2}{2Fr^2\left(D-1\right)} \tag{4.32}$$

$$\frac{P_s}{\rho_4 u_2^2} = \frac{DP_{tw}'}{2} - \frac{D^2\left(R' - 1\right)}{Fr^2\left(D-1\right)\left(1 - r_0'\right)} + \frac{D\left(r_1' - 1\right)}{Fr^2\left(D-1\right)\left(1 - r_0'\right)} \tag{4.33}$$

Combining these together gives the final equation for the height-ratio: $r_1' = r_1/r_4$.

$$\begin{aligned} &2DFr^2 u_1'^2\left(D-1\right)r_1'^4 - \left(D-2\right)\left(1 + r_0'\right)r_1'^3 + \left[Dr_0'\left(1 - r_0'\right) - 2\left(1 + r_0'\right) + 2D + \right. \\ &\left. Fr^2 u_1'^2\left(2r_0'^2 D\left(3 - 2D\right) - 2D + 2\left(1 - r_0'^2\right)\right)\right]r_1'^2 + \\ &\left(1 - r_0'\right)\left(Dr_0'^2 - 2\right)r_1' + \left[-D\left(r_0'^3 + 1\right) + 2\left(r_0' + 1\right) + \right. \\ &\left. Fr^2 u_1'^2\left(2D\left(\left(D-2\right)r_0^4 + r_0^2\right) + 2r_0^2\left(r_0^2 - 1\right)\right)\right] = 0 \end{aligned} \tag{4.34}$$

4.3.2 Derivation of Velocity-Ratio Equation

For the derivation of the velocity ratio, the one-dimensional relations, which were used in the planar case, are still assumed to hold. To adapt the equation to cylindrical co-ordinates, it is necessary to

change the conservation of mass which is also applied. Combining the one-dimensional relations before mass conservation is introduced gives:

$$\left(\frac{u_1}{u_2}\right)^2 = \frac{\rho_1/\rho_4 - 1}{(P_1 - P_4)/(\frac{1}{2}\rho_1 u_1^2) + 1 - (\rho_4/\rho_1)(u_4/u_1)^2} \tag{4.35}$$

In the planar case, mass conservation:

$$\rho_1 u_1 \delta_1 = \rho_4 u_4 \delta_4 \tag{4.36}$$

can be used to substitute for u_4/u_1 to give Equation 6 of Ruetsch et al. (1995):

$$\left(\frac{u_1}{u_2}\right)^2 = \frac{\rho_1/\rho_4 - 1}{(P_1 - P_4)/(\frac{1}{2}\rho_1 u_1^2) + 1 - (\rho_1/\rho_4)(\delta_1/\delta_4)^2} \tag{4.37}$$

To change this to axi-symmetric co-ordinates mass conservation can again be introduced:

$$\pi\rho_1 u_1 \left(r_1^2 - r_0^2\right) = \pi\rho_4 u_4 \left(r_4^2 - r_0^2\right) \tag{4.38}$$

and again substituted for u_4/u_1:

$$\left(\frac{u_1}{u_2}\right)^2 = \frac{\rho_1/\rho_4 - 1}{(P_1 - P_4)/(\frac{1}{2}\rho_1 u_1^2) + 1 - (\rho_1/\rho_4)((r_1^2 - r_0^2)/(r_4^2 - r_0^2))^2} \tag{4.39}$$

The equations for P_1 and P_4 can now be introduced, where they are again assumed to be given by integrating the pressure from the top wall using the uniform body force, g:

$$P_1 = P_{tw} - \rho_1 g\,(R - r_0) \tag{4.40}$$

$$P_4 = P_{tw} - \rho_1 g\,(R - r_4) - \rho_4 g\,(r_4 - r_0) \tag{4.41}$$

These equations are then converted to give the non-dimensional forms of P_1 and P_4:

$$P_1' = \frac{P_1}{\frac{1}{2}\rho_1 u_2^2} = P_{tw}' - \frac{2D\,(R' - r_0')}{Fr^2\,(D-1)\,(1 - r_0')} \tag{4.42}$$

$$P_4' = \frac{P_4}{\frac{1}{2}\rho_1 u_2^2} = P_{tw}' - \frac{2D\,(R' - 1)}{Fr^2\,(D-1)\,(-r_0' + 1)} + \frac{2\,(r_0' - 1)}{Fr^2\,(D-1)\,(-r_0' + 1)} \tag{4.43}$$

Substituting these into Equation 4.39 and simplifying gives:

$$u_1'^2 = \frac{D - 1 + \frac{2}{Fr^2}}{D\frac{(r_1'^2 - r_0'^2)}{(r_0'^2 - 1)} - 1} \tag{4.44}$$

Consistency with Ruetsch et al. (1995)

Equation 4.39 can also be shown to give the same result as Ruetsch et al. (1995) when used with the same assumptions for the pressure.

Taking the conservation of mass and momentum for the control volume:

$$\pi(r_1^2 - r_0^2)\rho_1 u_1 = \pi(r_4^2 - r_0^2)\rho_4 u_4 \tag{4.45}$$

$$\pi\left(r_1^2 - r_0^2\right)\left(\overline{P}_{in} + \rho_1 u_1^2\right) + \pi\left(r_4^2 - r_1^2\right)P_s = \pi\left(r_4^2 - r_0^2\right)\left(\overline{P}_{out} + \rho_4 u_4^2\right) \tag{4.46}$$

and applying the same assumptions used by Ruetsch et al. (1995) in deriving the expression for the height ratio ($P_1 = P_4 = P_s = \overline{P}_{in} = \overline{P}_{out}$) gives:

$$\frac{(r_1^2 - r_0^2)}{(r_4^2 - r_0^2)} = \frac{\rho_4}{\rho_1} \tag{4.47}$$

This result can then be substituted into the velocity-ratio equation, Equation 4.39:

$$\left(\frac{u_1}{u_2}\right)^2 = \frac{\rho_1/\rho_4 - 1}{1 - (\rho_4/\rho_1)} = \frac{\rho_1}{\rho_4} \tag{4.48}$$

to show that this result is independent of the geometry.

4.3.3 Summary: Unconfined Model

The final equations then give the radial height-ratio (r_1') and velocity-ratio (u_1') based on the independent variables of the Froude number (Fr), density ratio (D) and inner-radius ratio ($r_0' = r_0/r_4$), which can be expressed in terms of the annulus radius ratio and confinement ratio ($r_0' = H'/(R^* + H' - 1)$):

$$\begin{aligned}
&2DFr^2u_1'^2\left(D-1\right)r_1'^4 - \left(D-2\right)\left(1+r_0'\right)r_1'^3 + \left[Dr_0'\left(1-r_0'\right) - 2\left(1+r_0'\right) + 2D + \right.\\
&Fr^2u_1'^2\left(2r_0'^2D\left(3-2D\right) - 2D + 2\left(1-r_0'^2\right)\right)\left.\right]r_1'^2 +\\
&\left(1-r_0'\right)\left(Dr_0'^2 - 2\right)r_1' + \left[-D\left(r_0'^3+1\right) + 2\left(r_0'+1\right) + \right.\\
&\left.Fr^2u_1'^2\left(2D\left(\left(D-2\right)r_0'^4 + r_0'^2\right) + 2r_0'^2\left(r_0'^2-1\right)\right)\right] = 0
\end{aligned} \tag{4.49a}$$

$$u_1'^2 = \frac{D - 1 + \frac{2}{Fr^2}}{D\frac{\left(r_1'^2 - r_0'^2\right)}{\left(r_0'^2 - 1\right)} - 1} \tag{4.49b}$$

4.4 Solution

The equations derived above form the basis for the planar confined and unconfined models, and annular unconfined model. All of the equations are solved numerically using the Powell hybrid root-finding algorithm as implemented in MINPACK (Garbow et al., 1980) with the Jacobian calculated using forward differencing. Initial guesses for the dependent variables are made using the Ruetsch et al. (1995) model ($\delta_1' = 1/D; u_1'^2 = D$) and assuming the configuration is unconfined ($\Delta P' = 0$). The iterative procedure uses a value of 1.5×10^{-8} to define convergence. For the confined model, the solution procedure starts by numerically solving the height-ratio and velocity-ratio equations with $\Delta P' = 0$. The pressure drop is then updated based on this initial solution and the height-ratio and velocity-ratio solved for again. This continues until the pressure drop and height ratio converge.

4.5 Additive Model

A second, unconfined model is derived from the first and describes the flame-speed enhancement from a combination of the model of Ruetsch et al. (1995), accounting for flame propagation, and that of gravity currents, which accounts for pressure-driven flows:

$$\left(\frac{u_1}{u_2}\right)^2 = \frac{\rho_u}{\rho_b} + \frac{2}{Fr^2}. \tag{4.50}$$

In the limit of Fr$\rightarrow \infty$ the model reverts to that of Ruetsch et al. (1995) and in the limit of Fr$\rightarrow 0$ to the model of gravity currents.

It is also possible to derive this equation from the velocity-ratio equation of the planar, confined model:

$$u_1'^2 = \frac{D - 1 + \frac{2}{Fr^2}}{1 - (\rho_1/\rho_4)(\delta_1/\delta_4)^2 - \Delta P'} \tag{4.51}$$

Firstly, assuming an unconfined configuration gives $\Delta P' = 0$. Separating the two components into flame-propagation and gravity-current then: for the flame propagation, δ_1/δ_4 can be assumed to be $1/D$ to give the Ruetsch et al. (1995) component D; for the gravity current part the height-ratio tends to zero at the limit of zero Fr, because there is no flow through the flame front, such that this part is assumed to be $2/Fr^2$. This then gives the additive model of above.

4.6 Summary

In this chapter, models of flashback speed were developed that describe the effect of swirl, confinement and volumetric expansion on flashback speed, streamline height ratio (describing flow diversion) and pressure drop along the channel. The model of Ruetsch et al. (1995) is based on a momentum balance in an unconfined triple flame and describes the effect of volumetric expansion and flame propagation on the propagation speed of a triple flame. The analogy was made between this configuration and flashback along an adiabatic, slip-wall. The Ruetsch model was extended, in planar and cylindrical co-ordinates, by including a uniform body force to describe the effect of swirl,

and in planar co-ordinates with a second control volume to describe the effect of confinement. The flashback-speed predictions transition from being dominated by flame propagation and volumetric expansion to being dominated by swirl or pressure-driven flashback. This pressure-driven flashback is that originally described by Heeger et al. (2010). At the limit of no flame propagation, the model and configuration describe a gravity current and the analogy is made between a gravity current and pressure-driven flashback. The transition from flame-propagation dominated to pressure-driven motivated the development of a third, additive, model which describes unconfined flashback and that contains the combination of the Ruetsch model and that of a gravity current (Benjamin, 1968).

Chapter 5

Laminar Boundary-Layer Flashback

In this chapter, two-dimensional laminar simulations in annular channels are conducted to evaluate the effect of swirl and wall velocity gradient on flashback. The effect of swirl on flashback, and the physical mechanisms which cause boundary-layer flashback in swirling flows, have not previously been described. In this chapter, two-dimensional, laminar simulations are used to investigate the trends in flashback speed with swirl and to evaluate whether the predictions of the momentum-balance models developed in the previous chapter capture these trends. The effect of a developing boundary layer has also been identified as an area not covered by previous investigations of boundary-layer flashback (Kalantari et al., 2017). In this investigation, the wall velocity gradient, and its dependence on the velocity profile, channel height and bulk velocity, is investigated to help evaluate the effect of boundary layer development on flashback speed.

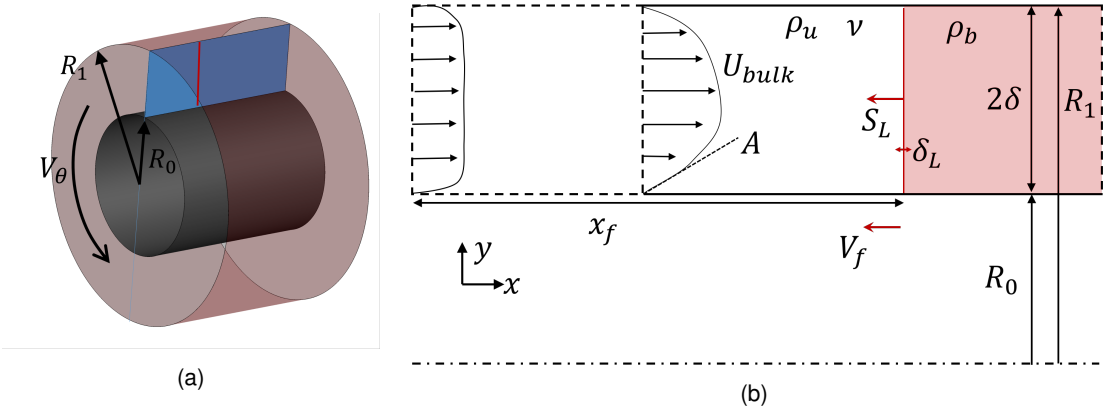

(a) (b)

Figure 5.1: Diagrams of the annular problem configuration.

5.1 Simulation Setup

5.1.1 Independent Non-Dimensional Parameters

Figure 5.1 shows the problem configuration to be investigated. Figure 5.1a shows the overall three-dimensional annulus, which includes a swirling flow of circumferential velocity V_θ extending from the inner radius, R_0, to the outer radius, R_1. Figure 5.1b shows the two-dimensional slice of the overall domain which will be used in the simulations in this chapter. The flame propagates against the oncoming flow in which the two main parameters of swirl velocity, V_θ, and wall velocity gradient, V', will be varied. The effect of these on the flashback speed $(U_{bulk} - V_f)$ will be measured, where V_f is the lab-frame propagation speed and U_{bulk} the bulk velocity.

Three important velocity scales are identified. The first two of these are: the flashback speed $(U_{bulk} - V_f)$; and the local flame displacement speed, S_f, which, for the experimental design, is assumed to be equal to the laminar flame speed, S_L. The final velocity scale is the buoyancy velocity, $\sqrt{g'\delta}$, where g' is magnitude of the densiometric body force. This velocity scale characterises the effect of swirl and the radial pressure gradient on the pressure-driven flame propagation. These velocity scales are used to define a non-dimensional flashback speed, $(U_{bulk} - V_f)^* = (U_{bulk} - V_f)/S_L$, and a Froude number which represents the relative importance of flame propagation and buoyancy: $Fr = S_L/\sqrt{g'\delta}$, where $g' = g(\rho_u - \rho_b)/\rho_u$. In this case g is the body force resulting from swirl and the generated radial pressure gradient:

$$g = \frac{1}{\rho}\frac{\partial P}{\partial r} = \frac{V_\theta^2}{r} \tag{5.1}$$

The aim is also to investigate the effect of the developing boundary layer and flame position within the developing boundary layer. The relevant changes with flame position are the change in the shape of the velocity profile and wall velocity gradient, which has been shown to be an important parameter in flame flashback (Lewis and von Elbe, 1943). The wall velocity gradient does not change linearly with flame position, x_f. The effect of the developing boundary layer will therefore be characterised using the wall velocity gradient, V', rather than flame position.

As the flame moves upstream through the developing boundary layer the velocity profile becomes flatter in shape, with higher wall velocity gradient. The overall wall velocity gradient is characterised using a Karlovitz number, $K = V'\delta_T/S_L$ (Kurdyumov et al., 2000), where δ_T is the diffusive flame thickness ($\delta_T = \alpha/S_L$, where α is the thermal diffusivity). The wall velocity gradient is increased by increases in bulk velocity and decreases in channel half-height, δ. However, the developing boundary layer gives a higher wall velocity gradient for the same bulk velocity and channel height. Normalising the wall velocity gradient by the flow parameters U_{bulk} and δ gives a non-dimensional velocity gradient $A' = V'\delta/U_{bulk}$. The effect of the developing boundary layer is then captured in the relative velocity gradients of the developing flow and that of the fully developed flow, A'_0: $K_0 = A'/A'_0$. This captures the effect of the developing boundary layer on the parameter of interest, the wall velocity gradient. Defining the non-dimensional bulk velocity, $u^* = U_{bulk}/S_L$, and channel half-height, $\delta^* = (R_1 - R_0)/(2\delta_L)$, where R_1 and R_0 are the outer and inner radii of the annulus and δ_L the thermal flame thickness, means the overall K can be defined from a combination of these

terms:

$$K = \frac{V'\delta_T}{S_L} = A_0' \frac{\delta_T}{\delta_L} \frac{K_0 u^*}{\delta^*} \tag{5.2}$$

The remaining non-dimensional numbers required to characterise the configuration are the Reynolds number, $Re = 2U_{bulk}(R_1 - R_0)/\nu$, the radius ratio, $R^* = R_1/R_0$, and density ratio, $D = \rho_u/\rho_b$. The full set of non-dimensional parameters is given in Table 5.1.

Table 5.1: Non-dimensional numbers characterising the annular configuration.

$$D = \frac{\rho_u}{\rho_b} \tag{5.3}$$

$$R^* = \frac{R_1}{R_0} \tag{5.4}$$

$$\delta^* = \frac{(R_1 - R_0)}{2\delta_L} \tag{5.5}$$

$$u^* = \frac{U_{bulk}}{S_L} \tag{5.6}$$

$$Re = \frac{2U_{bulk}(R_1 - R_0)}{\nu} \tag{5.7}$$

$$K_0 = \frac{A'}{A_0'} = \frac{\left|\frac{\partial(u/U_{bulk})}{\partial(r/\delta)}\right|_w}{\left|\frac{\partial(u/U_{bulk})}{\partial(r/\delta)}\right|_{w,0}} \tag{5.8}$$

where:

$$Fr = \frac{S_L}{\sqrt{\overline{g'}\frac{(R_1 - R_0)}{2}}} \tag{5.9}$$

$$\overline{g'} = \frac{\overline{V_\theta}^2}{R_0}\frac{(\rho_u - \rho_b)}{\rho_u}$$

$$(U_{bulk} - V_f)^* = \frac{(U_{bulk} - V_f)}{S_L} \tag{5.10}$$

Froude Number

The Froude number, Fr, given in Table 5.1, represents the effect of the radial pressure gradient on flashback. For a given channel size and density ratio, Fr can be changed by changing the swirl velocity, V_θ. This definition of Fr can be calculated a priori using the bulk azimuthal velocity and channel size. The use of R_0 in $\frac{V_\theta^2}{r}$ reflects that flashback is more likely to occur on the inner wall of the annulus as a result of the radially outward pressure gradient.

However, it is possible to define swirl and Froude numbers in different ways, some of which may better reflect the physical processes occurring. The buoyancy velocity within Fr is usually defined for gravity currents, with a uniform body force due to gravity. In swirling flows, the body force is not uniform and depends on the swirl velocity and r. Therefore a relevant characteristic body force must be defined.

The swirl number defines the axial fluxes of azimuthal and axial momentum (Ebi and Clemens, 2016):

$$Sw = \frac{\int_{R_0}^{R_1} \rho V_\theta u r^2 dr}{(R_1 - R_0)\int_{R_0}^{R_1} \rho u^2 r dr} \tag{5.11}$$

Fr could also be defined by calculating the average body force across the annulus:

$$\overline{g} = \frac{\int_{R_0}^{R_1} V_\theta^2/r dr}{(R_1 - R_0)} \tag{5.12}$$

$$Fr = \frac{S_L}{\sqrt{\overline{g}\frac{(R_1-R_0)}{2}\left(\frac{\rho_u-\rho_b}{\rho_u}\right)}} = \frac{S_L}{\sqrt{\frac{1}{2}\left(\int_{R_0}^{R_1} V_\theta^2/r dr\right)\left(\frac{\rho_u-\rho_b}{\rho_u}\right)}} \tag{5.13}$$

While this may more accurately represent the body force acting, the flow diversion around the leading point of the flame means this value will change with axial distance. A local representation of this value around the flame front may better describe the trend in flashback speed, but at the disadvantage that this could not be measured in practice or evaluated a priori. In this work, the definition of Fr based on the mean swirl velocity $\bar{V}_\theta$ given in Table 5.1 will be therefore be used.

5.1.2 Simulation Cases

In this section, the simulations to be conducted will be outlined. These simulations will investigate the effect of swirl and the wall velocity gradient.

The first set of experiments will investigate the effect of swirl on laminar flashback. Table 5.2 gives the set of parameters held constant while Fr, u^*, δ^* and K_0 are varied. These parameters were informed by the grid- and domain-independence studies shown in Section 3.2.4.

Table 5.2: Common parameters for laminar simulations in annular sections.

$L_x \times L_y = 20\delta \times 2\delta$	$T_u = T_w = 350K$
$\phi = 0.55$	$D = 4.60$
$R^* = 2$	$\delta_L/\Delta x = 10$
$N_y = 240$	$x_f^* = 4$

To vary K_0, different velocity profiles will be imposed at the inlet to the domain. These profiles were determined using a non-reacting simulation of a developing boundary layer: the domain was initialised using a flat velocity profile and the profile allowed to develop downstream over time. Characterising these using the wall velocity gradient and wall velocity gradient of the fully developed flow gives the velocity profiles shown in Figure 5.2.

For all of the simulations in this chapter the moving frame-of-reference control (described in Section 3.1.7) is used to update the velocity of the moving frame-of-reference to maintain the position of the flame.

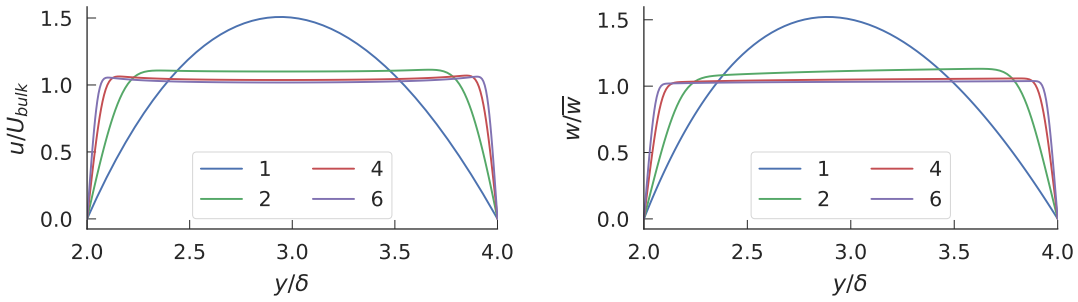

(a) u

(b) w

Figure 5.2: Velocity-profile development of a laminar, annular flow. The lines show the velocity profile for different values of K_0, as indicated in the legend.

5.2 Results

In this section, the results for changing Fr, K_0 (velocity-profile shape), u^* (bulk-velocity) and δ^* (channel height) are reviewed. The results are presented as varying with Fr or K, the non-dimensional wall velocity gradient. When varying with Fr, there are four sets of results: two at $K_0 = 1$ (fully developed flow) and two at $K_0 = 2$, where each set of two has a set at $u^* = 1$ and a set at $u^* = 4$. When varying K, there are two sets: one at high Fr ($Fr = \infty$) and one at low Fr ($Fr = 0.1$), where there is variation in K_0, u^* and δ^* within each set. Some of the simulations appear in both sets of results.

5.2.1 Overall effects of swirl and near-wall velocity gradient

Figure 5.3 shows the simulation results for the effect of Fr on flashback speed. The figure also includes the predictions of models derived in Chapter 4: the additive model (Equation 4.50), the annular model (Equation 4.49) and the planar model: unconfined (Equation 4.21) and at confinement ratios (H') of 4 and 2 (Equation 4.20). The models were solved for a density ratio of 4.6, matching the conditions of the simulations.

Figure 5.3 shows that at high Fr (low swirl) there is little effect of Fr on flashback speed while at low Fr (high swirl) the flashback speed is strongly dependent on Fr. The results at different u^* and K_0 are offset from each other but all retain a similar trend of changing flashback speed with Fr. The trend in flashback speed is the same as that predicted by the model suggesting that there is a transition from flame-propagation to buoyancy-dominated behaviour. However, the flashback speed does not increase as quickly with decreasing Fr as predicted by the model, and the transition curve between flame-propagation and buoyancy dominated regions is offset with the model predicting that this occurs at a higher Fr than is shown by the simulation results. There is also a discrepancy in the magnitude of the flashback-speed predictions at high Fr where the simulated flashback speed is significantly larger than the predictions of the model.

Figure 5.4 shows the flame shape at $Fr = \infty$ and $Fr = 0.1$, marking the region of reversed flow, in the lab frame-of-reference, and three streamlines. Figure 5.4 shows that at high Fr there is a small region of reversed flow ahead of the flame, matching that found by Gruber et al. (2012); Eichler and Sattelmayer (2012), and at low Fr this region is significantly larger. The overall length of the flame is

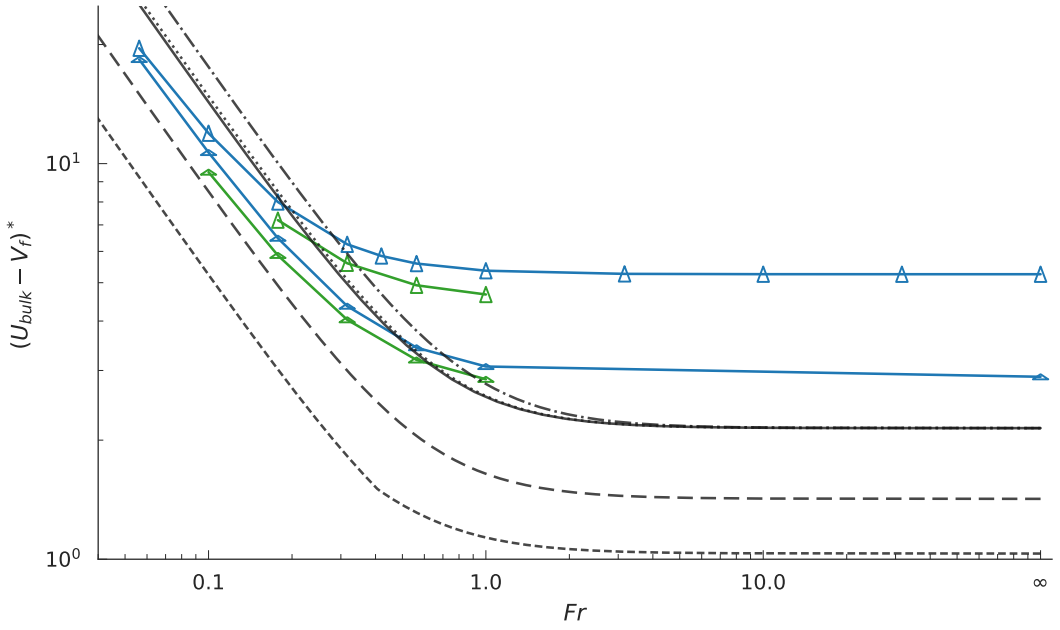

Figure 5.3: Flashback speed as a function of Fr. The triangles show the relative u^* (symbol height) and δ^* (symbol width) for $K_0 = 1$ (blue) and $K_0 = 2$ (green). The model predictions are shown for the additive model (solid black) and the momentum-balance models: unconfined annular (dot-dashed), unconfined planar (dotted) and the confined planar (dashed) at confinement ratios of 4 and 2 (the larger dashes are for the larger confinement ratio).

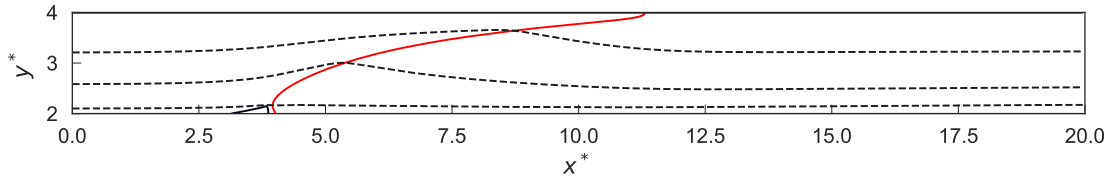

(a) $Fr = \infty$

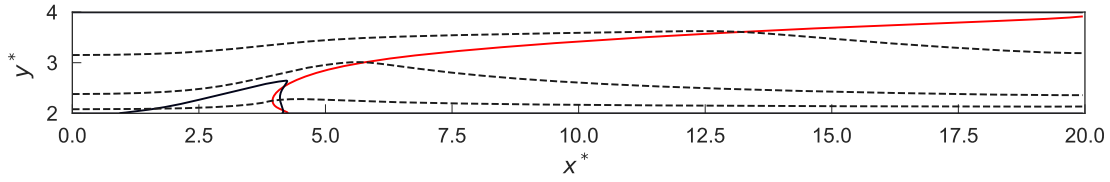

(b) $Fr = 0.1$

Figure 5.4: Plot of flame shape, $c = 0.7$ (red line); streamlines (black dashed) intersecting the flame at h_f, δ and 1.5δ; and region of reversed flow (black solid) in the lab frame-of-reference.

significantly longer at low Fr as well. This long length helps justify the assumption in the momentum-balance models that the flow is parallel when exiting the control volume. Further evidence is provided for this in Chapter 6. The effect on the reversed-flow region will be characterised using the length scales shown in Figure 5.5: the maximum height of the reversed-flow region, h_{rf}, and the streamline height ratio ($\delta_1' = \delta_{1,s}/h_f$). The height ratio represents flow diversion: the smaller the ratio, the greater the expansion in the height of the streamline and the greater the flow diversion around the leading point of the flame. The height ratio could be calculated for any streamline as the ratio of the

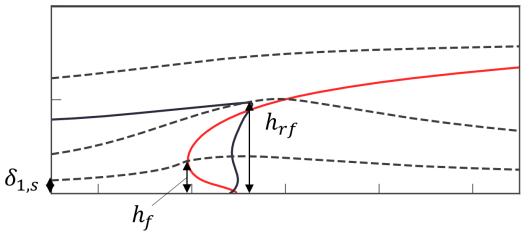

Figure 5.5: Diagram illustrating the calculation of the length scales: maximum height of the reversed-flow region, h_{rf} and streamline height ratio, $\delta_1' = \delta_{1,s}/h_f$.

streamline height at the domain inlet and at the point of intersection with the flame front. The results calculated in this work use the streamline through the leading point of the flame but the trends still apply for height ratios calculated for streamlines at different wall distances.

Figure 5.6 shows the results for flashback speed against K, at high Fr (low swirl, Figure 5.6a) and low Fr (high swirl, Figure 5.6b). At both high and low Fr, as K_0 is increased (red lines in Figure 5.6) and the velocity profile becomes flatter, the flashback speed decreases and seems to decay towards a converged value. For both high and low Fr, increasing u^* (blue lines) increases the flashback speed, with an approximately linear relation between the two. At high Fr each of these series converges on the same point, where $u^* = 0$. At low Fr each series converges on a different point at $u^* = 0$ with the shape of the swirl-velocity distribution having an impact on the flashback speed, even for no bulk velocity. Increasing δ^* increases the flashback speed, although this has a larger effect at high Fr than low Fr. Figure 5.6 also shows that for different K_0 the effect of K is different. At low K_0 the effect of K is larger, and at high K_0 the effect is smaller. Figure 5.7 shows an example of the velocity profile and flame shape for $K_0 = 1$ and 6. The velocity gradient at the position of the flame will change with K_0: as the velocity profile becomes flatter the flame leading point is less likely to be in the boundary layer and more likely to be in the main part of the flow. This means that the effect of changing K will be dependent on K_0. To represent this relationship a ratio of boundary-layer thickness to flame height is introduced, δ_1^*. The flame thickness is taken as representative of the flame height. The flame height is assumed to scale better with this value than with the other possible length scale, the channel half-height. The displacement thickness is then taken as representative of the boundary-layer thickness (the momentum thickness was also investigated but found to give poorer predictions for how the effect of K varies). Using these definitions gives large values of δ_1^* when the flame leading point is more likely to be in the boundary layer, subjected to higher velocity gradients, and small values when it is more likely to be in the bulk flow, and subjected to lower velocity gradients.

The effect of K is also dependent on Fr: comparing Figures 5.6a and 5.6b shows that the slopes of the series in u^* are higher at high Fr than at low Fr.

Overall, this shows that the flashback speed does not depend uniquely on K at a given Fr but is dependent on u^*, K_0 and δ^*. There are a number of contributory factors which could explain this, for example the flame-flow interaction (both the effect of thermal expansion on the flow field and the effect of curvature, stretch and near-wall quenching on the displacement speed of the flame). These effects will be explored in the subsequent sub-sections of this chapter.

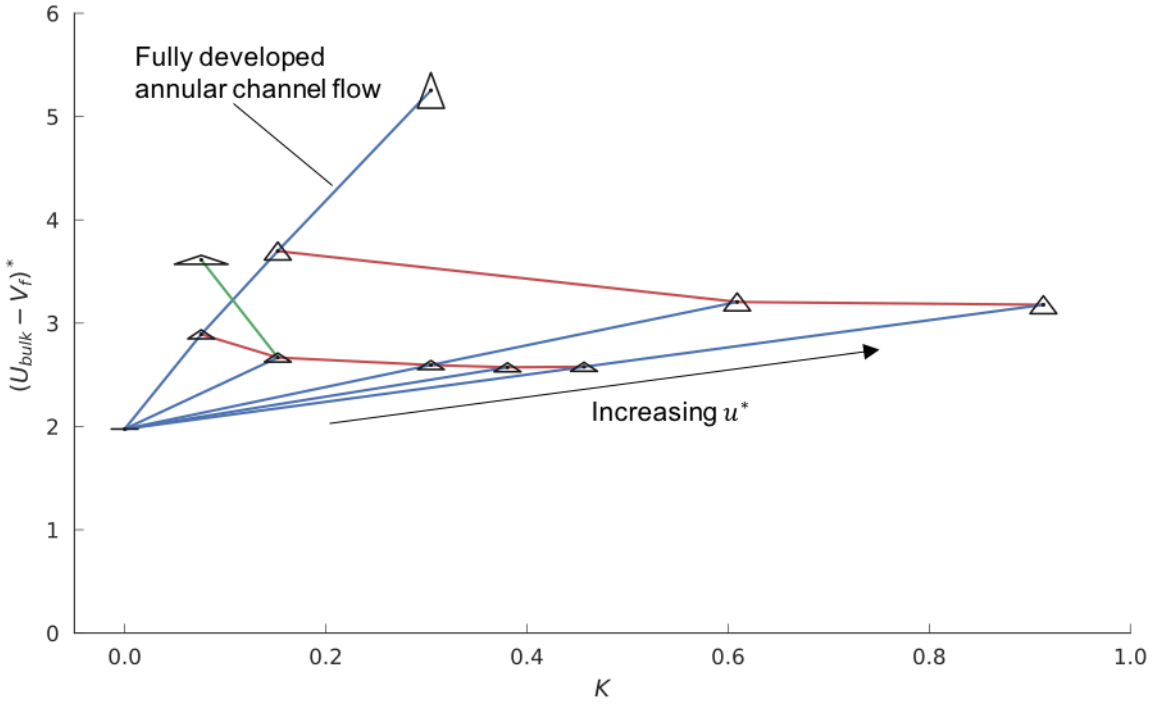

(a) High Fr.

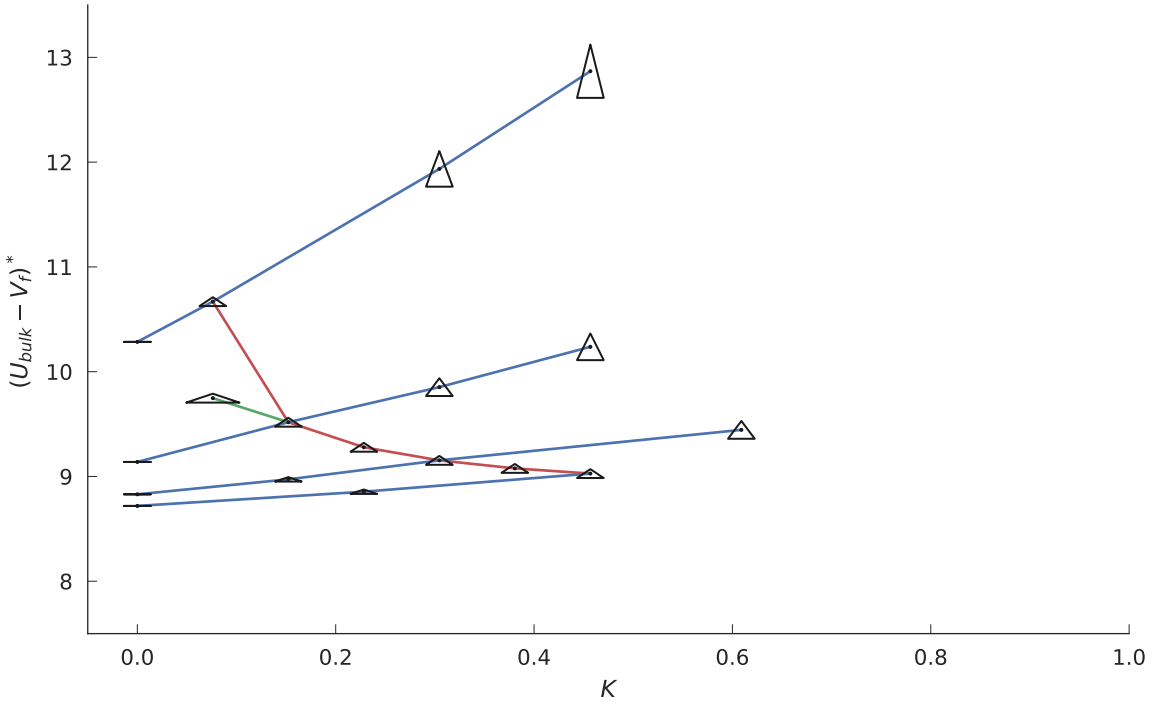

(b) Low Fr.

Figure 5.6: Flashback speed as a function of non-dimensional wall velocity gradient, K. The triangles show the relative u^* (height of symbol) and δ^* (width of symbol) - combined with K from the x-axis gives K_0. Lines connect points of varying: K_0 (red), u^* (blue) and δ^* (green).

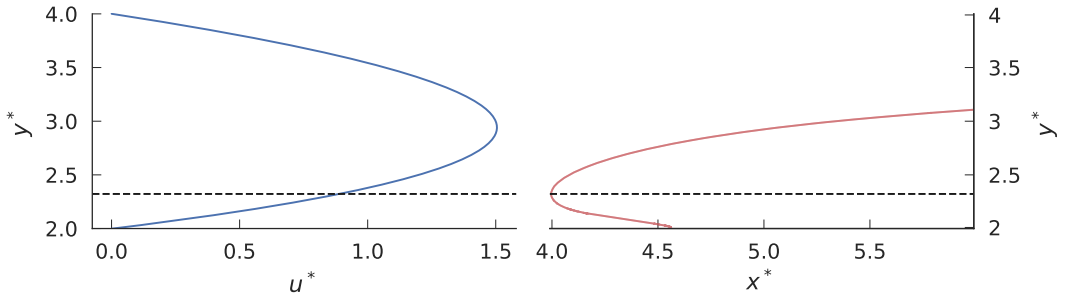

(a) $K_0 = 1$.

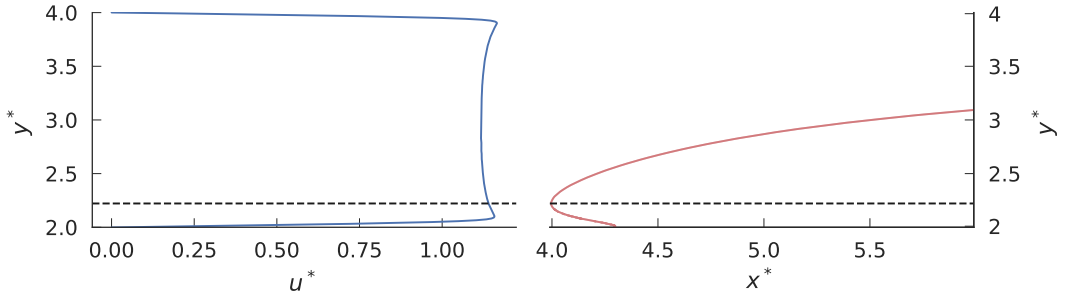

(b) $K_0 = 6$.

Figure 5.7: Comparison of flame shape ($c = 0.7$, red line) and velocity-profile shape (blue line) for different K_0. The dotted black line shows the height of the flame leading point.

5.2.2 Flame-Flow Interaction

This sub-section will focus on the flame-flow interaction, investigating the flame shape, the reversed-flow region and the flame response to curvature and stretch.

Flame Shape

Figures 5.8 and 5.9 show the flame shape for a selection of cases at high and low Fr, respectively. Increases in u^* and K_0 at high and low Fr reduce the size of the reversed-flow region ahead of the flame. At high Fr, increases in u^* also impact the flame shape with the flame leading point being located closer to the bottom wall and the flames becoming flatter, with longer overall extent. The low Fr cases all have similar flame shapes and position of the streamlines. Figure 5.10 shows a direct comparison of the flame shapes at different Fr for two different u^*, demonstrating that at high Fr there is a larger difference in flame shape with u^* than at low Fr. Figures 5.8 and 5.9 also show that the streamlines diverge around the leading point of the flame, and that there is greater divergence at low Fr compared to high Fr. This is particularly shown by the lower streamlines. The figures also shows that the leading point of the flame becomes more curved at low Fr: the upper branch of the flame front becomes slightly flatter as the flame extent increases and the point where the lower branch meets the bottom wall also extends further downstream.

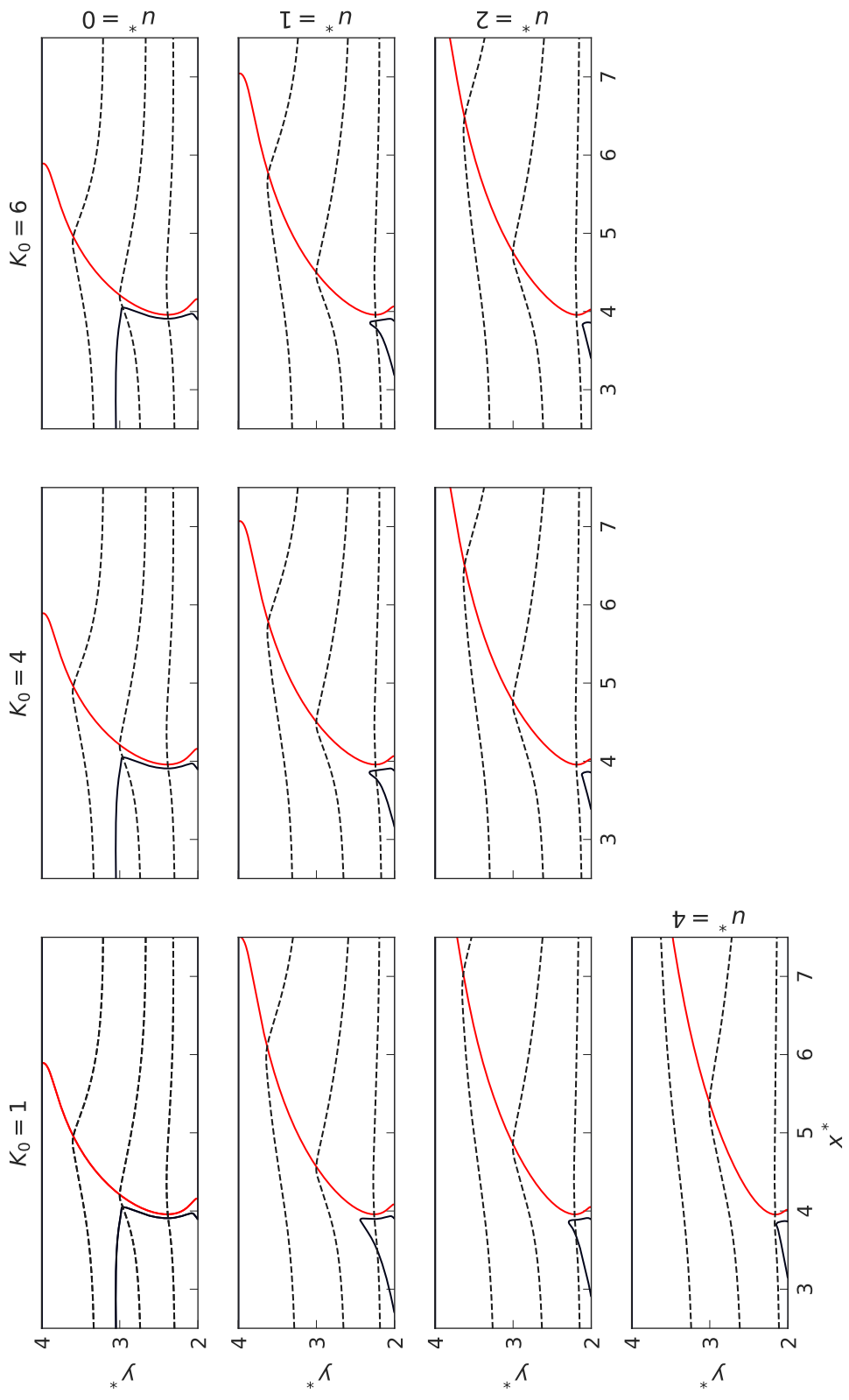

Figure 5.8: Plot of flame shape at high Fr, $c = 0.7$ (red line); streamlines (black dashed) intersecting the flame at h_f, δ and 1.5δ; and region of reversed flow (black solid) in the lab frame-of-reference. The rows show increasing u^* (0, 1, 2, 4) and the columns increasing K_0 (1, 4, 6) for the high Fr cases. N.B. the figures along the top row are the same but are repeated to allow comparison down the columns.

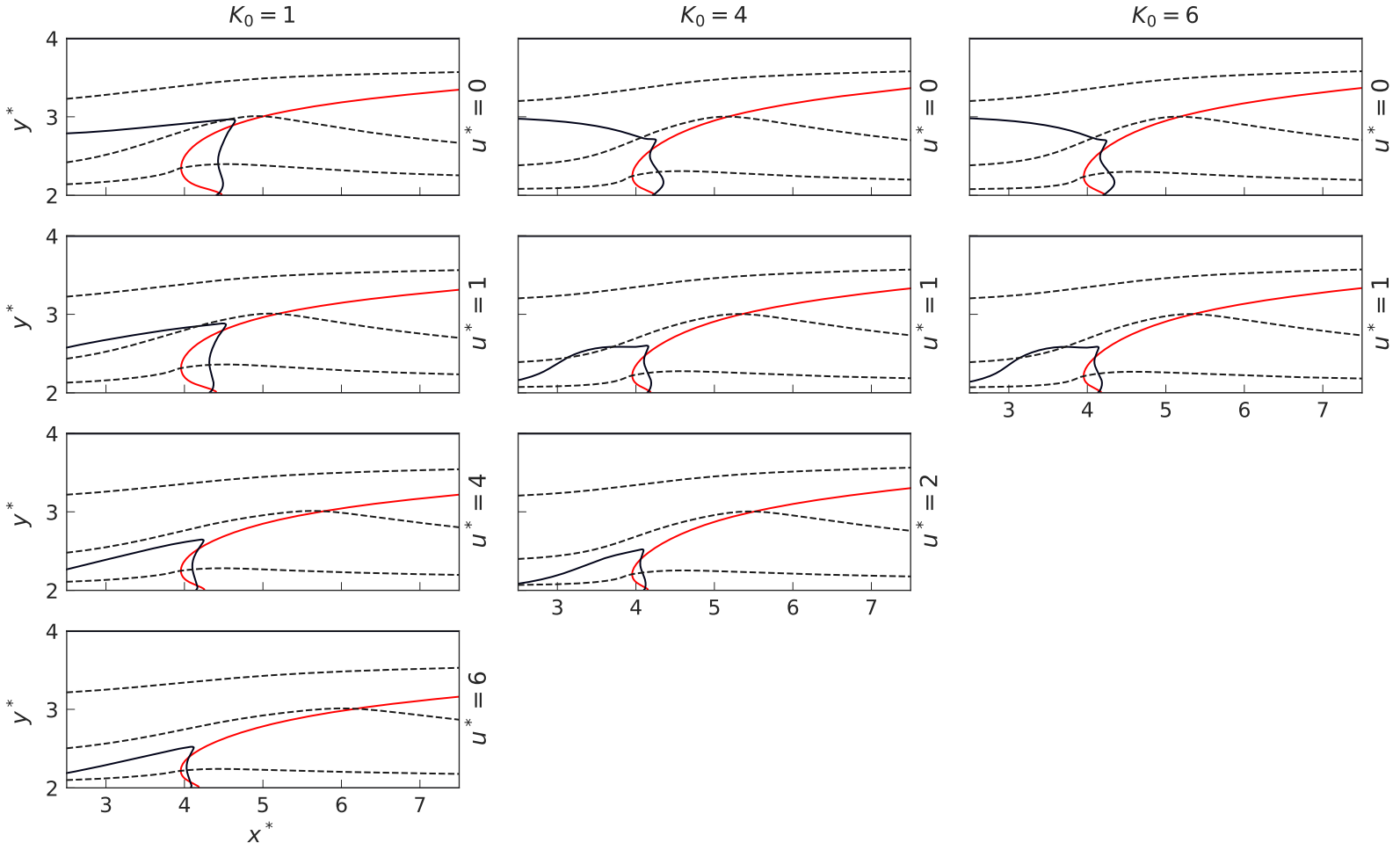

Figure 5.9: Plot of flame shape at low Fr, $c = 0.7$ (red line); streamlines (black dashed) intersecting the flame at h_f, δ and 1.5δ; and region of reversed flow (black solid) in the lab frame-of-reference. The rows show increasing u^* and the columns increasing K_0 (1, 4, 6) for the low Fr cases. The rows show $u^* = (0, 1, 4, 6), (0, 1, 2), (0, 1)$, respectively for each column.

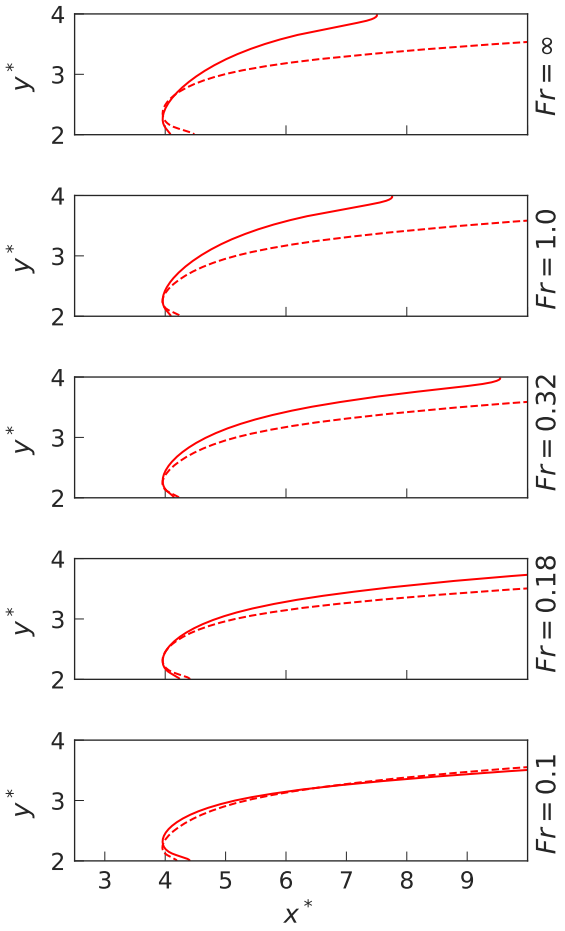

Figure 5.10: Comparison of flame shapes, $c = 0.7$, for different Fr at $u^* = 1$ (solid red) and 4 (dashed red).

Flow Field

The flow field and reversed-flow region will now be investigated quantitatively using the height of the reversed-flow region and the height ratio, representing flow diversion. The effect of the flame on the flow field is very important because greater flow diversion and larger region of reversed-flow is likely to result in higher flashback speeds.

Figure 5.11 shows the effect of K on height ratio, where the trend in height ratio matches that seen in the flame shapes. At low Fr, K_0, u^* and δ^* have little effect on the height ratio and flow diversion around the leading point of the flame. However, at high Fr there are significant changes in height ratio with K_0, u^* and δ^*. Increases in u^* and K_0 decrease height ratio, while an increase in δ^* is shown to cause a significant decrease in height ratio compared to the points at smaller δ^* and at the same K.

Figure 5.12 shows the ratio of the height of the lower streamline at the inlet to the point of intersection with the flame. A smaller height ratio represents a greater flow diversion around the leading point of the flame. Figure 5.12 shows that again at high Fr the height ratio is consistent but as Fr increases the height ratio decreases and there is greater flow diversion.

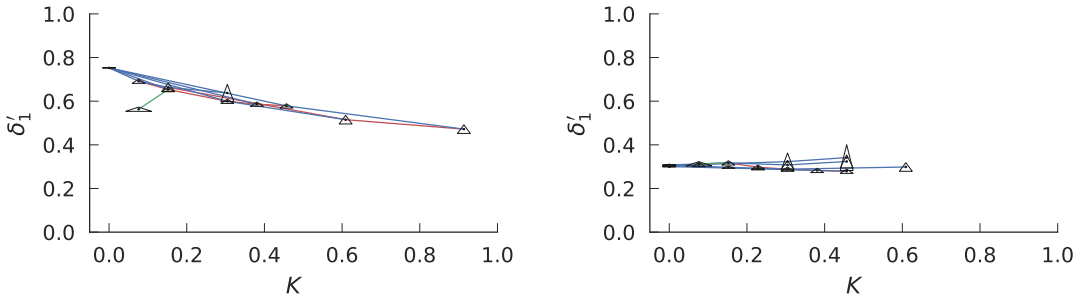

(a) High Fr.

(b) Low Fr.

Figure 5.11: Height ratio ($\delta_1' = \delta_{1,s}/h_f$) against non-dimensional wall velocity gradient, K. The triangles show the relative u^* (height of symbol) and δ^* (width of symbol) - combined with K from the x-axis gives K_0. Lines connect points of varying: K_0 (red), u^* (blue) and δ^* (green).

Figure 5.12 also shows the model results allowing a qualitative comparison to the simulation results. The values for the height ratio depend on the streamline chosen, but the trend of height ratio with Fr is consistent. The planar models are shown to reflect the trend of height ratio with Fr, where height ratio is uniform with Fr at high Fr before decreasing with decreasing Fr at sufficiently low Fr. The models all predict that at sufficiently low Fr, the height ratio is uniform with Fr. The simulation results appear to be tailing off at low Fr but are still decreasing with decreasing Fr for the range of Fr investigated. As with the flashback-speed predictions, there is an offset with Fr for the curve of height ratio, but the trend is correctly predicted. This could mean that the magnitude of Fr defined for the simulations does not correctly capture the quantitative relationship between buoyancy and flame propagation but that is does correctly predict the trend with changing Fr. The annular model predicts the opposite trend to the simulation results and planar models, where height ratio increases with decreasing Fr. The effect of Fr on height ratio would be expected to be different in the annular configuration compared to the planar. In the annular configuration the volume of a sector of the annulus, of a given height and angular width, will increase with radius. This means flow diversion around the leading point of the flame is likely to have a smaller effect in an annular configuration.

Figure 5.13 shows the height of the region of reverse flow, h_{rf} (as representative of the overall extent of the region) with changing Fr. At high Fr there is little change in the height but as the flashback speed increases with decreasing Fr, h_{rf} increases as well.

Overall these results for flow diversion and the region of reversed flow show that as swirl increases (Fr decreases) there is greater flow diversion and larger region of reversed flow, leading to larger flashback speeds. This may help explain why the hydrostatic modelling used in Chapter 4 is able to reproduce the trend in flashback speed with swirl, particularly when swirl effects dominate.

Flame Response

The effect of the flow field on the flame can also be investigated, using measurements of the curvature and tangential strain to evaluate stretch at the flame leading point. This can then be linked to the displacement speed of the flame leading point, where a larger stretch rate would be expected to lead to a higher displacement speed.

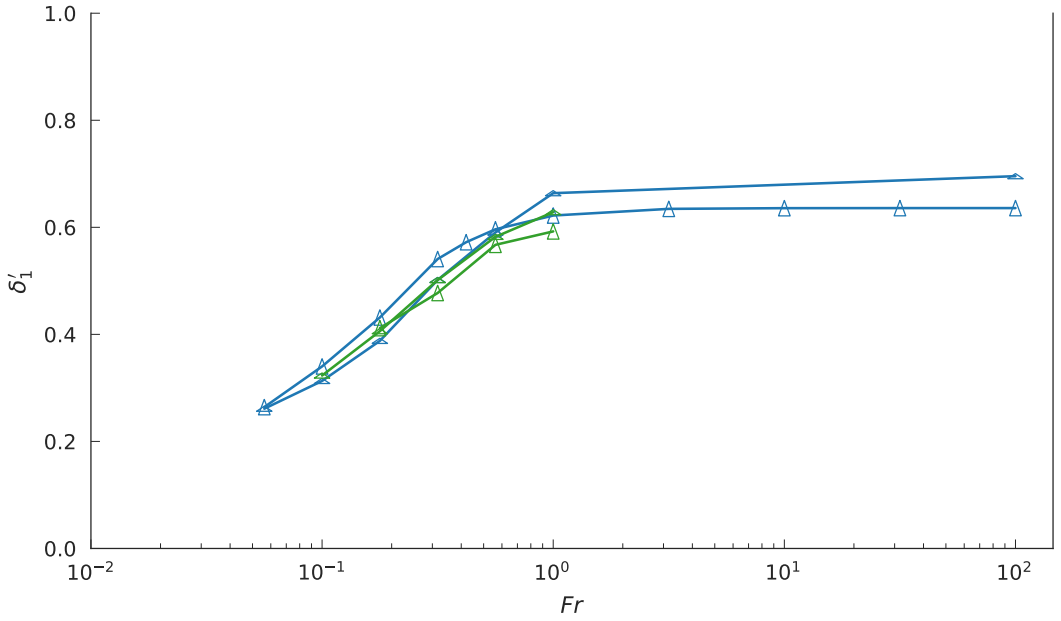

(a) Simulation.

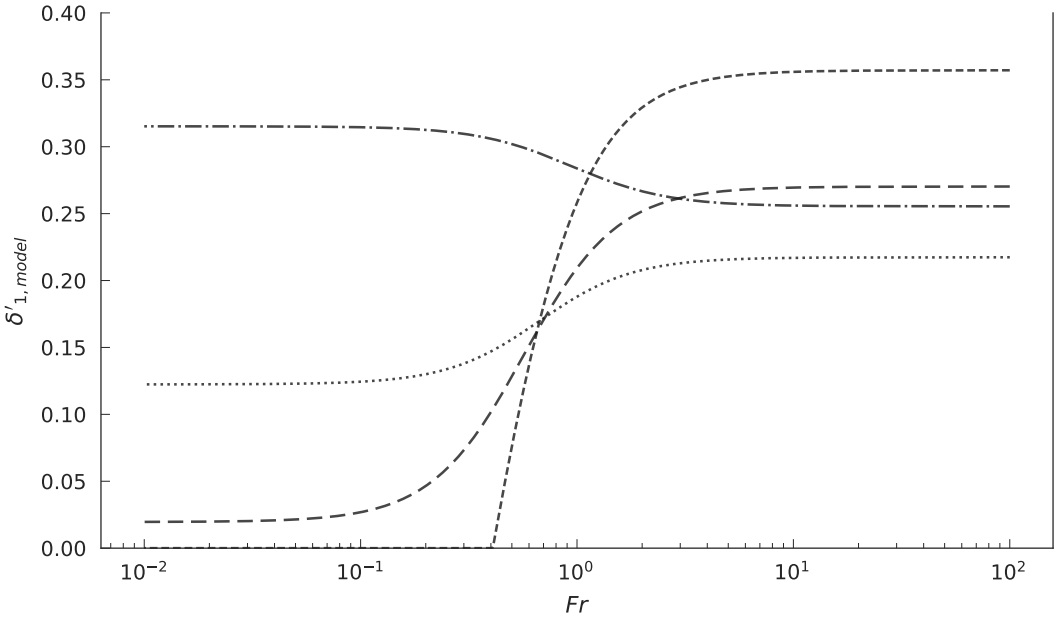

(b) Models.

Figure 5.12: Height ratio as a function of Fr for the streamline passing through the leading point of the flame. The simulation results (a) show triangles show the relative u^* (symbol height) and δ^* (symbol width) for $K_0 = 1$ (blue) and $K_0 = 2$ (green); and the model results (b) show the momentum-balance models: unconfined annular (dot-dashed), unconfined planar (dotted) and the confined planar (dashed) at confinement ratios of 4 and 2 (the larger dashes are for the larger confinement ratio).

Figure 5.14a shows that as Fr decreases (swirl increases) and the flame is flatter against the inner wall, the curvature of the flame leading point increases. Figure 5.14c shows that this results in

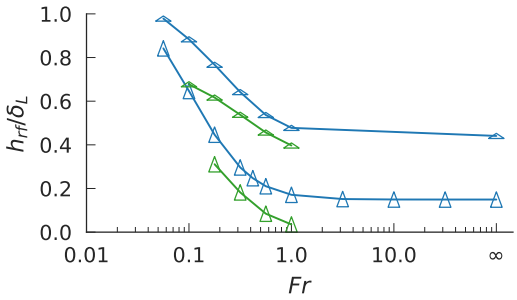

Figure 5.13: Plot of the maximum height of the reversed-flow region. The triangles show the relative u^* (symbol height) and δ^* (symbol width) for $K_0 = 1$ (blue) and $K_0 = 2$ (green).

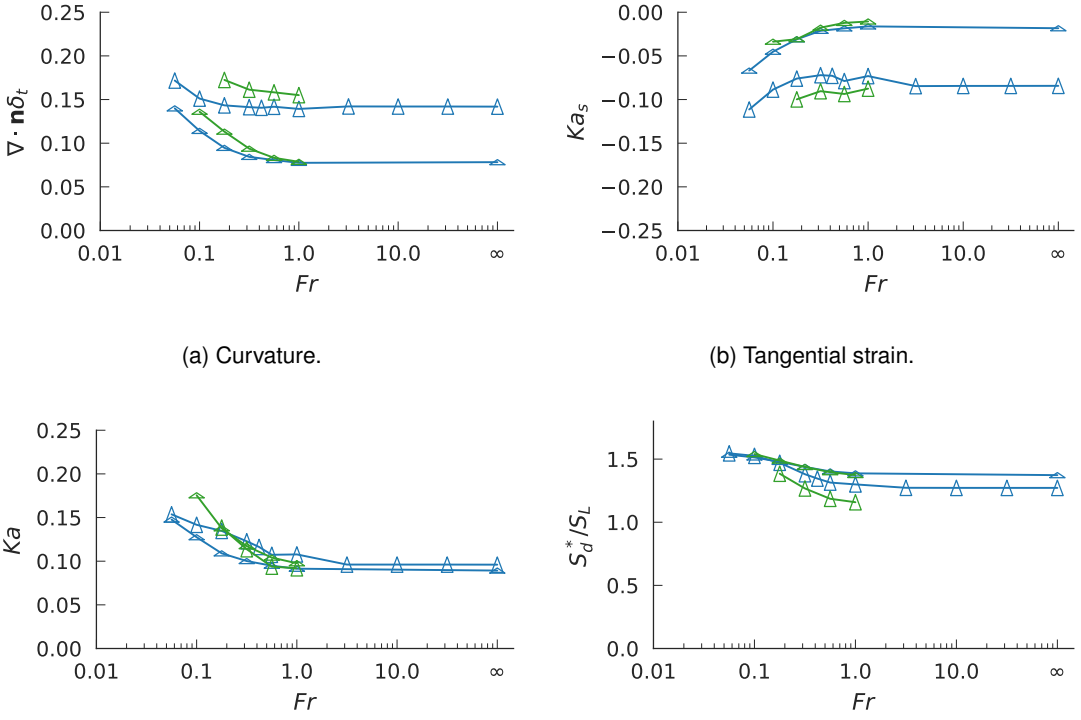

(a) Curvature.

(b) Tangential strain.

(c) Stretch.

(d) Displacement speed.

Figure 5.14: Stretch effects on flame leading point as a function of Fr for $K_0 = 1$, $u^* = 1$ (green) and $u^* = 4$ (blue), and $K_0 = 2$, $u^* = 1$ (purple) and $u^* = 4$ (red).

an increase in stretch ($Ka = Ka_s + S_d^* \nabla \cdot \mathbf{n}\delta_t$) on the leading point of the flame with decreasing Fr, despite the tangential strain (Figure 5.14b) becoming more negative with decreasing Fr. Figure 5.14d also shows that, as Fr decreases, the displacement speed of the flame leading point increases. This aligns with the expectation, for this configuration, that displacement speed will increase for convex curved flame fronts.

Figure 5.15 shows the displacement speed of the flame leading point relative to the laminar flame speed. Figure 5.15a shows that, at high Fr, K_0, u^* and δ^* have very little effect on the displacement speed. However, Figure 5.15b shows that, at low Fr, K_0, u^* and δ^* do affect the displacement speed more significantly. Increases in u^* and K_0 both give increased displacement speed, while an increase in δ^* is shown to give reduced displacement speed. Increases in u^* and K_0, and decreases in δ^*,

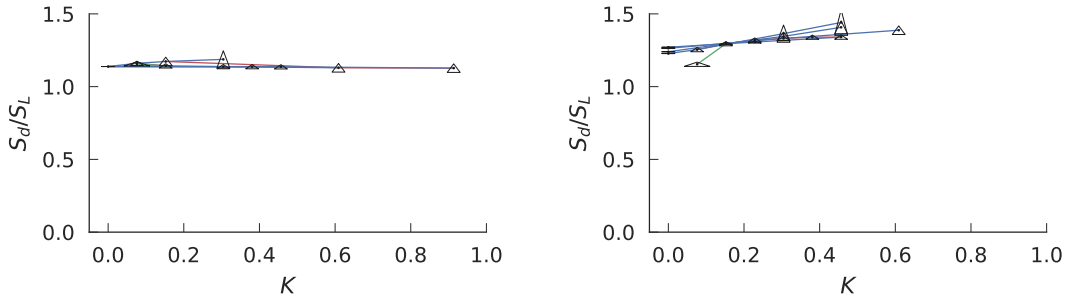

(a) High Fr. (b) Low Fr.

Figure 5.15: Displacement speed of flame leading points as a function of the non-dimensional wall velocity gradient, K. The triangles show the relative u^* (height of symbol) and δ^* (width of symbol) - combined with K from the x-axis gives K_0. Lines connect points of varying: K_0 (red), u^* (blue) and δ^* (green).

will increase the wall velocity gradient and therefore the stretch rate to which the flame is subjected. For these conditions, an increase in stretch rate is likely to increase the local displacement speed of the flame.

Overall, this has shown that at high Fr increasing K (through K_0 or u^*) results in changes in flame shape and flow diversion but with little change in displacement speed. At low Fr the opposite is seen: with increasing K there is little change in flame shape and flow diversion but with changes in displacement speed. This suggests that at low Fr buoyancy is controlling of the flame position relative to the wall. As u^* is increased the stretch on the leading point of the flame increases and flashback speed increases accordingly. At high Fr the buoyancy has little effect and does not control the flame position. This means that the effect of increasing u^* is to move the flame closer to the wall, increasing the diversion of the flow around the flame and the flashback speed, but having little impact on the displacement speed of the flame leading point.

5.2.3 Empirical Modelling

In the remainder of this chapter, an empirical model will be developed for the effect of u^* on flashback speed at different levels of boundary-layer development. This will extend the additive model of Chapter 4, which accounts for the effect of density ratio and swirl only, but does not account for the effect of the magnitude or shape of the boundary layer. The extended additive model will then account for the effect of the magnitude and shape of the boundary layer, density ratio and swirl.

Effect of K and K_0

The model will be based on simple linear regression for the effect of K on flashback speed:

$$\left(U_{bulk} - V_f\right)^* = m\left(Fr, K_0\right) K + c\left(Fr, K_0\right) \tag{5.14}$$

Table 5.3: Results of linear regression for the effect of K on flashback speed. Each row represents a linear regression model for the points connected by blue lines in Figure 5.6. m and c are the slope and intercept of the linear model, p the statistical significance and R^2 the coefficient of determination.

(a) High Fr.

K_0	δ_1^*	m	c	p	R^2
1.0	4.14	10.79	2.03	0.00	1.00
4.0	0.47	2.02	1.98	0.00	1.00
6.0	0.26	-0.74	3.78	0.23	0.87

(b) Low Fr.

K_0	δ_1^*	m	c	p	R^2
1.0	4.14	5.65	10.26	0.00	1.0
2.0	1.13	2.39	9.14	0.00	1.0
4.0	0.47	1.02	8.83	0.00	1.0
6.0	0.26	0.68	8.71	0.04	1.0

where m and c are the slope and intercept of the linear model. Using the data at high and low Fr to justify this form of model, Table 5.3 demonstrates the strong correlation between K and flashback speed, at a given channel height, fitting a linear relationship at a 5% significance level.

Figure 5.16 shows the previous plots of flashback speed against K, at low and high Fr, with the relative boundary-layer thickness, δ_1^* also included. Using the relative boundary-layer thickness and the simple linear regression applied for the effect of K on flashback speed (Table 5.3), the effect of the relative boundary-layer thickness on the slope of the simple linear regression can be investigated. Figure 5.17 shows that δ_1^* and m are linearly related at a 5% significance level. However, there is currently insufficient data to model how this effect changes with Fr. K_0 will have two different effects through its effects on the axial and swirl velocity, V_θ. The effect on the axial velocity is seen with no swirl (high Fr), where changing the shape of the velocity profile changes the wall velocity gradient but also changes the boundary-layer thickness relative to the flame thickness, δ_1^*. This means that the velocity gradient at the flame leading point becomes smaller as δ_1^* decreases, reducing the effect of the velocity gradient on the flame. For high swirl (low Fr), the effect of the swirl velocity is also seen. The results at low Fr show that the flashback speed at $u^* = 0$ is dependent on K_0. K_0 changes the swirl velocity profile which will change the hydrostatic pressure profile, in turn affecting the flashback speed. More data is needed to evaluate these two effects and evaluate how the effects vary with Fr. Modelling these laminar cases with such small channels also means that there is a large variation in the boundary-layer thickness relative to the flame thickness. For larger channels, this variation would be much smaller, which may mean that modelling the effect of the boundary layer would be simpler. The empirical modelling will continue, fitting separate models for the two different values of K_0.

The data at varying Fr will now be used to fit the empirical model. Two datasets have been created for different K_0 at a range of Fr, with each dataset containing a set of two different u^*. Figure 5.18 shows the fit of the data to the model, and how the intercept and slope vary with Fr. The intercept follows a very similar trend to the additive model of flashback speed (solid black line in Figure 5.18a). The intercept here represents the flashback speed with no bulk flow, which is shown to match the

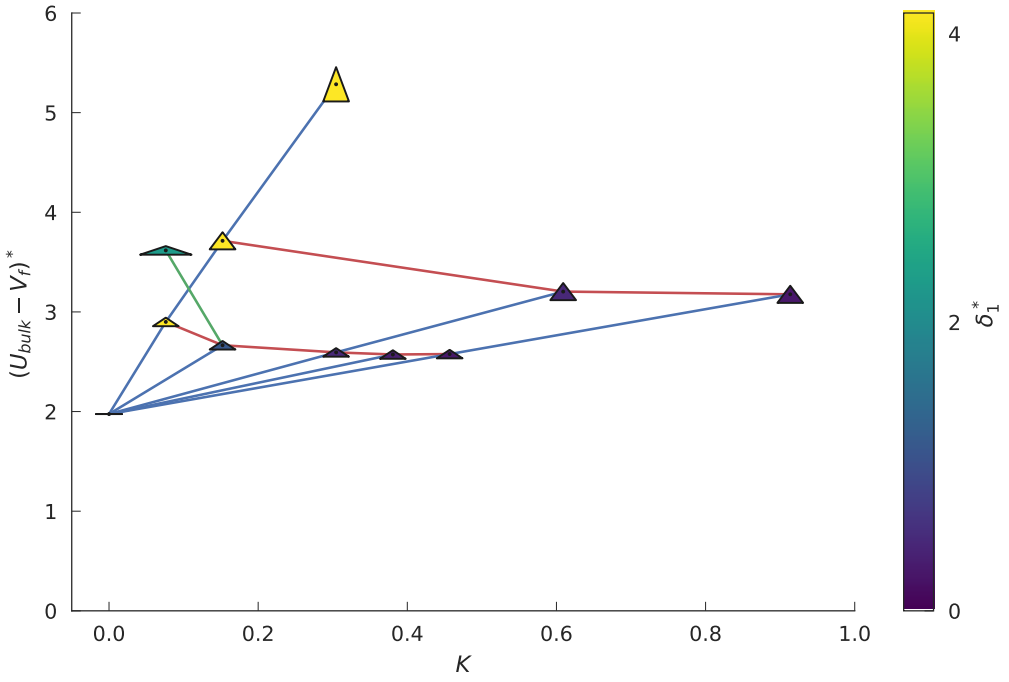

(a) High Fr.

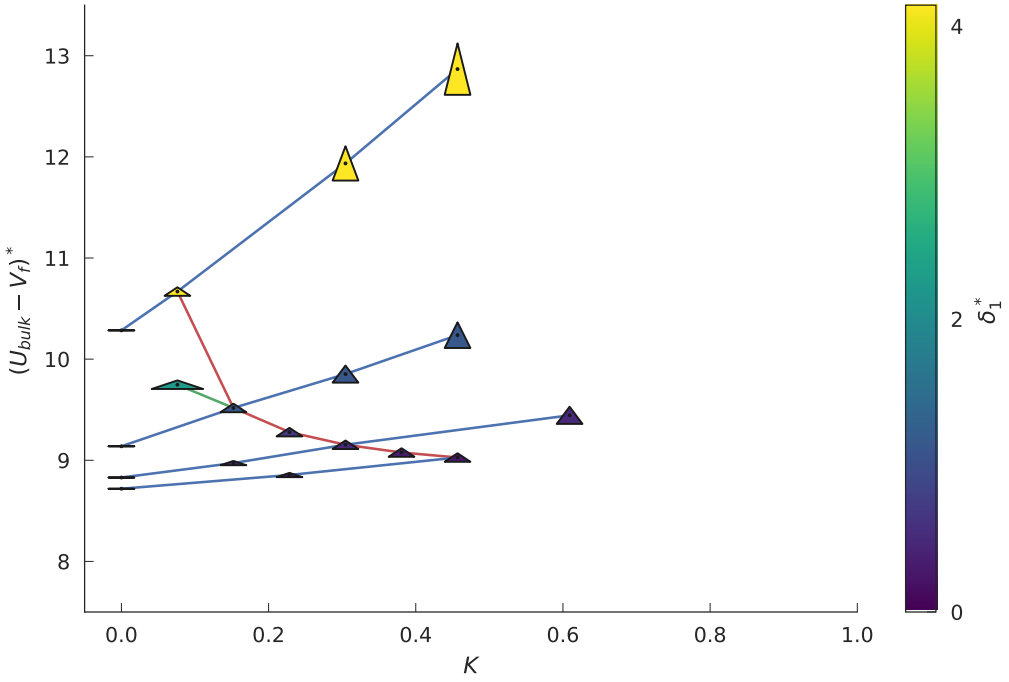

(b) Low Fr.

Figure 5.16: Flashback speed as a function of non-dimensional wall velocity gradient, K, and relative boundary-layer thickness, δ_1^*. The triangles show the relative u^* (height of symbol) and δ^* (width of symbol) - combined with K from the x-axis gives K_0. Lines connect points of varying: K_0 (red), u^* (blue) and δ^* (green). The fill colour of the triangles shows the boundary-layer thickness relative to the flame thickness, δ_1^*.

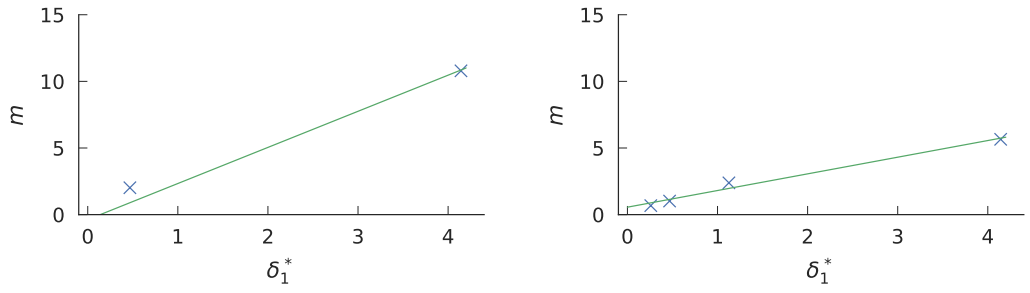

(a) High Fr. (b) Low Fr.

Figure 5.17: Slope of linear regression (m), for the effect of K on flashback speed, as a function of relative boundary-layer thickness. This models the relationship between m and δ_1^* from Table 5.3.

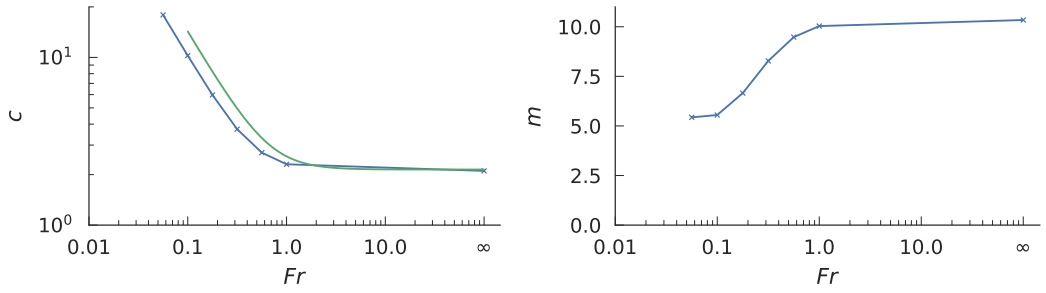

(a) Intercept, c. (b) Slope, m.

Figure 5.18: Effect of Fr on linear-regression fit ($y = mx + c$) to effect of K on flashback speed, for: $K_0 = 1$ (blue) and $K_0 = 2$ (green). For the intercept, the additive model (solid black) is also shown.

additive model very closely at high Fr and match the trend of the additive model with Fr at lower Fr, although with an offset in the predictions.

The slope of the linear regression transitions from being high at high Fr, starting to decrease from $Fr = 1$ and then continuing to decrease with decreasing Fr, appearing to level off from $Fr \simeq 0.1$. This matches what would be expected in the limits of low and high Fr. At low and high Fr flashback speed will be dominated by buoyancy or flame-propagation, respectively. At sufficiently low and high Fr the other physical effects would therefore be negligible. This would mean that the effect of K on flashback speed should become constant with Fr at sufficiently high and low Fr, as shown in Figure 5.18b.

Given the similarity in the trend of the intercept with Fr and the close match between the prediction at high Fr, the change in intercept with Fr is modelled using:

$$c = \sqrt{D + \frac{c_2(K_0)}{Fr^2}} \tag{5.15}$$

This gives a convergence to the result of Ruetsch et al. (1995) at high Fr while retaining the trend in Fr at low Fr. The constant c_2 can then be fitted for $K_0 = 0$ and 1. Figure 5.19a and Table 5.4 show that the fitted values of $c_2 = 1.00$ and 0.78 for $K_0 = 0$ and 1, respectively, reproduce the intercept values well.

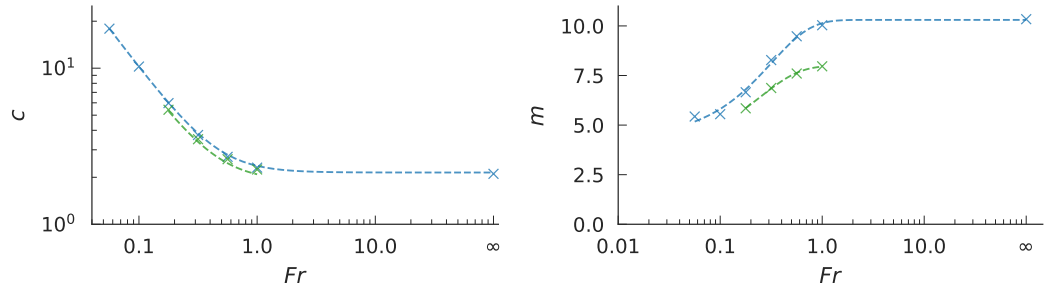

(a) Intercept, c.

(b) Slope, m.

Figure 5.19: Predicted intercepts and slope for linear-regression fit ($y = mx + c$) to effect of K on flashback speed, for: K_0= 1 (blue) and K_0= 2 (green). Shown are the simulation results (markers) and the predictions given by Equations 5.15 and 5.16 (dashed lines).

Table 5.4: Fitted parameters and performance for the models describing the effect of K and Fr on flashback speed (Equations 5.15 and 5.16).

(a) Intercept, c.

K_0	c_2	p	R^2
1	1.00	0.00	1.0
2	0.78	0.00	1.0

(b) Slope, m.

K_0	c_3	m_3	m_4	p	R^2
1	-0.22	10.30	1.97	0.00	0.99
2	-0.20	-7.99	-2.49	0.03	1.00

The slope is modelled using:

$$m = m_3(K_0)\tanh\left[m_4(K_0)(Fr - c_3(K_0))\right] \tag{5.16}$$

This gives constant values at the limits of $Fr = \infty$ and $Fr = 0$. Figure 5.19b and Table 5.4 show that using this approach reproduces the expected m values well, at least over the range of Fr investigated.

Taking Equation 5.14 and substituting in Equations 5.15 and 5.16 gives the overall model:

$$(U_{bulk} - V_f)^*_{pred} = c + Km = \sqrt{D + \frac{c_2(K_0)}{Fr^2}} + Km_3(K_0)\tanh\left[m_4(K_0)(Fr - c_3(K_0))\right] \tag{5.17}$$

Figure 5.20 shows the results from combining these models and predicting the flashback speed as a function of Fr. It shows that the combined analytical and empirical model give excellent predictions accounting for the effect of Fr and K on flashback speed at different K_0.

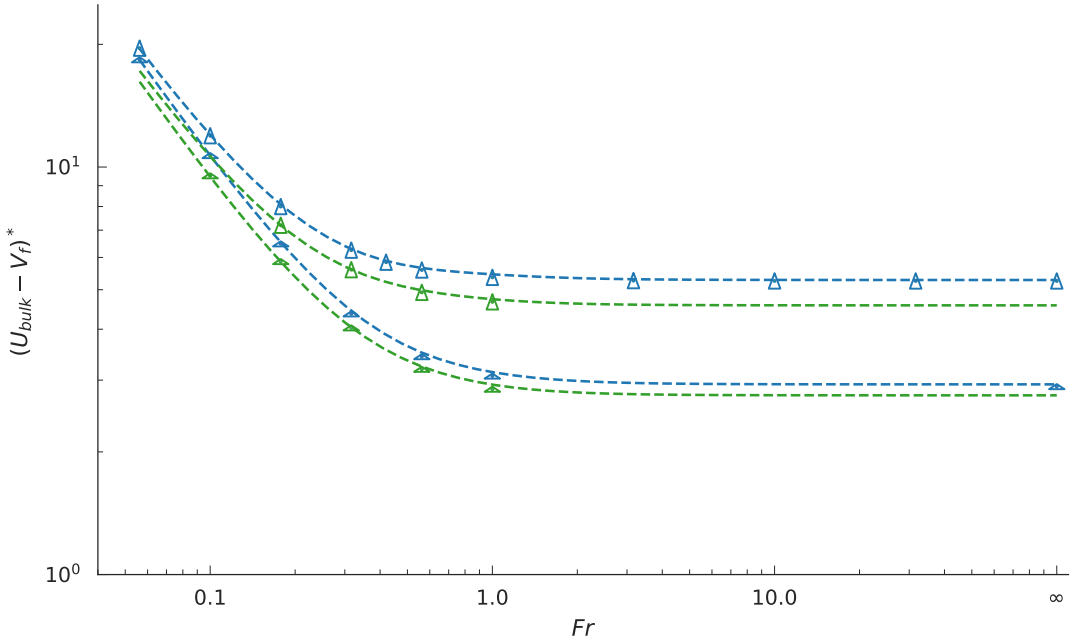

Figure 5.20: Predicted flashback speeds as a function of Fr at different u^* and K_0. The triangles show the simulation results and the dashed lines the results of the empirical model for: $K_0 = 1$, $u^* = 1$ (green) and $u^* = 4$ (blue), and $K_0 = 2$, $u^* = 1$ (purple) and $u^* = 4$ (red).

5.2.4 Effect of Confinement

These simulation results can also be used to test the outputs from the momentum-balance model for the effect of confinement. In the momentum-balance model the effect of confinement is taken into account by solving the mass and momentum balance in the control volume for the upper half of the channel. This gives a pressure drop along the top wall of the channel, ΔP, which is used in calculating the pressures at the outlet from the two control volumes in the model. Figure 5.21 shows the non-dimensional pressure drop along the top wall of the annulus at $x^* = 20$ for each set of laminar simulation results. Figure 5.22a shows the non-dimensional pressure drop predicted by the confined model as a function of Fr. The pressure drop predicted by the model is shown to be an underestimate compared to the pressure drop from the simulations.

The simulations conducted here have limited data for different channel heights, with more data needed to evaluate the effects of confinement fully. The simulations conducted here with double channel height both show larger flashback speed for the larger channel. However, the difference is much larger at high Fr. The effect of channel height may be different where the different physical effects are important. This is suggested by Figures 5.11 and 5.15 where at high Fr the double channel height shows much larger flow diversion, which is not seen at low Fr. Whereas at low Fr the double channel height shows smaller displacement speed, which is not seen at high Fr.

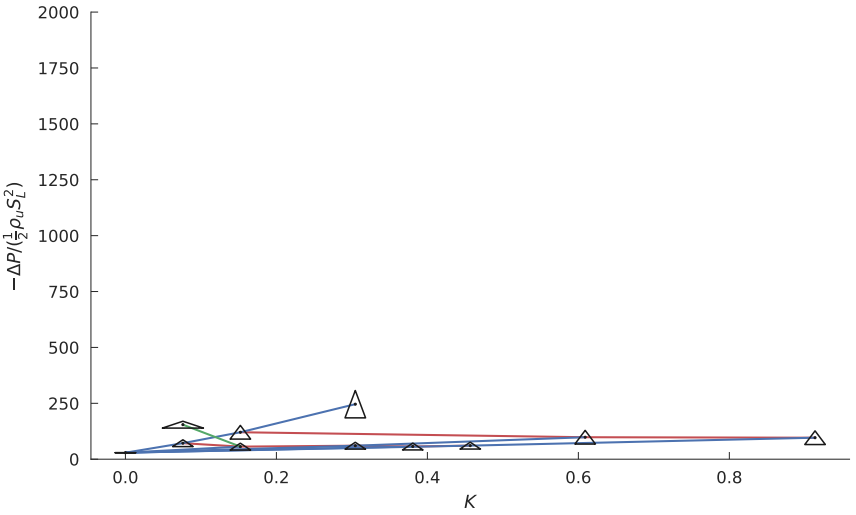

(a) Effect of K, high Fr.

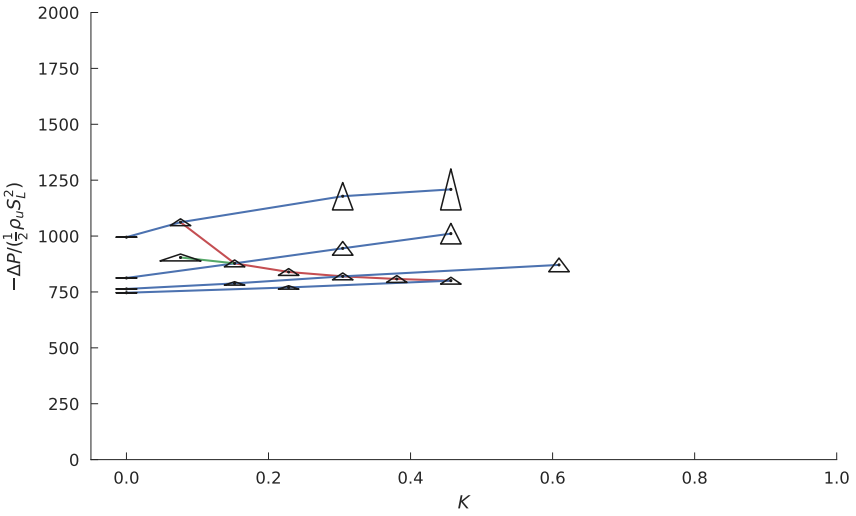

(b) Effect of K, low Fr.

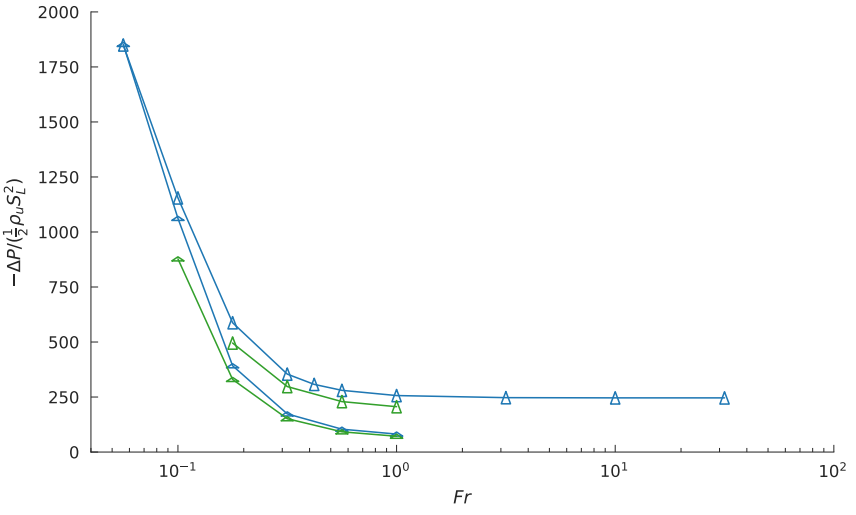

(c) Effect of Fr.

Figure 5.21: Pressure drop along the top wall of the annulus for each of the cases in this chapter.

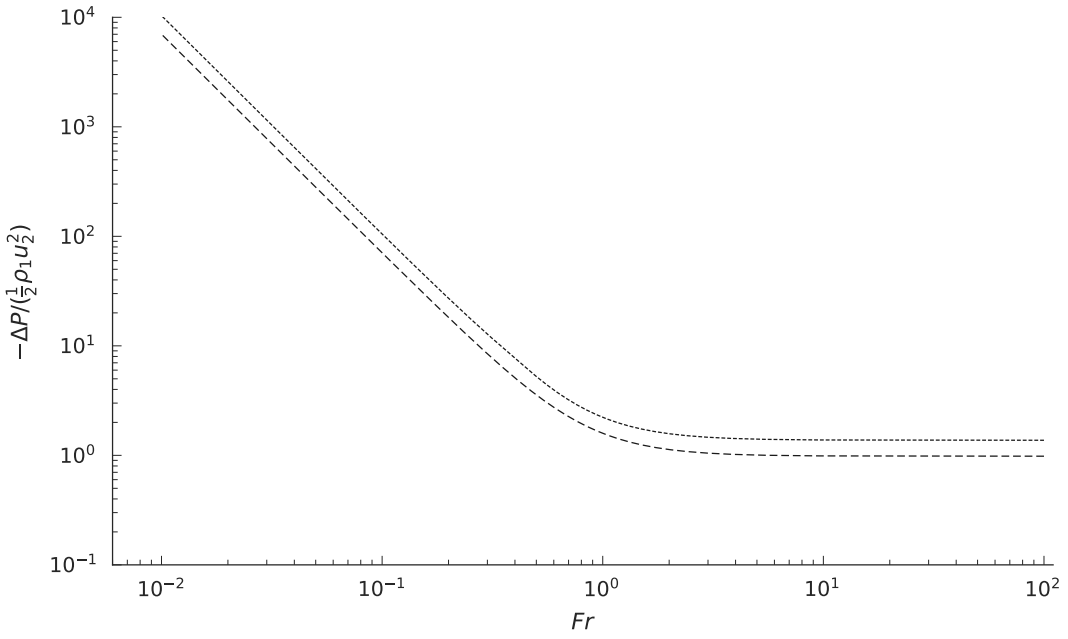

(a) Pressure drop.

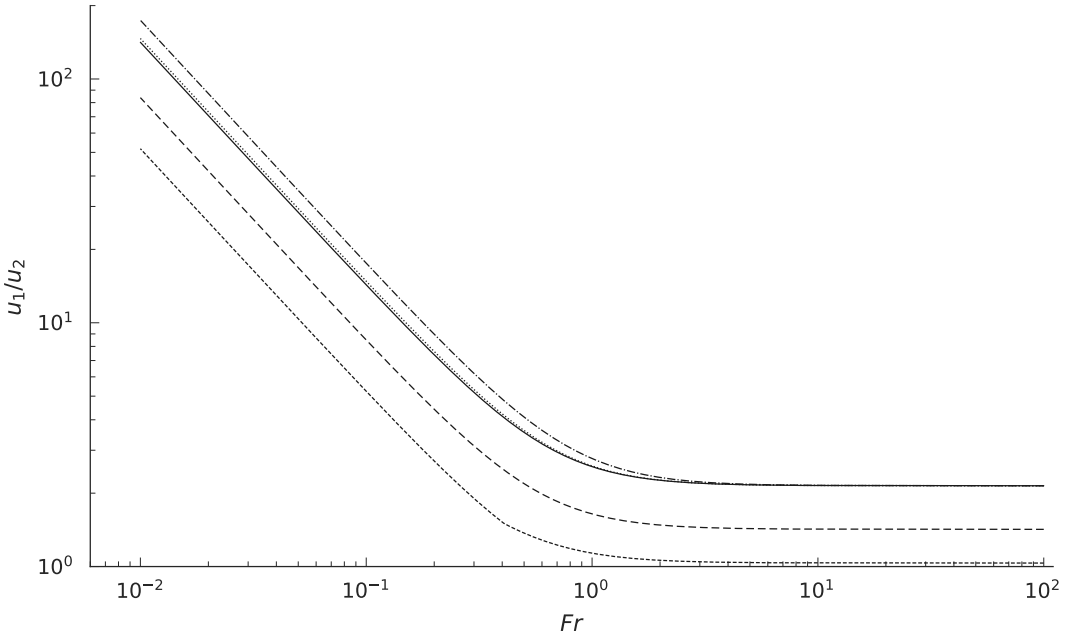

(b) Flashback speed.

Figure 5.22: Model predictions of flashback speed and pressure drop. The model predictions are shown for the additive model (Equation 4.50)(solid black) and the momentum-balance models: unconfined annular (dot-dashed), unconfined planar (dotted) and the confined planar (dashed) at confinement ratios of 4 and 2 (the larger dashes are for the larger confinement ratio).

5.3 Summary and conclusions

The effect of Froude number and wall velocity gradient on boundary-layer flashback have been investigated and compared to the models of flashback from the previous chapter. The models in Chapter 4 do not account for the effect of wall velocity gradient, however it is found that the flashback speed depends on the boundary-layer velocity profile. The developing boundary-layer velocity profile is characterised in terms of the wall velocity gradient and the effect of changing the profile compared to changing the bulk velocity and channel height, which also change the wall velocity gradient.

The effect of swirl, characterised by Fr, on flashback speed was shown to be predicted well by the simple additive model. At high Fr with no bulk velocity, the flashback speed is around $\sqrt{D}$. At low Fr the flashback speed is shown to follow the relation $1/Fr$. Boundary-layer flashback therefore transitions from being dominated by flame propagation to being dominated by buoyancy effects as swirl increases and Fr decreases. In swirling flows the radial pressure gradient causes an increased adverse pressure gradient which increases flow reversal and therefore flashback speed.

The flashback speed is shown to linearly increase with the wall velocity gradient where the gradient of this relation decreases with increasing K_0. As K_0 increases, the boundary layer is less developed and the velocity profile becomes flatter. However, the boundary layer is also thinner and this means that the flame leading point is more likely to be outside of the boundary layer, where the velocity gradient is smaller and therefore has a smaller effect on flashback speed. This is characterised using a relative boundary-layer thickness: the displacement thickness relative to the laminar flame thickness. As the relative boundary-layer thickness increases then the flame is more likely to be in the boundary layer, where the velocity gradient is similar to the wall velocity gradient. As the relative boundary-layer thickness decreases the flame is more likely to be in the bulk part of the flow, where the velocity gradient is significantly smaller than the wall velocity gradient.

Increasing u^* or K_0 is shown: at high Fr, to increase flow diversion and therefore flashback speed but have little effect on the local displacement speed; at low Fr, to increase the local displacement speed and flashback speed but have little effect on flow diversion.

An empirical model was developed which accounts for the effect of u^* at different K_0, supplementing the additive model of Chapter 4 to give a model which describes the effect of u^*, density ratio and swirl at different K_0. This empirical model is shown to reproduce the results of the simulations very well.

Part III

Turbulent Flows

Chapter 6

Flashback in Turbulent Planar Channel Flow

6.1 Introduction

Flashback within a swirling flow is illustrated in Figure 6.1. Compared to boundary-layer flashback in a planar channel there are two additional physical aspects. The first of these is the wall-normal pressure gradient resulting from the centripetal acceleration in the swirling flow. The second is the misalignment of flow and flashback directions. The objective of this chapter is to investigate how the wall-normal pressure gradient and the misalignment of flow and flashback directions contribute to the different flashback behaviour of swirling and non-swirling flows.

Three DNS cases (Table 6.1) have been conducted to study the effect of the wall-normal pressure gradient and the misalignment of flow and flashback directions. Case P1 involves a flame that propagates directly against the oncoming flow direction, similar to the configuration studied by Gruber et al. (2012). In Case P2 the flow direction is rotated so that it is at an angle of 45° relative to the leading flame edge. Case P3 differs from Case P1 due to the introduction of a wall-normal pressure gradient. Comparison between the three cases therefore allows the effects of the flame-flow orientation and wall-normal pressure gradient to be isolated and analysed independently. The factors

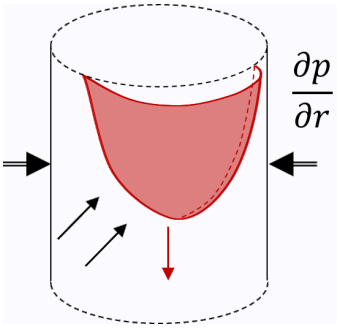

Figure 6.1: Schematic of flame flashback against the centre body of a mixing within a swirling flow. The black arrows indicate the direction of the oncoming flow, the red arrow the mean direction of flame propagation and the double-lined arrows indicate the radial pressure gradient.

Table 6.1: Simulation parameters for the reacting cases

Case	Flow orientation	g	Fr
Planar 1 (P1)	Normal ($0°$)	0	∞
Planar 2 (P2)	Oblique ($45°$)	0	∞
Planar 3 (P3)	Normal ($0°$)	$3 \times 10^6 m/s^2$	0.07

Table 6.2: Configuration parameters for the reacting cases

Case	δ/δ_L	$L_x \times L_y \times L_z$	Re_τ	Da_w
P1	11.1	$5\delta \times 2\delta \times 3\delta$	180	0.14
P2	11.1	$5\delta \times 2\delta \times 3\delta$	180	0.14
P3	11.1	$7.5\delta \times 2\delta \times 3\delta$	180	0.14

affecting global flame propagation will be explored, looking at turbulent flame propagation: increase in flame surface area due to turbulent wrinkling and intensification of burning rate through the effect of stretch, as well as the overall hydrodynamics. The friction-velocity Reynolds number, Re_τ and channel-flow Damköhler number, Da_w are maintained for each (Table 6.2). The domain for Case P3 is extended - the higher flashback speed of this case means a longer domain is required to allow for the flame to develop to a similar extent.

6.2 Results - Direct Numerical Simulations

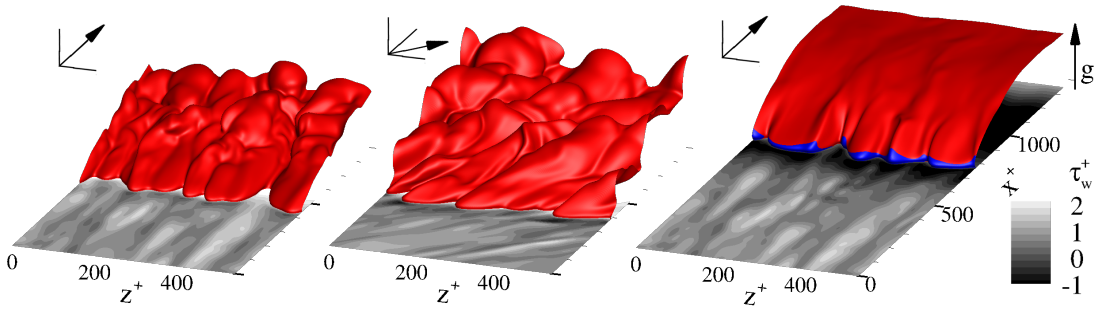

(a) Case P1. (b) Case P2. (c) Case P3.

Figure 6.2: Flame shape ($c = 0.7$ isosurface) after around 40 wall time units for Cases P1-P3 (left to right), coloured red for positive x-direction velocity and blue for back-flow regions. The shading of the bottom wall shows non-dimensional wall shear stress, τ_w^+. Arrows show the mean flow direction and orientation of the body force g.

Figures 6.2 and 6.3 show the shape of the flame surface for each case, and the presence of high- and low-velocity streaks in the boundary layer. The flame front is defined by a progress variable isosurface $c = 0.7$, defined in terms of the hydrogen mass fraction. The bottom wall shows the wall shear stress in wall units, τ_w^+.

The flames propagate along the boundary layer with the high-velocity streaks cutting the flame into lobes that are aligned with the mean flow direction of the respective cases. Oblique flow (Case P2) produces asymmetrical flame lobes, with the side leading flame propagation longer than the side which is trailing. The definitions of these leading and trailing sides is shown in Figure 6.4, where the angle of the flame normal relative to that opposing the oncoming flow, θ_f, is used to define the leading, $\theta_f < 0$ and trailing, $\theta_f >= 0$, sides.

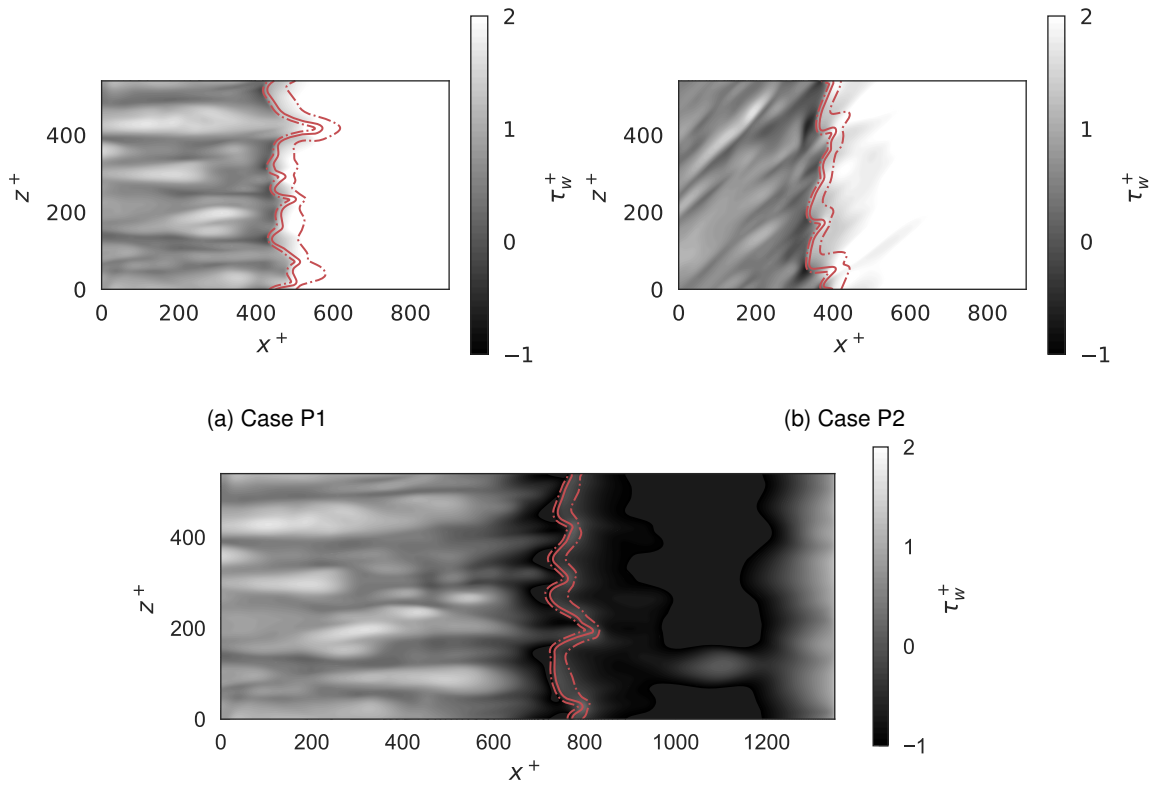

Figure 6.3: Flame shape at $y^+ = 5$ after around 40 wall time units for Cases P1-P3. The solid red line is at $c = 0.7$ while the dot-dashed red lines are at $c = 0.1$ and $c = 0.9$. The shading shows the non-dimensional wall shear stress, τ_w^+ on the bottom wall.

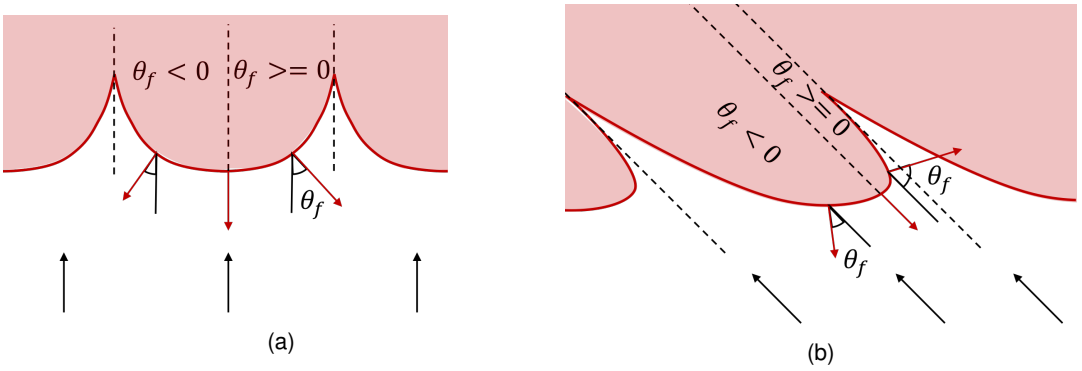

Figure 6.4: Schematic showing the definition of the flame angle relative to that opposing the mean oncoming flow, θ_f, and the leading ($\theta_f < 0$) and trailing ($\theta_f >= 0$) sides of the flame front. The black arrows show the mean stream-wise flow direction, red lines show the flame front with red arrows indicating the flame normal, black dashed lines denote the boundaries of each leading and trailing side.

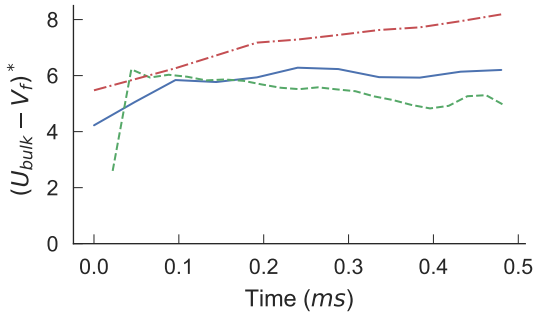

Figure 6.5: Temporal evolution of relative flashback speed, $(U_{bulk} - V_f)^* = (U_{bulk} - V_f)/S_L$. Case P1 - solid blue; Case P2 - green dashed; Case P3 - red dot-dashed.

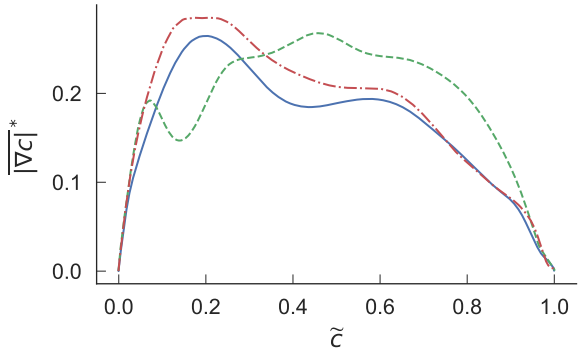

Figure 6.6: Time- and z-averaged flame surface density versus Favre-averaged progress variable at $y^+ = 5$. Case P1 - solid blue; Case P2 - green dashed; Case P3 - red dot-dashed.

In Case P3 the flame surface wrinkling is attenuated away from the wall due to stable density stratification, which is produced by the layer of low-density combustion products against the wall and the positive wall-normal pressure gradient. Case P3 also shows a long flame extent which is close to parallel with the wall. This, along with the long flame extents seen in Chapter 5 for high-swirl flames, helps justify the assumption in the momentum-balance model that the flame is parallel to the wall at the exit of the control volume.

Figure 6.5 shows the temporal evolution of the flashback speed (lab-frame propagation speed, V_f, relative to the bulk velocity, U_{bulk}, normalised by S_L: $(U_{bulk} - V_f)^* = (U_{bulk} - V_f)/S_L$). After 0.2ms the flame evolution is weakly time-dependent and the flashback speeds are in the region of 6.2, 4.9, 8.5 S_L for Cases P1-P3 respectively, indicating that misalignment of flow and propagation directions reduces flashback speed, while the body force increases flashback speed. In the oblique-flow case, the lab-frame propagation speed increases but relative to the lower axial bulk velocity the relative flashback speed is lower. The proceeding analysis aims to understand the important aspects governing these changes in flashback speed.

6.2.1 Turbulent flame propagation

Figure 6.6 shows the flame surface density $\overline{|\nabla c|}$, as a function of the Favre-averaged progress variable on a plane at $y^+ = 5$. The flame surface density is normalised by the laminar flame progress-variable gradient at $c = 0.7$ to give a normalised flame surface density, $\overline{|\nabla c|}^*$. The $y^+ = 5$

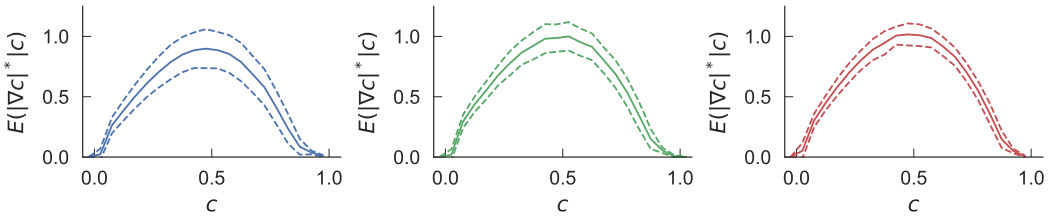

(a) Case P1 (b) Case P2 (c) Case P3

Figure 6.7: Average surface density function conditioned on progress variable on a plane at $y^+ = 5$. The solid line shows the conditional mean while the dashed lines show the mean plus and minus one conditional standard deviation.

plane was chosen as being representative of the flames' leading points, which are between $y^+ = 2$ and 6 for Cases P1 and P2 and between $y^+ = 5$ and 13 for Case 3. The flame surface density shows slight increases for both the oblique flow and the body force. Figure 6.7 shows the conditional average of surface density function (Kollmann and Chen, 1998) on the $y^+ = 5$ plane. There is little difference between the three cases in terms of these conditional means. Increased flame surface density or surface density function typically increases turbulent flame speed, however there is little difference between these cases, alongside large standard deviations. The higher turbulent flame speed for Case P3 is therefore not explained by the trend in flame surface density or surface density function.

Figure 6.8 presents the probability density function (pdf) of curvature, tangential strain and displacement speed of the $c = 0.7$ isosurface at $y^+ = 5$. Similar trends are observed in Figure 6.9 for the global pdf (over all y^+). The mean curvature and tangential strain rate are both positive for all cases, which is expected to increase the displacement speed for fuel-lean hydrogen flames. Misalignment of the flame propagation with respect to the mean flow direction (Case P2) produces a small reduction in average flame curvature and halves the average tangential strain rate. Conditioning the pdfs on the leading and trailing sides of the flame lobes (Figure 6.10) shows that the trailing side of the flame lobe experiences substantially higher tangential strain and has lower displacement speed than the leading side for the oblique case. The distribution of curvature is similar for the leading and trailing sides. The surface area of the trailing sides is smaller, therefore the overall pdf shape is dominated by the contribution of the leading sides. For the other cases Figure 6.10 shows that the flame lobes are symmetrical and the differences between the leading and trailing sides are minimal. The pdfs show that the correlation of displacement speed with tangential strain for the $c = 0.7$ isosurface is opposite to the usual trend for fuel-lean hydrogen flames, however we note that this observation is dependent on the proximity to the wall, and hence wall heat transfer and mean curvature at the leading edge of the flame, and also sensitive to the choice of progress variable and value used to define the flame. However the net effect on the average of displacement speed over the whole flame surface is rather small, increasing from 0.95 S_L in Case P1 to 0.96 S_L in Case P2. The stabilising effect of the wall-normal pressure gradient (Case P3) narrows the distributions of curvature, strain and displacement speed at $y^+ = 5$, contributing to reduction of the overall surface-averaged displacement speed of 0.87 S_L.

Figure 6.11 shows the turbulent consumption speed calculated from the time- and z-averaged reaction-rate fields as a function of the wall-normal distance. All cases show a peak in turbulent consumption speed at between $y^+ = 2$ and 10, at the highly-curved leading edge of the flame. The peak turbulent consumption speed is highest for Case P1, although the average consumption speed is higher in

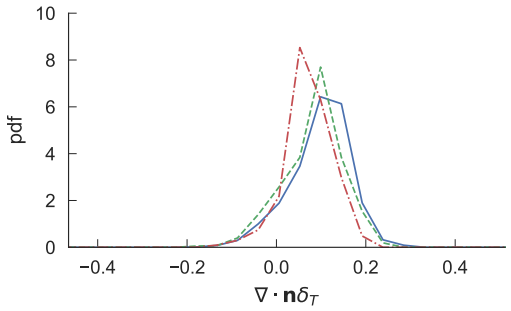

(a) Curvature.

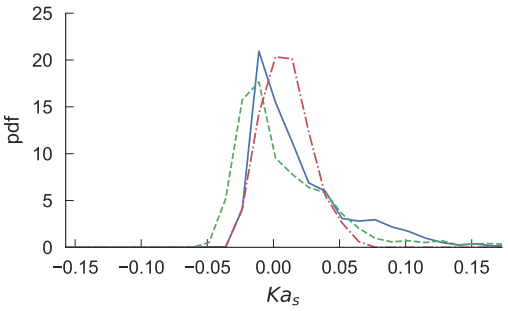

(b) Tangential strain.

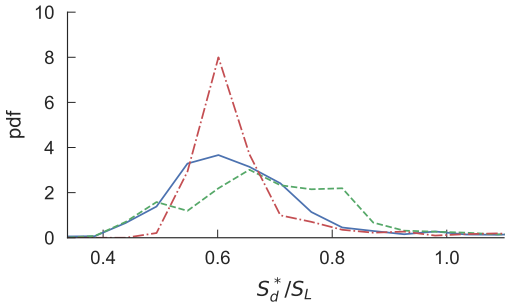

(c) Displacement speed.

Figure 6.8: Probability density function (pdf) of normalised curvature ($\nabla \cdot \mathbf{n}\delta_T$), tangential strain ($Ka_s = a_T\delta_T/S_L$) and density-weighted displacement speed, S_d^*/S_L, at the flame front (c=0.7) on a plane $y^+ = 5$. Case P1 - solid blue; Case P2 - green dashed; Case P3 - red dot-dashed.

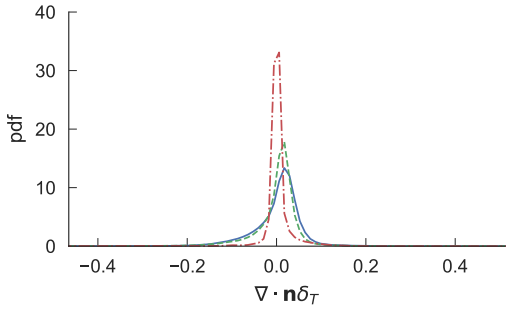

(a) Curvature.

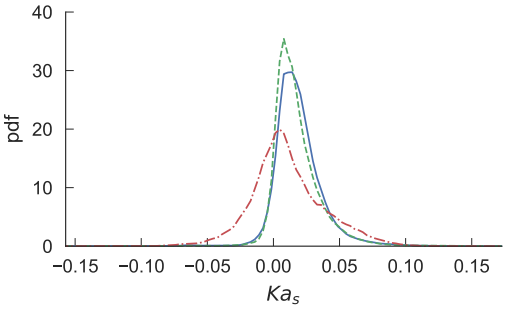

(b) Tangential strain.

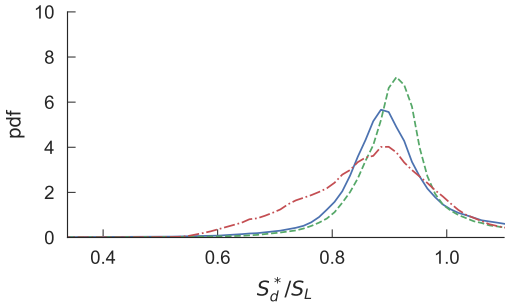

(c) Displacement speed.

Figure 6.9: Probability density function (pdf) of normalised curvature ($\nabla \cdot \mathbf{n}\delta_T$), tangential strain ($Ka_s = a_T\delta_T/S_L$) and density-weighted displacement speed, S_d^*/S_L, at the flame front (c=0.7) across all y^+. Case P1 - solid blue; Case P2 - green dashed; Case P3 - red dot-dashed.

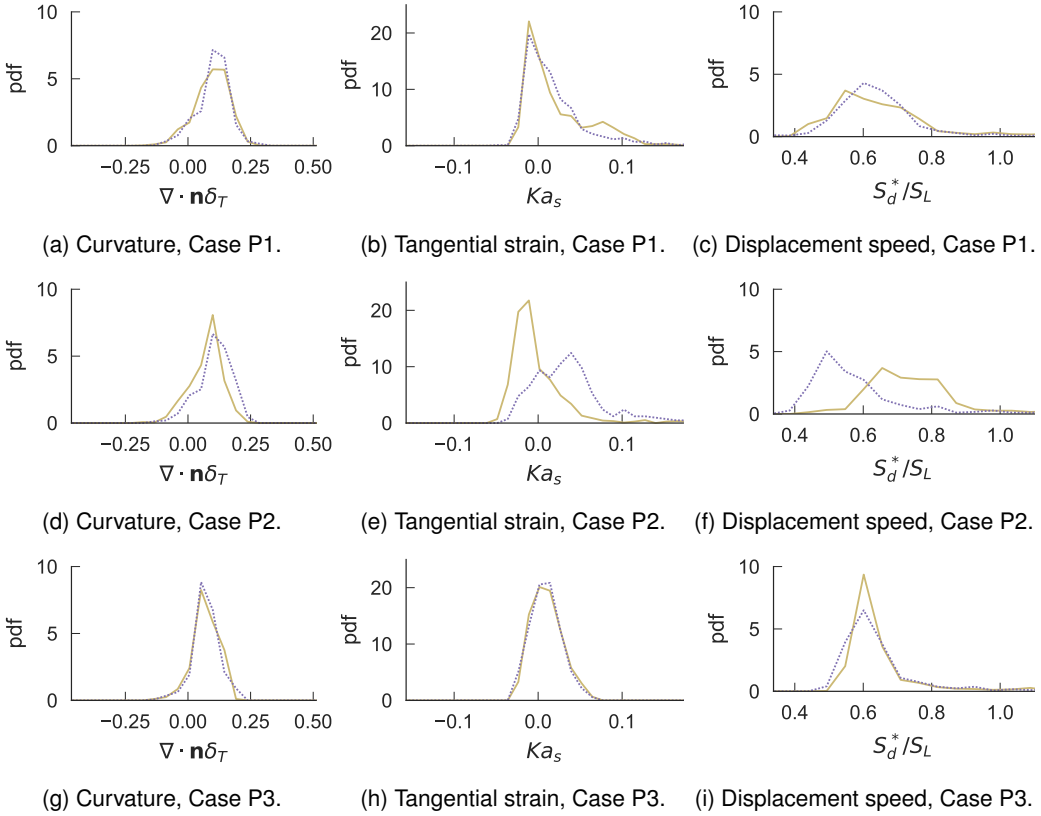

(a) Curvature, Case P1. (b) Tangential strain, Case P1. (c) Displacement speed, Case P1.

(d) Curvature, Case P2. (e) Tangential strain, Case P2. (f) Displacement speed, Case P2.

(g) Curvature, Case P3. (h) Tangential strain, Case P3. (i) Displacement speed, Case P3.

Figure 6.10: Probability density function (pdf) of normalised curvature ($\nabla \cdot \mathbf{n}\delta_T$), tangential strain ($Ka_s = a_T\delta_T/S_L$) and density-weighted displacement speed, S_d^*/S_L, at the flame front (c=0.7) at $y^+ = 5$. The pdfs are conditioned on the flame normal to give the leading (solid yellow) and trailing sides (dotted magenta) of the lobes in the oblique case. The rows of figures show Cases P1, P2 and P3 respectively from top to bottom.

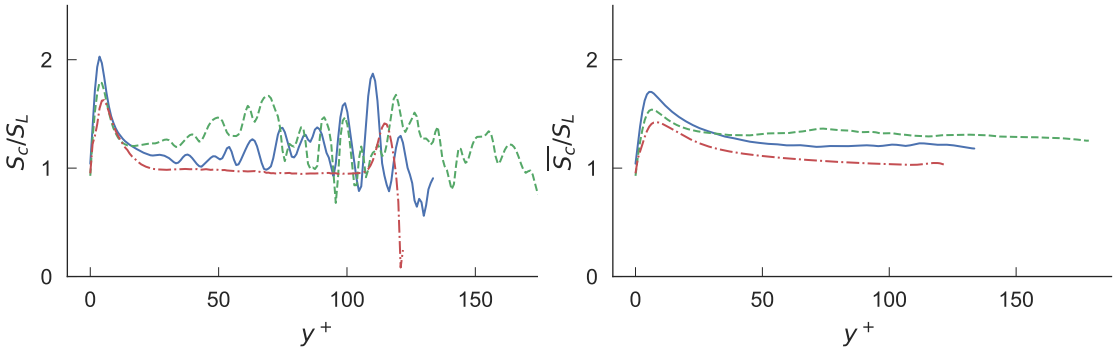

(a) (b)

Figure 6.11: Consumption speed of time- and Favre-averaged reaction rate integrated in y-planes as a function of wall-normal distance (y^+). (a) shows the consumption speed as a function of y^+ while (b) shows the consumption speed averaged between each point and $y^+ = 0$. Case P1 - solid blue; Case P2 - green dashed; Case P3 - red dot-dashed.

Case P2. The wall-normal pressure gradient reduces the turbulent consumption speed for all y^+ for Case P3, consistent with its lower displacement speed, and suppression of flame wrinkling away from the wall (at $y^+ < 5$).

6.2.1.1 Sensitivity to Progress Variable Definition

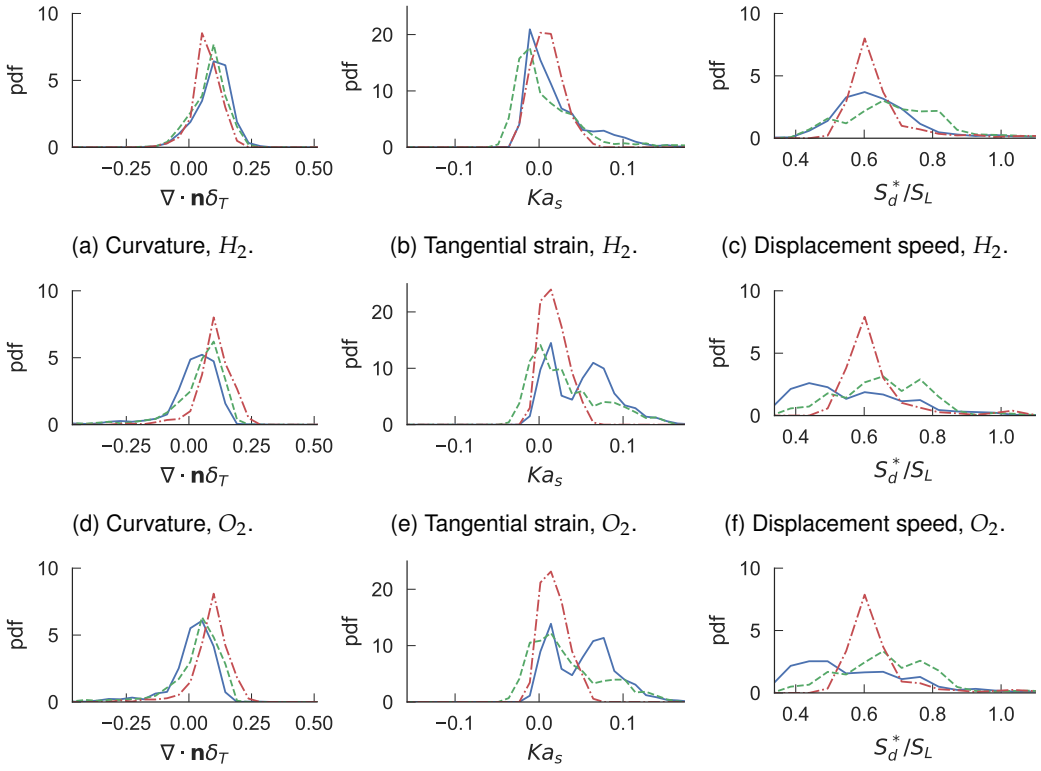

(a) Curvature, H_2. (b) Tangential strain, H_2. (c) Displacement speed, H_2.

(d) Curvature, O_2. (e) Tangential strain, O_2. (f) Displacement speed, O_2.

(g) Curvature, H_2O. (h) Tangential strain, H_2O. (i) Displacement speed, H_2O.

Figure 6.12: Probability density function (pdf) of normalised curvature ($\nabla \cdot \mathbf{n}\delta_T$), tangential strain ($a_T\delta_T/S_L$) and density-weighted displacement speed, S_d^*/S_L, at the flame front (c=0.7) on a plane at $y^+ = 5$. The pdfs are calculated using progress variables based on H_2, O_2 and H_2O, respectively, from top to bottom.

Figures 6.12 and 6.13 show the sensitivity of these results to the definition of progress variable. The pdfs are conditioned on the flame front for $y^+ = 5$ and all y^+, respectively. The definitions of progress variable are based on H_2, O_2 and H_2O, with definitions of the flame front of 0.7, 0.5 and 0.5. Figure 6.14 shows the conditional average heat-release rate for each progress-variable definition. The figure shows that these flame-front definitions correspond to the maximum heat-release rate in each case.

The results show that there is some sensitivity to the choice of progress variable for $y^+ = 5$. In general the pdfs based on O_2 and H_2O are very similar to each other. There are differences between the pdfs based on H_2, and those based on O_2 and H_2O, particularly for Case P1. For curvature the H_2-pdf shows a distribution which is wholly positive, while those based on O_2 and H_2O are more symmetrical around zero. For tangential strain the pdf shows a shift to be more positive when based on O_2 or H_2O. For displacement speed the pdfs based on O_2 and H_2O show a smaller magnitude of displacement speed than for H_2.

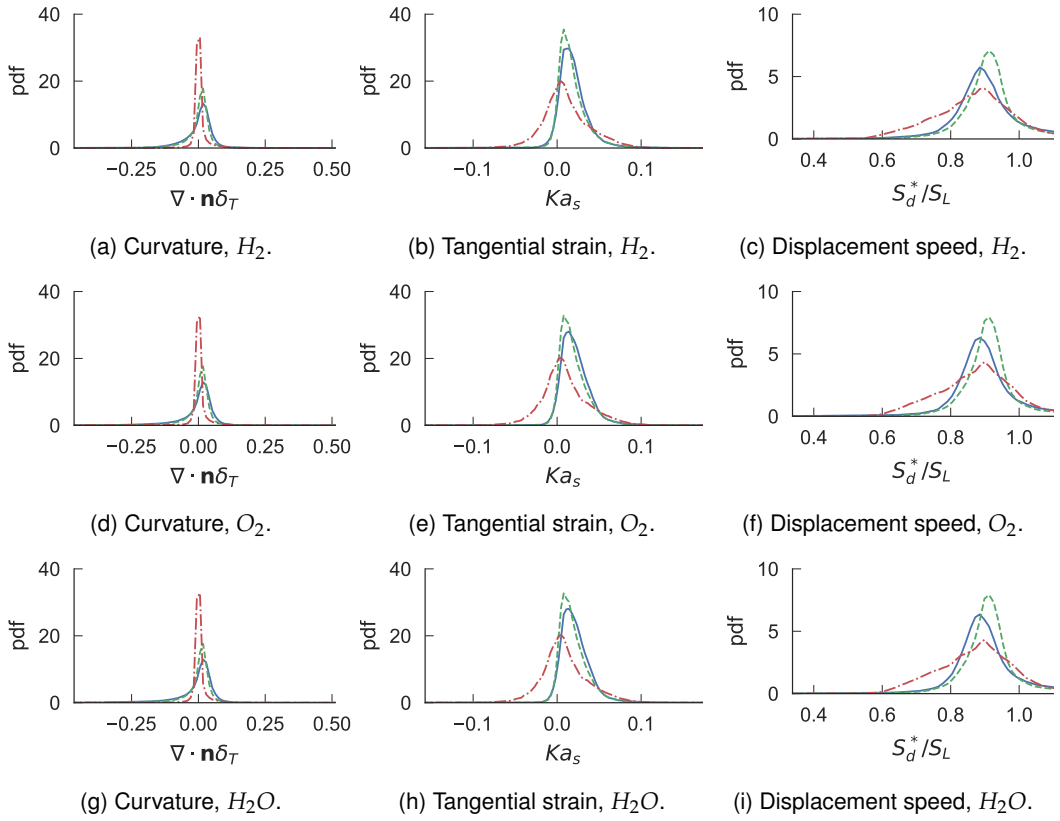

(a) Curvature, H_2. (b) Tangential strain, H_2. (c) Displacement speed, H_2.

(d) Curvature, O_2. (e) Tangential strain, O_2. (f) Displacement speed, O_2.

(g) Curvature, H_2O. (h) Tangential strain, H_2O. (i) Displacement speed, H_2O.

Figure 6.13: Probability density function (pdf) of normalised curvature ($\nabla \cdot \mathbf{n}\delta_T$), tangential strain ($a_T\delta_T/S_L$) and density-weighted displacement speed, S_d^*/S_L, at the flame front (c=0.7) for all y^+. The pdfs are calculated using progress variables based on H_2, O_2 and H_2O, respectively, from top to bottom.

The global pdfs (Figure 6.13), for all y^+, show very little sensitivity to the choice of progress variable. Each of the cases shows very similar distributions using each of the three progress-variable definitions.

While the pdfs at $y^+ = 5$ (Figure 6.12) show sensitivity to the choice of progress variable, they do not change the overall conclusions from these results, which is that the change in turbulent flame propagation described by these pdfs does not explain the change in flashback speed.

6.2.1.2 Statistical Significance

Figure 6.15 shows the pdfs of curvature, tangential strain and displacement speed for: all of the samples, the first half of the samples and the second half of the samples. These results show that there is little difference in the pdfs and that the conclusions drawn could be made using either half of the set of samples, suggesting that sufficient samples have been taken.

6.2.2 Overall Hydrodynamics

The next set of figures investigate the effect of the flames on the oncoming flow and overall hydrodynamics. Figure 6.16 shows the stream surfaces of the averaged flow field in the frame of reference of

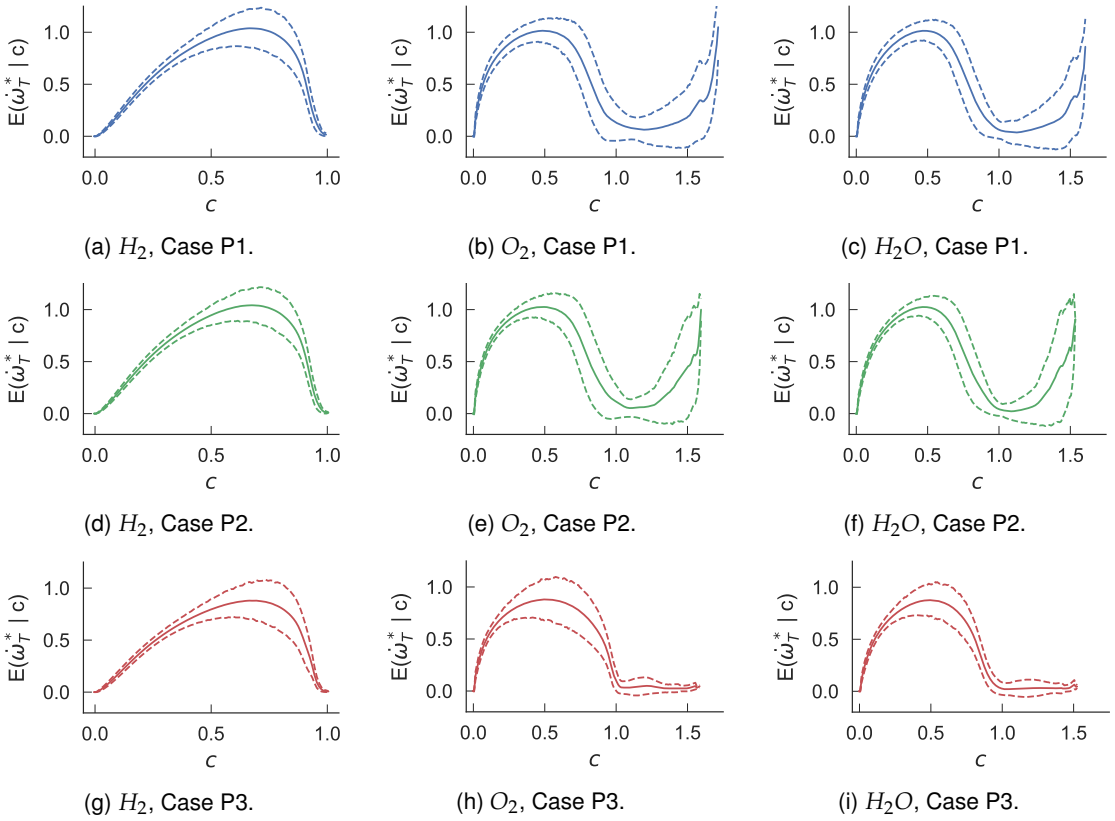

(a) H_2, Case P1. (b) O_2, Case P1. (c) H_2O, Case P1.

(d) H_2, Case P2. (e) O_2, Case P2. (f) H_2O, Case P2.

(g) H_2, Case P3. (h) O_2, Case P3. (i) H_2O, Case P3.

Figure 6.14: Heat-release rate, conditioned on progress variable for all y^+, normalised by maximum heat-release rate in laminar flame. The conditional mean is shown as a solid line; the conditional mean plus and minus one standard deviation is shown by the dashed lines. The rows of figures show from top to bottom Cases P1, P2 and P3. The columns of figures show from left to right progress-variable definitions based on H_2, O_2 and H_2O.

the leading flame edge, averaged over time and the homogeneous z-direction. A $\tilde{c} = 0.7$ iso-surface of Favre-averaged progress variable represents the mean flame location. Figure 6.17 shows the averaged pressure and axial pressure gradient, the location of the flame front ($\tilde{c} = 0.7$) and extent of the flame brush ($\tilde{c} = 0.1$ and 0.9). Figure 6.18 shows an instantaneous flame isosurface and wall shear stress (as in Figure 6.2) and an isosurface of zero u in blue.

Cases P1 and P2 present similar flow and flame profiles, with a negative stream-wise pressure gradient in the burned region and a small region of adverse pressure gradient in the x-direction upstream of the flame front, which in the averaged flow field (Figure 6.16) does not show reversed flow. Figure 6.18a shows that for Case P1, regions of reversed flow are found ahead of the leading points of the flame intermittently, although the regions in this case are very small. For the oblique case (Case P2), flow is reversed in the x-direction (Figure 6.18b) as well as in the streamwise direction (Figure 6.18d), although the size of the regions of reversed flow in this direction are smaller. The observation of stream-wise reversed flow contrasts with that from the swirling annular flows of Ebi and Clemens (2016) who did not find reversed flow in the streamwise direction. Ebi and Clemens (2016) observed the flame propagating as a wedge where the trailing side, facing the oncoming flow, was only a wake from the leading side and the wedge precessed around the centre-body of the mixing tube. The presence of stream-wise reversed flow in Figure 6.18d suggests that the flame can still propagate upstream against the oncoming stream-wise flow, which the flame could not do in

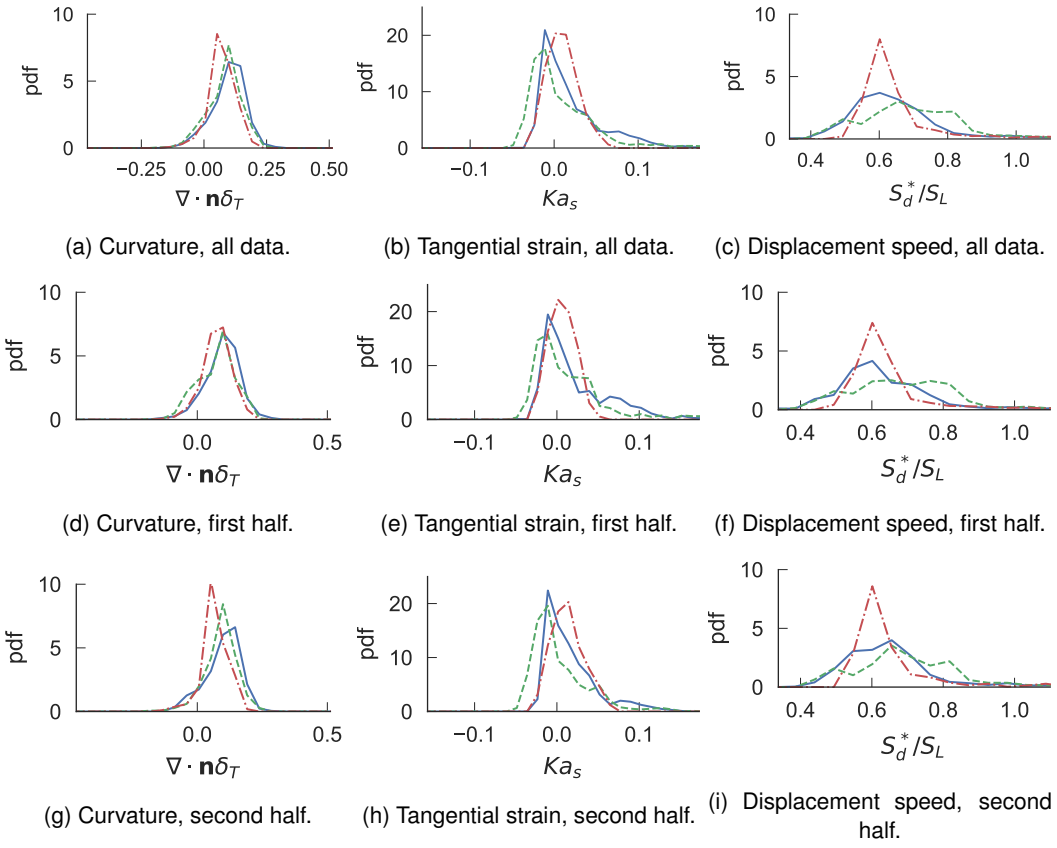

(a) Curvature, all data. (b) Tangential strain, all data. (c) Displacement speed, all data.

(d) Curvature, first half. (e) Tangential strain, first half. (f) Displacement speed, first half.

(g) Curvature, second half. (h) Tangential strain, second half. (i) Displacement speed, second half.

Figure 6.15: Probability density function (pdf) of normalised curvature ($\nabla \cdot \mathbf{n}\delta_T$), tangential strain ($a_T\delta_T/S_L$) and density-weighted displacement speed, S_d^*/S_L, at the flame front (c=0.7) on a plane $y^+ = 5$. Case P1 - solid blue; Case P2 - green dashed; Case P3 - red dot-dashed. The set of time samples are split in two and the pdfs calculated using, respectively: all time samples, the first half of the samples and the second half of the samples.

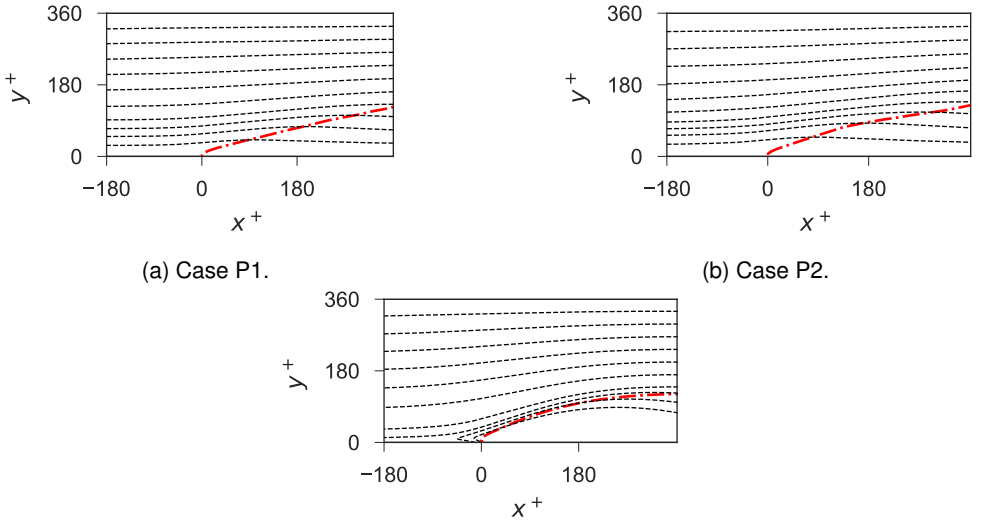

(a) Case P1. (b) Case P2.

(c) Case P3.

Figure 6.16: Time- and z-averaged stream surfaces (dashes) and flame position ($\tilde{c} = 0.7$, red dash-dot) in the frame of reference of the flame's leading edge.

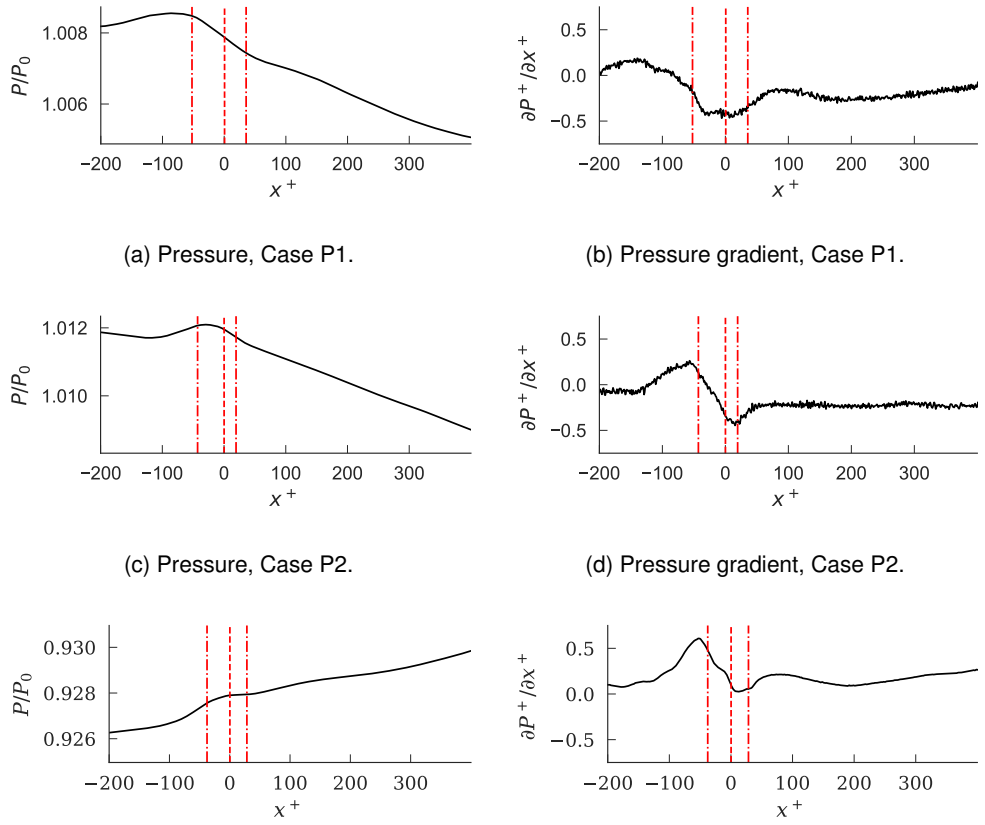

(a) Pressure, Case P1.

(b) Pressure gradient, Case P1.

(c) Pressure, Case P2.

(d) Pressure gradient, Case P2.

(e) Pressure, Case P3.

(f) Pressure gradient, Case P3.

Figure 6.17: Non-dimensional pressure (P/P_0) and axial pressure gradient ($\partial P^+/\partial x^+ = \partial P/\partial x(\delta_\nu/\rho_u u_\tau^2)$) along the line $y^+ = 5$ for the pressure field averaged in time and the homogeneous z-direction. The axial distance is shown relative to the leading point of the flame. The flame front ($c = 0.7$) is a dashed red line; the extent of the flame brush ($c = 0.1$, $c = 0.9$) is shown as dot-dashed red lines.

previous work (Ebi and Clemens, 2016). In this way, the global flame structure may be more similar to that of Ebi et al. (2020), where the flame, in a similar configuration to Ebi and Clemens (2016) but with different conditions, propagated upstream as a series of bulges and cusps, more similar to that seen in non-swirling boundary-layer flashback. However, the propagation of these leading and trailing sides in Case P2 will still help explain flame propagation in swirling flows, where there is a flame-flow misalignment.

In Case P3 the wall-normal pressure gradient produces a region of elevated pressure upstream of the flame front, as seen in the swirling annular flows studied by Karimi et al. (2015) and Ebi and Clemens (2016), that drives a large region of (lab-frame) reversed flow that extends downstream through the flame leading edge. Figure 6.17 shows that the axial pressure gradient is positive throughout the range shown. The peak ahead of the flame front is larger in magnitude than in Cases P1 and P2, and the pressure gradient continues to be positive in the burned region, due to the body force. The reversed flow can be seen even in the averaged flow field (Figure 6.16) where a re-circulation bubble can be seen. Figure 6.18c shows the instantaneous reversed-flow bubble extending across almost the entire flame front. Figure 6.18c also shows the large recirculation zone downstream of the flame front, where the low-density burned gases are being driven upstream by the pressure gradient, as seen in gravity currents.

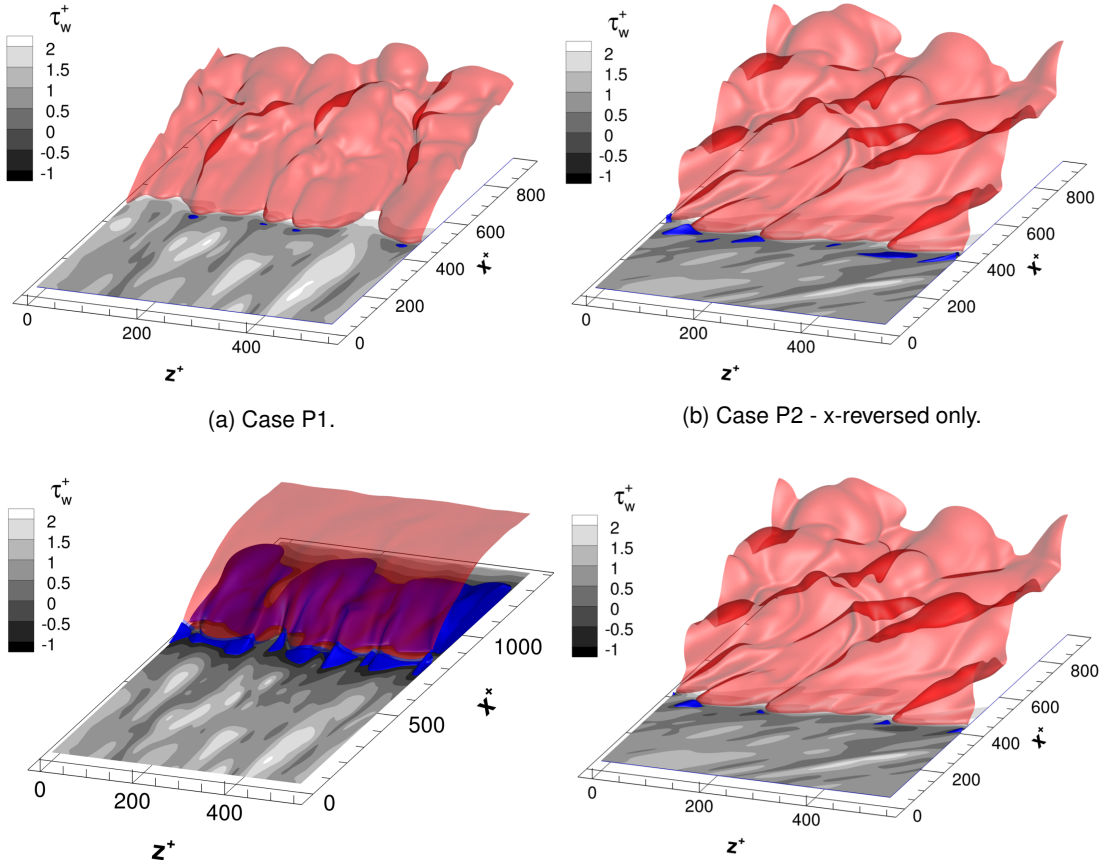

(a) Case P1.

(b) Case P2 - x-reversed only.

(c) Case P3.

(d) Case P2 - stream-wise reversed.

Figure 6.18: Regions of reversed flow (blue isosurface) and flame shape ($c = 0.7$ isosurface) after 0.5 ms. The shading of the bottom wall shows non-dimensional wall shear stress, τ_w^+.

6.3 Conclusions

In this chapter boundary-layer flashback was investigated using planar DNS. The two additional physical aspects of a swirling flow (radial pressure gradient and flame-flow misalignment) were studied by independently applying these effects to two DNS. This allowed comparison between a case with neither effect (Case P1), one with flame-flow misalignment (Case P2) and another with a radial pressure gradient (Case P3). The factors affecting global flame propagation and flashback speed were evaluated.

The overall hydrodynamics described here were shown to explain the overall change in flashback speed for the pressure-driven flow (Case P3). The wall-normal pressure gradient increases the flow reversal ahead of the flame front and diversion of the flow around the flame front. This means that, although the turbulent consumption speed is lower in this case, the relative flashback speed is higher.

The overall hydrodynamics also explain the change in flashback speed for the oblique flow (Case P2). Due to the misalignment of the flow and mean flame propagation, the flow is able to propagate upstream against the smaller axial bulk velocity. Larger regions of flow are reversed in the x-direction than in the direction of the mean flow, increasing the flashback speed and axial flame propagation. This is aided by an increase in the displacement speed for the leading sides of the flame lobes, compared to Case P1 and the trailing sides of Case P2.

Chapter 7

Flashback in Turbulent Annular Channel Flow

The objective of this chapter is to investigate how the wall-normal pressure gradient and the misalignment of flow and flashback directions contribute to the different flashback behaviour of swirling and non-swirling flows. In this chapter, simulations of annuli will be conducted, where swirl produces both the wall-normal pressure gradient and flame-flow misalignment. Auxiliary non-reacting-flow simulations will again be conducted to feed realistic, time-evolving turbulence into the reacting-flow simulations. In these annular cases the curvature of the walls could result in differences in the structure of the turbulence, firstly between the planar and annular cases, and secondly between the annular swirling and non-swirling cases. The first part of this chapter therefore presents analysis of the non-reacting-flow simulations where the flow is either axial-only or swirling. The second part of the chapter uses these non-reacting flows in reacting-flow simulations to investigate flashback.

7.1 Non-Reacting Flow

Table 7.1 gives the simulation parameters for the annular, non-reacting cases, while Table 7.2 gives the mean-flow parameters. A ratio of outer to inner radius of 2 is used to match the flashback investigations of Ebi and Clemens (2016) and annular non-reacting simulations of Chung et al. (2002). Both non-reacting simulations use the same axial and wall-normal grids, with grid stretching in the wall-normal direction to give a ratio of around 14 between the smallest and largest grid spacings. The domain for the axial-only case is $\pi/2$ radians in θ and for the swirling case is π radians. The sufficiency of the domain's axial and circumferential extents will be reviewed for each case. These non-reacting simulations will be used to study flashback, which is most likely to occur against the inner wall of the annulus. The aim for each non-reacting case was therefore to maintain $Re_\tau = 180$ along the inner wall, with $Re_\tau = 182$ and 162 achieved for the axial-only and swirling cases, respectively. The Mach number, based on the velocity magnitude $(u^2 + w^2)^{\frac{1}{2}}$, was limited to 0.2. A time-step of 4×10^{-9} was used, giving a maximum Courant number ($c\Delta r/\Delta t$, where c is the speed

Table 7.1: Simulation parameters for the annular, non-reacting cases.

Flow orientation	Axial-only	Swirling
$\delta(m)$	2.5×10^{-3}	2.5×10^{-3}
$L_x \times L_r \times L_\theta$	$8.7\delta \times 2\delta \times \pi/2$	$8.7\delta \times 2\delta \times \pi$
L_x^+	3540	3700
$L_{\theta_i}^+$	582	1020
$L_{\theta_o}^+$	1100	2780
$N_x \times N_r \times N_z$	$240 \times 120 \times 168$	$240 \times 120 \times 336$
Δx^+	14.8	15.5
$R_0 \Delta\theta^+$	3.5	3.0
$R_1 \Delta\theta^+$	6.6	8.3
Δr_i^+	0.46	0.41
Δr_o^+	0.44	0.56
Δr_{max}^+	6.2	6.4
R_1/R_0	2	2
γ	0.5	0.5

of sound) of 0.35. The simulations were initialised and run until Re_τ was constant with time, samples were then taken every 25 ms until the averaged wall-normal velocity profile was zero across the annulus ($\sim 80\delta/\overline{|u|}$, where $|u|$ is the velocity magnitude, $(u^2 + w^2)^{\frac{1}{2}}$).

Table 7.2: Mean flow parameters for the annular, non-reacting cases. For the swirling case, u is taken to be the velocity magnitude $(u^2 + w^2)^{\frac{1}{2}}$.

Flow orientation	Axial-only	Swirling
Re_{D_h}	10970	11900
Re_δ	3198	3492
Re_τ (Inner)	182	162
Re_τ (Outer)	172	221
$-K_{p,x}$ (Inner)	5.33×10^{-3}	4.77×10^{-3}
$-K_{p,x}$ (Outer)	6.27×10^{-3}	1.89×10^{-3}
$-K_{p,\theta}/R_0$ (Inner)	0.00	1.36×10^{-2}
$-K_{p,\theta}/R_1$ (Outer)	0.00	2.70×10^{-3}
u_c/u_τ (Inner)	17.6	21.5
u_c/u_τ (Outer)	18.6	15.8
u_m/u_τ (Inner)	15.1	18.3
u_m/u_τ (Outer)	15.9	17.3
M	0.160	0.175

7.1.1 Annular Flow without Swirl

In this section, the results from the non-reacting annular flow without swirl are reviewed. The overall structure of the turbulence is reviewed through the mean and fluctuation velocity, and Reynolds stress profiles. The results are also compared to previous investigations of non-reacting flow in a channel (Moser et al., 1999) ($Re_\tau = 180$) and an annulus (Chung et al., 2002) ($Re_{\tau,inner} = 153$).

Figure 7.1 shows the two-point correlation coefficients, r_{ij}, in x and θ for each velocity component (u, v, w) at around $y^+ = 5$ (further results are shown in D.1 for different y^+). The results show that the correlation coefficients decay to zero by the halfway point of the domain, in each direction. This is used to show the sufficiency of the size of the domain.

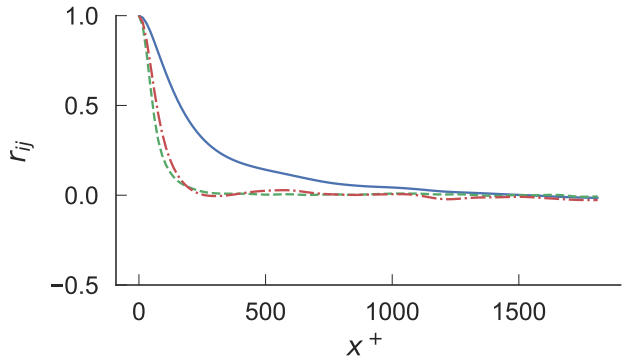

(a)

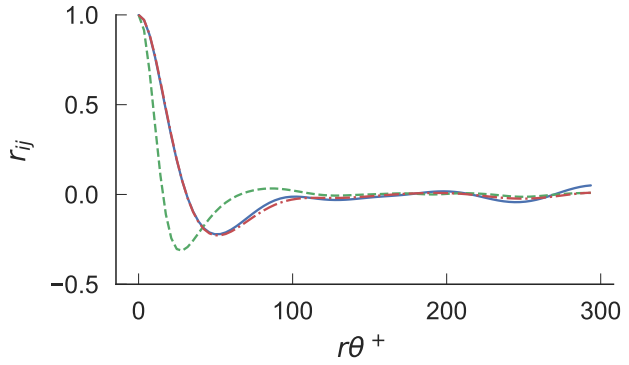

(b)

Figure 7.1: Two-point correlation coefficients in x and θ for each velocity component: u (solid blue), v (dashed green), w (dot-dashed red) at the inner wall at around $y^+ = 5$ for the axial-only annular flow. Normalisation is by the local wall scales.

Figure 7.2 shows the mean velocity profile across the channel, and the mean velocity profile becoming asymmetrical across the channel with the transverse curvature. The wall shear stresses at the inner and outer wall also begin to differ, with Table 7.2 showing the inner wall having a higher Re_τ than the outer wall (182 and 172, respectively).

Figure 7.3 shows the mean velocity profile plotted with the mean velocity profile of Chung et al. (2002). The mean velocity profiles are very similar, with only slight differences which may be due to the slightly higher Re_τ here (Chung et al. (2002) found 153 and 144 for the inner and outer wall).

Figure 7.4 also shows the mean velocity profile but here compared to the planar channel flow of Moser et al. (1999). This shows only small differences in the mean velocity profiles, when normalised by the local wall shear stresses. At this level of transverse curvature ($\gamma = 0.5$ and $a^+ = 360$), there is little impact on either the inner or outer regions of the flow. Neves et al. (1994) showed that effects are seen on the outer flow of the inner boundary-layer for large γ, and, for the inner flow, for large γ and small a^+. Neves et al. (1994) gave an updated linear velocity profile for the inner part of the flow for axisymmetric flows:

$$u^+ = a^+ \ln\left(1 + \frac{y^+}{a^+}\right) \tag{7.1}$$

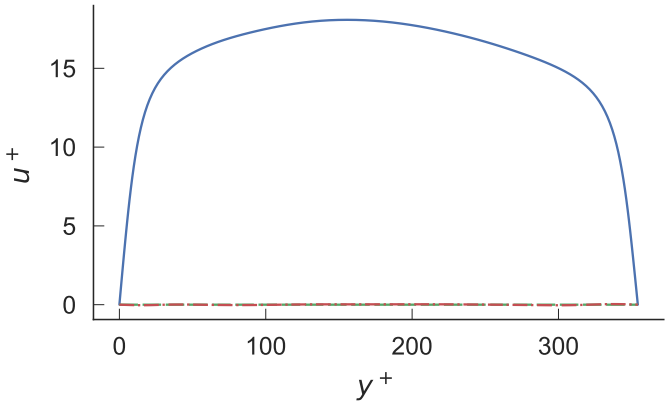

Figure 7.2: Mean velocity profile for the axial-only annular flow, for each velocity component: u (solid blue), v (dashed green), w (dot-dashed red), in wall units for the whole channel. The wall scales used are based on the combination of the inner and outer scales: $u_\tau^2 = \frac{1}{2}\left(u_{\tau,o}^2 + u_{\tau,i}^2\right)$.

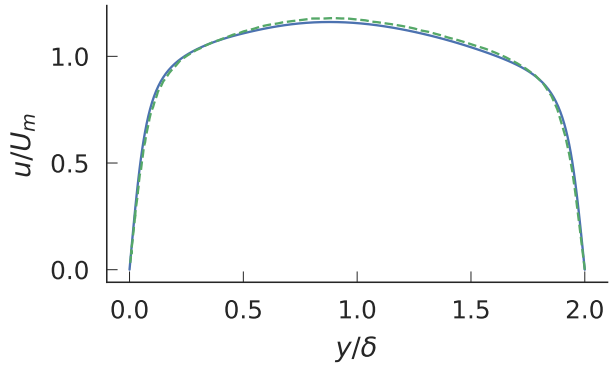

Figure 7.3: Mean axial velocity profile for the axial-only annular flow (solid blue), normalised by the mean velocity (U_m), shown in comparison to the annular axial-only results of Chung et al. (2002) (dashed green).

which to second-order is:

$$u^+ = y^+\left(1 + \frac{y^+}{2a^+}\right) \tag{7.2}$$

which for the current simulations would give a difference from the linear profile of less than 3% at $y^+ = 20$.

Figure 7.5 shows the fit of the current mean velocity profile to a log-law profile (Bagheri and Wang, 2019):

$$\begin{aligned} \langle u\rangle^+ &= \frac{1}{\kappa}\ln y^+ + \beta \\ \frac{1}{\kappa} &= y^+\frac{\partial\langle u\rangle^+}{\partial y^+} \\ \beta &= \langle u\rangle^+ - y^+\frac{\partial\langle u\rangle^+}{\partial y^+}\ln y^+ \end{aligned} \tag{7.3}$$

and shows that κ and β are not completely consistent in a log-law region. Bagheri and Wang (2019) investigated annular non-reacting flow at different radius ratios ($R_0/R_1 = 0.1$, 0.3, 0.5, 0.7) using DNS. The authors showed more consistent values of κ and β with y^+. κ remained around 0.35

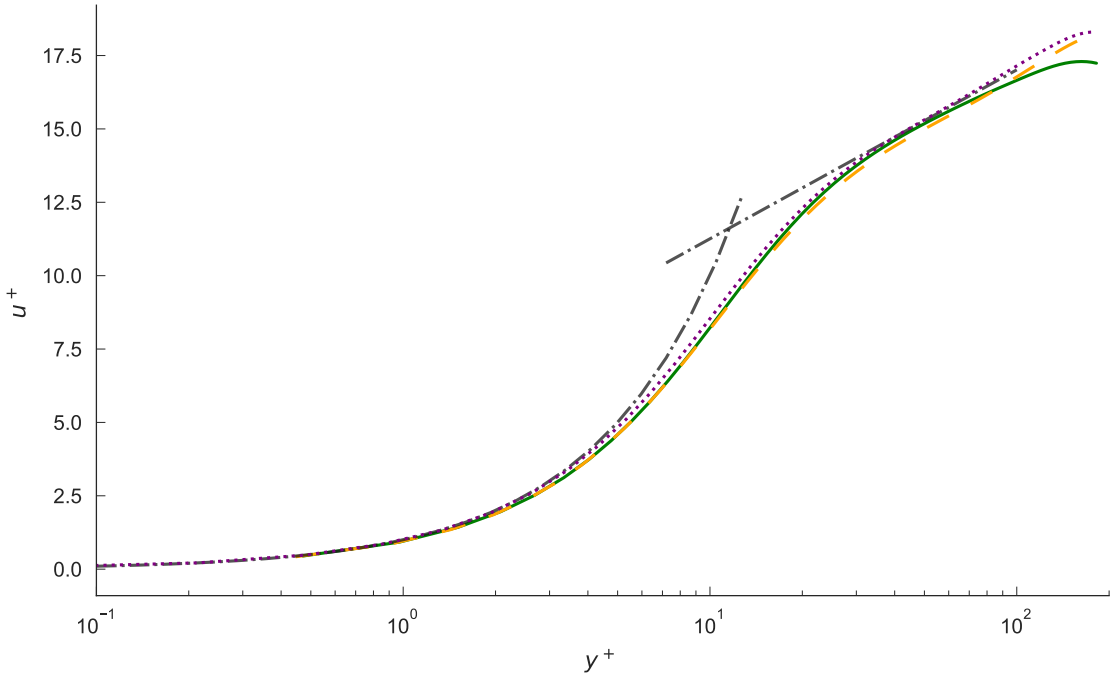

Figure 7.4: Mean axial velocity profile for the axial-only annular flow, normalised by the local wall time scales for the inner (green solid) and outer (orange dashed) walls, shown in comparison to the planar channel-flow results of Moser et al. (1999) (purple dotted), and linear ($u^+ = y^+$) and log-law ($u^+ = 2.5 \ln y^+ + 5.5$) velocity profiles (black dot-dashed).

across the range of radius ratios. The outer walls showed a larger region of y^+ where κ and β are constant ($y^+ \sim 50$ to ~ 100) compared to the inner walls. κ was shown to be consistent between the inner and outer walls, where β was shown to be smaller on the inner than the outer walls, with the difference increasing as R_0/R_1 decreased. For $R_0/R_1 = 0.5$, the same as the radius ratio used here, β was similar for the inner and outer walls, at around 4. Here β was found to be larger for the inner than the outer wall, and overall to be larger at around 5 at $y^+ = 50$.

Figure 7.6 shows the mean profiles of the velocity fluctuations, including the results of Chung et al. (2002) and Moser et al. (1999), which are for a similar Re_τ to the case here. For the inner wall each of the velocity components shows a reduction in fluctuation compared to planar flows, whereas the fluctuation profiles for the outer walls are similar. For u, the peak fluctuation is very similar at the inner wall compared to a planar channel flow but in the outer part of the inner flow there is a reduction in magnitude. This is in slight disagreement with the results of Chung et al. (2002) which showed a reduction in magnitude across the inner half of the channel. For v and w, the fluctuations are slightly larger in the outer parts of the outer flow ($y^+ > 50$) compared to a planar channel flow. For v there is also a slight movement of the peak fluctuation out from the wall, although the magnitude of the peak is maintained. For w the location and magnitude of the fluctuation peak are both similar. Compared to Chung et al. (2002) the results here show higher fluctuations in the outer part of the inner flow. Neves et al. (1994) showed the magnitude of the fluctuations decreasing with curvature across the inner part of the flow over the inner wall. They also showed that the peak in u moved closer to the wall, which was not found here. Neves et al. (1994) attributed the reduction in magnitude of turbulent kinetic energy to the smaller wall-surface-area-to-volume ratio for the inner flow as curvature increased, but not a change in the efficiency of the wall surfaces. Chung et al. (2002) showed that at a radius ratio of 2 the velocity fluctuations for the outer wall were slightly lower

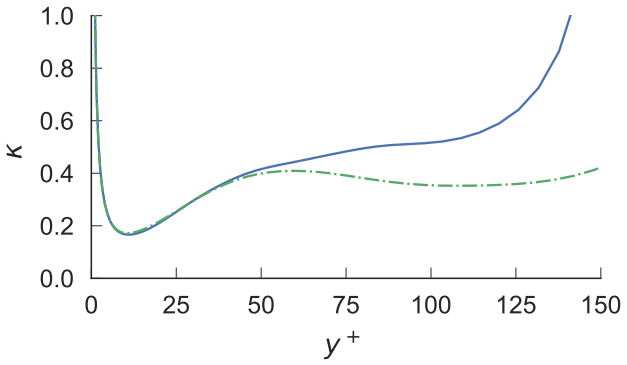

(a)

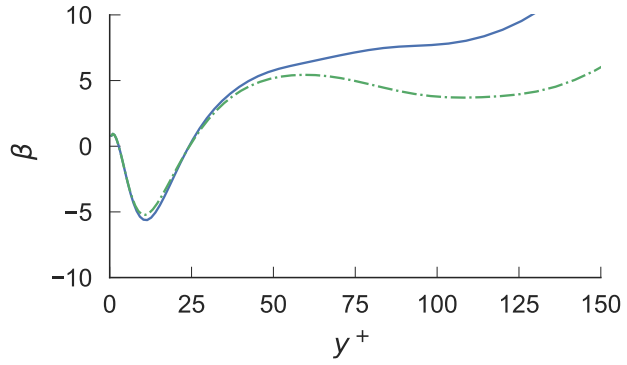

(b)

Figure 7.5: Fits of mean velocity profiles to a log-law relation for the inner (solid blue) and outer (dot-dashed green) walls of the axial-only annular flow using the parameters κ and β: $\frac{1}{\kappa} = y^+ \frac{\partial \langle u \rangle^+}{\partial y^+}$,

$$\beta = \langle u \rangle^+ - y^+ \frac{\partial \langle u \rangle^+}{\partial y^+} \ln y^+.$$

than for a planar channel flow, while, at a radius ratio of 10, the velocity fluctuations increased for the outer wall. Overall some differences between these results and those of Chung et al. (2002) may be expected because of the difference in Re_τ (182 compared to 153). However, these differences are shown to be small and to validate this annular flow without swirl.

Figure 7.7 shows the profile of Reynolds stresses, where the profile of $u'v'^+$ is qualitatively similar to that of a planar channel flow. It is also shown that the other Reynolds-stress components have almost averaged out to zero across the annulus.

Figure 7.8 shows the mean profiles of Reynolds stress, normalised by their local wall scales, against the annular axial-only flow of Chung et al. (2002) and the planar channel flow of Moser et al. (1999). The figure shows that the reduction in magnitude of the velocity fluctuations translates into a reduction in Reynolds stress for the inner wall, while the outer region is much more similar to that of a planar channel flow. Chung et al. (2002) and Neves et al. (1994) both showed a reduction in Reynolds stresses with increasing curvature, for the inner wall, while Chung et al. (2002) showed that the profile is similar for the outer wall for a radius ratio of 2 and that there is a slight increase at a radius ratio of 10. Overall, for this case there is a slight reduction in the Reynolds stresses for

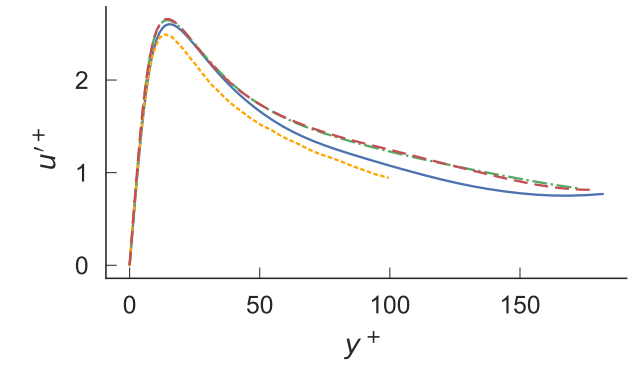

(a)

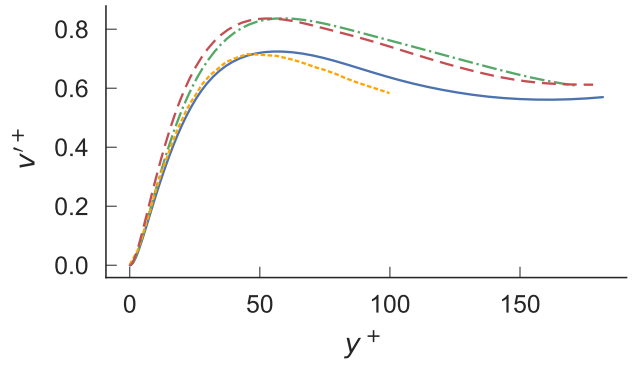

(b)

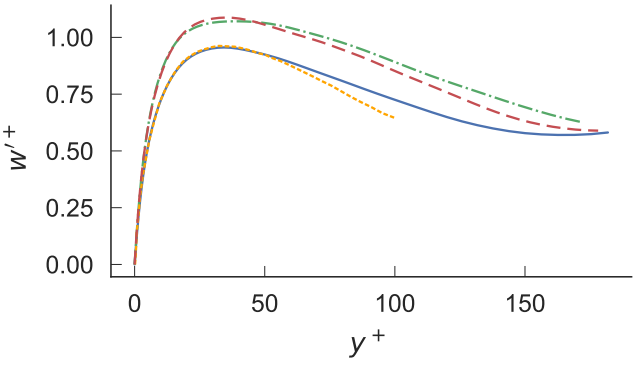

(c)

Figure 7.6: Mean profiles of velocity fluctuations for the axial-only annular flow for each velocity component, normalised by the local wall scales for the inner (solid blue) and outer (dot-dashed green) walls. In comparison are the axial-only annular results for the inner wall of Chung et al. (2002) (dashed orange) and the planar channel-flow of Moser et al. (1999) (longer dashed red).

the inner wall but, given that the differences are around 20%, they are unlikely to have a significant effect on turbulent flame dynamics.

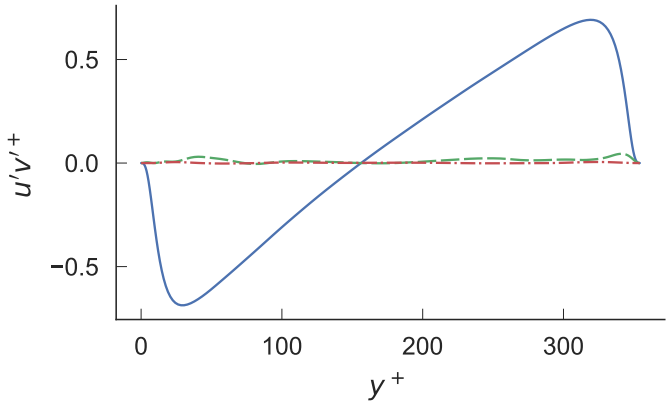

Figure 7.7: Mean profiles of Reynolds stress terms: $u'v'^+$ (solid blue); $u'w'^+$ (green dashed) and $v'w'^+$ (dot-dashed red), normalised by a combination of the inner and outer wall scales, $u_\tau^2 = \frac{1}{2}\left(u_{\tau,o}^2 + u_{\tau,i}^2\right)$.

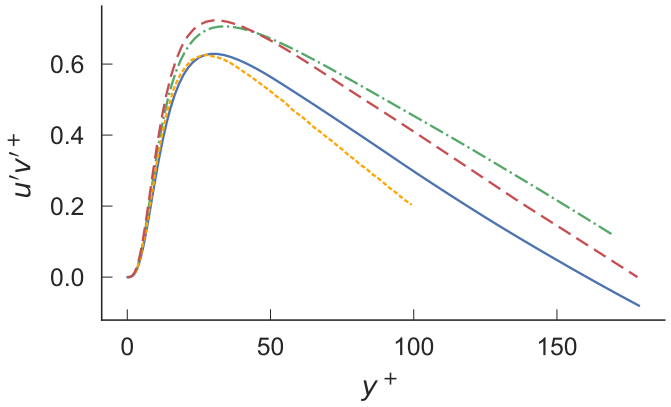

Figure 7.8: Mean profile of Reynolds stress $u'v'^+$ for the inner (solid blue) and outer (green dot-dashed) walls, compared to results of Chung et al. (2002), inner wall, (orange dotted) for annular axial-only flow and of Moser et al. (1999) (longer dashed red) for planar channel flow.

Figure 7.9 shows the mean azimuthal streak spacing for this axial-only annular flow compared to the channel flows of Kristoffersen and Andersson (1993), Kim et al. (1987) ($Re_\tau = 180$) and Smith and Metzler (1983) (experimental results over a range of Re). The mean azimuthal streak spacing is calculated as double the wall distance where the minimum in the two-point correlation $r_{uu}(z)$ occurs. The spacing below $y^+ = 20$ is shown to be larger at the outer wall compared to the inner for this annular flow but, in general, the streak spacing is similar for the annular flow and the channel flows. Kristoffersen and Andersson (1993) found decreasing streak spacing with increasing rotation rate for their spanwise-rotating channel flows. Here, without any rotation, the annular flow shows similar streak spacing to the non-rotating channel flows.

In summary, the current DNS is adequately verified against previous simulations. For annuli with small $\gamma = \delta / R_0$, the velocity-fluctuation profiles and structure of the turbulent flow are similar to that of planar channels.

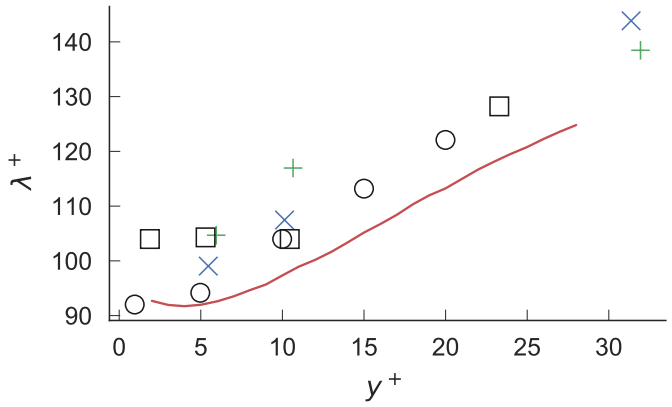

Figure 7.9: Mean azimuthal streak spacing for the axial-only annular flow, normalised by the local wall scales, for the inner (blue $\times$) and outer (green $+$) walls. Also shown are the channel-flow results of Kristoffersen and Andersson (1993) (solid red line), Kim et al. (1987) ($\square$) and Smith and Metzler (1983) ($\bigcirc$).

7.1.2 Annular Flow with Swirl

In this section the results of the swirling annular non-reacting flow will be reviewed. The results will also be compared to those of Kristoffersen and Andersson (1993), for span-wise rotating channel flows, to provide a qualitative comparison.

Figure 7.10 shows the two-point correlation coefficients in the axial and azimuthal directions for each velocity component (further results are shown in D.1 for different y^+). The correlation in both directions decays to zero within half of the domain length, demonstrating the sufficiency of the domain. For the swirling flow, a domain of size $\pi/2$ radians in θ was simulated but shown to be insufficiently large. The size was therefore increased to π radians, which is shown to be sufficiently large.

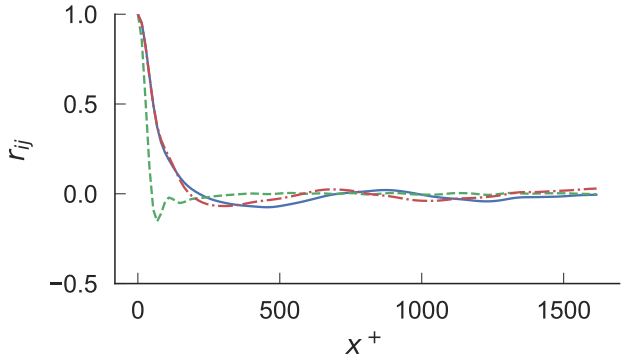

(a)

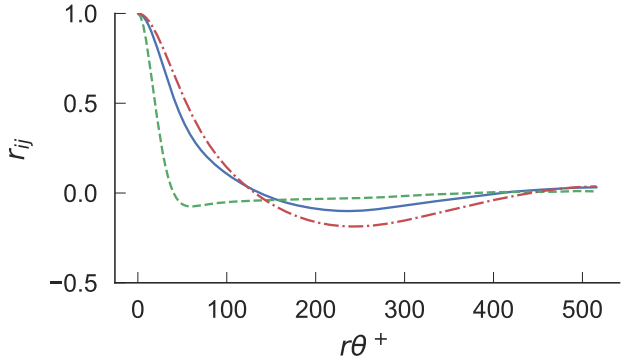

(b)

Figure 7.10: Two-point correlation coefficients in x and θ for each velocity component: u (solid blue), v (dashed green), w (dot-dashed red) at the inner wall at around $y^+ = 5$ for the axial-only annular flow. Normalisation is by the local wall scales.

Figure 7.11 shows the average velocity profile for the swirling flow. The profiles of both u and w are highly asymmetric. The pattern of wall shear stress has also changed from the axial-only case, with the wall shear stress now higher on the outer wall than the inner ($Re_\tau = 161$ and 219 for the inner and outer walls, respectively). This matches the pattern seen in rotating channel flows (Kristoffersen and Andersson, 1993) where as the rotation rate was increased, the outer wall (referred to as the

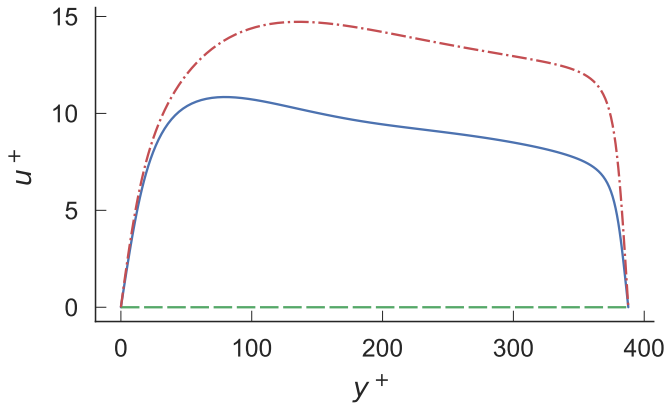

Figure 7.11: Mean velocity profile for the swirling annular flow, for each velocity component: u (solid blue), v (dashed green), w (dot-dashed red), in wall units for the whole channel. The wall scales used are based on the combination of the inner and outer scales: $u_\tau^2 = \frac{1}{2}\left(u_{\tau,o}^2 + u_{\tau,i}^2\right)$.

pressure side) has increasing Re_τ, while the inner wall (referred to as the suction side) had decreasing Re_τ. Figure 7.12 shows the flow angle ($\tan^{-1}(w/u)$) as a function of the wall-normal distance. This shows that the level of swirl is higher near the outer wall than the inner wall.

The average flow angle is 55.2°; this gives rotation numbers ($Ro = 2|\Omega|\delta/\overline{u}$, where Ω is the angular velocity) equivalent to $Ro = 23$, 8.8, 1.7, 0.18, 0.41, 0.78, 5.0 and 26.0 at $y^+ = 10$, 20, 50, 100 from each wall. Both Kristoffersen and Andersson (1993) and Xia et al. (2016), in their investigations of span-wise rotating channel flows, showed that the central region of the velocity profile fits a linear relation with y equal to 2Ω. In this case the velocity gradient in this central region varies between 4000 and 7000 s^{-1} (based on the gradient of u or $\sqrt{u^2 + w^2}$) while Ω varies between 7000 and 14000 $rad.s^{-1}$ in this central region, meaning that they are still of the same order of magnitude, although a direct relation does not apply in this case.

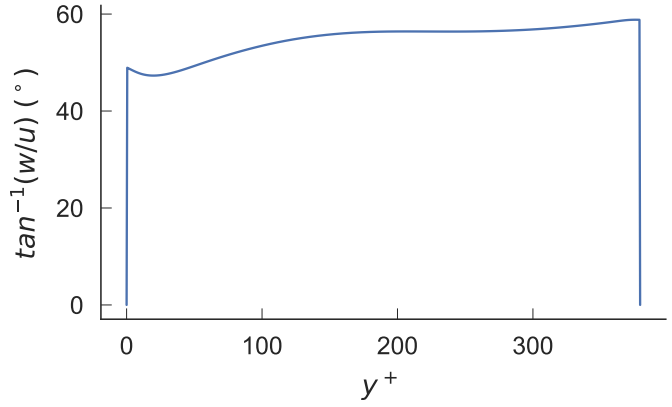

Figure 7.12: Mean flow angle ($\tan^{-1}(w/u)$) for the swirling annular flow calculated from the mean velocity profile. The wall scales used are based on the combination of the inner and outer scales: $u_\tau^2 = \frac{1}{2}\left(u_{\tau,o}^2 + u_{\tau,i}^2\right)$.

Figure 7.13 shows the mean velocity profile, where u_s and w_{cs} have been calculated as the stream-wise and cross-stream-wise velocity components using the mean flow angle, 55.2°. This shows that w_{cs} does not average out to zero, due to the variation in mean flow angle with wall distance. It also

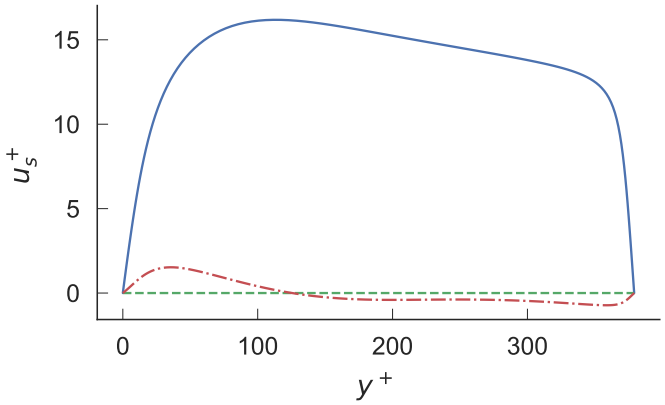

Figure 7.13: Mean velocity profile for the swirling annular flow as: stream-wise, u_s, (solid blue); cross-stream-wise, w_{cs}, (dot-dashed red); and wall-normal components, v, (dashed green). The components are calculated using the mean flow angle, 55.2°. The wall scales used are based on the combination of the inner and outer scales: $u_\tau^2 = \frac{1}{2}\left(u_{\tau,o}^2 + u_{\tau,i}^2\right)$.

shows the highly asymmetric velocity profile for u_s, with a significantly larger wall velocity gradient at the outer than the inner wall.

Figure 7.14 shows the mean velocity profiles for u and u_s normalised by the local wall scales in comparison to the results of Moser et al. (1999), and linear and log-law velocity profiles. Figure 7.14a shows that there is significant deviation from the planar-channel-flow profile when the axial velocity, u, is used. However, when the stream-wise velocity, u_s, is plotted in Figure 7.14b, the mean velocity profile matches the results of the planar channel flow up to around $y^+ = 10$, deviating above this where the velocity at the inner wall is larger than the planar channel flow and at the outer wall is smaller. This is similar to that from rotating channel flow (Kristoffersen and Andersson, 1993) where the inner and outer walls diverge from the results of the non-rotating channel flow, with the divergence growing with increasing rotation rate.

Figures 7.15 and 7.16 shows the velocity profile again being fitted to a log-law profile. It shows that the profile of the outer wall retains a similarity to a log-law profile, with κ and β being reasonably constant between $y^+ = 50$ and 100. For the inner wall, the values of κ and β using either velocity definition vary significantly with y^+.

Figure 7.17 shows the mean velocity-fluctuation profiles normalised by the local wall scales. Figure 7.17a shows that for both the inner and outer walls, the magnitude of the peak in fluctuations of u has decreased compared to a planar channel flow and axial-only annular flow, although the fluctuations further from the wall have increased. It also shows that, while the absolute magnitude of fluctuations at the inner wall are lower than at the outer wall, when normalised by the local wall scales, the axial velocity fluctuations are higher at the inner rather than the outer wall. For the outer wall, the position of the peak in u'^+ remains at the same wall distance, while for the inner wall the peak has moved further from the wall. Figure 7.17b shows the mean profile for v'^+. Here there is significant deviation from the planar channel flow of Moser et al. (1999) and the axial-only annular flow of Chung et al. (2002). The magnitude of the fluctuations in v^+ are similar near the wall (below $y^+ = 30$) but in the centre of the flow the fluctuations are significantly larger, and continue increasing with y^+ up to the centre of the channel. Figure 7.17c shows the profile for w'^+. Here the comparison of the profile to Moser et al. (1999) and Chung et al. (2002) is complicated by the presence of a mean flow in θ.

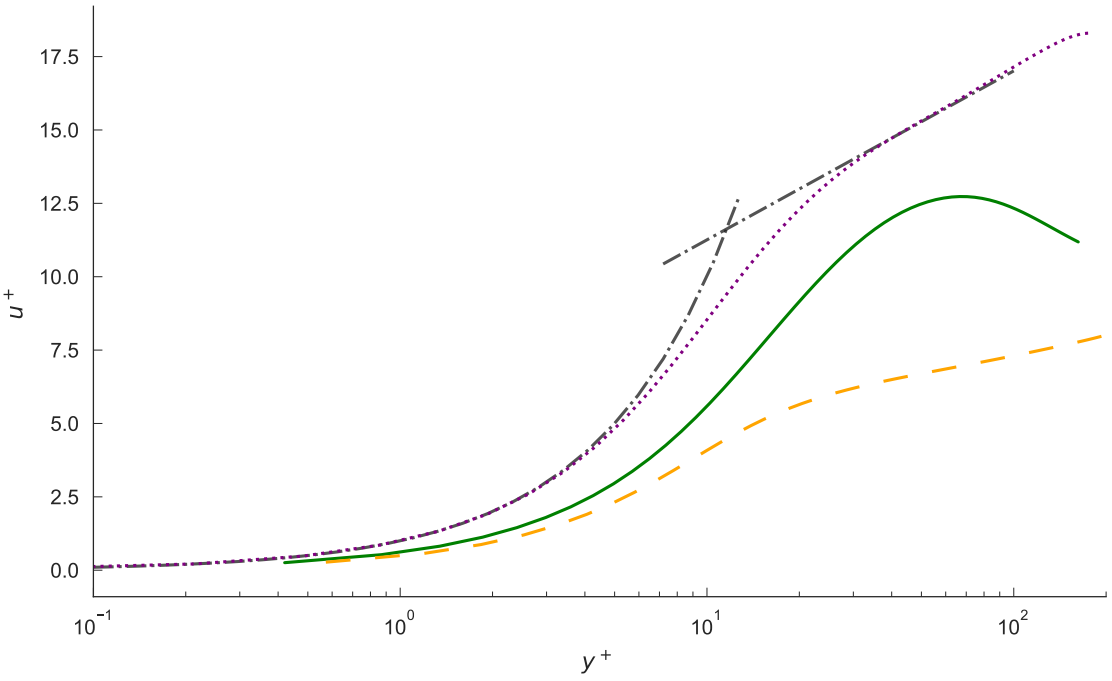

(a) Axial velocity, u.

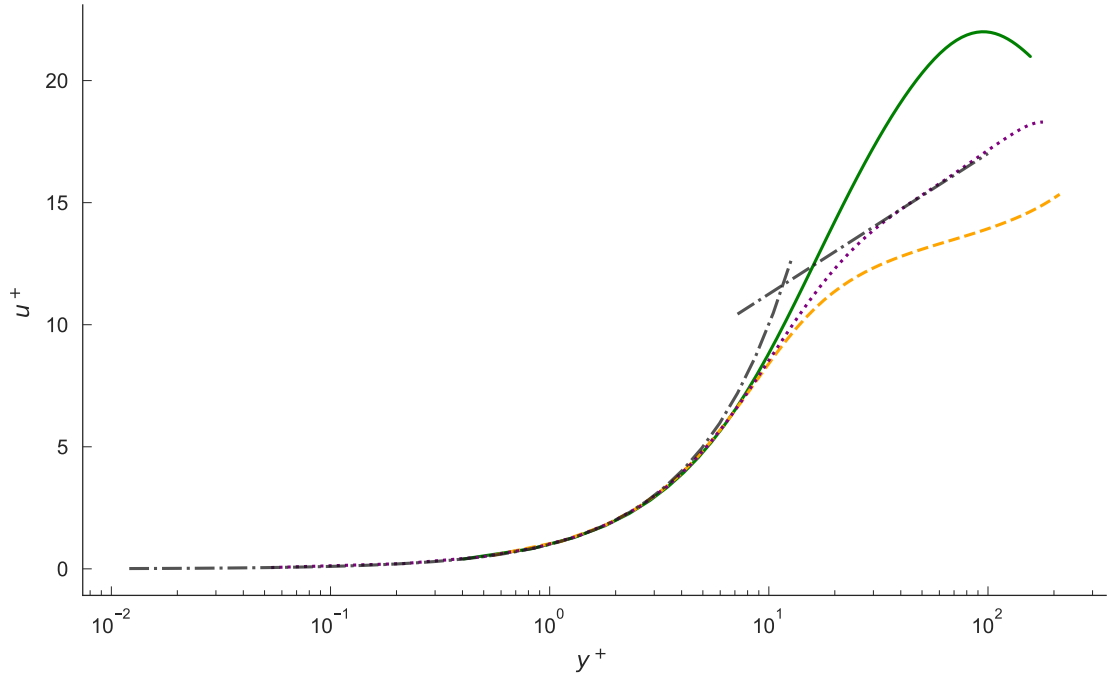

(b) Stream-wise velocity, u_s.

Figure 7.14: Mean axial (a) and stream-wise (b) velocity profiles for the swirling annular flow, normalised by the local wall scales for the inner (green solid) and outer (orange dashed) walls, shown in comparison to the planar channel-flow results of Moser et al. (1999) (purple dotted), and linear and log-law velocity profiles (black dot-dashed).

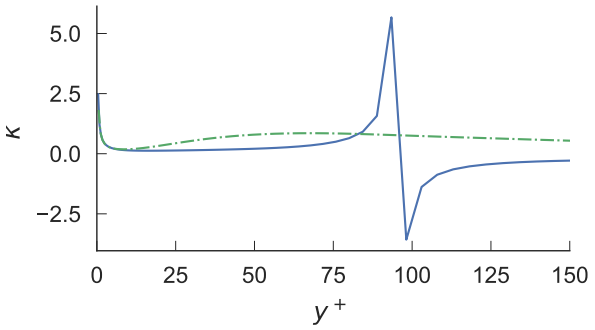

(a) Stream-wise velocity, u_s.

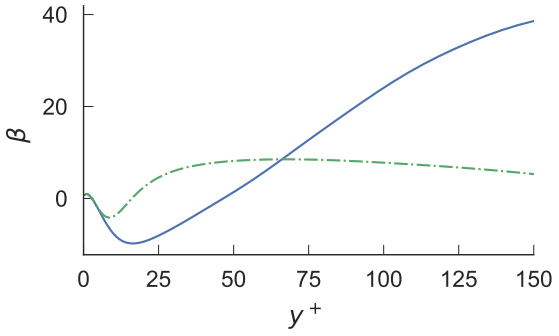

(b) Stream-wise velocity, u_s.

Figure 7.15: Fits of mean axial velocity profiles to a log-law relation for the inner (solid blue) and outer (dot-dashed green) walls for the swirling annular flow using the parameters κ and β: $\frac{1}{\kappa} = y^+ \frac{\partial \langle u \rangle^+}{\partial y^+}$, $\beta = \langle u \rangle^+ - y^+ \frac{\partial \langle u \rangle^+}{\partial y^+} \ln y^+$.

At the inner wall, the profile has a similar shape to the planar channel flow and axial-only annular flow but the magnitude of the fluctuations is much larger. At the outer wall the shape and magnitude of the profile are more similar to that of u. These profiles are similar to those of Kristoffersen and Andersson (1993), where, as the rotation rate was increased, the magnitude of the fluctuations at the inner wall decreased for all velocity components, the magnitude of the fluctuations at the outer wall increased at small rotation rates but decreased at the largest rotation rate investigated ($Ro = 0.50$), while the magnitude of the fluctuations in v and w both increased with increasing rotation at the outer wall and both showed significant magnitude in the centre of the flow. Here u'^+ decreases in magnitude at both the inner and outer walls, which qualitatively matches the rotating channel flow given the large equivalent rotation rates of this swirling annular flow.

Kristoffersen and Andersson (1993) showed that the large v'^+ in the centre of the channel results from the formation of Taylor-Görtler vortices rotating about the mean stream-wise direction. The authors averaged these vortices in the stream-wise direction and estimated their contribution to the velocity fluctuations using this averaging procedure. For this annular swirling flow the mean flow is helical with the swirl angle varying across the annulus so that stream-wise flow averaging is not simple to define. It is not therefore possible to isolate their contribution to the velocity fluctuations. Figures 7.18 and 7.19 show the azimuthal vorticity on $x - r$ planes for the axial-only and swirling

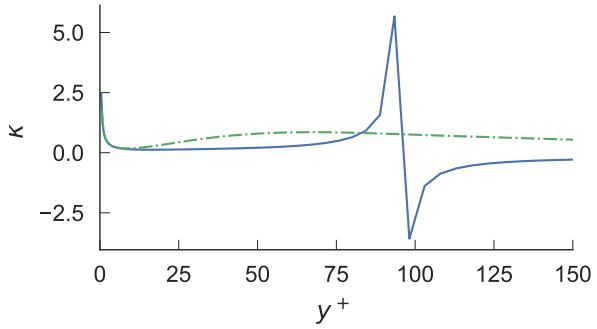

(a) Stream-wise velocity, u_s.

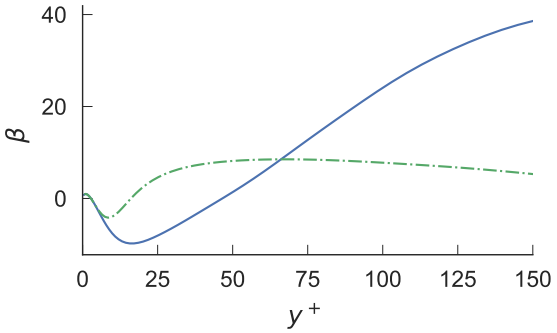

(b) Stream-wise velocity, u_s.

Figure 7.16: Fits of mean stream-wise velocity profiles to a log-law relation for the inner (solid blue) and outer (dot-dashed green) walls for the swirling annular flow using the parameters κ and β: $\frac{1}{\kappa} = y^+ \frac{\partial \langle u \rangle^+}{\partial y^+}$, $\beta = \langle u \rangle^+ - y^+ \frac{\partial \langle u \rangle^+}{\partial y^+} \ln y^+$.

annular flows. For the axial-only flow, the vorticity in the centre of the flow is small. However, for the swirling flow, there is now significant azimuthal vorticity due to the instability on the top wall and the helical curvature of the flow.

Figure 7.20 shows the profiles of the Reynolds-stress terms uv', uw' and vw' normalised by the local wall scales. Noting that the present flow follows a helical path, when uv' and vw' are combined to a give a stream-wise-cross-stream-wise Reynolds stress their profile matches qualitatively the stream-wise-cross-stream-wise Reynolds stress seen by Kristoffersen and Andersson (1993) for which there is a general upward shift of the profile of Reynolds stress. Compared to a non-rotating planar channel flow, where the profile of Reynolds stress magnitude is symmetrical between the inner and outer wall, this gives a smaller magnitude of Reynolds stress at the inner wall and higher magnitude at the outer wall.

Figure 7.21 shows u' on $x - \theta$ planes at around $y^+ = 5$ for the inner and outer walls, while Figure 7.22 shows the same for the axial-only annular flow. The axial-only flow is similar to the pattern of high- and low-velocity streaks seen in planar channel flows, with similar streak spacings (as shown in Figure 7.9). For the swirling flow, the outer wall shows a similar pattern of streaks, although with a reduced magnitude of the fluctuations and now angled with the swirling flow. At the inner wall the pattern is qualitatively different: the magnitude of the fluctuations is significantly smaller

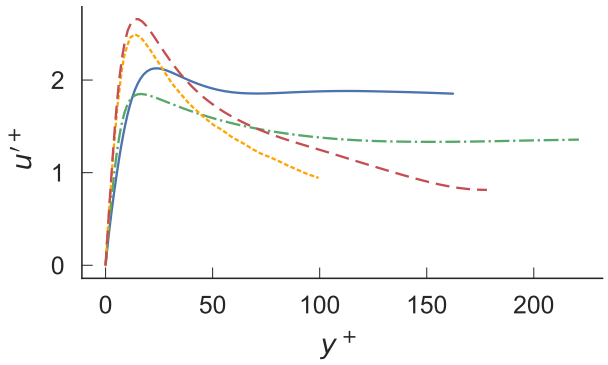

(a)

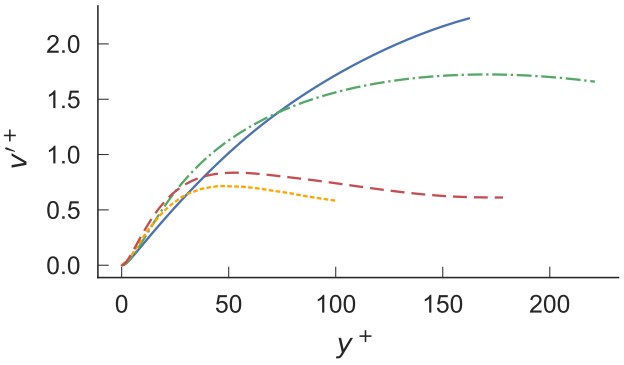

(b)

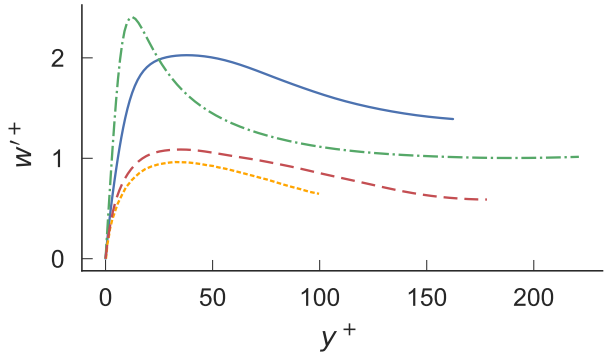

(c)

Figure 7.17: Mean profiles of velocity fluctuations for the swirling annular flow for each velocity component, normalised by the local wall scales for the inner (solid blue) and outer (dot-dashed green) walls. In comparison are the axial-only annular results of Chung et al. (2002) (dashed orange) and the planar channel-flow of Moser et al. (1999) (longer dashed red).

and the pattern of high- and low-velocity streaks is much less clearly defined. This is also shown quantitatively by Figure 7.10b where the minimum in the correlation coefficient for each velocity component has a much smaller magnitude, suggesting a weaker pattern of high- and low-velocity

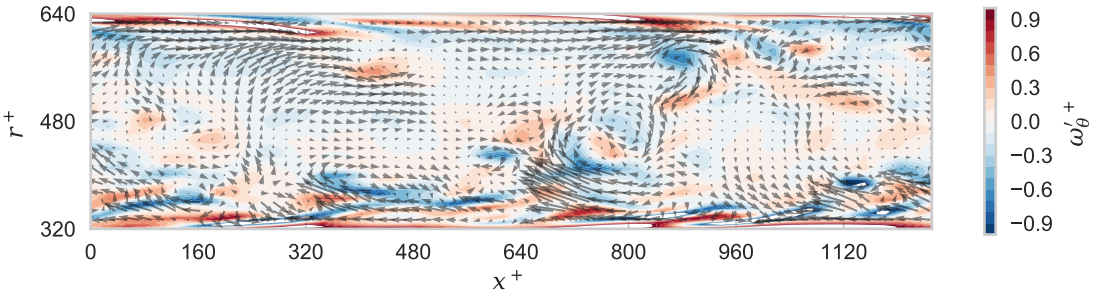

Figure 7.18: Azimuthal vorticity (ω_θ) for the axial-only annular flow on an $x-r$ plane, normalised by a combination of the inner and outer wall scales $\left(u_\tau^2 = \frac{1}{2}\left(u_{\tau,o}^2 + u_{\tau,i}^2\right)\right)$. The arrows show the local flow direction in proportion to the velocity magnitude.

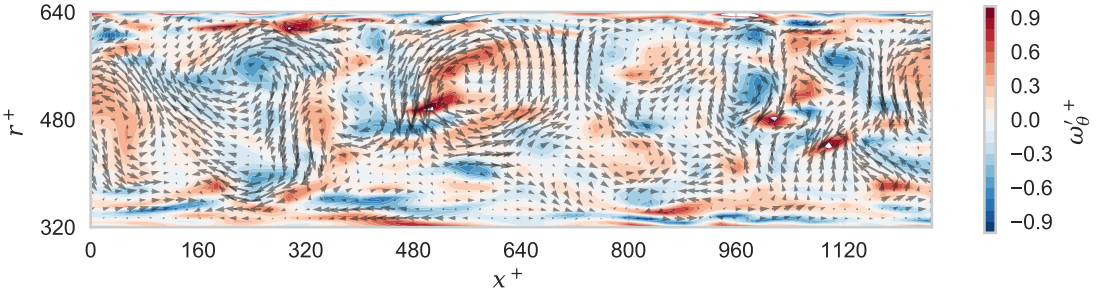

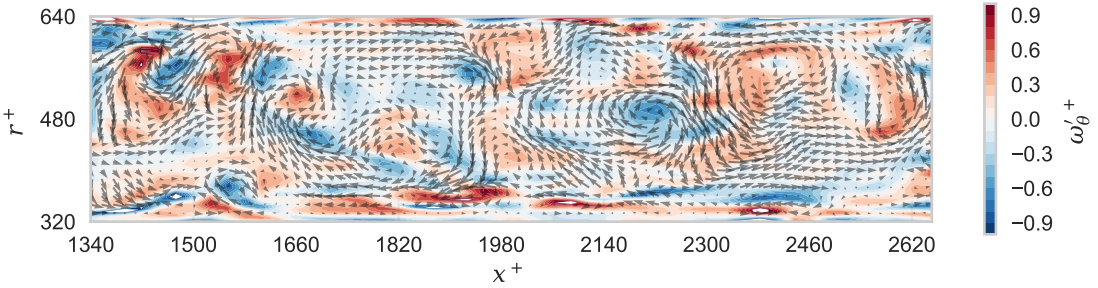

Figure 7.19: Azimuthal vorticity (ω_θ) for the swirling annular flow on an $x-r$ plane, normalised by a combination of the inner and outer wall scales $\left(u_\tau^2 = \frac{1}{2}\left(u_{\tau,o}^2 + u_{\tau,i}^2\right)\right)$. The arrows show the local flow direction in proportion to the velocity magnitude. The two plots show the two halves of the channel in the axial direction.

streaks. This result again matches the structure found by at the inner wall of a rotating channel flow (Kristoffersen and Andersson, 1993), where increasing rotation rates caused a reduction in the magnitude of fluctuations and a breakdown of the pattern of high- and low-velocity streaks.

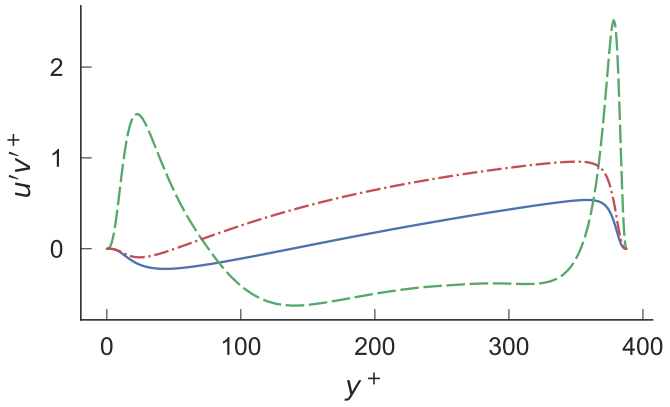

Figure 7.20: Mean profiles of Reynolds stress terms: $u'v'^+$ (solid blue); $u'w'^+$ (green dashed) and $v'w'^+$ (dot-dashed red), normalised by a combination of the inner and outer wall scales, $u_\tau^2 = \frac{1}{2}\left(u_{\tau,o}^2 + u_{\tau,i}^2\right)$.

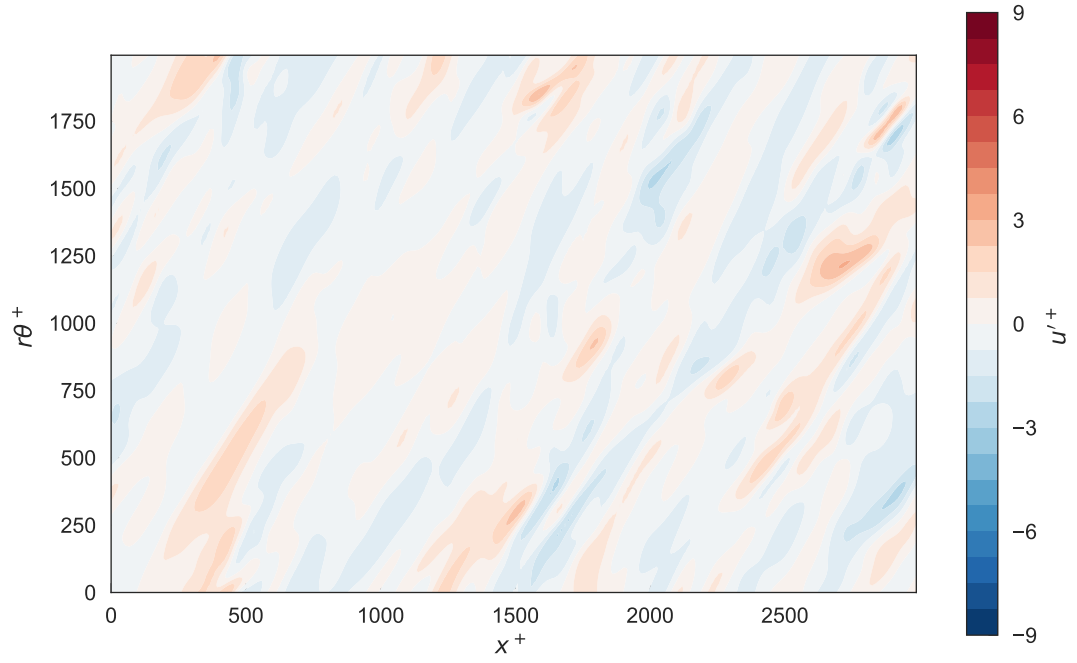

(a) Inner wall - $y^+ = 5$

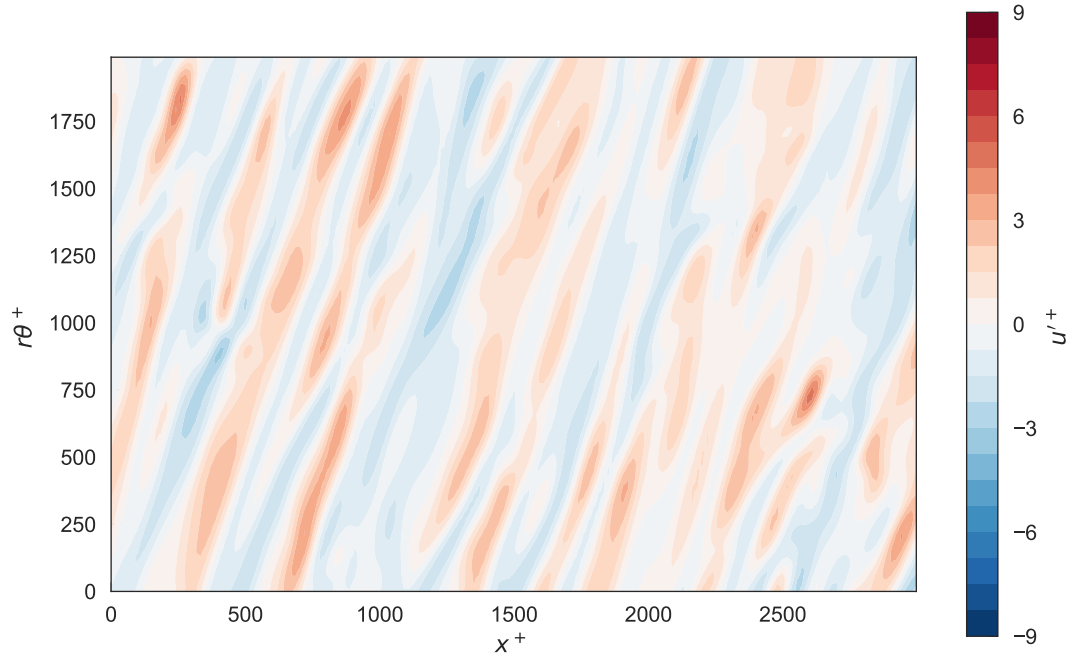

(b) Outer wall - $y^+ = 5$

Figure 7.21: Axial-velocity fluctuations for the swirling annular flow on an $x - r\theta$ plane ($0 \leq x^+ \leq 3000$, $0 \leq r\theta^+ \leq 2000$), for the inner and outer walls both at around $y^+ = 5$, normalised by the local wall scales.

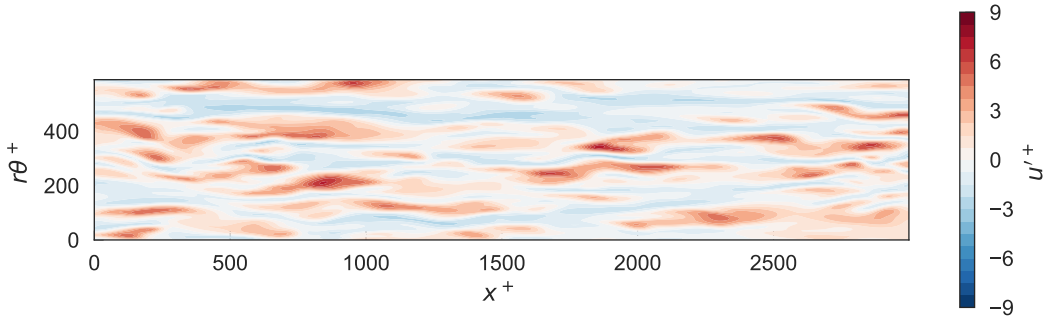

(a) Inner wall - $y^+ = 5$

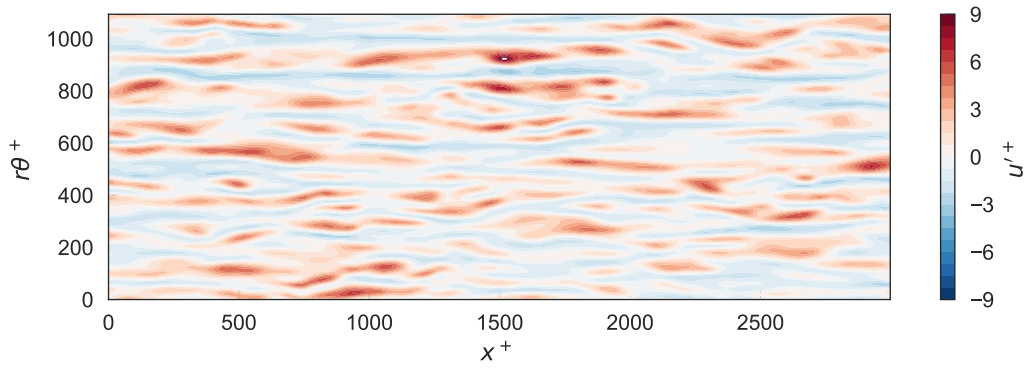

(b) Outer wall - $y^+ = 5$

Figure 7.22: Axial velocity fluctuations for the axial-only annular flow on an $x - r\theta$ plane for the inner and outer walls, both at around $y^+ = 5$, normalised by the local wall scales.

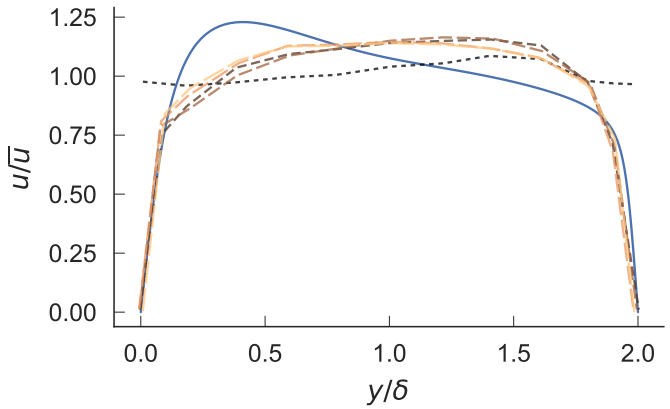

(a) u, Morsi and Clayton (1986).

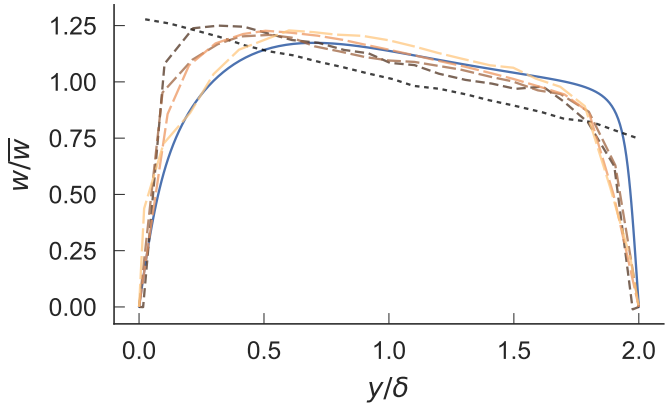

(b) w, Morsi and Clayton (1986).

Figure 7.23: Mean velocity profiles for u and w, normalised by the mean velocity, for the swirling annular flow (solid blue) in comparison to the mean profiles from decaying swirling flow generated by 45^o swirl vanes (Morsi and Clayton, 1986). The data is shown for the initial profile (black) and increasing distance downstream (increasing dash length and lightening colour). The points are at Stations 0, 2, 4, 6, 8 as described by Morsi and Clayton (1986).

These non-reacting flow simulations will be used to feed realistic, time-evolving turbulence into the reacting-flow simulations and so the final part of this section reviews the velocity profiles generated by these simulations, using periodic boundary-conditions and an applied pressure gradient, in comparison to the velocity profiles generated by a set of swirl vanes, which were used to generate swirl in the experimental flashback investigations of Ebi and Clemens (2016) and to study decaying swirling turbulent flow (Morsi and Clayton, 1986). Figures 7.23 and 7.24 show the mean velocity profile of u and w in comparison to experimental investigations of decaying swirling flow (Morsi and Clayton, 1986) ($R_1/R_0 = 2.0$, $Re = 28700$) and flashback in annular swirling flows (Ebi and Clemens, 2016) ($R_1/R_0 = 2.0$, $Re_{D_h} = 4000$ and 8000) which both used swirl vanes to generate a swirling flow in an annulus. Morsi and Clayton (1986) measured the velocity profile at different stations downstream from the inlet. Ebi and Clemens (2016) measured an average velocity profile 60mm upstream of the mixing tube exit.

Figures 7.23b and 7.24b show that the profiles of w for this fully developed swirling flow are similar to that in swirling flow generated using swirling vanes. In Figure 7.23b, this is particularly true for distances further downstream, with the most downstream distance being particularly similar at the

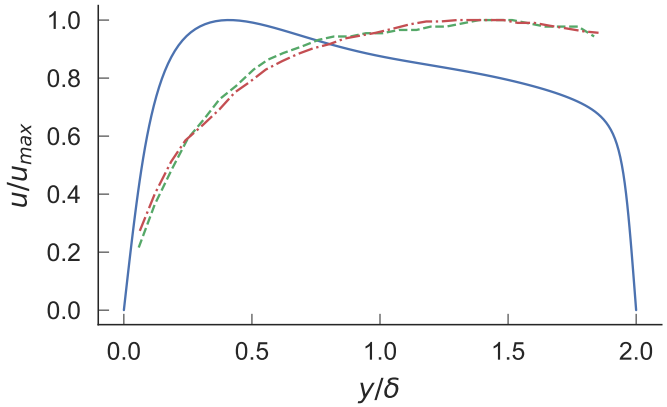

(a) u, Ebi and Clemens (2016).

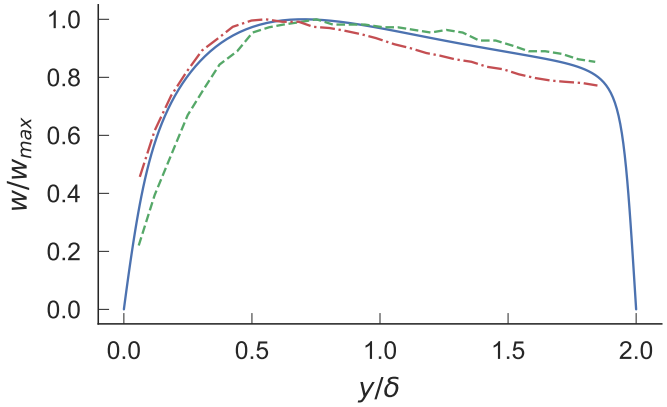

(b) w, Ebi and Clemens (2016).

Figure 7.24: Mean velocity profiles for u and w, normalised by the peak velocity, for the swirling annular flow (solid blue) in comparison to the mean profiles from decaying swirling flow generated by swirl vanes (Ebi and Clemens, 2016). The experimental data is for $Re_{D_h} = 4000$ (dashed green) and 8000 (dot-dashed red).

inner wall. However, Figures 7.23a and 7.24a show that the profiles of u are less similar. Figure 7.23a shows the u profile to be more symmetrical, and therefore less similar, in the centre of the channel, although the velocity gradients at the inner wall are very similar. Figure 7.24a shows u profiles which are significantly more rounded, with wall velocity gradients that are much less steep. Overall the velocity profiles are similar to the data of Morsi and Clayton (1986), particularly when considering the near-wall velocities. The u velocity profile is different from the results of Ebi and Clemens (2016), which may cause some differences in flashback speed due to the lower wall velocity gradient. However, the profile has been shown to vary with the swirl vanes used, and so may be dependent on the particular experimental or practical burner used. In addition, the effect of local interactions between the turbulence and the flame, and the effect of the radial pressure gradient can still be investigated and used to understand the dominating effects on flashback. Simple Radial Equilibrium theory gives, for the swirl-velocity distributions found here and by Ebi and Clemens (2016) and Morsi and Clayton (1986), an axial velocity profile which increases towards the inner wall of the annulus, without the effect of the boundary layer. The data of Ebi and Clemens (2016) may not have developed sufficiently to reach this distribution or it may be affected by the pressure distribution at the exit from the mixing tube.

Table 7.3: Simulation parameters for the annular, reacting cases.

Case	Flow orientation	Sw	Fr
Annular 1 (A1)	Axial-only (0°)	0	∞
Annular 2 (A2)	Swirling (55.2°)	2.2	0.35

Table 7.4: Configuration parameters for the annular, reacting cases.

Case	δ/δ_L	$L_x \times L_y \times L_\theta$	R_1/R_0	Re_τ	Da_w
A1	11.1	$5\delta \times 2\delta \times \pi/2$	2	182	0.16
A2	11.1	$5\delta \times 2\delta \times \pi$	2	162	0.20

7.2 Reacting Flow

The objective of this section is to investigate the effect of swirl on boundary-layer flashback using an annular configuration. Case A1 uses an axial-only flow fed by the non-reacting, axial-only flow shown in the previous section. Case A2 uses a swirling flow fed by the non-reacting, swirling flow of the previous section. Comparisons will be made between these two cases, and between the annular cases of this chapter and the planar cases of the previous chapter.

Tables 7.3 and 7.4 give the parameters for the reacting-flow simulations. The simulations in this chapter also used the moving frame-of-reference within the turbulent feed data (described in Section 3.1.7). The moving frame-of-reference velocities were 1.35 S_L for Case A1 and 1.28 S_L for Case A2.

Figure 7.25 shows the flame shape after around 50 wall time units coloured by the axial flow direction, along with the wall shear stress on the inner wall of the annulus. The axial-only flow (Figure 7.25a) appears very similar to Case P1 (axial flow direction and no body force, Figure 6.2a), with the pattern of high- and low-velocity streaks of the turbulent boundary layer, which is common to both non-reacting flows, wrinkling the flame front to produce the pattern of bulges and cusps. This is also shown by Figure 7.26, which shows the flame and wall shear stress on an xθ-plane. The small reduction in turbulent fluctuations of the annular non-reacting flow has not visually impacted the wrinkling of the flame front. The extent of reverse flow is small, with only the leading points of the bulges showing reverse flow at the flame front. Figure 7.27 shows a translucent flame front and an isosurface of zero axial velocity to show the overall extent of reverse flow. This shows that there are small regions of reverse flow ahead of the flame leading points. These are larger than those seen in Case P1 and could be related to the effect of confinement. In the planar case the cross-sectional area of the flow is constant with y. In the annular case the cross-sectional area increases with r. This effectively reduces the confinement of the flow, which will allow greater flow diversion and a greater extent of reversed flow.

Figure 7.25b shows the flame front for the swirling annular flow. This shows that the pattern of flame bulges and cusps is significantly reduced, with a much smoother flame front along the inner wall. This is also apparent by comparing Figure 7.26b for the swirling flow with Figure 7.26a for the axial-only flow. Due to the curvature of the wall, the swirling non-reacting flow shows reduced turbulent fluctuations on the inner wall, along with a weakening of the pattern of high- and low-velocity streaks. This will lead to a reduction in the growth of bulges and cusps. However, the flame front is still hydrodynamically unstable and Gruber et al. (2012) showed that the growth rate of the bulges and cusps due to the Darrieus-Landau instability is still significant. This means that the bulges and cusps may still form but at a slower rate without the effect of the turbulent-boundary

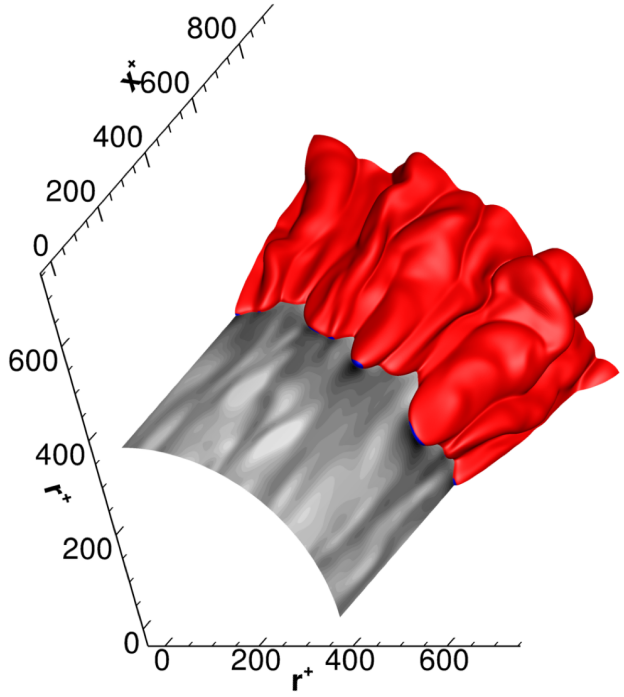

(a) Case A1: Axial-only flow.

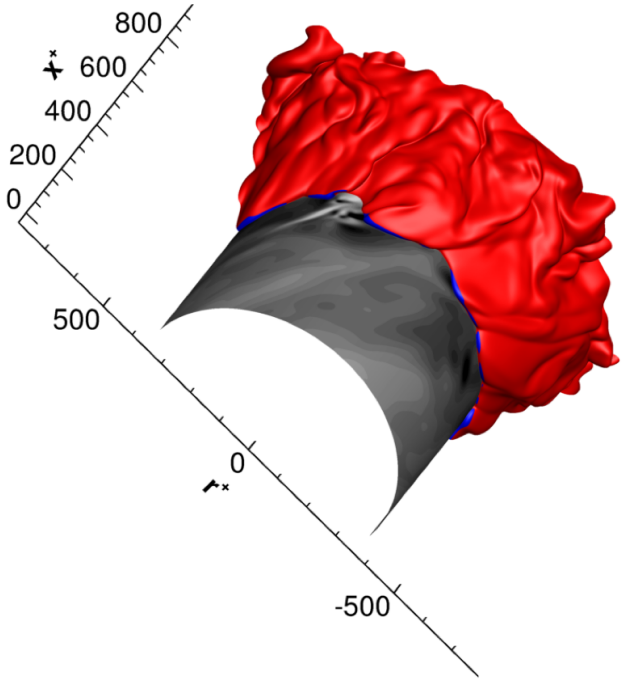

(b) Case A2: Swirling flow.

Figure 7.25: Flame shape ($c = 0.7$ isosurface) after around 50 wall time units for the axial-only and swirling flow, coloured red for positive x-direction velocity and blue for back-flow regions. The shading of the bottom wall shows non-dimensional wall shear stress, τ_w^+.

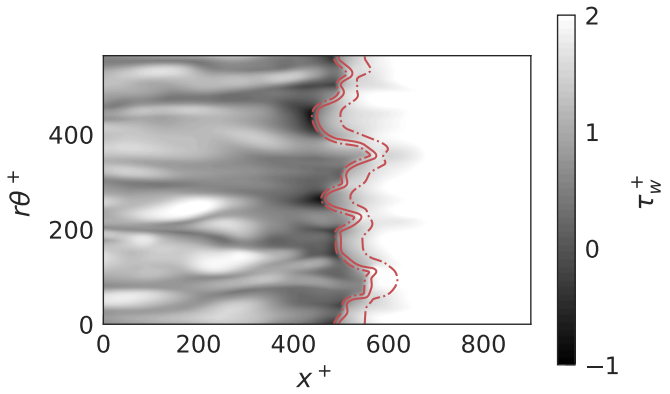

(a) Case A1: Axial-only flow.

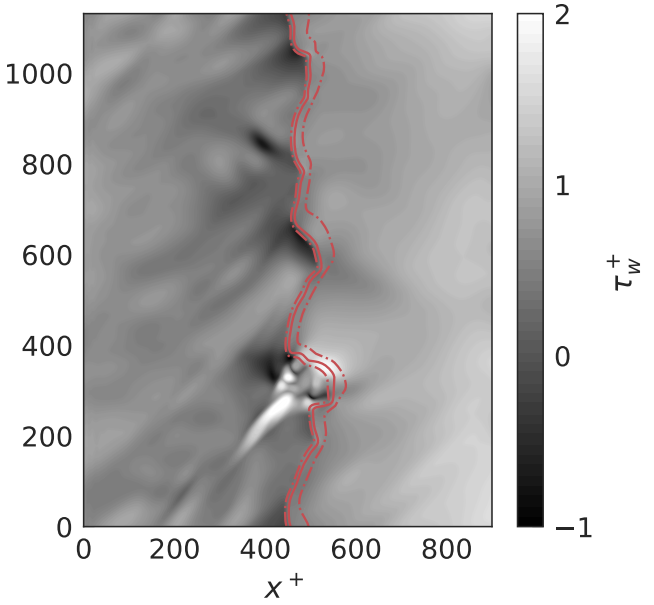

(b) Case A2: Swirling flow.

Figure 7.26: Flame shape after 0.5 ms for Cases A1 and A2 at $y^+ = 5$. The solid red line is at $c = 0.7$ while the dot-dashed red lines are at $c = 0.1$ and $c = 0.9$. The shading shows the non-dimensional wall shear stress, τ_w^+ on the bottom wall.

layer streaks. Figure 7.25b also shows significant flame wrinkling further from the inner wall. The presence of the radial pressure gradient from the swirling flow would be expected to reduce flame wrinkling through density stratification, as seen in Case P3 (axial flow with body force, Figure 6.2c). However the non-reacting swirling flow shows increased velocity fluctuations above around $y^+ = 40$ which are partly due to the Taylor-Görtler-like secondary flows generated by the curvature of the outer wall. This increase in turbulent fluctuations gives the increased flame wrinkling for the swirling flow. Figures 7.25b and 7.27b also show that there is a much greater region of reversed flow ahead of the swirling flame compared to the axial-only. The regions of reversed flow are still ahead of the flame leading points, not quite covering the entire flame front, but show a much greater extent axially and circumferentially. The smoother flame front and reduction in strength of the turbulent-boundary layer streaks will increase the extent of reverse flow circumferentially. The lower axial bulk velocity of the swirling flow (where the velocity magnitude is the same as the axial-only flow) will also increase

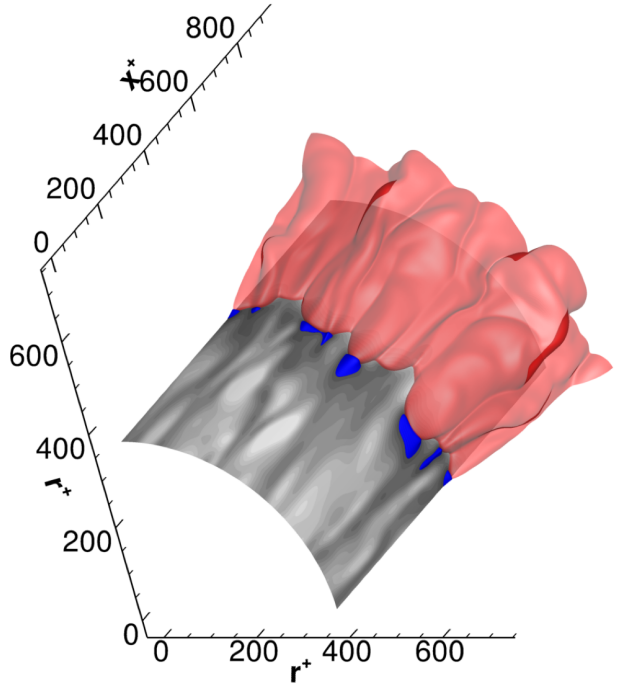

(a) Case A1: Axial-only flow.

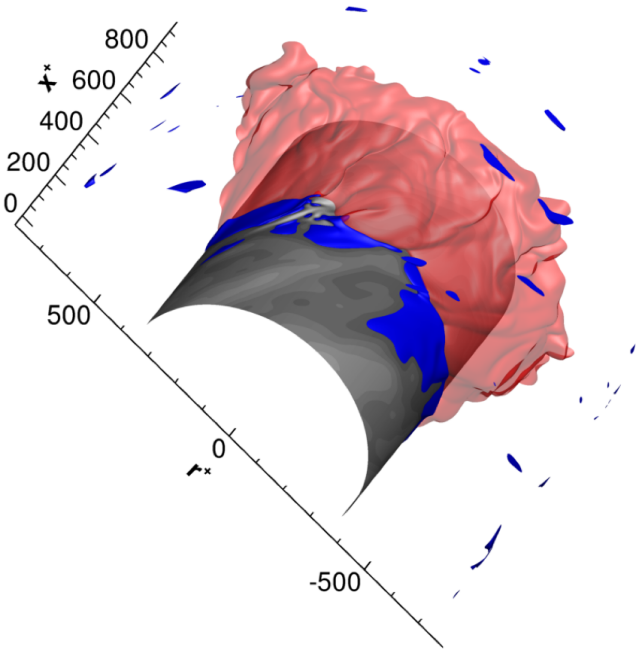

(b) Case A2: Swirling flow, axial-reversed flow only.

Figure 7.27: Flame shape ($c = 0.7$ isosurface, translucent) after around 50 wall time units for the axial-only and swirling flow, coloured red for positive x-direction velocity and blue for reverse-flow regions. Also shown in blue are isosurfaces of reverse flow in the lab frame-of-reference. For the swirling flow, (b) shows the reversed flow in the axial direction and (c) shows the reversed flow in the mean stream-wise direction. The shading of the bottom wall shows non-dimensional wall shear stress, τ_w^+.

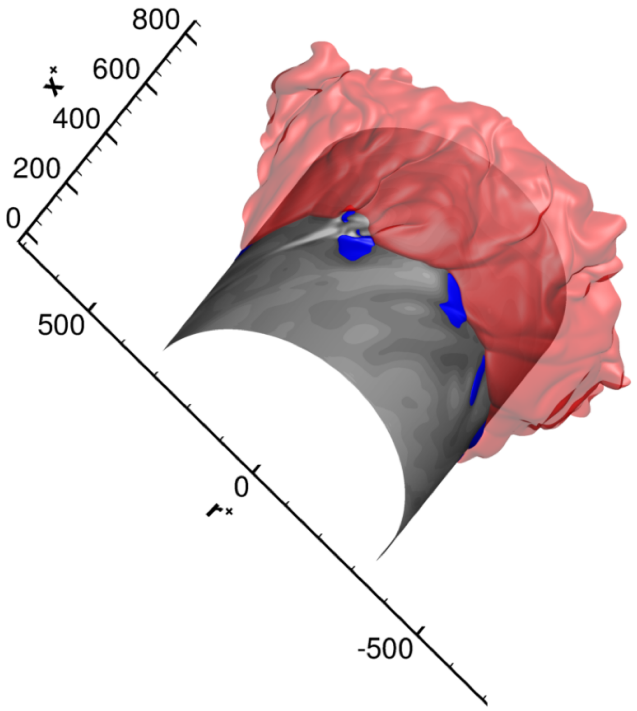

Figure 7.28: Flame shape ($c = 0.7$ isosurface, translucent) for Case A2: Swirling flow after around 50 wall time units for the axial-only and swirling flow, coloured red for positive stream-wise velocity and blue for stream-wise reverse-flow regions. Also shown in blue are isosurfaces of stream-wise reverse flow in the lab frame-of-reference. The shading of the bottom wall shows non-dimensional wall shear stress, τ_w^+.

the extent of reverse flow axially. This was seen in the planar cases where Case P2 (oblique flow, no body force, Figure 6.18b) had larger regions of reverse flow when compared to Case P1 (Figure 6.18a). The increased reverse flow will also result from the radial pressure gradient in the swirling flow increasing the pressure gradient against the oncoming flow and increasing reverse flow, as seen for Case P3 (Figure 6.18c). In this annular case the size of the reversed flow region is smaller when compared to Case P3 and there is no longer a recirculation region behind the flame front. This case has a swirl number of 2.2 which gives a larger Froude number when compared to the Case P3 (0.35 compared to 0.07). Figure 7.27b also shows that the region of reverse flow ahead of the flame is much smaller in r while being much larger in x and θ compared to Cases P2 and P3.

Figure 7.28 shows the same information as Figure 7.27b but based on the mean-streamwise rather than the axial velocity. This shows significantly smaller regions of reverse flow which are only present ahead of the leading points of the flame. This matches the result found for planar Case A2 (Figures 6.18b and 6.18d) which also showed significantly less reverse flow in the mean-streamwise direction; and the results of Heeger et al. (2010), and Ebi and Clemens (2016) where reverse flow was only found for the axial velocity.

Figure 7.29 shows the relative flashback speeds for the axial-only and swirling cases. The swirling flow shows a lower flashback speed (5.15 S_L) compared to the axial-only (7.05 S_L). The interpretation of the relative flashback speeds is complicated by the lower axial bulk velocity of the swirling case, which shows a higher lab-frame propagation speed, V_f. The flame propagates against the local oncoming flow to propagate upstream. Where the axial bulk velocity changes, the local flow,

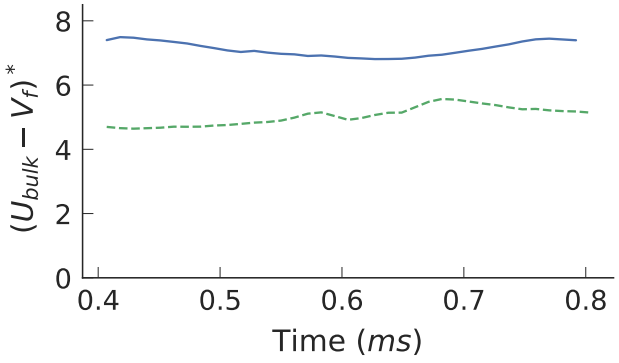

Figure 7.29: Temporal evolution of relative flashback speed $(U_{bulk} - V_f)^*$. Case A1 (axial-only) - solid blue; Case A2 (swirling) - green dashed.

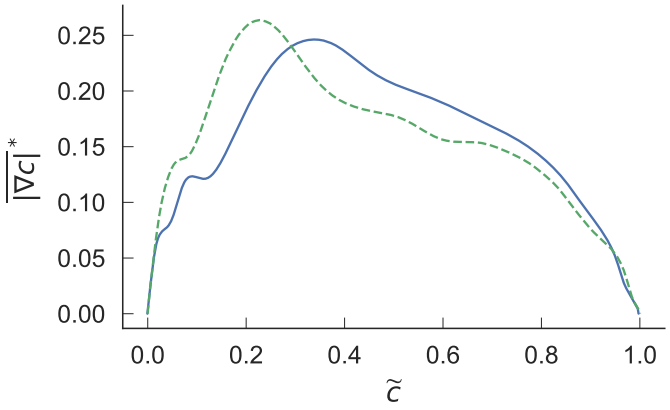

Figure 7.30: Time- and z-averaged flame surface density versus Favre-averaged progress variable at $y^+ = 5$. Case A1 (axial-only) - solid blue; Case A2 (swirling) - green dashed.

against which the flame is propagating, is likely to change by a different amount, with the slower flow near the wall. This complicates the flashback-speed comparisons between the two cases.

In Chapter 5 it was shown that the flashback speed is a linear function of the wall velocity gradient in two-dimensional laminar flashback, with the magnitude of the linear relation dependent on the relative boundary-layer thickness. The lower axial bulk velocity of the swirling case will therefore explain some of the difference in flashback speed. The flashback speed for Case A2 may also be lower because of the weaker pattern of bulges and cusps. The bulges will divert flow around the leading points of the flame, increasing the propagation speed of the flame relative to the oncoming flow. A weaker pattern of bulges and cusps will reduce this flow diversion and, therefore, flashback speed.

The axial-only flame shows a higher flashback speed than the planar Case A1 which had a flashback speed of 6.2 S_L (Figure 6.5). This increase in flashback speed will be affected by the reduced effect of confinement and increased flow diversion around the flame giving the larger region of reverse flow ahead of the flame. This swirling case does show a higher flashback speed than the oblique-flow planar Case A2 (4.9 S_L) which also had a smaller axial bulk velocity than the planar Case A1.

Figure 7.30 shows the flame surface density as a function of $\tilde{c}$ at $y^+ = 5$. The axial-only flow shows peak flame surface density at a larger $\tilde{c}$ than the swirling case with larger flame surface density at

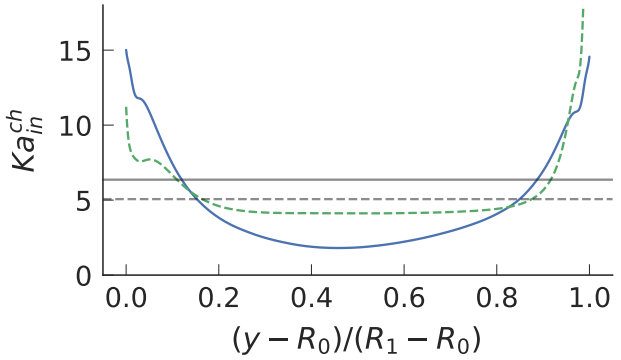

Figure 7.31: Nominal channel Ka across the annulus: axial-only - solid blue; swirling - green dashed.Case A1 - solid blue; Case A2 - green dashed; and inverse wall-scale Da: Case A1 - solid black; Case A2 - dashed black.

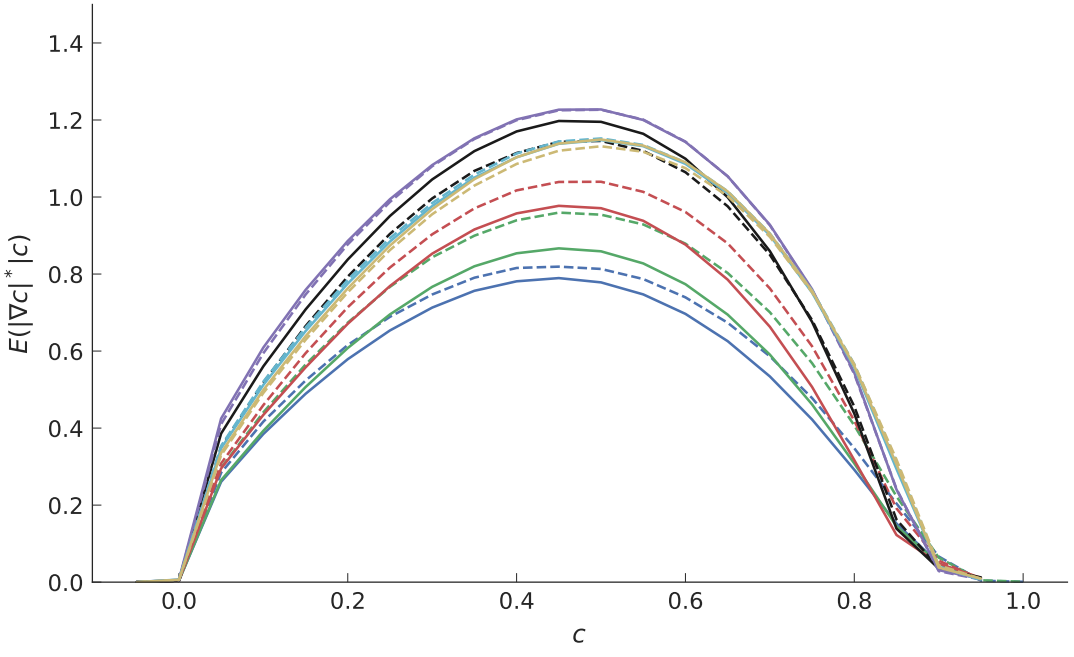

Figure 7.32: Surface density function, normalised by the laminar surface density function, conditioned on progress variable versus progress variable. Case A1 - solid; Case A2 - dashed. Blue - $y^+ = 1$; Green - $y^+ = 2.5$; Red - $y^+ = 5$; Black - $y^+ = 10$; Magenta - $y^+ = 20$; Cyan - $y^+ = 50$; Yellow - $y^+ = 100$.

low $\tilde{c}$ and higher at higher $\tilde{c}$. The swirling-flow profile is similar to that of Cases P1 and P2 (Figure 6.6). At the flame front, $\tilde{c} = 0.7$, both annular cases show similar values of flame surface density as well as similar peak values, although these peaks are at different $\tilde{c}$. Figure 7.26 also shows a larger pre-heat zone between $c = 0.1$ and $c = 0.7$ for the axial-only case compared to the swirling, also indicating a lower flame surface density at low c. The effect of turbulence on the flame is evaluated using Da and Ka. The two cases have similar wall-scale Da (0.16 and 0.20 for the axial-only and swirling), with the difference resulting from the different average Re_τ for the two non-reacting flows. A local Ka can be evaluated using Ka_{in}^{ch} (Gruber et al., 2018). Ka_{in}^{ch} uses the wall-normal variation in turbulent-kinetic-energy dissipation rate, ϵ:

$$Ka_{in}^{ch}(r) = \frac{\delta_L / S_L}{(\nu/\epsilon(r))^{1/2}} \tag{7.4}$$

Figure 7.31 shows the variation in Ka_{in}^{ch} with wall distance for the two cases. The swirling-flow case shows a smaller Ka_{in}^{ch} partly due to the lower nominal $Ka = 1/Da$ and also because of the lower turbulent-kinetic-energy dissipation rate of the swirling flow. It should be noted that in evaluating the effect of turbulence on the flame, this definition does not account for the effect of flame quenching by the wall. Figure 7.32 shows the surface density function conditioned on progress variable at different y^+ (the sharp change in distribution near $c = 0$ results from the bin size used). For $y^+ = 1$, 2.5 and 5 the swirling flow shows higher surface density function than Case A1. At $y^+ = 10$ this trend is reversed with the axial-only having higher surface density function. Above this point there is little difference between the two cases. For very small y^+, the flame will be thickened by heat loss to the wall and the thickening will not solely be due to turbulent thickening.

Figure 7.33 shows the probability density functions (pdfs) of curvature, tangential strain and displacement speed at the flame front at $y^+ = 5$ for the two annular cases. Case A2 shows a curvature distribution with smaller curvature than Case A1. Case A1 is similar to planar Case A1 (Figure 6.8) and Case A2 similar to Case P3. This lower curvature reflects the smoother flame front of Case A2, with reduced pattern of bulges and cusps at the leading points. The tangential strain pdfs for the annular cases are very similar to each other with only small differences; they are also similar to the planar results. Despite the change in pattern of the flame leading points, the tangential strain to which they are subjected is very similar. The displacement-speed pdfs show Case A2 to have a higher displacement speed with narrower distribution than Case A1. Case A2 matches the distribution shape of Case P3 but with higher average displacement speed. Case A1 shows a similar distribution to Case P1. The narrower distribution of displacement speed for Case A2 is the result of the reduced wrinkling at the flame leading edge. Figure 7.34 shows the global distributions of curvature, tangential strain and displacement speed. It shows very similar distributions for the two cases, with the swirling flow showing a slightly smaller average curvature and tangential strain, and slightly higher displacement speed.

Figure 7.35 shows the pdfs of curvature, tangential strain and displacement speed for each case conditioned on the leading and trailing sides of the flame front. Case A1 shows very little difference in the pdfs of curvature and tangential strain, with each flame lobe expected to be symmetrical and therefore show the same pdf. For displacement speed there are slight differences in the pdfs for the two sides, although these differences are not present when looking at the global pdfs (Figure 7.36). For Case A2, where the flame lobes are asymmetric in their propagation, the curvature and tangential strain pdfs are similar at $y^+ = 5$. For the global pdfs the trailing side does show a higher

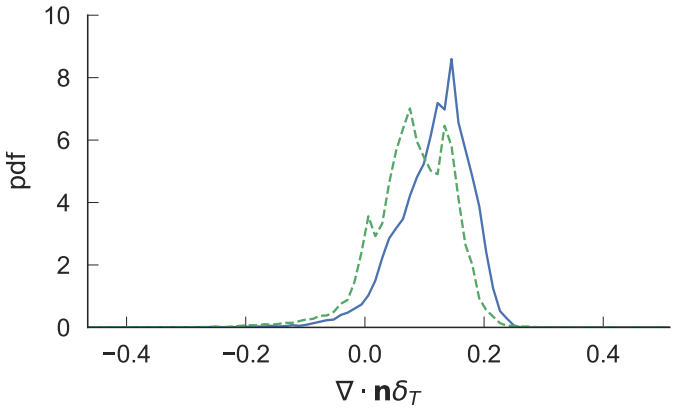

(a)

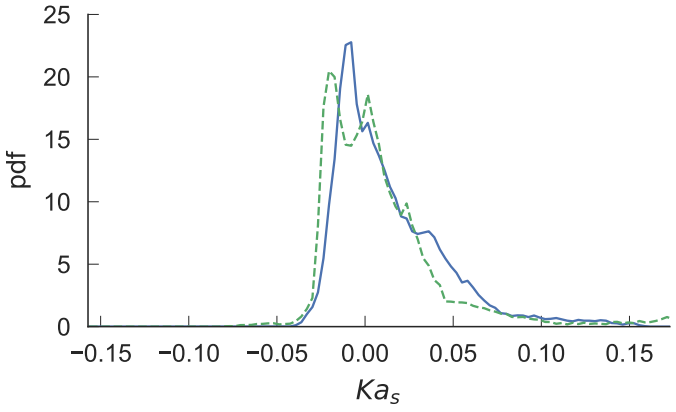

(b)

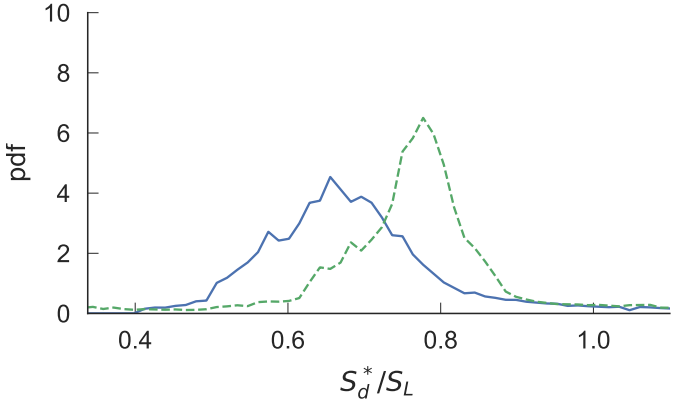

(c)

Figure 7.33: Probability density function (pdf) of normalised curvature ($\nabla \cdot \mathbf{n}\delta_T$), tangential strain ($Ka_s = a_T\delta_T/S_L$) and density-weighted displacement speed, S_d^*/S_L, at the flame front (c=0.7) on a plane $y^+ = 5$. Axial-only - solid blue; swirling - green dashed.

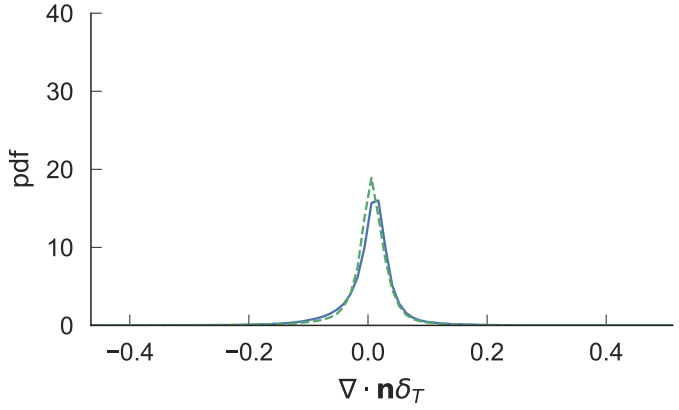

(a)

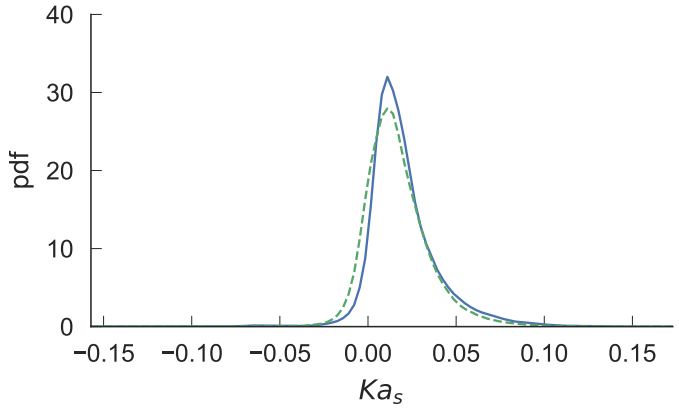

(b)

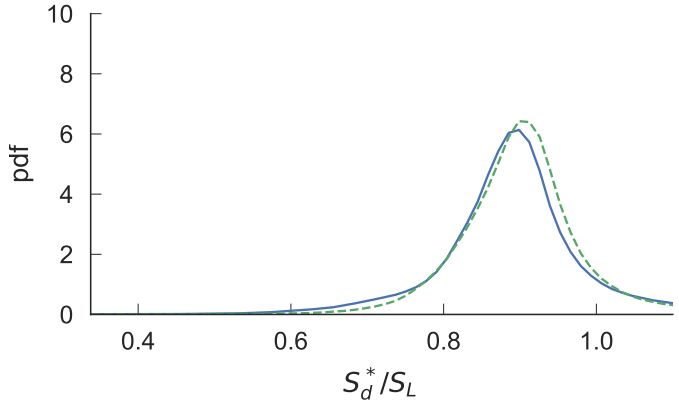

(c)

Figure 7.34: Probability density function (pdf) of normalised curvature ($Ka_s = \nabla \cdot \mathbf{n}\delta_T$), tangential strain ($a_T\delta_T/S_L$) and density-weighted displacement speed, S_d^*/S_L, at the flame front (c=0.7) across all y^+. Axial-only - solid blue; swirling - green dashed.

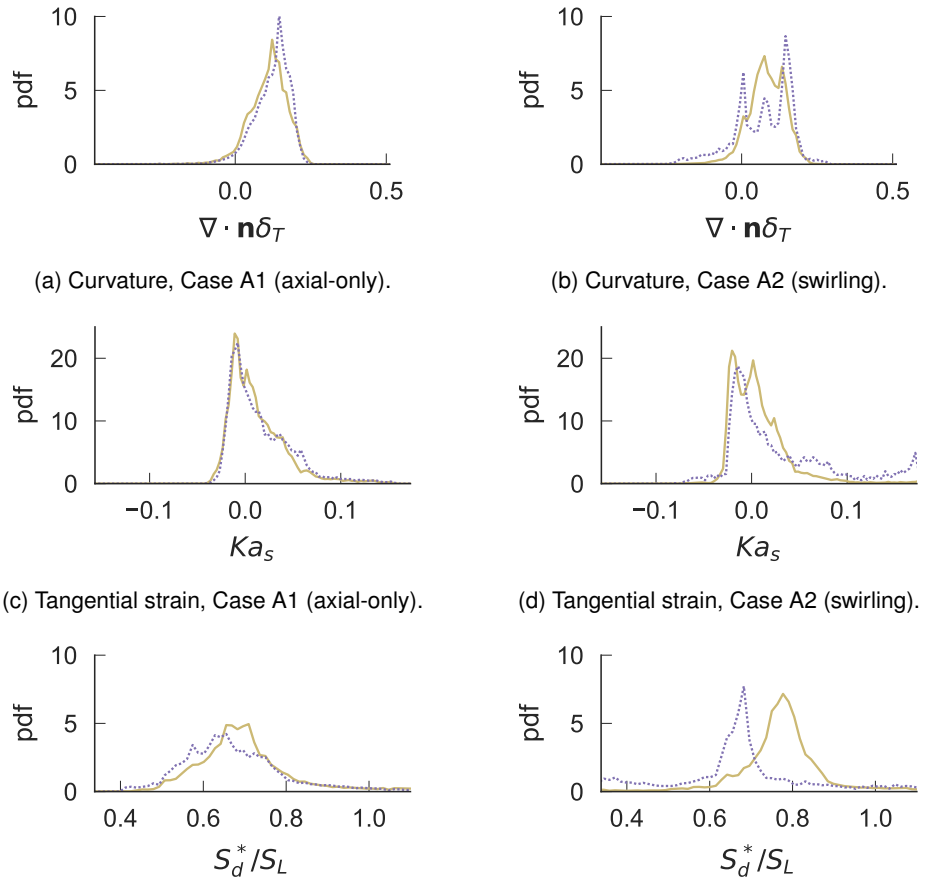

(a) Curvature, Case A1 (axial-only).

(b) Curvature, Case A2 (swirling).

(c) Tangential strain, Case A1 (axial-only).

(d) Tangential strain, Case A2 (swirling).

(e) Displacement speed, Case A1 (axial-only).

(f) Displacement speed, Case A2 (swirling).

Figure 7.35: Probability density function (pdf) of normalised curvature ($\nabla \cdot \mathbf{n}\delta_T$), tangential strain ($Ka_s = a_T\delta_T/S_L$) and density-weighted displacement speed, S_d^*/S_L, at the flame front (c=0.7) at $y^+ = 5$. The pdfs are conditioned on the flame normal to give the leading (solid yellow) and trailing sides (dotted magenta) of the lobes in Case A2. The rows of figures show Cases A1 (axial-only) and A2 (swirling), respectively.

tangential strain. At $y^+ = 5$ the leading sides of the flame show a much higher displacement speed than the trailing sides. The global pdf, however, shows little difference for displacement speed. The trend for Case A2 matches that of Case P2 (Figure 6.10) with little difference in the pdf of curvature, a higher tangential strain and very similar trend in the pdf of displacement speed with the leading sides having higher displacement speed than the trailing sides.

Figure 7.37 shows the time- and z-averaged consumption speed. Case A2 has a smaller peak consumption speed but shows the peak at a similar wall-normal position. Overall the average consumption speed is very similar for the two cases. This trend is very similar to that of the planar cases where Cases P2 and P3 (oblique and body-force) had smaller peaks but showed the same position of the peak. The reduced wrinkling of the swirling flame in the near-wall region would contribute to a reduction in the consumption speed, as found for Case P3. This trend in consumption speed is opposite to that of displacement speed where Case A2 shows a higher displacement speed compared Case A1.

Figure 7.38 shows the mean flame shape and stream surfaces for the two annular cases. The swirling flow shows a higher mean flame height and greater flow diversion around the flame. The

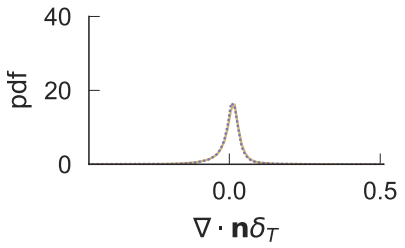

(a) Curvature, Case A1 (axial-only).

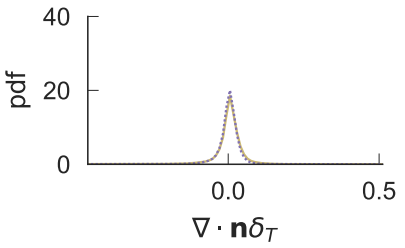

(b) Curvature, Case A2 (swirling).

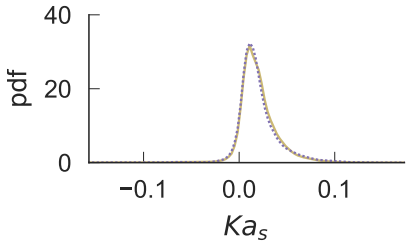

(c) Tangential strain, Case A1 (axial-only).

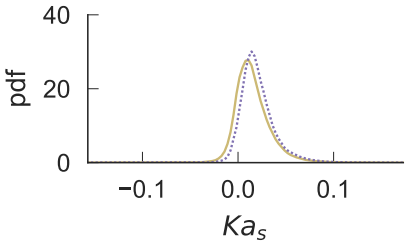

(d) Tangential strain, Case A2 (swirling).

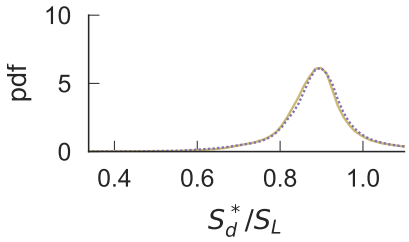

(e) Displacement speed, Case A1 (axial-only).

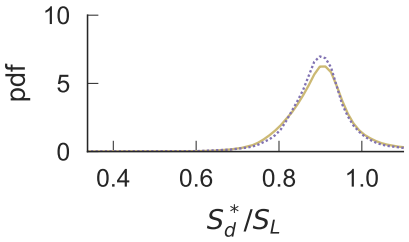

(f) Displacement speed, Case A2 (swirling).

Figure 7.36: Probability density function (pdf) of normalised curvature ($\nabla \cdot \mathbf{n}\delta_T$), tangential strain ($Ka_s = a_T\delta_T/S_L$) and density-weighted displacement speed, S_d^*/S_L, at the flame front (c=0.7) for all y^+. The pdfs are conditioned on the flame normal to give the leading (solid yellow) and trailing sides (dotted magenta) of the lobes in Case A2. The rows of figures show Cases A1 (axial-only) and A2 (swirling), respectively.

flow diversion will be increased by the radial pressure gradient giving an increased adverse pressure gradient. The Case P2 (Figure 6.16) also showed greater flow diversion although it did not have the increased flame height. The Case P3 showed significantly increased flow diversion and a recirculation zone. The flow diversion for Case A2 is not as significant due to the smaller relative body force and larger Fr.

Figure 7.39 shows the non-dimensional pressure and axial-pressure-gradient profile for the averaged pressure field at $y^+ = 5$. Both cases show the adverse pressure gradient ahead of the flame front. Behind the flame front the axial pressure gradient is larger for Case A2 as a result of the radial pressure gradient. The pressure gradient does not return to being positive behind the flame front as seen for Case P3 (Figure 6.17) but this is due to the lower relative strength of the body force here compared to Case P3.

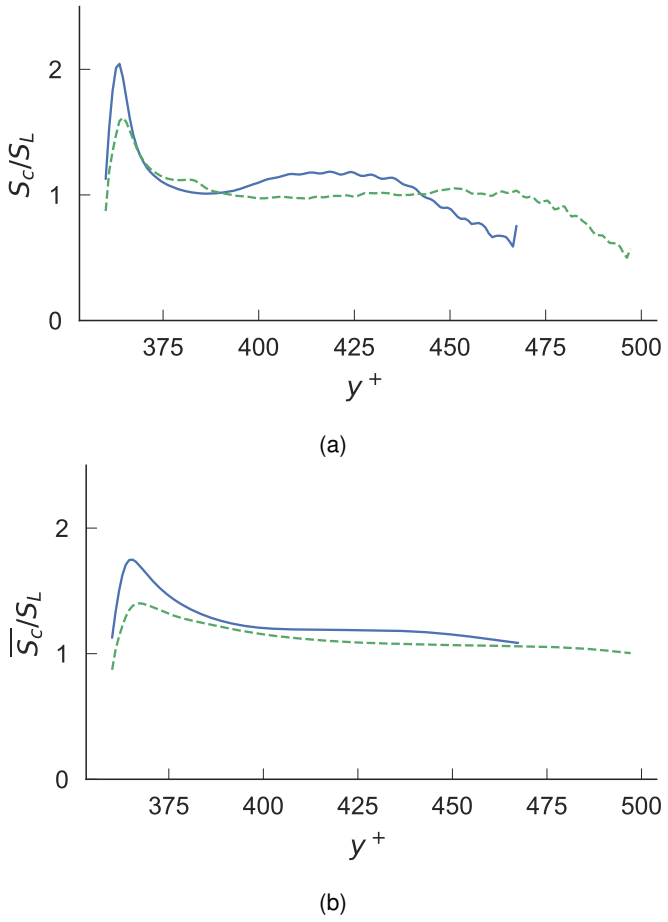

Figure 7.37: Consumption speed of time- and Favre-averaged reaction rate integrated in y-planes as a function of wall-normal distance (y^+). (a) shows the consumption speed as a function of y^+ while (b) shows the consumption speed averaged between each point and $y^+ = 0$. Axial-only - solid blue; swirling - green dashed.

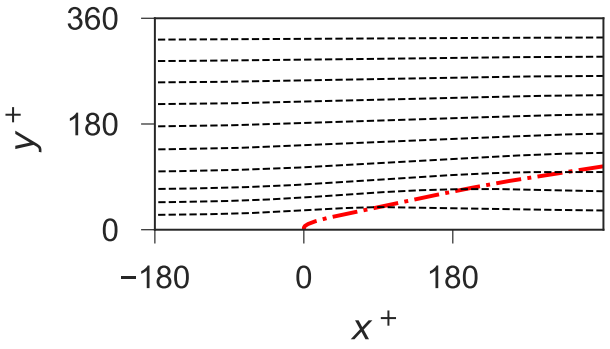

(a) Case A1: Axial-only flow.

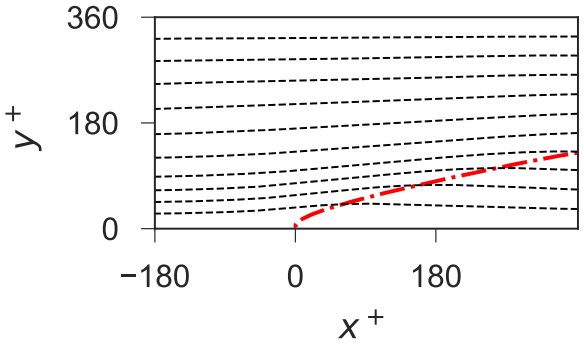

(b) Case A2: Swirling flow.

Figure 7.38: Mean stream surfaces (dashes) and flame position ($\tilde{c} = 0.7$, red dash-dot) in the frame of reference of the flame's leading edge for the time- and θ-averaged fields.

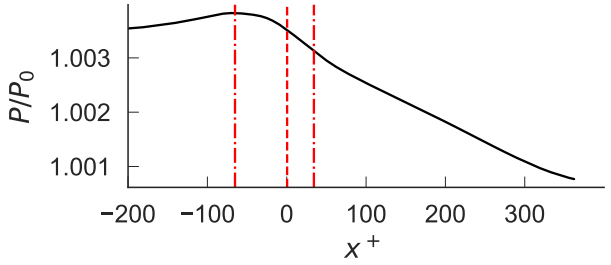

(a) Case A1: Axial-only flow.

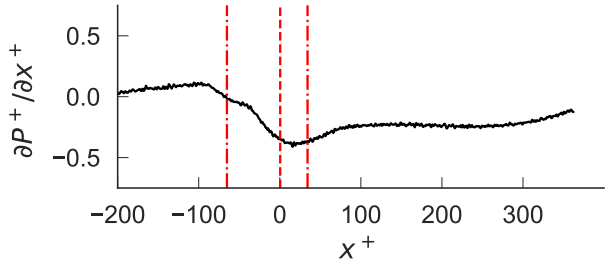

(b) Case A1: Axial-only flow.

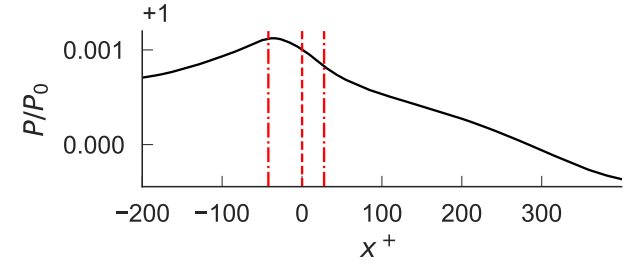

(c) Case A2: Swirling flow.

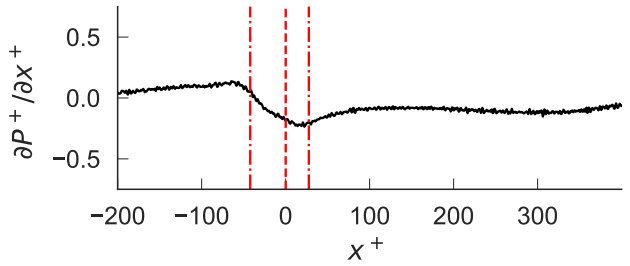

(d) Case A2: Swirling flow.

Figure 7.39: Non-dimensional pressure (P/P_0) and axial pressure gradient ($\partial P^+/\partial x^+ = \partial P/\partial x(\delta_\nu/\rho_u u_\tau^2)$) for the pressure field averaged in time and the homogeneous θ-direction at $y^+ = 5$. The axial distance is shown in the frame of reference of the leading point of the flame. The flame front ($c = 0.7$) is a dashed red line; the extent of the flame brush ($c = 0.1$, $c = 0.9$) are shown as dot-dashed red lines. The columns show Cases A1 (axial-only) and A2 (swirling), respectively.

7.3 Conclusions

In this Chapter the non-reacting flows within annuli with axial-only and swirling flows were studied. The axial-only flow showed an asymmetric velocity profile with higher wall shear stress on the inner wall, although the profile matched that of a planar channel flow when normalised by the local wall scales. In terms of fluctuation velocities and Reynolds stress the outer wall also remains very similar to a planar channel flow but on the inner wall the fluctuations and Reynolds stress decrease.

The swirling flow showed a more asymmetric velocity profile, for both u and w, but now showed a higher wall shear stress on the outer wall than the inner. The linear velocity relation $u^+ = y^+$ held below $y^+ = 10$ but above this the mean velocity diverged from planar channel flows with larger velocity on the inner wall than the outer. The swirling flow also showed decreasing turbulence on the inner wall, a reduction in the pattern of high- and low-velocity streaks, a general upward shift in Reynolds stress and increased v fluctuations in the centre of the channel caused by Taylor-Görtler vortices aligned helically with the mean flow direction. In general these trends align with the results from spanwise-rotating channel flows.

The non-reacting flows were then used as the turbulent feed data to study boundary-layer flashback and evaluate the effect of swirl on flashback. The flames were affected by the changes in the non-reacting flow: the swirling flow showed reduced growth of bulges and cusps in θ due to the reduced strength of the high- and low-velocity streaks in the non-reacting flow. The differences in turbulent fluctuations for the same inner-wall Re_τ affected the flame surface density profile through the flame. In general the body-force effect was not seen to the same extent as the planar body-force case (P3), with this annular case (A2) having a higher Fr.

Chapter 8

Evaluation of Momentum-Balance Models

In Chapter 4, a number of models were developed, with a momentum-balance approach used to derive a confined or unconfined planar model and an unconfined annular model. An additive model, consisting of a combination of flame-propagation and gravity-current effects was also shown. This chapter presents an assessment of these models against flashback in turbulent planar and annular channel flows. The DNS results of Chapters 6 and 7 will be used along with experimental data from swirling annular and non-swirling planar boundary-layer flashback to evaluate the momentum-balance models as well as comparing them to the boundary-layer flashback model of Hoferichter et al. (2016).

8.1 Predictions of Momentum-Balance Model

Figures 8.1, 8.2 and 8.3 show the model's predicted flashback speed as a function of the Froude number at different density ratios and levels of confinement, along with experimental results from swirling flows. For those experimental flows Fr was calculated using:

$$Fr = \frac{S_L}{\sqrt{\delta \frac{\overline{V_\theta}^2}{R_0} \frac{(\rho_u - \rho_b)}{\rho_u}}} \tag{8.1}$$

The solid black lines show the results of the planar unconfined model for a density ratio of 2.5 (matching the conditions of the turbulent DNS cases) and the dotted green line shows the results from the additive model (Figure 8.1). The results show a transition from high Fr where the body force has little influence and the original Ruetsch et al. (1995) model is recovered, to low Fr where the body force is dominant.

Figure 8.2 shows the predicted effect of density and confinement ratio. The dashed blue lines show the predicted flashback speed for different density ratios (1.5, 4.0 and 6.0). The effect of density and confinement ratio on flashback speed and height ratio, at high and low Fr, are also shown in Figure 8.4. The dotted black lines on each plot show the result from the Ruetsch et al. (1995)

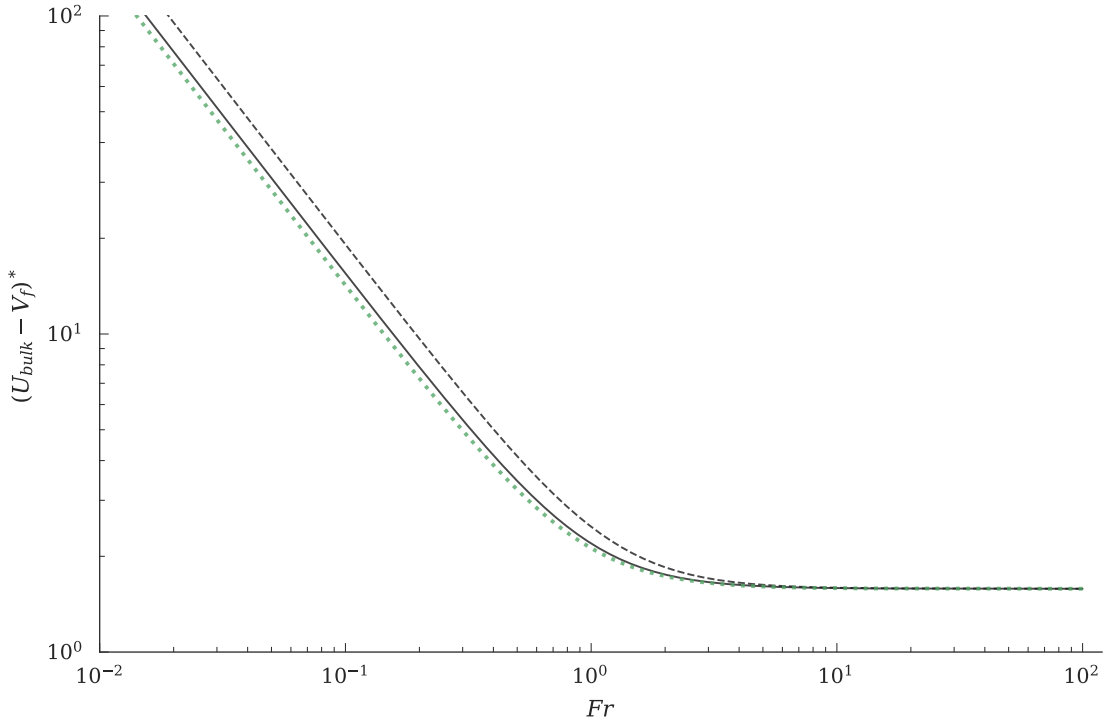

Figure 8.1: Relative flashback speed as a function of Froude number comparing the unconfined momentum-balance models: planar (solid black) and annular (dashed black) and the additive model, $(U_{bulk} - V_f)^* = \sqrt{D + 2/Fr^2}$ (dashed green). All of the models use a density ratio of 2.5, matching the conditions of the DNS results of Chapters 6 and 7.

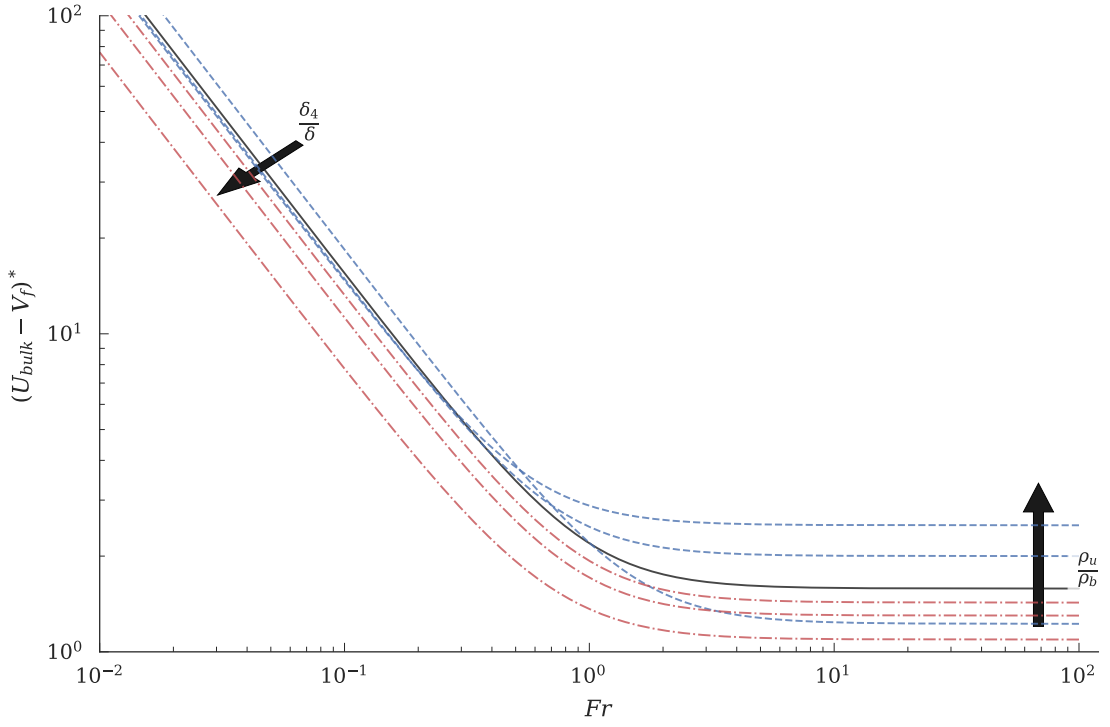

Figure 8.2: Relative flashback speed as a function of Fr for the planar model. Shown are the planar unconfined model for $D = 2.5$ (solid black), the planar unconfined model for density ratios of 1.5, 4.0 and 6.0 (dashed blue lines) and the planar confined model for confinement ratios (δ/δ_4) of 4, 2 and 1 (red dot-dashed).

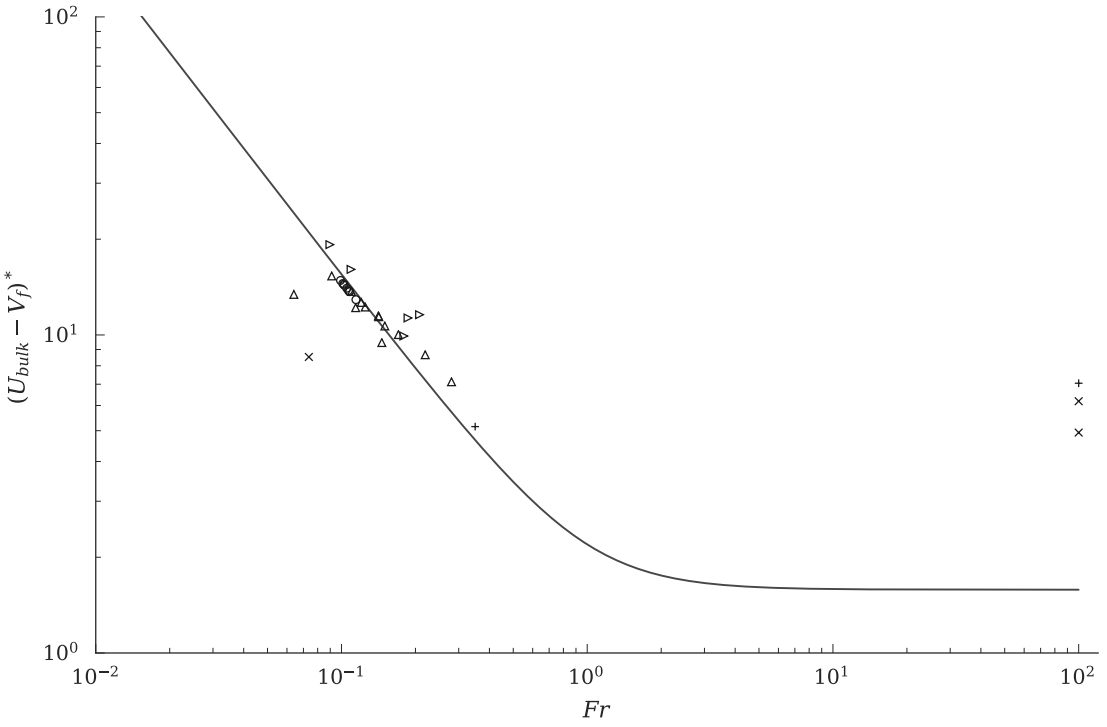

Figure 8.3: Relative flashback speed as a function of Fr, with the unconfined planar model for$D = 2.5$ (solid black), experimental data on swirling, turbulent boundary-layer flashback from Ebi and Clemens (2014, 2015, 2016); Ebi et al. (2018); Ranjan et al. (2019) (▷), Heeger et al. (2010) (◯), Nauert et al. (2007) (△). The $\times$ are the planar DNS cases from Chapter 6 and the $+$ the annular DNS cases from Chapter 7.

and gravity current models. For the unconfined model at high Fr the result of Ruetsch et al. (1995) is recovered and the flashback speed varies as $\sqrt{\rho_u/\rho_b}$. This is the predicted propagation speed increase resulting from flow diversion around the leading point of the flame. At low Fr, with increasing density ratio the predicted flashback-speed ratio drops sharply from around 250 at a density ratio of 1.5 to around 175 at density ratio 2. The predicted flashback-speed ratio then gradually reduces, approaching the gravity-current result ($\sqrt{2}/Fr$) as density ratio increases. The buoyancy velocity is $\sqrt{g(1-1/D)}$ such that this term tends to zero as the density ratio approaches one, giving a prediction for flashback speed which increases very sharply as density ratio decreases.

The red dot-dashed lines in Figure 8.2 show the effect of confinement, for confinement ratios 4 and 2 (the solid black line shows no confinement), showing confinement to have a consistent effect across the range of Fr. Figure 8.4 also shows the effect of confinement, showing that the effect of confinement becomes greater as density ratio increases, and the volumetric expansion through the flame, which the upper wall of the channel constrains, also increases. For a density ratio of 1.5 at both high and low Fr confinement is shown to have little impact on the predicted flashback-speed ratio. In terms of the height ratio, representing flow diversion around the flame, confinement is predicted to have a small impact on δ_1', as the volumetric expansion is constrained. Density ratio was predicted by Ruetsch et al. (1995) to vary with ρ_b/ρ_u, a result which is recovered here, and the density ratio is shown to have a significant impact on height ratio. At high Fr, where the buoyancy velocity is zero, a propagating flame must have oncoming flow passing through the flame front so the height ratio must always be greater than zero. At low Fr, where the buoyancy velocity is greater than zero, it is now possible for the flame to propagate purely as a gravity current, with minimal effect

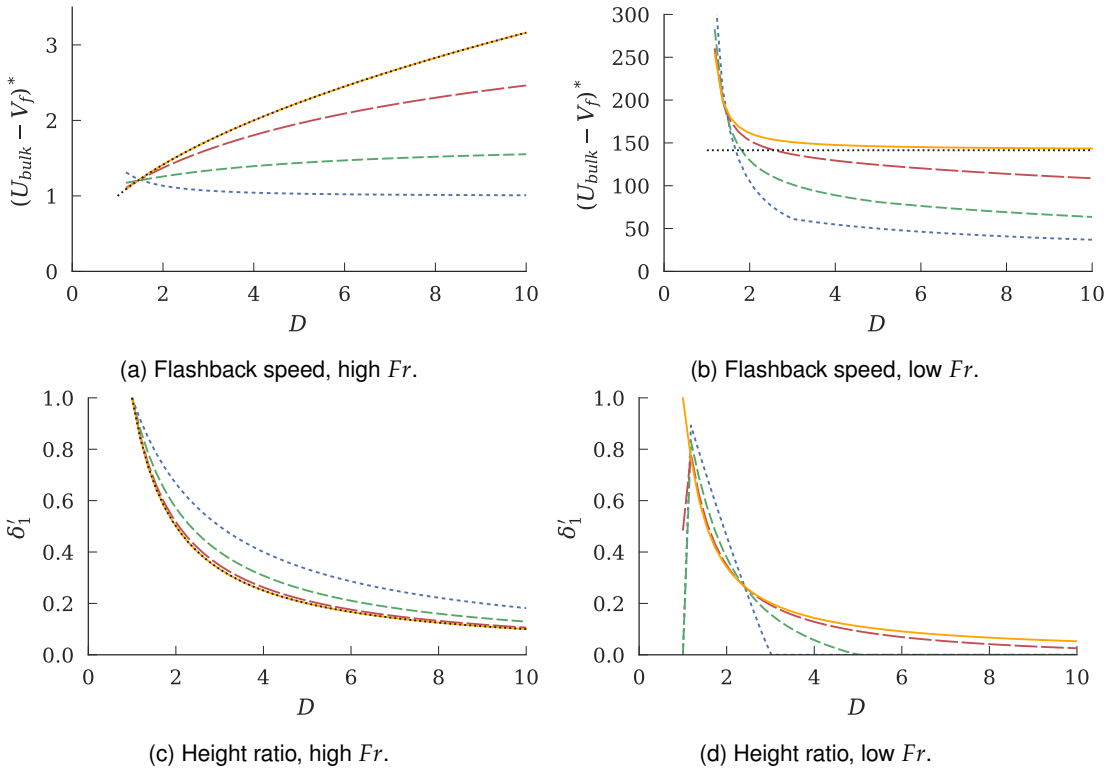

(a) Flashback speed, high Fr.

(b) Flashback speed, low Fr.

(c) Height ratio, high Fr.

(d) Height ratio, low Fr.

Figure 8.4: The effect of density ratio, D, on the predicted height ratio, δ_1', and flashback speed, $(U_{bulk} - V_f)^*$, at different confinement ratios (δ/δ_4). The results are shown for high ($Fr = 100$) and low ($Fr = 0.01$) Froude number, at confinement ratios of 1 (blue), 2 (green) and 8 (red) (where increasing dash length shows increasing confinement ratio) and for the unconfined model (solid orange). The black dotted line for high Fr shows the result of Ruetsch et al. (1995) and for low Fr shows the flashback speed of $\sqrt{2}/Fr$.

of flame propagation. At this point there is minimal oncoming flow passing through the flame front and the height ratio becomes zero. Figure 8.4d shows that as confinement increases, the volumetric expansion caused by flame propagation is limited and the height ratio becomes zero for sufficiently large confinement. This trend breaks down for $D = 1$ but this is likely to be to numerical issues as the flashback speed tends towards infinity.

A comparison will now be made between the momentum-balance model predictions, the experimental data and the predictions of the existing boundary-layer flashback models. The aim is to evaluate the predictions of each model and understand which effects are important to represent. The momentum-balance model includes the effect of flame propagation, flow diversion, wall-normal pressure gradient and confinement. However, as described in Chapter 5, there are also effects from the wall velocity gradient and boundary-layer profile. The model also only represents wall-normal flow diversion where, for a three-dimensional flow, flow diversion will also occur in the span-wise direction. Flow diversion will also be impacted by the flame topology, whether the flame propagates as a tongue or an edge, with a series of bulges and cusps. As these experimental data were measured for turbulent flow, there is also the effect of turbulence on flame propagation.

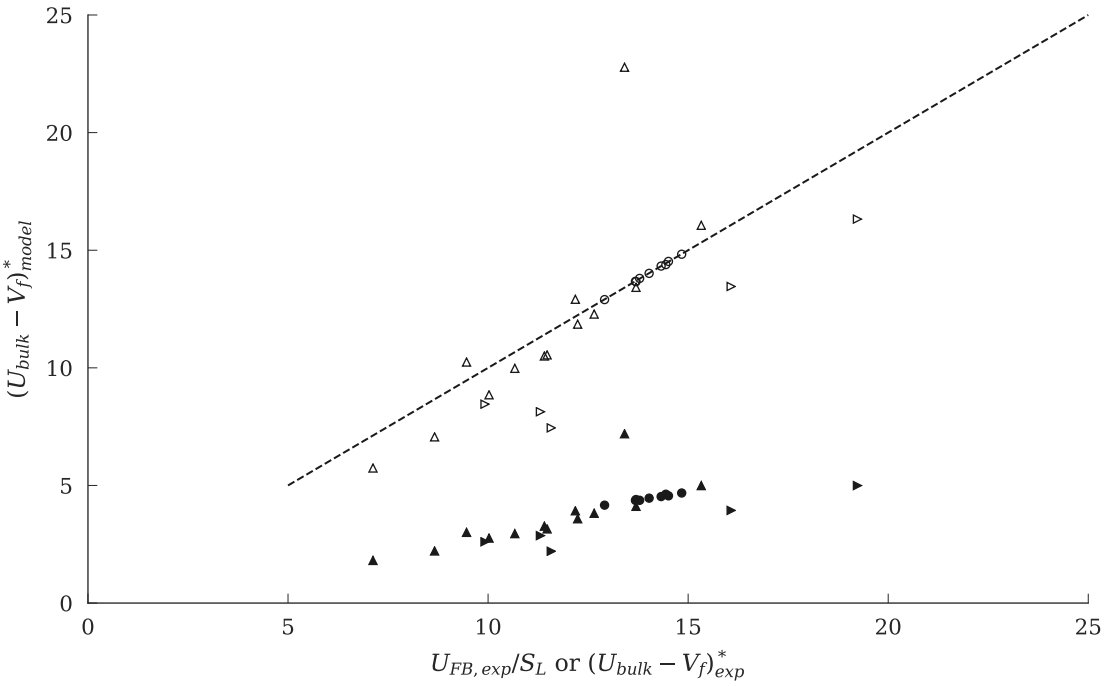

Figure 8.5: Plot of model-predicted flashback-speed ratio against experimental flashback-limit or flashback-speed ratios for swirling flows (▷ Ebi and Clemens (2014, 2015, 2016); Ebi et al. (2018); Ranjan et al. (2019), ◯ Heeger et al. (2010), △ Nauert et al. (2007)). Open symbols are for the unconfined model and the closed symbols are for a confinement ratio of 2. The dashed line shows $y = x$.

8.2 Swirling Flow

Figures 8.3 and 8.5 show a comparison between the predicted flashback-speed ratio and experimental results for swirling flow. Figure 8.5 shows the predicted flashback-speed ratio on the y-axis against the experimental flashback-limit or flashback-speed ratio, normalised by S_L. The open symbols show predictions for an unconfined flame while the closed symbols are at a confinement ratio of 2. The dashed black line is at $y = x$.

These results show very good prediction of the experimental results using the unconfined model. Each set of results follows the scaling predicted by the model: the flashback limits determined by Heeger et al. (2010) agree particularly closely with the unconfined model and the results of Nauert et al. (2007) show slightly greater scatter around the predictions of the model but, with one exception which has a particularly high flashback speed, the data still follow the predicted trend. The results of Ebi and Clemens (2014, 2015, 2016); Ebi et al. (2018); Ranjan et al. (2019) are all offset from the model predictions, showing flashback speeds larger than those predicted by the model, but still show a trend of increasing model prediction, with the increase in measured flashback speed.

The results using the confined model consistently under-predict the flashback-speed ratio. This could be due to a reduced importance of confinement, which could be because of the three-dimensional flow-diversion or because the flames in these experiments propagated as a tongue rather than edge and so the effect of confinement is reduced. The difference with the confined model could also be because of the effect of the bulk velocity, which is not accounted for in the momentum-balance model. In Chapter 5, it was shown how increasing bulk velocity increases flashback speed. If the

confined results were adjusted by accounting for the bulk velocity then it may be that they predict the experimental results more closely. The key point here is that, for these low Fr results, the flashback speed follows the trend of $1/Fr$ predicted by the momentum-balance and additive models.

The planar turbulent DNS with wall-normal pressure gradient (Case P3) shows significantly smaller flashback speed than that predicted by the model. There could be a number of reasons for this. The first is the smaller channel in the DNS compared to the experiments, increasing confinement and reducing flashback speed. The second reason is the small Re, being only just turbulent, and potentially reducing the effect of turbulence on flame speed for the DNS. The final effect is the short domain in the DNS which could constrain the recirculation bubble and therefore reduce the flashback speed.

The annular swirling turbulent DNS (Case A2) is a larger Fr (lower swirl) but shows a flashback speed much closer to the model. For this case, the channel size is the same but the recirculation bubble is much smaller, negating the effect of the small domain. The channel height and Re_τ remain the same as Case P3, however. These cases do have different axial bulk velocities, making comparisons of their flashback speeds more difficult.

A difficulty arises in the comparison of flashback speeds for different bulk velocities or velocity profiles. The local flow velocity, against which the flame is propagating, will differ to varying extents from the bulk velocity. For a flat velocity profile the local and bulk velocities may be similar, while for a parabolic velocity profile or for a large channel, there may be a much greater difference. Using the approach of measuring flashback speed maintains the fuel properties and turbulence level. However, the oncoming axial velocity depends on the level of swirl in the annular cases or the flow angle in the planar cases. This contrasts with experimental data where flashback limits are measured, commonly defined using either bulk velocity or equivalence ratio, for example for different swirl numbers. This means there will be some effect from the change in bulk velocity or equivalence ratio, as well as the effect of changing swirl. To evaluate flashback limits from the DNS data requires extrapolation for the effects of bulk velocity, equivalence ratio or swirl number to find the point where $V_f = 0$.

8.3 Non-Swirling Flow

Figure 8.6 shows a comparison between the predicted flashback speed and experimental results for non-swirling flow. Figure 8.6 shows that at high Fr there is significant variation in flashback speed, with the measured flashback limits being significantly larger than the model predictions, when normalised by S_L. For the non-swirling data the flashback-speed prediction is simply the result from Ruetsch et al. (1995) where $u_1/u_2 = \sqrt{\rho_u/\rho_b}$, which does not capture the variation in flashback speed.

Comparing the confined results of Hoferichter et al. (2016) and the turbulent DNS results of Chapters 6 and 7, the DNS show a smaller flashback speed than the experimental results. However, the DNS results are for a smaller channel height than the results used by Hoferichter et al. (2016). The channel height for the DNS was 11 δ_L while it varied between 11 and 51 δ_L for the experimental results. This means that the experimental results will have a reduced effect of confinement and also means that the Reynolds numbers for the experimental results are higher, giving a larger effect of

turbulence. Both of these would help explain the lower flashback speeds found for the DNS results compared to the experiments.

As mentioned earlier, there are a number of effects present in the turbulent experimental data which are not accounted for by the model. One of these is the effect of turbulence. The model of Hoferichter et al. (2016) was shown to give good predictions for non-swirling data, where a boundary-layer separation criterion was used with existing turbulent-flame-speed models to evaluate flashback limits. Using the predicted turbulent flame speed, Figure 8.6b shows the predicted flashback-speed ratio against the experimental flashback-speed or flashback-limit ratio but where the experimental data is now normalised by the turbulent flame speed calculated in the model of Hoferichter et al. (2016). This shows that, while the experimental values are still higher than those predicted by the model, they are now significantly more similar. The unconfined model captures some of the variation in the experimental results. There is a large variation in the flashback speeds for the experimental confined results. These results were obtained across three different pre-heat temperatures (293, 473, 673 K) and equivalence ratio (0.3 to 1). This gives a wide variation in laminar flame properties (laminar flame speed, flame thickness, density ratio, Lewis number) and results in wide variation in measured flashback limits (5 to 90 m/s). There remain a number of phenomena here which are not included in the model: the effect of bulk velocity, velocity-profile shape, three-dimensional flow diversion and Le. Each of these is likely to give an increased flashback speed.

This does show that turbulence plays a significant role in determining the flashback speed and, at least part of, this effect can be captured by the model of Hoferichter et al. (2016). The momentum-balance models developed contain a displacement speed of the flame leading point, which in Chapter 5 was taken to be the laminar flame speed. However, this displacement speed could equally be taken to be a turbulent flame speed, incorporating the models for turbulent flame speed used by Hoferichter et al. (2016).

The DNS results at high Fr (Cases P1, P2, A1) are intermediate in flashback speed between the model and the experimental data. The effects present in the experimental data not captured by the model (turbulence, flow diversion, wall velocity gradient and boundary-layer profile) also apply to the DNS data, helping to explain the difference between the DNS data and the momentum-balance model.

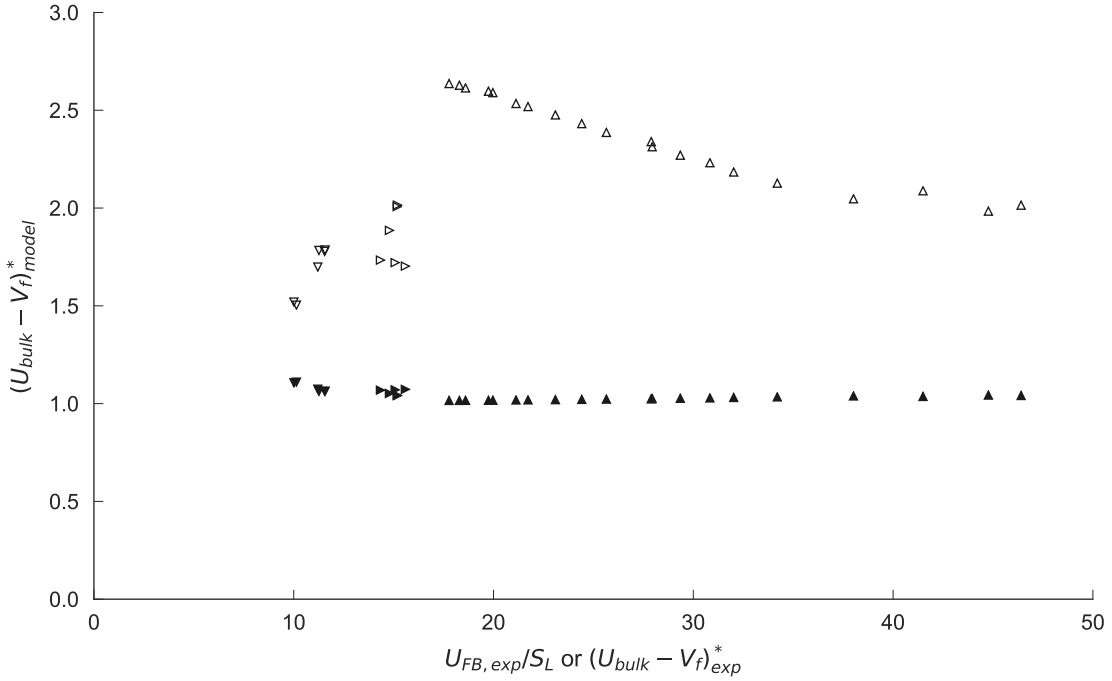

(a) Normalised by S_L.

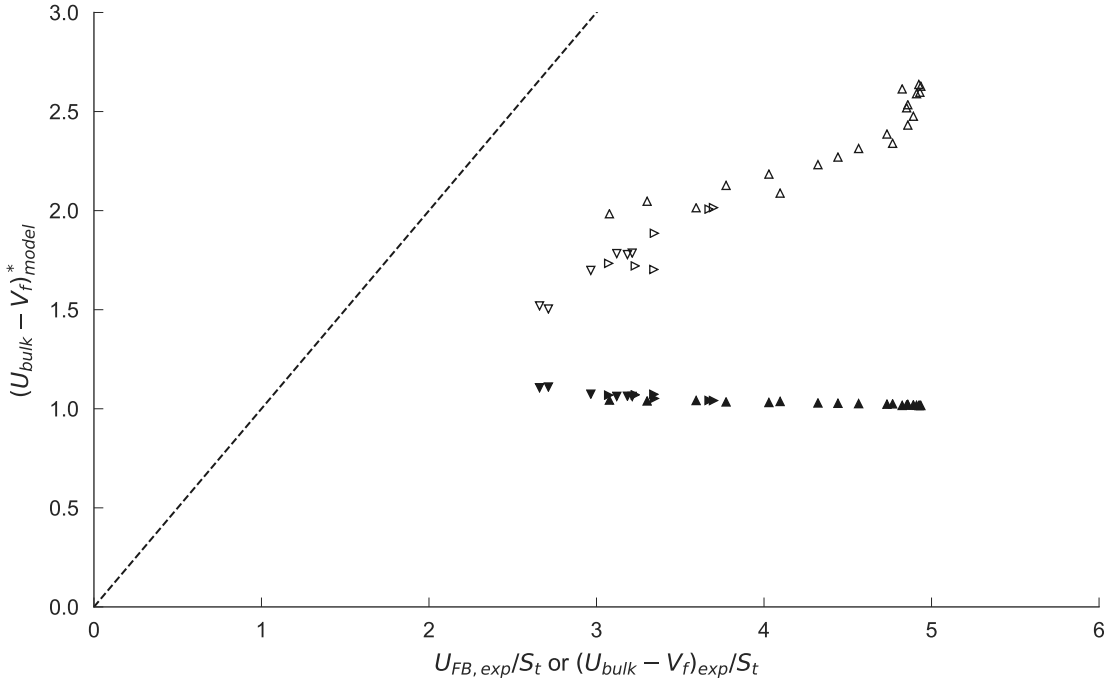

(b) Normalised by S_t.

Figure 8.6: Plot of model-predicted flashback-speed ratio against experimental flashback-limit ratios (Hoferichter et al., 2016) for non-swirling flows for pre-heat temperatures 293 K (△), 473 K (▷) and 673 K (▽). Open symbols are for the unconfined model and the closed symbols are for a confinement ratio of 2.

8.4 Comparison to existing boundary-layer flashback models

The model of Hoferichter et al. (2016) uses a boundary-layer-separation approach to predict the speed at which the pressure rise upstream of the flame front will cause boundary-layer separation, which was linked to the onset of flashback. The authors showed that this gave good predictions across a range of equivalence ratio and unburned-gas temperatures in a confined configuration. The model gave a predicted flashback-speed ratio as:

$$\frac{U_{FB}}{S_t} = \sqrt{\frac{\rho_u}{\rho_b} - 1} \tag{8.2}$$

where U_{FB} is the predicted flashback limit and S_t is the turbulent flame speed. This means that the predicted flashback speed varies with $\sqrt{\rho_u/\rho_b - 1}$ compared to $\sqrt{\rho_u/\rho_b}$ for the unconfined model presented here. The empirical correlations found by Kalantari et al. (2017), for unconfined boundary-layer flashback, gave a relationship of $U_{FB}/S_L \sim (T_b/T_u)^{0.25} \sim (\rho_u/\rho_b)^{0.25}$ for the effect of density ratio on flashback limits. The presence of density ratio in each of these models shows the importance of flow diversion in evaluating flashback speeds or limits. Even for the unconfined configuration, where flow diversion is less significant and the effect of density ratio smaller, density ratio remains a factor in predicting flashback speed. Figure 8.7 shows how the flashback limit relative to S_t varies with density ratio for the data used by Hoferichter et al. (2016). It shows that density ratio is strongly correlated with U_{FB}/S_t up to a density ratio of around 6.

The other difference between the models is in the flame-front displacement speed. In the modelling in Chapter 4 the laminar flame speed is used as the flame-front displacement speed whereas Hoferichter et al. (2016) used a model for a turbulent flame speed. The use of this model gives an additional connection between the oncoming flow and the flame because as the predicted flashback speed increases, the velocity fluctuations of the turbulent channel flow also increase. This in turn increases the predicted flame-front displacement speed. However, the model of Hoferichter et al. (2016) predicts a pressure rise upstream of the flame front which is used in predicting boundary-layer separation. Recent investigations (Endres and Sattelmayer, 2019) have suggested that the predicted pressure rise does not match that found in numerical simulations which reproduced the experimental flashback limits. However, the modelling using S_t clearly captures a number of the important effects influencing flashback speed and gives good predictions of flashback speed across a range of equivalence ratio and pre-heat temperatures.

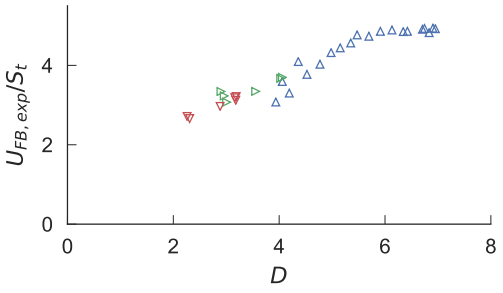

Figure 8.7: Effect of density ratio on flashback speed normalised by S_t. Experimental flashback-limit ratios (Hoferichter et al., 2016) for non-swirling flows for pre-heat temperatures 293 K (△), 473 K (▷) and 673 K (▽), normalised by predicted turbulent flame speed, S_t.

8.5 Conclusions

In this chapter the momentum-balance models of Chapter 4 have been evaluated using experimental data for turbulent swirling and non-swirling flows, and compared to the model of Hoferichter et al. (2016). The momentum-balance model derived in this thesis shows very good predictions for flashback speed at low Fr. The experimental data are clustered around the flashback-speed predictions, and for each set of experimental data, for different conditions, the measured flashback speeds follow the trend predicted by the model. This suggests that the derived analytical model describes the physical processes which are occurring during boundary-layer flashback in swirling flows.

At high Fr, the set of turbulent experimental data were produced over a range of conditions (varying pre-heat temperature and equivalence ratio) and subsequently show a large variation in flashback speed normalised by the laminar flame speed. This range of flashback speeds are also significantly higher than those predicted by the momentum-balance models. The model of Hoferichter et al. (2016), which showed good predictions for non-swirling flows, was used to normalise the flashback speeds by the predicted turbulent flame speed. Using this normalisation, the predictions of the momentum-balance models and the experimental data become much more similar and the momentum-balance model captures some of the remaining variation in flashback speed. Hoferichter et al. (2016) predicted a variation of $U_{FB}/S_t \sim \sqrt{\rho_u/\rho_b - 1}$ whereas the momentum-balance model predicts $(U_{bulk} - V_f)/S_t \sim \sqrt{\rho_u/\rho_b}$, so the two models predict very similar trends with density ratio at high Fr. Given that the flow is turbulent, it is appropriate to include a model for the effect of turbulence on the speed of the flame leading point in the momentum-balance models.

Even with the effect of turbulence accounted for, there is still a difference between the predicted and measured flashback speeds. The momentum-balance model does not account for the effect of the boundary-layer velocity gradient, which was shown in Chapter 5 to increase flashback speed, and so the model could also be enhanced by accounting for the effect of the boundary-layer velocity gradient.

The effect of confinement still remains unclear: in the momentum-balance model confinement reduces the predicted flashback speed, but in this chapter that was shown to reduce the quality of the predictions made. This could suggest that the effect of confinement is much smaller than predicted, for example: flow diversion occurs in both the wall-normal and span-wise directions in a three-dimensional flow, rather than in just the wall-normal direction included in the model, which may reduce the effect of confinement. The effect may also be reduced because of the flame topology: for the swirling flow, the flame propagates as a tongue rather than an edge with bulges and cusps.

Chapter 9

Summary, Conclusions and Future Work

9.1 Summary

This thesis presents an investigation of the boundary-layer flashback of hydrogen and hydrogen-rich fuels as relevant to the swirling flows of industrial gas turbines. This work evaluates the additional effects on boundary-layer flashback from a swirling annular flow compared to a non-swirling planar flow. Figure 9.1 illustrates all of the effects influencing boundary-layer flashback in different configurations: two-dimensional and three-dimensional laminar flow, turbulent, annular and swirling annular flow, for unconfined and confined boundary layers. Based on these effects, a number of research questions were posed:

- As relevant to the use of hydrogen and hydrogen-rich fuels within industrial gas turbines:
  - what is the physical mechanism for boundary-layer flashback within swirling flows?
  - how does a wall-normal pressure gradient affect flashback speed?
  - how does an oblique flow orientation affect flashback?
  - how does the annular geometry affect flashback in non-swirling and swirling flows?
  - how does a developing boundary layer affect flashback speeds?

In this work analytical models were derived describing the effect of a radial or wall-normal pressure gradient, thermal expansion and confinement on flashback speeds in planar channels and annuli. An additive model was developed which predicts flashback speeds as a combination of flame-propagation, enhanced by volumetric expansion, and pressure-driven or buoyancy terms. These models build on the models of Ruetsch et al. (1995) and those of gravity currents (Benjamin, 1968), to describe a physical mechanism for boundary-layer flashback within swirling flows and predict how a wall-normal pressure gradient affects flashback speed.

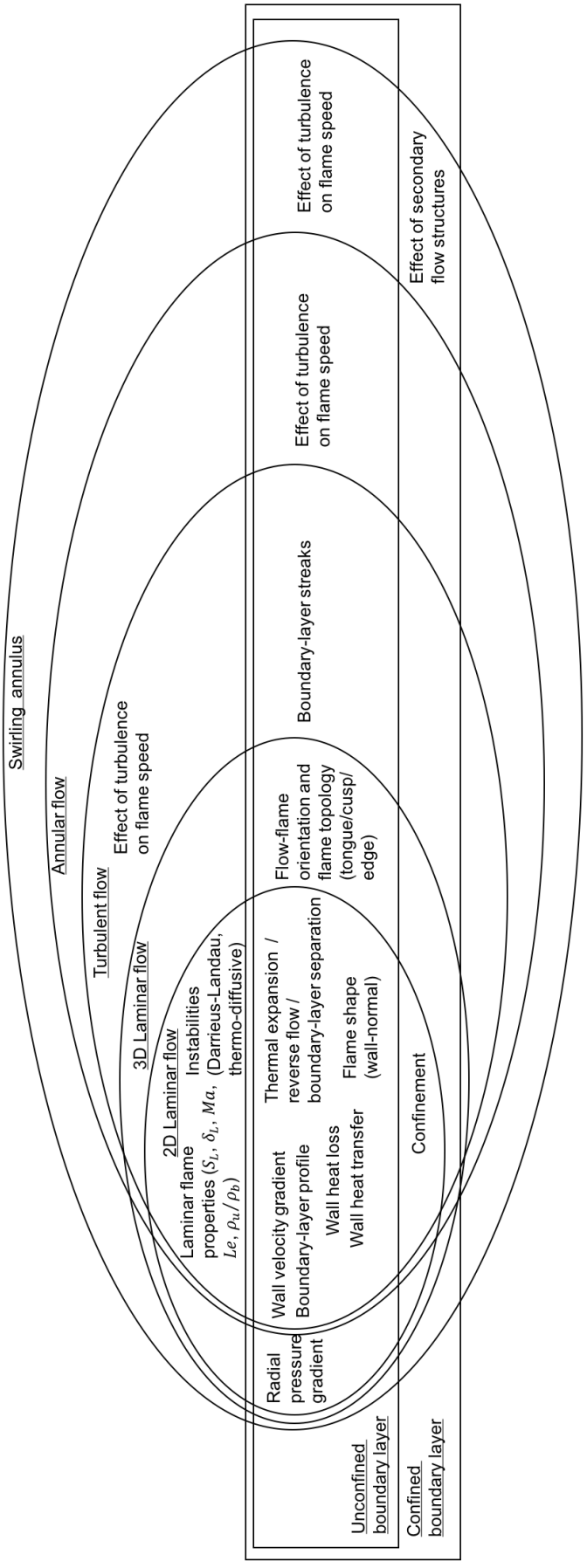

Figure 9.1: Diagram illustrating the effects influencing boundary-layer flashback.

An investigation was presented into the effect of swirl, bulk velocity and a developing boundary layer in two-dimensional laminar annular sections. This investigation investigated the trends for how swirl and a wall-normal pressure gradient affect flashback speed. The investigation was also used to develop empirical models for the effect of bulk velocity and a developing boundary layer on flashback speeds at different levels of swirl.

An investigation was also presented into the effect of swirl in three-dimensional turbulent planar channels and annuli. These investigations covered the physical aspects of a turbulent swirling flow in an annulus: turbulence, the radial pressure gradient, oblique flow orientation and curvature of the walls, for non-swirling and swirling flows. A radial pressure gradient and oblique flow orientation were investigated independently using planar channels, alongside the effect of planar-channel-flow turbulence. The effect of swirl, covering all of these physical aspects, was then studied for turbulent annular flows. This covered how the structure of the non-reacting turbulent flow in non-swirling and swirling flows was affected. For the reacting turbulent annular flows, the effect of the radial pressure gradient, oblique flow orientation and turbulence on boundary-layer flashback were then evaluated.

9.2 Conclusions

The conclusions from this thesis, referring to each research question, are:

1. Boundary-layer flashback in swirling flows has been described as the result of the radial pressure gradient and density change through the flame front acting to oppose the oncoming flow. In this way the mechanism is similar to that in non-swirling flows where an adverse pressure gradient is generated ahead of the flame which causes boundary layer separation, flow diversion around the leading point of the flame and a region of reversed flow into which the flame propagates. In a non-swirling flow this adverse pressure gradient is generated by the flame-flow interaction, while in a swirling flow it is also the result of the radial pressure gradient and density change. However, this mechanism is similar to that in combustion-induced vortex breakdown where the misalignment of density and pressure gradients generates baroclinic torque and a negative axial velocity. This work has not evaluated whether the same conclusions could be drawn by describing the process in terms of baroclinic torque. Using the radial pressure gradient description, the analogy between this swirling-flow pressure-driven flashback and gravity currents, in the limit of no flame propagation, is shown.

2. The effect of a wall-normal or radial pressure gradient can be characterised using a Froude number ($Fr = S_L/\sqrt{g'\delta}$). Its effect on flashback speed can then be described by a momentum-balance model or an additive model which comprises a flame-propagation effect enhanced by volumetric expansion, and a pressure-driven effect, as seen in gravity currents:

$$\frac{(U_{bulk} - V_f)}{S_L} = \sqrt{\frac{\rho_u}{\rho_b} + \frac{2}{Fr^2}} \tag{9.1}$$

   Using two-dimensional laminar simulations and previous experimental investigations, these models are shown to give very good predictions of flashback speed, particularly confirming the trend in flashback speed of $1/Fr$ at high swirl.

3. The oblique flow orientation, relative to the mean direction of flame propagation, results in asymmetric propagation of the flame bulges. Not only do the leading sides of the bulges (those not facing the oncoming flow) propagate into a slower oncoming flow but they are also shown to have a higher local displacement speed than the trailing sides and than the symmetric flame bulges with a normal flow orientation. This will enhance the flashback speed.

4. The effect of an annular geometry can be broken down into three aspects: for a non-swirling flow, the effect on turbulence; and for a swirling annular flow, the effect on turbulence and the effect of the secondary flow structures generated.

   4.1 For non-swirling annular flow, the curvature has little impact on the non-reacting flow at the level of curvature investigated in this work. The flashback process in this non-swirling flow is shown to behave similarly to boundary-layer flashback in a planar channel. In general, a turbulent flow significantly increases the flashback speed. At least part of this effect can be captured in the momentum-balance or additive models by incorporating existing turbulent-flame-speed models.

   4.2 For a swirling flow, the curvature in the direction of the flow has a larger impact: there is a turbulence reduction on the inner wall of the annulus which weakens the high- and low-velocity streaks of the turbulent boundary layer. For the flashback process, this means a reduced growth rate of the bulges and cusps forming the leading edge of the flame as well as reducing the nominal channel Ka for the same wall-scale Da. The effect of the swirling flow, and the generated radial pressure gradient, were shown to be smaller at the level of swirl investigated and as characterised using Fr.

   4.3 The curvature on the outer wall also means that there is a centrifugal instability which gives rise to Taylor-Görtler-like vortices which increase the wall-normal velocity fluctuations across the channel centre. This contribution to velocity fluctuations means that, despite a reduction in velocity fluctuations at the inner wall, there is still significant flame wrinkling further from the wall.

5. The final set of conclusions cover the effect of wall velocity gradient and boundary-layer profile.

   5.1 Flashback speed is strongly affected by bulk velocity, linearly increasing with increasing bulk velocity, at least for the bulk flows used in this work. The effect of bulk velocity is shown to depend on Fr, with a lower Fr giving a lower effect of bulk velocity. At high Fr bulk velocity has little effect on the local displacement speed but causes an increase in flow diversion around the flame, increasing flashback speed. At low Fr bulk velocity has little effect on flow diversion but causes an increase in the local displacement speed of the flame, increasing flashback speed.

   5.2 Flashback speed is reduced by a flatter boundary-layer profile, with bulk velocity reducing the effect of bulk velocity on flashback speed. The velocity profile was characterised using the boundary-layer displacement thickness relative to the flame, which was shown to linearly reduce the effect of the bulk velocity on flashback speed.

9.3 Future Work

- The momentum-balance models derived in this thesis make predictions for the effect of density ratio and confinement on flashback speed. These predictions have not been evaluated and so

future work is required to evaluate and possibly develop the predictive models further. This could be informed by simulations which investigate the effect of: density ratio; confinement, by varying the channel height; and flame topology, for example whether the flame propagates as a tongue or edge.

- The three-dimensional flame shape and propagation velocity for flames in laminar flows within a channel or annulus have yet to be described. This will be affected by flame instabilities, such as Darrieus-Landau and the thermo-diffusive instability, and may alter the flow diversion around the flame, changing the effect of thermal expansion/density ratio and confinement. It is suggested to investigate the effect of density ratio on: the wavelength and growth rate of bulges and cusps; and flashback speed where the cross-stream-wise confinement is varied.

- In this work an empirical model was developed which described the effect of bulk velocity on flashback speed using a linear relation. The effect of stretch on flame propagation has a limit in the linear relation between stretch and propagation speed. The limit of the derived linear relation between bulk velocity and flashback speed should also be evaluated.

- Within turbulent flows, turbulence causes wrinkling of the flame front, increasing the flame surface area and consumption speed. Within a swirling flow, the effect of the radial pressure gradient and spreading of the lower-density burned gases could reduce this wrinkling and impact the turbulent flame propagation speed. Future work should therefore evaluate these competing effects and their effect on turbulent flame propagation speed. This could include simulations which vary bulk velocity, and therefore turbulence levels, and swirl or wall-normal pressure gradient.

- The flashback models derived in this thesis use a momentum balance and a uniform body force to describe pressure increases in the burned gases resulting from the misalignment of pressure and density gradients. This misalignment is also present in combustion-induced vortex breakdown with the baroclinic torque it generates shown to explain this flashback process. Future work could analyse baroclinic torque and investigate whether these two descriptions and predictions can be unified.

Appendices

Appendix A

Calculation of Pure-Species Transport Properties

A.1 Viscosity

The single-species viscosities are calculated using:

$$\mu_k = \frac{5}{16}\frac{\sqrt{\pi m_k k_B T}}{\pi \sigma_k^2 \Omega^{(2,2)*}} \tag{A.1}$$

where σ_k is the Lennard-Jones collision diameter, m_k the molecular mass, k_B the Boltzmann constant and T the temperature. The collision integral $\Omega^{(2,2)*}$ depends on the reduced temperature and reduced dipole moment:

$$T_k^* = \frac{k_B T}{\epsilon_k} \tag{A.2}$$

$$\delta_k^* = \frac{1}{2}\frac{d_k^2}{\epsilon_k \sigma_k^3} \tag{A.3}$$

where ϵ_k is the Lennard-Jones potential well depth and d_k the dipole moment. The collision integral is based on quadratic interpolation of tables of Stockmayer potentials.

A.1.1 Binary Diffusion Coefficients

The binary diffusion coefficients are calculated using:

$$D_{jk} = \frac{3}{16}\frac{\sqrt{2\pi k_B^3 T^3 / W_{jk}}}{P \pi \sigma_{jk}^2 \Omega^{(1,1)*}} \tag{A.4}$$

for species j and k, where W_{jk} is the reduced molecular mass for the species pair:

$$W_{jk} = \frac{W_j W_k}{W_j + W_k} \tag{A.5}$$

and σ_{jk} is the reduced collision diameter. The collision integral $\Omega^{(1,1)*}$ is again based on Stockmayer potentials and depends on the reduced temperature (T^*_{jk}), species dipole moments (d_k) and polarisabilities (α_k). For a species pair where both are non-polar or both are polar:

$$\frac{\epsilon_{jk}}{k_B} = \sqrt{\left(\frac{\epsilon_j}{k_B}\right)\left(\frac{\epsilon_k}{k_B}\right)} \tag{A.6}$$

$$\sigma_{jk} = \frac{1}{2}\left(\sigma_j + \sigma_k\right) \tag{A.7}$$

$$d^2_{jk} = d_j d_k \tag{A.8}$$

For a species pair where one is polar (p) and one is non-polar (n):

$$\frac{\epsilon_{np}}{k_B} = \xi^2\sqrt{\left(\frac{\epsilon_n}{k_B}\right)\left(\frac{\epsilon_p}{k_B}\right)} \tag{A.9}$$

$$\sigma_{np} = \frac{1}{2}\left(\sigma_n + \sigma_p\right)\xi^{-\frac{1}{6}} \tag{A.10}$$

$$d^2_{np} = 0 \tag{A.11}$$

$$\xi = 1 + \frac{1}{4}\alpha^*_n d^*_p \sqrt{\frac{\epsilon_p}{\epsilon_n}} \tag{A.12}$$

where α^*_n is the reduced polarisability for the non-polar molecule and d^*_p the reduced dipole moment for the polar molecule.

$$\alpha^*_n = \frac{\alpha_n}{\sigma^3_n} \tag{A.13}$$

$$d_{p*} = \frac{d_p}{\sqrt{\epsilon_p \sigma^3_p}} \tag{A.14}$$

For this collision integral ($\Omega^{(1,1)*}$) the reduced temperature and dipole moment take the following forms:

$$T^*_{jk} = \frac{k_B T}{\epsilon_{jk}} \tag{A.15}$$

$$\delta^*_{jk} = \frac{1}{2} d^{*2}_{jk} \tag{A.16}$$

A.2 Thermal Conductivity

The species thermal conductivities for a given species, k:

$$\lambda_k = \frac{\mu_k}{W_k}\left(f_{trans} C_{v,trans} + f_{rot} C_{v,rot} + f_{vib} C_{v,vib}\right) \tag{A.17}$$

Here $C_{v,trans}$, $C_{v,rot}$ and $C_{v,vib}$ are constants which depend on whether the molecule is linear or not. f_{trans}, f_{rot} and f_{vib} are given by:

$$f_{trans} = \frac{5}{2}\left(1 - \frac{2}{\pi}\frac{C_{v,rot}}{C_{v,trans}}\frac{A}{B}\right) \tag{A.18}$$

$$f_{rot} = \frac{\rho D_{kk}}{\mu_k}\left(1 + \frac{2}{\pi}\frac{A}{B}\right) \tag{A.19}$$

$$f_{vib} = \frac{\rho D_{kk}}{\mu_k} \tag{A.20}$$

$$A = \frac{5}{2} - \frac{\rho D_{kk}}{\mu_k} \tag{A.21}$$

$$B = Z_{rot} + \frac{2}{\pi}\left(\frac{5}{3}\frac{C_{v,rot}}{R} + \frac{\rho D_{kk}}{\mu_k}\right) \tag{A.22}$$

$$D_{kk} = \frac{3}{16}\frac{\sqrt{2\pi k_B^3 T^3 / W_k}}{P\pi\sigma_k^2\Omega^{(1,1)*}} \tag{A.23}$$

$$\rho = \frac{PW_k}{RT} \tag{A.24}$$

$$Z_{rot}(T) = Z_{rot}(298)\frac{F(298)}{F(T)} \tag{A.25}$$

$$F(T) = 1 + \frac{\pi^{\frac{3}{2}}}{2}\left(\frac{\epsilon/k_B}{T}\right)^{\frac{1}{2}} + \left(\frac{\pi^2}{4} + 2\right)\left(\frac{\epsilon/k_B}{T}\right) + \pi^{\frac{3}{2}}\left(\frac{\epsilon/k_B}{T}\right)^{\frac{3}{2}} \tag{A.26}$$

Appendix B

Annular NSCBC

The following equations give the annular NSCBC in the x-direction. The following give the non-conservative forms of the Navier-Stokes equations with their characteristic waves:

$$\frac{\partial \rho}{\partial t} = -\left(L_2^x + \frac{1}{c^2}\left(L_5^x + L_1^x\right) - \left(\frac{1}{r}\frac{\partial r\rho v}{\partial r} + \frac{1}{r}\frac{\partial(\rho w)}{\partial \theta}\right)\right) \tag{B.1a}$$

$$\frac{\partial u}{\partial t} = -\frac{1}{\rho c}\left(L_5^x - L_1^x\right) - \left(v\frac{\partial u}{\partial r} + \frac{w}{r}\frac{\partial u}{\partial \theta}\right) + d_u \tag{B.1b}$$

$$\frac{\partial v}{\partial t} = -L_3^x - v\left(v\frac{\partial v}{\partial r} + \frac{w}{r}\frac{\partial v}{\partial \theta} - \frac{w^2}{r} + \frac{1}{\rho}\frac{\partial p}{\partial r}\right) + d_v \tag{B.1c}$$

$$\frac{\partial w}{\partial t} = -L_4^x - \left(v\frac{\partial w}{\partial r} + \frac{w}{r}\frac{\partial w}{\partial \theta} + \frac{vw}{r} + \frac{1}{\rho r}\frac{\partial p}{\partial \theta}\right) + d_w \tag{B.1d}$$

$$\frac{\partial p}{\partial t} = -\left(L_5^x + L_1^x\right) - \left(v\frac{\partial p}{\partial r} + \frac{w}{r}\frac{\partial p}{\partial \theta} + \gamma p\left(\frac{1}{r}\frac{\partial(rv)}{\partial r} + \frac{1}{r}\frac{\partial w}{\partial \theta}\right)\right) + d_p + s_p \tag{B.1e}$$

$$\frac{\partial Y_i}{\partial t} = -L_{5+i}^x - \left(v\frac{\partial Y_i}{\partial r} + \frac{w}{r}\frac{\partial Y_i}{\partial \theta}\right) + d_{Y_i} + s_{Y_i} \tag{B.1f}$$

This includes the viscous and source terms:

$$d_u = \frac{1}{\rho}\left(\frac{\partial \tau_{xx}}{\partial x} + \frac{1}{r}\frac{\partial(r\tau_{xr})}{\partial r} + \frac{1}{r}\frac{\partial \tau_{x\theta}}{\partial \theta}\right) \tag{B.2a}$$

$$d_v = \frac{1}{\rho}\left(\frac{\partial \tau_{rx}}{\partial x} + \frac{1}{r}\frac{\partial(r\tau_{rr})}{\partial r} + \frac{1}{r}\frac{\partial \tau_{r\theta}}{\partial \theta} - \frac{\tau_{\theta\theta}}{r}\right) \tag{B.2b}$$

$$d_w = \frac{1}{\rho}\left(\frac{\partial \tau_{\theta x}}{\partial x} + \frac{1}{r}\frac{\partial(r\tau_{\theta r})}{\partial r} + \frac{1}{r}\frac{\partial \tau_{\theta\theta}}{\partial \theta} + \frac{\tau_{r\theta}}{r}\right) \tag{B.2c}$$

$$d_\rho = 0 \tag{B.2d}$$

$$d_p = (\gamma - 1)\left[V_e + \Psi + \sum_{i=1}^{N}\left(h_i - c_p TW/W_i\right)\nabla \cdot (\rho Y_i \mathbf{V}_i)\right] \tag{B.2e}$$

where:

$$V_e = -\nabla \cdot \mathbf{q} = -\left(\frac{\partial}{\partial x}\left(-\lambda\frac{\partial T}{\partial x} + \rho\sum_{i=1}^{N} h_i Y_i V_{i,x}\right) + \frac{1}{r}\frac{\partial}{\partial r}\left(-r\lambda\frac{\partial T}{\partial r} + r\rho\sum_{i=1}^{N} h_i Y_i V_{i,r}\right) + \frac{1}{r}\frac{\partial}{\partial \theta}\left(-\frac{\lambda}{r}\frac{\partial T}{\partial \theta} + \rho\sum_{i=1}^{N} h_i Y_i V_{i,\theta}\right)\right) \tag{B.2f}$$

$$d_{Y_i} = -\frac{1}{\rho}\left(\frac{\partial}{\partial x}\left(\rho Y_i V_{i,x}\right) + \frac{1}{r}\frac{\partial}{\partial r}\left(r\rho Y_i V_{i,r}\right) + \frac{1}{r}\frac{\partial}{\partial \theta}\left(\rho Y_i V_{i,\theta}\right)\right) \tag{B.2g}$$

$$s_p = (\gamma - 1)\sum_{i=1}^{N}\left[-\left(h_i - c_p T W/W_i\right) W_i \dot{\omega}_i\right] \tag{B.3a}$$

$$s_{Y_i} = \frac{1}{\rho} W_i \dot{\omega}_i \tag{B.3b}$$

The characteristic waves in x are given by:

$$L_1^x = \frac{(u-c)}{2}\left(\frac{\partial p}{\partial x} - \rho c\frac{\partial u}{\partial x}\right) \tag{B.4a}$$

$$L_2^x = u\left(\frac{\partial p}{\partial x} - \frac{1}{c^2}\frac{\partial p}{\partial x}\right) \tag{B.4b}$$

$$L_3^x = u\frac{\partial v}{\partial x} \tag{B.4c}$$

$$L_4^x = u\frac{\partial w}{\partial x} \tag{B.4d}$$

$$L_5^x = \frac{(u+c)}{2}\left(\frac{\partial p}{\partial x} + \rho c\frac{\partial u}{\partial x}\right) \tag{B.4e}$$

$$L_{5+i}^x = u\frac{\partial Y_i}{\partial x} \tag{B.4f}$$

$$d_1^x = L_2^x + \frac{1}{c^2}\left(L_1^x + L_5^x\right) \tag{B.5a}$$

$$d_2^x = L_1^x + L_5^x \tag{B.5b}$$

$$d_3^x = \frac{1}{\rho c}\left(L_5^x - L_1^x\right) \tag{B.5c}$$

$$d_4^x = L_3^x \tag{B.5d}$$

$$d_5^x = L_4^x \tag{B.5e}$$

$$d_{5+i}^x = L_{5+i}^x \tag{B.5f}$$

with the transverse terms given by:

$$L_{1,trans}^x = -\frac{1}{2}\left\{\left(v\frac{\partial p}{\partial r} + \frac{w}{r}\frac{\partial p}{\partial \theta}\right) + \gamma p\left(\frac{1}{r}\frac{\partial (rv)}{\partial r} + \frac{1}{r}\frac{\partial w}{\partial \theta}\right) - \rho c\left(v\frac{\partial u}{\partial r} + \frac{w}{r}\frac{\partial x}{\partial \theta}\right)\right\} \tag{B.6a}$$

$$L^x_{2,trans} = -\left\{ v\left(\frac{\partial \rho}{\partial r} - \frac{1}{c^2}\frac{\partial p}{\partial r}\right) + \frac{w}{r}\left(\frac{\partial \rho}{\partial \theta} - \frac{1}{c^2}\frac{\partial p}{\partial \theta}\right)\right\} \tag{B.6b}$$

$$L^x_{3,trans} = -\left(v\frac{\partial v}{\partial r}\frac{w}{r}\frac{\partial v}{\partial \theta} - \frac{w^2}{r} + \frac{1}{\rho}\frac{\partial p}{\partial r}\right) \tag{B.6c}$$

$$L^x_{4,trans} = -\left(v\frac{\partial w}{\partial r} + \frac{w}{r}\frac{\partial w}{\partial \theta} + \frac{vw}{r} + \frac{1}{\rho r}\frac{\partial p}{\partial \theta}\right) \tag{B.6d}$$

$$\begin{aligned} L^x_{5,trans} = -\frac{1}{2}\Bigg\{ &\left(v\frac{\partial p}{\partial r} + \frac{w}{r}\frac{\partial p}{\partial \theta}\right) + \gamma p\left(\frac{1}{r}\frac{\partial (rv)}{\partial r} + \frac{1}{r}\frac{\partial w}{\partial \theta}\right) \\ &+\rho c\left(v\frac{\partial u}{\partial r} + \frac{w}{r}\frac{\partial u}{\partial \theta}\right)\Bigg\} \end{aligned} \tag{B.6e}$$

$$L^x_{5+i,trans} = -\left(v\frac{\partial Y_i}{\partial r} + \frac{w}{r}\frac{\partial Y_i}{\partial \theta}\right) \tag{B.6f}$$

Appendix C

Model Formulation

C.1 Detailed Derivation of Height-Ratio Equation

This section gives a detailed derivation of the height-ratio equation originally derived in section 4.2.1.

Starting from the mass and momentum balances over the first control volume:

$$\rho_1 u_1 \delta_1 = \rho_4 u_4 \delta_4 \tag{C.1}$$

$$\rho_1 u_1^2 \delta_1 + \delta_1 P_{in} + (\delta_4 - \delta_1) P_s = \rho_4 u_4^2 \delta_4 + \delta_4 P_{out} \tag{C.2}$$

And substituting in the expressions for P_{in}, P_{out} and P_s, and $\delta_4 \rho_4 u_4^2$ from the conservation of mass:

$$P_{in} = P_0 - \rho_1 g(H - \delta_1) - \rho_1 g \frac{\delta_1}{2} \tag{C.3}$$

$$P_{out} = P_0 + \Delta P - \rho_1 g(H - \delta_4) - \rho_4 g \frac{\delta_4}{2} \tag{C.4}$$

$$P_s = P_0 - \rho_1 g(H - \delta_4) - \rho_1 g \left(m_1 \delta_1 + m_2 \delta_4\right) + (1 - \sigma)\Delta P - \rho_4 g \left(n_1 \delta_4 + n_2 \delta_1\right) \tag{C.5}$$

$$\rho_4 u_4^2 \delta_4 = \rho_1 u_1^2 \delta_1 \frac{\rho_1}{\rho_4} \frac{\delta_1}{\delta_4} \tag{C.6}$$

$$\begin{aligned} &\rho_1 u_1^2 \delta_1 + \delta_1 \left(P_0 - \rho_1 g(H - \delta_1) - \rho_1 g \frac{\delta_1}{2} \right) \\ &+ (\delta_4 - \delta_1) \left(P_0 - \rho_1 g(H - \delta_4) - \rho_1 g \left(m_1 \delta_1 + m_2 \delta_4\right) \right. \\ &+ \left. (1 - \sigma)\Delta P - \rho_4 g \left(n_1 \delta_4 + n_2 \delta_1\right) \right) \\ &= \rho_1 u_1^2 \delta_1 \frac{\rho_1}{\rho_4} \frac{\delta_1}{\delta_4} + \delta_4 \left(P_0 + \Delta P - \rho_1 g(H - \delta_4) - \rho_4 g \frac{\delta_4}{2} \right) \end{aligned} \tag{C.7}$$

Collecting terms gives:

$$\begin{aligned}
&\rho_1 u_1^2 \delta_1 \left(1 - \frac{\rho_1}{\rho_4}\frac{\delta_1}{\delta_4}\right) = P_0 \left(\delta_4 - \delta_1 - (\delta_4 - \delta_1)\right) \\
&+ \Delta P \left(\delta_4 - (\delta_4 - \delta_1)(1-\sigma)\right) \\
&+ \rho_1 g \left(-\delta_4(H - \delta_4) + \delta_1 \left(H - \frac{\delta_1}{2}\right) + (\delta_4 - \delta_1)(H - \delta_4) + (\delta_4 - \delta_1)\left(m_1\delta_1 + m_2\delta_4\right)\right) \\
&+ \rho_4 g \left(-\delta_4 \frac{\delta_4}{2} + (\delta_4 - \delta_1)\left(n_1\delta_4 + n_2\delta_1\right)\right)
\end{aligned} \tag{C.8}$$

Showing that P_0 and H can be eliminated. The equation can then be non-dimensionalised by dividing through by $\rho_4 \delta_4^2 g$.

$$\begin{aligned}
&\frac{\rho_1}{\rho_4}\frac{u_1^2}{\delta_4 g}\frac{\delta_1}{\delta_4}\left(1 - \frac{\rho_1}{\rho_4}\frac{\delta_1}{\delta_4}\right) = \frac{\Delta P}{\rho_4 g \delta_4}\left(1 - \left(1 - \frac{\delta_1}{\delta_4}\right)(1-\sigma)\right) \\
&+ \frac{\rho_1}{\rho_4}\left(+1 - \frac{1}{2}\frac{\delta_1^2}{\delta_4^2} + \frac{\delta_1}{\delta_4} - \left(1 - \frac{\delta_1}{\delta_4}\right) + \left(1 - \frac{\delta_1}{\delta_4}\right)\left(m_1\frac{\delta_1}{\delta_4} + m_2\right)\right) \\
&+ \left(-\frac{1}{2} + \left(1 - \frac{\delta_1}{\delta_4}\right)\left(n_1 + n_2\frac{\delta_1}{\delta_4}\right)\right)
\end{aligned} \tag{C.9}$$

Introducing the non-dimensional variables $D = \rho_1/\rho_4$, $\delta_1' = \delta_1/\delta_4$, $Fr = u_2/\sqrt{\delta_4 g \tau}$, $u_1' = u_1/u_2$, $\Delta P' = \Delta P/(1/2\rho_1 u_1^2)$.

$$\begin{aligned}
&D\delta_1' Fr^2 u_1'^2 \left(1 - D\delta_1'\right) = \frac{1}{2}\Delta P'(D-1)u_1'^2 Fr^2 \left(1 - \left(1 - \delta_1'\right)(1-\sigma)\right) \\
&+ D\left(+1 - \frac{1}{2}\delta_1'^2 - 1 + \delta_1' + (1-\delta_1')(m_1\delta_1' + m_2)\right) + \left(-\frac{1}{2} + (1-\delta_1')(n_1 + n_2\delta_1')\right)
\end{aligned} \tag{C.10}$$

Terms in δ_1' can now be collected to give the final form of the generalised model for the height ratio:

$$\begin{aligned}
0 =& \delta_1'^2\left[-D(D-1)u_1'^2 Fr^2 + D\left(m_1 + \frac{1}{2}\right) + n_2\right] \\
&+ \delta_1'\left[(D-1)Fr^2 u_1'^2 - D(m_1 + 1 - m_2) + n_1 - n_2 - (1-\sigma)\frac{1}{2}\Delta P' D u_1'^2 Fr^2\right] \\
&+ \left[\frac{1}{2} - n_1 - Dm_2 - \sigma\frac{1}{2}\Delta P' D u_1'^2 Fr^2\right]
\end{aligned} \tag{C.11}$$

C.1.1 Consistency with Ruetsch et al. (1995)

The consistency with Ruetsch et al. (1995) can be checked, starting with equation C.11. Dividing through by Fr^2 gives:

$$\begin{aligned} 0 =& \delta_1'^2 \left[-D(D-1)u_1'^2 + \frac{D}{Fr^2}\left(m_1 + \frac{1}{2}\right) + \frac{n_2}{Fr^2} \right] \\ &+ \delta_1' \left[(D-1)u_1'^2 - \frac{D}{Fr^2}(m_1 + 1 - m_2) + \frac{(n_1 - n_2)}{Fr^2} - (1-\sigma)\frac{1}{2}\Delta P' D u_1'^2 \right] \\ &+ \left[\frac{1}{2Fr^2} - \frac{(n_1 + Dm_2)}{Fr^2} - \sigma\frac{1}{2}\Delta P' D u_1'^2 \right] \end{aligned} \tag{C.12}$$

As Fr tends to ∞ the effect of the body force is removed, and dividing through by $(D-1)$ gives:

$$0 = -Du_1'^2\delta_1'^2 + \delta_1' \left[u_1'^2 - (1-\sigma)\Delta P' \frac{D}{(D-1)} \right] + \left[-\sigma\Delta P' \frac{D}{(D-1)} \right] \tag{C.13}$$

If $\Delta P'$ is also set to 0 then the result of Ruetsch et al. (1995) is recovered:

$$\delta_1' = \frac{1}{D} = \frac{\rho_4}{\rho_1} \tag{C.14}$$

C.2 Derivation of Initial Velocity-Ratio Equation (Ruetsch et al. (1995) Equation 6)

This section gives a detailed derivation of equation 6 in Ruetsch et al. (1995).

C.2.1 Rankine-Hugoniot Relations

$$\rho_2 u_2 = \rho_3 u_3 \tag{C.15}$$

$$P_2 + \rho_2 u_2^2 = P_3 + \rho_3 u_3^2 \tag{C.16}$$

C.2.2 Constant Density on each side of the flame

$$\rho_1 = \rho_2 \tag{C.17}$$

$$\rho_3 = \rho_4 \tag{C.18}$$

C.2.3 Conservation of Mechanical Energy

$$P_1 + \frac{1}{2}\rho_1 u_1^2 = P_2 + \frac{1}{2}\rho_2 u_2^2 \tag{C.19}$$

$$P_3 + \frac{1}{2}\rho_3 u_3^2 = P_4 + \frac{1}{2}\rho_4 u_4^2 \tag{C.20}$$

C.2.4 Conservation of Mass within Control Volume

$$\rho_1 u_1 \delta_1 = \rho_4 u_4 \delta_4 \tag{C.21}$$

C.2.5 Derivation

Start with equation C.19:

$$\frac{P_1 - P_2}{\frac{1}{2}\rho_1 u_1^2} + 1 = \frac{u_2^2}{u_1^2} \tag{C.22}$$

Relate P_2 to P_3 and P_3 to P_4:

$$P_2 = P_3 + \rho_3 u_3^2 - \rho_2 u_2^2 \tag{C.23}$$

$$P_3 = P_4 + \frac{1}{2}\rho_4 u_4^2 - \frac{1}{2}\rho_3 u_3^2 \tag{C.24}$$

Combine these to give:

$$P_2 = P_4 + \frac{1}{2}\rho_4 u_4^2 - \frac{1}{2}\rho_3 u_3^2 + \rho_3 u_3^2 - \rho_2 u_2^2 \tag{C.25}$$

Reduce and substitute equation C.15:

$$\begin{aligned} P_2 &= P_4 + \frac{1}{2}\rho_4 u_4^2 + \frac{1}{2\rho_3}\rho_2^2 u_2^2 - \rho_2 u_2^2 \\ &= P_4 + \frac{1}{2}\rho_4 u_4^2 + \rho_2 u_2^2 \left(\frac{1}{2}\frac{\rho_1}{\rho_4} - 1\right) \end{aligned} \tag{C.26}$$

Replace P_2 in equation C.22:

$$\frac{u_2^2}{u_1^2} = \frac{P_1 - P_4}{\frac{1}{2}\rho_1 u_1^2} + 1 - \frac{\frac{1}{2}\rho_4 u_4^2}{\frac{1}{2}\rho_1 u_1^2} - \frac{\rho_2 u_2^2}{\frac{1}{2}\rho_1 u_1^2}\left(\frac{1}{2}\frac{\rho_1}{\rho_4} - 1\right) \tag{C.27}$$

Conservation of mass relates u_4 and u_1 and can be substituted in:

$$\frac{u_4^2}{u_1^2} = \frac{\rho_1^2}{\rho_4^2}\frac{\delta_1^2}{\delta_4^2} \tag{C.28}$$

$$\begin{aligned} \frac{u_2^2}{u_1^2} &= \frac{P_1 - P_4}{\frac{1}{2}\rho_1 u_1^2} + 1 - \frac{\rho_1}{\rho_4}\frac{\delta_1^2}{\delta_4^2} - \frac{u_2^2}{u_1^2}\left(\frac{\rho_1}{\rho_4} - 2\right) \\ &= \frac{\frac{P_1 - P_4}{\frac{1}{2}\rho_1 u_1^2} + 1 - \frac{\rho_1}{\rho_4}\frac{\delta_1^2}{\delta_4^2}}{\frac{\rho_1}{\rho_4} - 1} \end{aligned} \tag{C.29}$$

As Ruetsch et al. (1995) equation 6:

$$\left(\frac{u_1}{u_2}\right)^2 = \frac{\rho_1/\rho_4 - 1}{(P_1 - P_4)/(\frac{1}{2}\rho_1 u_1^2) + 1 - (\rho_1/\rho_4)(\delta_1/\delta_4)^2} \tag{C.30}$$

C.3 Detailed Derivation of Velocity-Ratio Equation

This section gives a detailed derivation of the velocity-ratio equation originally derived in section 4.2.2.

The derivation of the velocity-ratio equation starts from Ruetsch et al. (1995) equation 6:

$$\left(\frac{u_1}{u_2}\right)^2 = \frac{\rho_1/\rho_4 - 1}{(P_1 - P_4)/(\frac{1}{2}\rho_1 u_1^2) + 1 - (\rho_1/\rho_4)(\delta_1/\delta_4)^2} \tag{C.31}$$

or in the non-dimensional variables defined here:

$$u_1'^2 = \frac{D - 1}{(P_1 - P_4)/(\frac{1}{2}\rho_1 u_1^2) + 1 - (\delta_1'^2/D)} \tag{C.32}$$

P_1 and P_4 are evaluated using the hydrostatic pressures at points 1 and 4:

$$P_4 = P_0 + \Delta P - \delta_4 \rho_4 g \tag{C.33}$$

$$P_1 = P_0 - \delta_4 \rho_1 g \tag{C.34}$$

Using these, $(P_1 - P_4)/(\frac{1}{2}\rho_1 u_1^2)$ can be evaluated:

$$\begin{aligned}\frac{(P_1 - P_4)}{\frac{1}{2}\rho_1 u_1^2} &= -\Delta P' - \frac{2\delta_4 g}{\rho_1 u_1^2}(\rho_1 - \rho_4) = -\Delta P' - \frac{2}{u_1'^2 Fr^2} \\ &= 2\frac{(1 - \delta_1')}{(H' - 1)} + \frac{(\delta_1' - 1)^2}{u_1'^2 Fr^2 (H' - \delta_1')} - \frac{2}{u_1'^2 Fr^2} \\ &= 2\frac{(1 - \delta_1')}{(H' - 1)} + \frac{1}{u_1'^2 Fr^2}\left(\frac{(\delta_1' - 1)^2}{(H' - \delta_1')} - 2\right)\end{aligned} \tag{C.35}$$

Substituting this into the velocity-ratio equation and re-arranging to isolate $u_1'^2$:

$$u_1'^2 = \frac{D - 1 + \frac{1}{Fr^2}\left(2 - \frac{(\delta_1' - 1)^2}{(H' - \delta_1')}\right)}{1 - (\delta_1'^2/D) + 2\frac{(1 - \delta_1')}{(H' - 1)}} \tag{C.36}$$

or by retaining $\Delta P'$ explicitly:

$$u_1'^2 = \frac{D - 1 + \frac{2}{Fr^2}}{1 - (\delta_1'^2/D) - \Delta P'} \tag{C.37}$$

As H' tends to ∞ then the velocity-ratio equation simplifies to:

$$u_1'^2 = \frac{D - 1 + \frac{2}{Fr^2}}{1 - (\delta_1'^2/D)} \tag{C.38}$$

C.3.1 Consistency with Ruetsch et al. (1995)

As Fr tends to ∞ and $\delta_1/\delta_4 = 1/D$, $u_1'^2$ reverts to the result of Ruetsch et al. (1995):

$$u_1'^2 = D = \left(\frac{u_1}{u_2}\right)^2 = \frac{\rho_1}{\rho_4} \tag{C.39}$$

C.4 Detailed Derivation of Pressure-Drop Equation

This section gives a detailed derivation of the pressure-drop equation originally derived in section 4.2.3.

P_s is again assumed to be given by equation 4.6:

$$\begin{aligned}
&\rho_1 v_1^2(H-\delta_1) + (P_0 - \frac{(H-\delta_1)}{2}\rho_1 g)(H-\delta_1) = \rho_1 v_4^2(H-\delta_4) \\
&+ (\delta_4 - \delta_1)\left(P_0 - \rho_1 g(H-\delta_4) - \rho_1 g\left(m_1\delta_1 + m_2\delta_4\right) + (1-\sigma)\Delta P - \rho_4 g\left(n_1\delta_4 + n_2\delta_1\right)\right) \\
&+ (P_0 + \Delta P - \frac{(H-\delta_4)}{2}\rho_1 g)(H-\delta_4)
\end{aligned} \tag{C.40}$$

Collecting terms and substituting in $\rho_1 v_4^2(H-\delta_4) = \rho_1 v_1^2(H-\delta_1)(H-\delta_1)/(H-\delta_4)$ from the mass balance.

$$\begin{aligned}
&\Delta P\left(-(1-\sigma)(\delta_4-\delta_1) - (H-\delta_4)\right) = \\
&\rho_1 v_1^2(H-\delta_1)\left(\frac{(H-\delta_1)}{(H-\delta_4)} - 1\right) + P_0\left(-(H-\delta_1) + (\delta_4-\delta_1) + (H-\delta_4)\right) \\
&+ \rho_1 g\left(\frac{(H-\delta_1)^2}{2} - (H-\delta_4)(\delta_4-\delta_1) - (\delta_4-\delta_1)(m_1\delta_1 + m_2\delta_4) - \frac{(H-\delta_4)^2}{2}\right) \\
&- \rho_4 g\left((\delta_4-\delta_1)(n_1\delta_4 + n_2\delta_1)\right)
\end{aligned} \tag{C.41}$$

Here to non-dimensionalise the equation is divided through by $\rho_4\delta_4 u_2^2$, with the same set of non-dimensional variables substituted in, including $H' = H/\delta_4$. P_0 again cancels out. Additionally, given

that the velocity at the channel inlet is assumed to be uniform across the channel, $v_1 = u_1$.

$$\begin{aligned}
&\frac{\Delta P'}{2} u_1'^2 D\left(\sigma(1-\delta_1') - (H'-\delta_1')\right) = D u_1'^2 (H'-\delta_1')\left(\frac{(H'-\delta_1')}{(H'-1)} - 1\right) \\
&+ \frac{D}{\tau Fr^2}\left(\frac{(H'-\delta_1')^2}{2} - (H'-1)(1-\delta_1') - (1-\delta_1')(m_1\delta_1' + m_2) - \frac{(H'-1)^2}{2}\right) \\
&- \frac{1}{\tau Fr^2}\left((1-\delta_1')(n_1 + n_2\delta_1')\right) \\
&= D u_1'^2 (H'-\delta_1')\left(\frac{(H'-\delta_1')}{(H'-1)} - 1\right) + \frac{(\delta_1'-1)}{2\tau Fr^2}\left[D\left((\delta_1'-1) + 2m_1\delta_1' + 2m_2\right) + 2(n_1 + n_2\delta_1')\right]
\end{aligned} \tag{C.42}$$

With the choice of the streamline pressure:

$$\Delta P'\left(H'-\delta_1'\right) = -2(H'-\delta_1')\left(\frac{(H'-\delta_1')}{(H'-1)} - 1\right) - \frac{(\delta_1'-1)}{(D-1)u_1'^2 Fr^2}\left[D(\delta_1'-1) - (\delta_1'-1)\right] \tag{C.43}$$

$$\Delta P' = -2\frac{(1-\delta_1')}{(H'-1)} - \frac{(\delta_1'-1)^2}{u_1'^2 Fr^2 (H'-\delta_1')} \tag{C.44}$$

Appendix D

Annular Correlation Coefficients

D.1 Annular Axial-Only Flow

The following pages show the two-point correlation coefficients for the annular, axial-only flow.

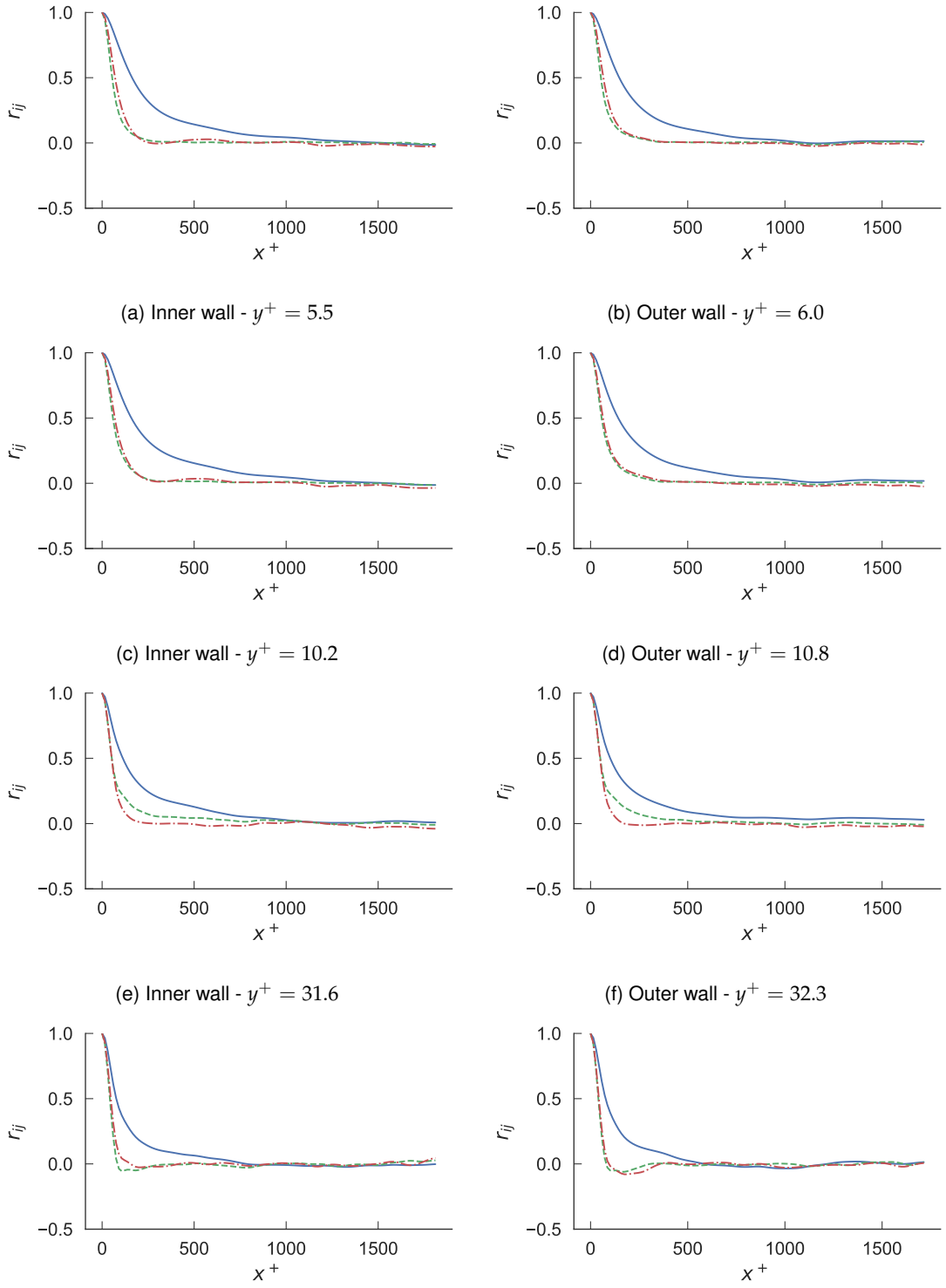

(a) Inner wall - $y^+ = 5.5$

(b) Outer wall - $y^+ = 6.0$

(c) Inner wall - $y^+ = 10.2$

(d) Outer wall - $y^+ = 10.8$

(e) Inner wall - $y^+ = 31.6$

(f) Outer wall - $y^+ = 32.3$

(g) Inner wall - $y^+ = 147.2$

(h) Outer wall - $y^+ = 154.7$

Figure D.1: Two-point correlation coefficients in the axial direction for the axial-only annular flow. Normalisation is by the local wall scales.

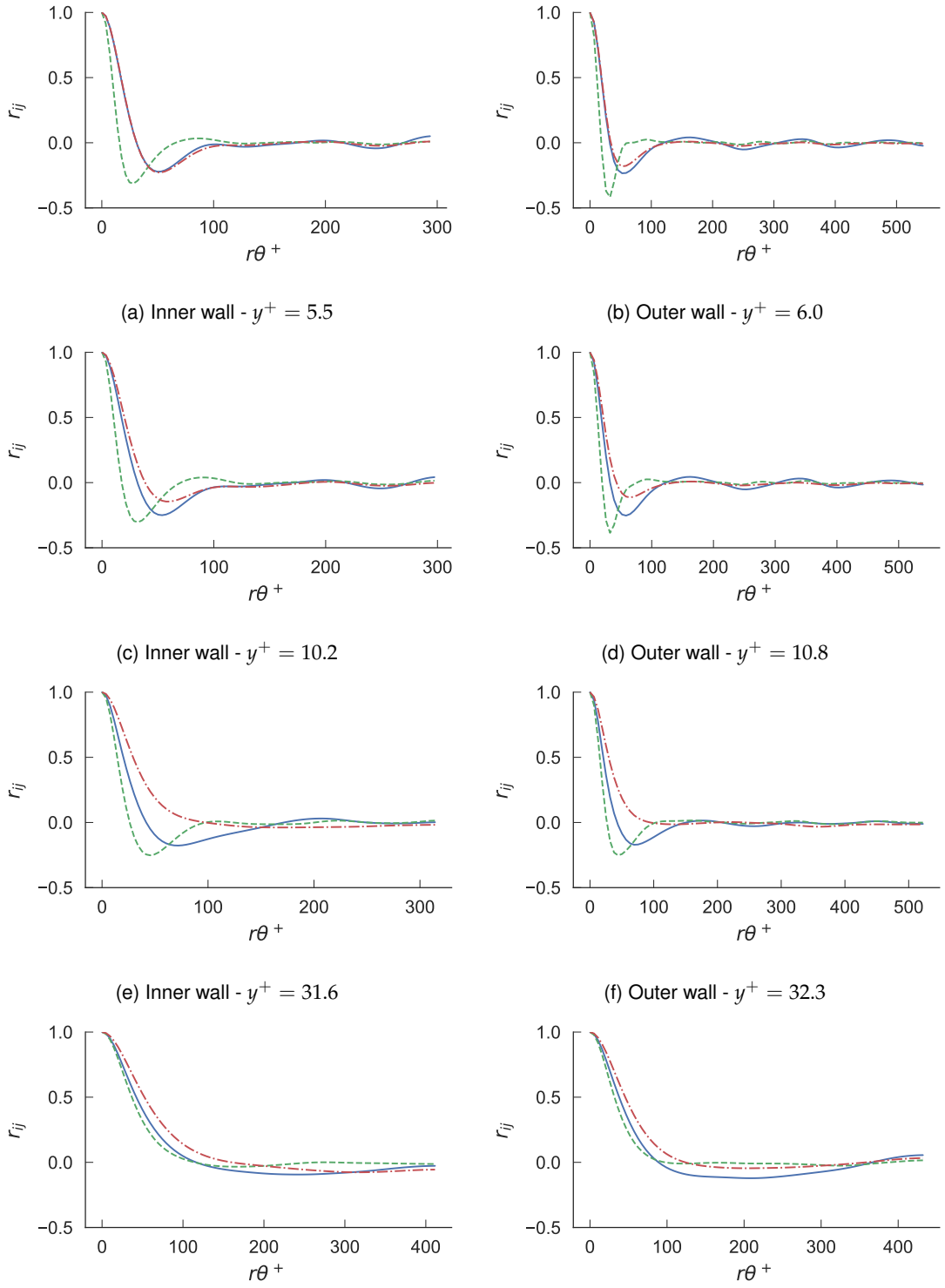

(a) Inner wall - $y^+ = 5.5$

(b) Outer wall - $y^+ = 6.0$

(c) Inner wall - $y^+ = 10.2$

(d) Outer wall - $y^+ = 10.8$

(e) Inner wall - $y^+ = 31.6$

(f) Outer wall - $y^+ = 32.3$

(g) Inner wall - $y^+ = 147.2$

(h) Outer wall - $y^+ = 154.7$

Figure D.2: Two-point correlation coefficients in the azimuthal direction for the axial-only annular flow. Normalisation is by the local wall scales.

D.2 Annular Swirling Flow

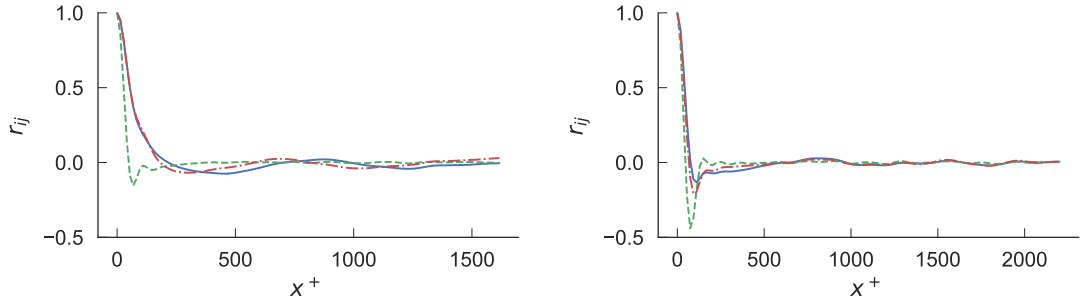

(a) Inner wall - $y^+ = 4.9$

(b) Outer wall - $y^+ = 7.6$

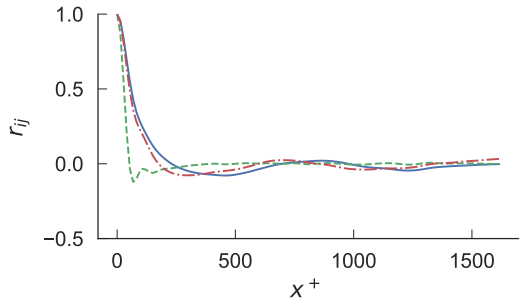

(c) Inner wall - $y^+ = 9.0$

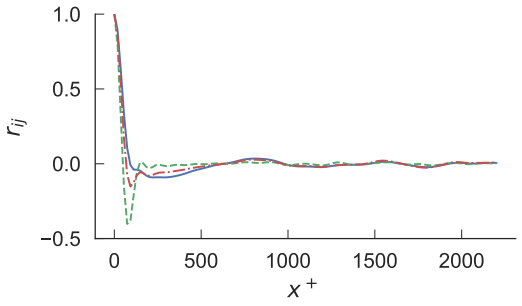

(d) Outer wall - $y^+ = 13.6$

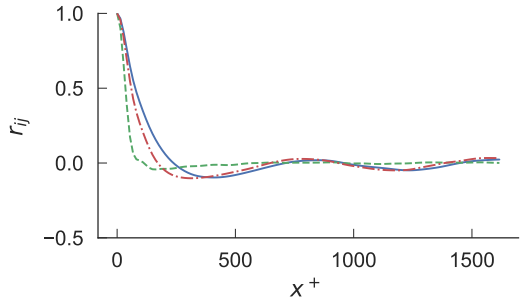

(e) Inner wall - $y^+ = 28.1$

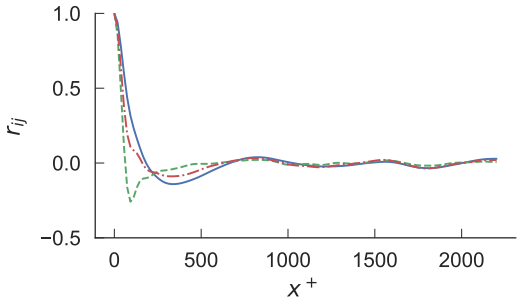

(f) Outer wall - $y^+ = 40.7$

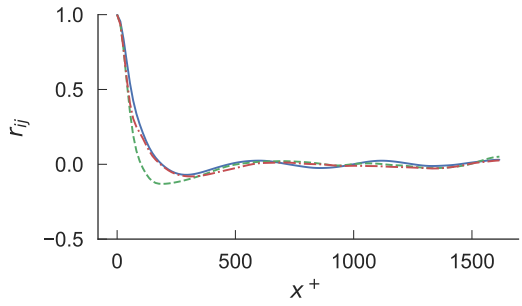

(g) Inner wall - $y^+ = 137.7$

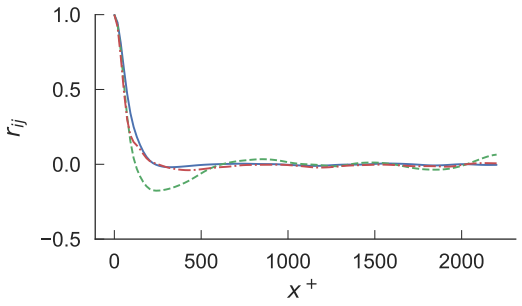

(h) Outer wall - $y^+ = 185.7$

Figure D.3: Two-point correlation coefficients in the axial direction for the swirling annular flow. Normalisation is by the local wall scales.

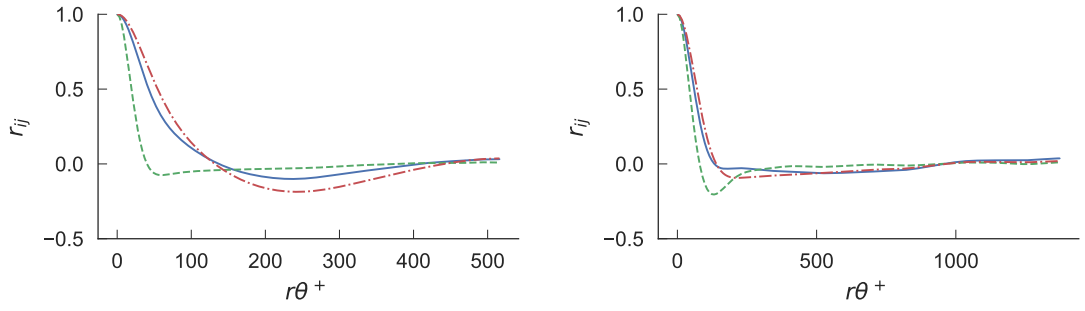

(a) Inner wall - $y^+ = 4.9$

(b) Outer wall - $y^+ = 7.6$

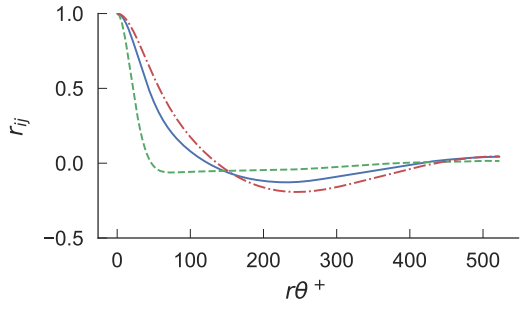

(c) Inner wall - $y^+ = 9.0$

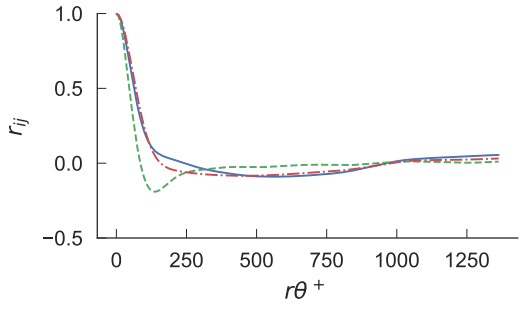

(d) Outer wall - $y^+ = 13.6$

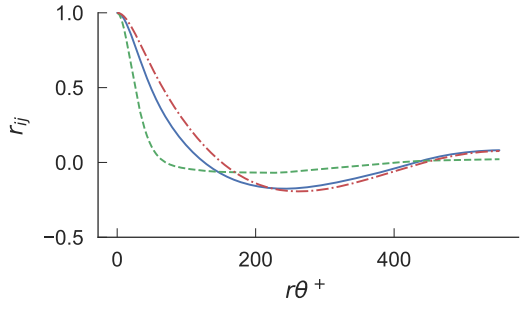

(e) Inner wall - $y^+ = 28.1$

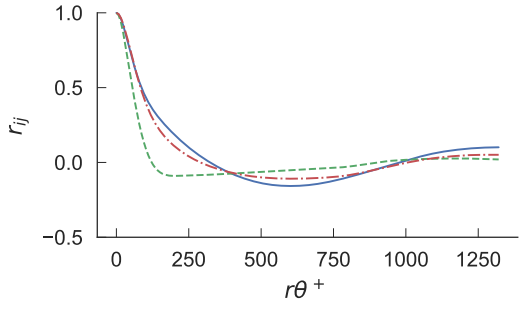

(f) Outer wall - $y^+ = 40.7$

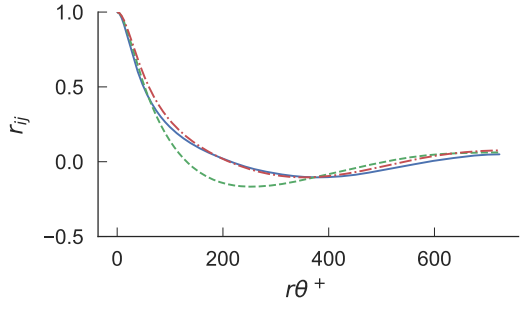

(g) Inner wall - $y^+ = 137.7$

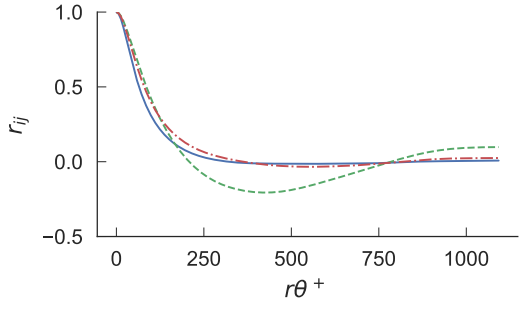

(h) Outer wall - $y^+ = 185.7$

Figure D.4: Two-point correlation coefficients in the azimuthal direction for the swirling annular flow. Normalisation is by the local wall scales.

References

Ahmed, U., Doan, N.A.K., Lai, J., Klein, M., Chakraborty, N. and Swaminathan, N. (2018) "Multi-scale analysis of head-on quenching premixed turbulent flames". *Physics of Fluids*, 30(10), page 105102. ISSN 10897666. doi:10.1063/1.5047061.

Ahmed, U., Pillai, A.L., Chakraborty, N. and Kurose, R. (2019) "Statistical behavior of turbulent kinetic energy transport in boundary layer flashback of hydrogen-rich premixed combustion". *Physical Review Fluids*, 4(10), page 103201. ISSN 2469-990X. doi:10.1103/physrevfluids.4.103201.

Ahmed, U., Pillai, A.L., Chakraborty, N. and Kurose, R. (2020) "Surface density function evolution and the influence of strain rates during turbulent boundary layer flashback of hydrogen-rich premixed combustion". *Physics of Fluids*, 32(5), page 055112. ISSN 1070-6631. doi:10.1063/5.0004850.

Alfredsson, P.H. and Persson, H. (1989) "Instabilities in channel flow with system rotation". *Journal of Fluid Mechanics*, 202(543), pages 543–557. ISSN 14697645. doi:10.1017/S002211208900128X.

Alshaalan, T. and Rutland, C.J. (2002) "Wall heat flux in turbulent premixed reacting flow". *Combustion Science and Technology*, 174(1), pages 135–165. ISSN 0010-2202. doi:10.1080/713712913.

Bagheri, E. and Wang, B.C. (2019) "Effect of transverse curvature on turbulent concentric annular pipe flow and structures". In "11th International Symposium on Turbulence and Shear Flow Phenomena, TSFP 2019", .

Benjamin, T.B. (1968) "Gravity currents and related phenomena". *Journal of Fluid Mechanics*, 31(2), pages 209–248. ISSN 14697645. doi:10.1017/S0022112068000133.

Bioche, K., Pieyre, A., Ribert, G., Richecoeur, F. and Vervisch, L. (2019) "The role of gravity in the asymmetry of flames in narrow combustion chambers". *Combustion and Flame*, 203, pages 238–246. ISSN 15562921. doi:10.1016/j.combustflame.2019.02.020.

Björnsson, Ó.H., Klein, S. and Tober, J. (2020) "Boundary Layer Flashback Model for Hydrogen Flames in Confined Geometries Including the Effect of Adverse Pressure Gradient". *Journal of Engineering for Gas Turbines and Power*. ISSN 0742-4795. doi:10.1115/1.4048566.

Bruneaux, G., Akselvoll, K., Poinsot, T. and Ferziger, J.H. (1996) "Flame-wall interaction simulation in a turbulent channel flow". *Combustion and Flame*, 107(1-2), pages 27–36. ISSN 00102180. doi:10.1016/0010-2180(95)00263-4.

Bychkov, V.V., Kovalev, K.A. and Liberman, M.A. (1999) "Nonlinear equation for curved nonstationary flames and flame stability". *Physical Review E - Statistical Physics, Plasmas, Fluids, and Related Interdisciplinary Topics*, 60(3), pages 2897–2911. ISSN 1063651X. doi:10.1103/PhysRevE.60.2897.

Cantero, M.I., Lee, J.R., Balachandar, S. and Garcia, M.H. (2007) “On the front velocity of gravity currents”. *Journal of Fluid Mechanics*, 586, pages 1–39. ISSN 00221120. doi:10.1017/S0022112007005769.

Chen, F. and Chang, M.H. (1992) “Stability of Taylor-Dean flow in a small gap between rotating cylinders”. *Journal of Fluid Mechanics*, 243, pages 443–455. ISSN 14697645. doi:10.1017/S0022112092002775.

Chen, J.H., Choudhary, A., De Supinski, B., Devries, M., Hawkes, E.R., Klasky, S., Liao, W.K., Ma, K.L., Mellor-Crummey, J., Podhorszki, N., Sankaran, R., Shende, S. and Yoo, C.S. (2009) “Terascale direct numerical simulations of turbulent combustion using S3D”. *Computational Science and Discovery*, 2(1), page 015001. ISSN 17494680. doi:10.1088/1749-4699/2/1/015001.

Chen, J.H. and Im, H.G. (1998) “Correlation of flame speed with stretch in turbulent premixed methane/air flames”. In “Symposium (International) on Combustion”, volume 27, pages 819–826. Elsevier. ISBN 0082-0784. ISSN 00820784. doi:10.1016/S0082-0784(98)80477-3.

Chung, S.Y., Rhee, G.H. and Sung, H.J. (2002) “Direct numerical simulation of turbulent concentric annular pipe flow part 1: Flow field”. *International Journal of Heat and Fluid Flow*, 23(4), pages 426–440. ISSN 0142727X. doi:10.1016/S0142-727X(02)00140-6.

Dabireau, F., Cuenot, B., Vermorel, O. and Poinsot, T. (2003) “Interaction of flames of H2+ O2with inert walls”. *Combustion and Flame*, 135(1-2), pages 123–133. ISSN 00102180. doi:10.1016/S0010-2180(03)00154-8.

Dam, B., Love, N. and Choudhuri, A. (2011) “Flashback propensity of syngas fuels”. *Fuel*, 90(2), pages 618–625. ISSN 00162361. doi:10.1016/j.fuel.2010.10.021.

Dejoan, A., Jiménez, C. and Kurdyumov, V.N. (2019) “Critical conditions for non-symmetric flame propagation in narrow channels: Influence of the flow rate, the thermal expansion, the Lewis number and heat-losses”. *Combustion and Flame*, 209, pages 430–440. ISSN 00102180. doi:10.1016/j.combustflame.2019.08.011.

Dejoan, A. and Kurdyumov, V.N. (2019) “Thermal expansion effect on the propagation of premixed flames in narrow channels of circular cross-section: Multiplicity of solutions, axisymmetry and non-axisymmetry”. *Proceedings of the Combustion Institute*, 37(2), pages 1927–1935. ISSN 15407489. doi:10.1016/j.proci.2018.06.153.

Dou, H.S., Khoo, B.C. and Tsai, H.M. (2005) “Determining the Critical Condition for Flow Transition in a Full-Developed Annulus Flow”. *Journal of Petroleum Science and Engineering*, 73(1-2), pages 41–47.

Dreizler, A. and Böhm, B. (2015) “Advanced laser diagnostics for an improved understanding of premixed flame-wall interactions”. *Proceedings of the Combustion Institute*, 35(1), pages 37–64. ISSN 15407489. doi:10.1016/j.proci.2014.08.014.

Ebi, D., Bombach, R. and Jansohn, P. (2020) “Swirl flame boundary layer flashback at elevated pressure: Modes of propagation and effect of hydrogen addition”. *Proceedings of the Combustion Institute*. ISSN 15407489. doi:10.1016/j.proci.2020.06.305.

Ebi, D. and Clemens, N.T. (2014) "Time-resolved PIV and flame front imaging of boundary layer flashback in a swirl combustor". In "17th International Symposium on Applications of Laser Techniques to Fluid Mechanics", Lisbon, Portugal.

Ebi, D. and Clemens, N.T. (2015) "Flow-flame interaction in turbulent boundary layer flashback of swirl flames". *Proceedings of the 9th International Symposium on Turbulence and Shear Flow Phenomena*.

Ebi, D. and Clemens, N.T. (2016) "Experimental investigation of upstream flame propagation during boundary layer flashback of swirl flames". *Combustion and Flame*, 168, pages 39–52. ISSN 15562921. doi:10.1016/j.combustflame.2016.03.027.

Ebi, D., Ranjan, R. and Clemens, N.T. (2018) "Coupling between premixed flame propagation and swirl flow during boundary layer flashback". *Experiments in Fluids*, 59(7), page 109. ISSN 0723-4864. doi:10.1007/s00348-018-2563-7.

Eichler, C., Baumgartner, G. and Sattelmayer, T. (2012) "Experimental Investigation of Turbulent Boundary Layer Flashback Limits for Premixed Hydrogen-Air Flames Confined in Ducts". *Journal of Engineering for Gas Turbines and Power*, 134(1), page 011502. ISSN 07424795. doi:10.1115/1.4004149.

Eichler, C. and Sattelmayer, T. (2011) "Experiments on Flame Flashback in a Quasi-2D Turbulent Wall Boundary Layer for Premixed Methane-Hydrogen-Air Mixtures". *Journal of Engineering for Gas Turbines and Power*, 133(1), page 011503. ISSN 07424795. doi:10.1115/1.4001985.

Eichler, C. and Sattelmayer, T. (2012) "Premixed flame flashback in wall boundary layers studied by long-distance micro-PIV". *Experiments in Fluids*, 52(2), pages 347–360. ISSN 07234864. doi:10.1007/s00348-011-1226-8.

Eichler, C.T. (2011) *Flame Flashback in Wall Boundary Layers of Premixed Combustion Systems*. Ph.D. thesis.

Endres, A. and Sattelmayer, T. (2018) "Large Eddy simulation of confined turbulent boundary layer flashback of premixed hydrogen-air flames". *International Journal of Heat and Fluid Flow*, 72(May), pages 151–160. ISSN 0142727X. doi:10.1016/j.ijheatfluidflow.2018.06.002.

Endres, A. and Sattelmayer, T. (2019) "Numerical investigation of pressure influence on the confined turbulent boundary layer flashback process". *Fluids*, 4(3). ISSN 23115521. doi:10.3390/fluids4030146.

Fernández-Galisteo, D. and Kurdyumov, V.N. (2019) "Impact of the gravity field on stability of premixed flames propagating between two closely spaced parallel plates". *Proceedings of the Combustion Institute*, 37(2), pages 1937–1943. ISSN 15407489. doi:10.1016/j.proci.2018.06.073.

Fernández-Galisteo, D., Kurdyumov, V.N. and Ronney, P.D. (2018) "Analysis of premixed flame propagation between two closely-spaced parallel plates". *Combustion and Flame*, 190, pages 133–145. ISSN 0010-2180. doi:10.1016/J.COMBUSTFLAME.2017.11.022.

Fritz, J., Kröner, M. and Sattelmayer, T. (2004) "Flashback in a Swirl Burner With Cylindrical Premixing Zone". *Journal of Engineering for Gas Turbines and Power*, 126(2), page 276. ISSN 07424795. doi:10.1115/1.1473155.

Garbow, B.S., Hillstrom, K.E. and More, J.J. (1980) “MINPACK”.
URL: *https://www.math.utah.edu/software/minpack/minpack/hybrd.html*

Gruber, A., Chen, J.H., Valiev, D. and Law, C.K. (2012) “Direct numerical simulation of premixed flame boundary layer flashback in turbulent channel flow”. *Journal of Fluid Mechanics*, 709, pages 516–542. doi:10.1017/jfm.2012.345.

Gruber, A., Kerstein, A.R., Valiev, D., Law, C.K., Kolla, H. and Chen, J.H. (2015) “Modeling of mean flame shape during premixed flame flashback in turbulent boundary layers”. *Proceedings of the Combustion Institute*, 35, pages 1485–1492. doi:10.1016/j.proci.2014.06.073.

Gruber, A., Richardson, E.S., Aditya, K. and Chen, J.H. (2018) “Direct numerical simulations of premixed and stratified flame propagation in turbulent channel flow”. *Physical Review Fluids*, 3(11), page 110507. ISSN 2469990X. doi:10.1103/PhysRevFluids.3.110507.

Gruber, A., Sankaran, R., Hawkes, E.R. and Chen, J.H. (2010) “Turbulent flame-wall interaction: a direct numerical simulation study”. *Journal of Fluid Mechanics*, 658, pages 5–32. ISSN 0022-1120. doi:10.1017/S0022112010001278.

Härtel, C., Carlsson, F. and Thunblom, M. (2000a) “Analysis and direct numerical simulation of the flow at a gravity-current head. Part 2. The lobe-and-cleft instability”. *Journal of Fluid Mechanics*, 418, pages 213–229. ISSN 00221120. doi:10.1017/S0022112000001270.

Härtel, C., Meiburg, E. and Necker, F. (2000b) “Analysis and direct numerical simulation of the flow at a gravity-current head. Part 1. Flow topology and front speed for slip and no-slip boundaries”. *Journal of Fluid Mechanics*, 418, pages 189–212. ISSN 00221120. doi:10.1017/S0022112000001221.

Hasse, C., Bollig, M., Peters, N. and Dwyer, H.A. (2000) “Quenching of laminar iso-octane flames at cold walls”. *Combustion and Flame*, 122(1-2), pages 117–129. ISSN 00102180. doi:10.1016/S0010-2180(00)00107-3.

Heeger, C., Gordon, R.L., Tummers, M.J., Sattelmayer, T. and Dreizler, A. (2010) “Experimental analysis of flashback in lean premixed swirling flames: Upstream flame propagation”. *Experiments in Fluids*, 49(4), pages 853–863. ISSN 07234864. doi:10.1007/s00348-010-0886-0.

Hoferichter, V., Boeck, L.R., Baumgartner, G. and Sattelmayer, T. (2014) “Flame Flashback in Hydrogen Combustion with Acoustic Excitation: Simultaneous PIV and OH PLIF Measurements at High Repetition Rate”. *Fachtagung Lasermethoden in der Strömungsmesstechnik*.

Hoferichter, V., Hirsch, C. and Sattelmayer, T. (2016) “Prediction of Confined Flame Flashback Limits Using Boundary Layer Separation Theory”. *Journal of Engineering for Gas Turbines and Power*, 139(2). ISSN 0742-4795. doi:10.1115/1.4034237.

Hoferichter, V., Hirsch, C. and Sattelmayer, T. (2017) “Analytic prediction of unconfined boundary layer flashback limits in premixed hydrogen-air flames”. *Combustion Theory and Modelling*, 21(3), pages 382–418. ISSN 17413559. doi:10.1080/13647830.2016.1240832.

Hoferichter, V. and Sattelmayer, T. (2017) “Boundary Layer Flashback in Premixed Hydrogen-Air Flames With Acoustic Excitation”. *Journal of Engineering for Gas Turbines and Power*, 140(5), page 051502. ISSN 0742-4795. doi:10.1115/1.4038128.

Huppert, H.E. (2006) “Gravity currents: A personal perspective”. doi:10.1017/S002211200600930X.

Ishizuka, S. (2002) “Flame propagation along a vortex axis”. *Progress in Energy and Combustion Science*, 28(6), pages 477–542. ISSN 03601285. doi:10.1016/S0360-1285(02)00019-9.

Ishizuka, S., Hamasaki, T., Koumura, K. and Hasegawa, R. (1998) “Measurements of flame speeds in combustible vortex rings: Validity of the back-pressure drive flame propagation mechanism”. In “Symposium (International) on Combustion”, volume 27, pages 727–734. Elsevier. ISBN 0082-0784. ISSN 00820784. doi:10.1016/S0082-0784(98)80466-9.

Ishizuka, S., Koumura, K. and Hasegawa, R. (2000) “Enhancement of flame speed in vortex rings of rich hydrogen/air mixtures in air”. *Proceedings of the Combustion Institute*, 28(2), pages 1949–1956. ISSN 15407489. doi:10.1016/S0082-0784(00)80600-1.

Jiménez, C., Fernández-Galisteo, D. and Kurdyumov, V.N. (2015) “DNS study of the propagation and flashback conditions of lean hydrogen-air flames in narrow channels: Symmetric and non-symmetric solutions”. *International Journal of Hydrogen Energy*, 40(36), pages 12541–12549. ISSN 03603199. doi:10.1016/j.ijhydene.2015.07.037.

Jiménez, C. and Kurdyumov, V.N. (2017) “Propagation of symmetric and non-symmetric lean hydrogen-air flames in narrow channels: Influence of heat losses”. *Proceedings of the Combustion Institute*, 36(1), pages 1559–1567. ISSN 15407489. doi:10.1016/j.proci.2016.06.066.

Jiménez, J. (2012) “Cascades in Wall-Bounded Turbulence”. *Annual Review of Fluid Mechanics*, 44(1), pages 27–45. ISSN 0066-4189. doi:10.1146/annurev-fluid-120710-101039.

Jimenez, J. (2013) “Near-wall turbulence”. *Phys. Fluids*, 25, page 101302.

Jimenez, J. and Moser, R.D. (2007) “What are we learning from simulating wall turbulence?” *Philosophical Transactions of the Royal Society A: Mathematical, Physical and Engineering Sciences*, 365(1852), pages 715–732. ISSN 1364-503X. doi:10.1098/rsta.2006.1943.

Jiménez, J. and Pinelli, A. (1999) “The autonomous cycle of near-wall turbulence”. *Journal of Fluid Mechanics*, 389, page S0022112099005066. ISSN 00221120. doi:10.1017/S0022112099005066.

Kalantari, A. and McDonell, V. (2017) “Boundary layer flashback of non-swirling premixed flames: Mechanisms, fundamental research, and recent advances”. doi:10.1016/j.pecs.2017.03.001.

Kalantari, A., Sullivan-Lewis, E. and McDonell, V. (2017) “Application of a turbulent jet flame flashback propensity model to a commercial gas turbine combustor”. *Journal of Engineering for Gas Turbines and Power*, 139(4), page 041506. ISSN 0742-4795. doi:10.1115/GT2016-58059.

Karimi, N., Heeger, C., Christodoulou, L. and Dreizler, A. (2015) “Experimental and theoretical investigation of the flashback of a swirling, bluff-body stabilised, premixed flame”. *Zeitschrift fur Physikalische Chemie*, 229(5), pages 663–689. ISSN 09429352. doi:10.1515/zpch-2014-0582.

Kee, R., Miller, J. and Jefferson, T, H. (1980) “CHEMKIN; A General-Purpose, Problem-Independent, Transportable, Fortran Chemical Kinetics Code Package”. *Sandia Laboratries Report*, (SAND80-8003), pages 1–182.

Kee, R.J., Coltrin, M.E. and Glarborg, P. (2003) *Chemically reacting flow : theory and practice*. Wiley-Interscience. ISBN 9780471461296.

Kee, R.J., Dixon-Lewis, G., Warnatz, J., Coltrin, M.E. and Miller, J.A. (1986) “A Fortran Computer Code Package for the Evaluation of Gas-Phase Multicomponent Transport Properties”. Technical report, Sandia National Laboratories Report SAND86-8246.

Kiesewetter, F., Konle, M. and Sattelmayer, T. (2007) “Analysis of Combustion Induced Vortex Breakdown Driven Flame Flashback in a Premix Burner With Cylindrical Mixing Zone”. *Journal of Engineering for Gas Turbines and Power*, 129(4), page 929. ISSN 07424795. doi:10.1115/1.2747259.

Kim, J., Moin, P. and Moser, R. (1987) “Turbulence statistics in fully developed channel flow at low Reynolds number”. *Journal of Fluid Mechanics*, 177(220), pages 133–166. ISSN 0022-1120. doi:10.1017/S0022112087000892.

Kollmann, W. and Chen, J.H. (1998) “Pocket formation and the flame surface density equation”. In “Symposium (International) on Combustion”, volume 27, pages 927–934. Elsevier. ISSN 00820784. doi:10.1016/S0082-0784(98)80490-6.

Konstantinou, I., Ahmed, U. and Chakraborty, N. (2021) “Effects of Fuel Lewis Number on the Near-wall Dynamics for Statistically Planar Turbulent Premixed Flames Impinging on Inert Cold Walls”. *Combustion Science and Technology*, 193(2), pages 235–265. ISSN 1563521X. doi:10.1080/00102202.2020.1799201.

Kristoffersen, R. and Andersson, H.I. (1993) “Direct Simulations of Low-Reynolds-Number Turbulent Flow in a Rotating Channel”. *Journal of Fluid Mechanics*, 256, pages 163–197. ISSN 14697645. doi:10.1017/S0022112093002757.

Kröner, M., Fritz, J. and Sattelmayer, T. (2003) “Flashback Limits for Combustion Induced Vortex Breakdown in a Swirl Burner”. *Journal of Engineering for Gas Turbines and Power*, 125(3), page 693. ISSN 07424795. doi:10.1115/1.1582498.

Kurdyumov, V., Fernández-Tarrazo, E., Truffaut, J.M., Quinard, J., Wangher, A. and Searby, G. (2007) “Experimental and numerical study of premixed flame flashback”. *Proceedings of the Combustion Institute*, 31 I(1), pages 1275–1282. ISSN 15407489. doi:10.1016/j.proci.2006.07.100.

Kurdyumov, V.N. (2011) “Lewis number effect on the propagation of premixed flames in narrow adiabatic channels: Symmetric and non-symmetric flames and their linear stability analysis”. *Combustion and Flame*, 158(7), pages 1307–1317. ISSN 00102180. doi:10.1016/j.combustflame.2010.11.011.

Kurdyumov, V.N., Fernández, E. and Liñán, A. (2000) “Flame flashback and propagation of premixed flames near a wall”. *Proceedings of the Combustion Institute*, 28(2), pages 1883–1889. ISSN 15407489. doi:10.1016/S0082-0784(00)80592-5.

Kurdyumov, V.N. and Fernández-Tarrazo, E. (2002) “Lewis number effect on the propagation of premixed laminar flames in narrow open ducts”. *Combustion and Flame*, 128(4), pages 382–394. ISSN 00102180. doi:10.1016/S0010-2180(01)00358-3.

Kurdyumov, V.N. and Jiménez, C. (2014) “Propagation of symmetric and non-symmetric premixed flames in narrow channels: Influence of conductive heat-losses”. *Combustion and Flame*, 161(4), pages 927–936. ISSN 00102180. doi:10.1016/j.combustflame.2013.10.002.

Lai, J. and Chakraborty, N. (2016a) "Effects of Lewis Number on Head on Quenching of Turbulent Premixed Flames: A Direct Numerical Simulation Analysis". *Flow, Turbulence and Combustion*, 96(2), pages 279–308. ISSN 15731987. doi:10.1007/s10494-015-9629-x.

Lai, J. and Chakraborty, N. (2016b) "Modeling of Progress Variable Variance Transport in Head-On Quenching of Turbulent Premixed Flames: A Direct Numerical Simulation Analysis". *Combustion Science and Technology*, 188(11-12), pages 1925–1950. ISSN 1563521X. doi:10.1080/00102202.2016.1211868.

Lapeyre, C.J., Mazur, M., Scouflaire, P., Richecoeur, F., Ducruix, S. and Poinsot, T. (2017) "Acoustically Induced Flashback in a Staged Swirl-Stabilized Combustor". *Flow, Turbulence and Combustion*, 98(1), pages 265–282. ISSN 15731987. doi:10.1007/s10494-016-9745-2.

Leibovich, S. (1978) "The Structure of Vortex Breakdown". *Annual Review of Fluid Mechanics*, 10(1), pages 221–246. ISSN 0066-4189. doi:10.1146/annurev.fl.10.010178.001253.

Lewis, B. and von Elbe, G. (1943) "Stability and Structure of Burner Flames". *The Journal of Chemical Physics*, 11(2), pages 75–97. ISSN 0021-9606. doi:10.1063/1.1723808.

Li, J., Zhao, Z., Kazakov, A. and Dryer, F.L. (2004) "An updated comprehensive kinetic model of hydrogen combustion". *International Journal of Chemical Kinetics*, 36(10), pages 566–575. ISSN 05388066. doi:10.1002/kin.20026.

Lieuwen, T. and C. Yang, V. (2013) "Environmental Impacts". In "Gas Turbine Emissions", chapter 2.4.8. Cambridge University Press.

Lieuwen, T., McDonell, V., Santavicca, D.A. and Sattelmayer, T. (2008) "Burner development and operability issues related with steady flowing syngas combustors". doi:10.1177/0964663912467814.

Lipatnikov, A.N. and Chomiak, J. (2010) "Effects of premixed flames on turbulence and turbulent scalar transport". doi:10.1016/j.pecs.2009.07.001.

Morsi, Y.S. and Clayton, B.R. (1986) "Determination of principal characteristics of turbulent swirling flow along annuli. Part 3: Numerical analysis". *International Journal of Heat and Fluid Flow*, 7(3), pages 208–222. ISSN 0142727X. doi:10.1016/0142-727X(86)90025-1.

Moser, R.D., Kim, J. and Mansour, N.N. (1999) "Direct numerical simulation of turbulent channel flow up to Re_τ=590". *Physics of Fluids*, 11(4), pages 943–945. ISSN 10706631. doi:10.1063/1.869966.

Nauert, A., Petersson, P., Linne, M. and Dreizler, A. (2007) "Experimental analysis of flashback in lean premixed swirling flames: Conditions close to flashback". *Experiments in Fluids*, 43(1), pages 89–100. ISSN 07234864. doi:10.1007/s00348-007-0327-x.

Neves, J., Moin, P. and Moser, R.D. (1994) "Effects of Convex Transverse Curvature on Wall-Bounded Turbulence. Part 1. The Velocity and Vorticity". *Journal of Fluid Mechanics*, 272, pages 349–382. ISSN 14697645. doi:10.1017/S0022112094004490.

Owston, R., Magi, V. and Abraham, J. (2007) "Interactions of hydrogen flames with walls: Influence of wall temperature, pressure, equivalence ratio, and diluents". *International Journal of Hydrogen Energy*, 32(12), pages 2094–2104. ISSN 03603199. doi:10.1016/j.ijhydene.2006.07.030.

Peters, N. (1999) "The turbulent burning velocity for large-scale and small-scale turbulence". *Journal of Fluid Mechanics*, 384, pages 107–132. ISSN 00221120. doi:10.1017/S0022112098004212.

Poinsot, T., Candel, S. and Trouvé, A. (1996) “Applications of Direct Numerical Simulation to Premixed Turbulent Combustion”. *Progress in Energy and Combustion Science*, 21(95), pages 531–576.

Poinsot, T. and Veynante, D. (2005) *Theoretical and numerical combustion*. 2nd edition.

Poinsot, T.J., Haworth, D.C. and Bruneaux, G. (1993) “Direct simulation and modeling of flame-wall interaction for premixed turbulent combustion”. *Combustion and Flame*, 95(1-2), pages 118–132. ISSN 00102180. doi:10.1016/0010-2180(93)90056-9.

Popp, P. and Baum, M. (1997) “Analysis of wall heat fluxes, reaction mechanisms, and unburnt hydrocarbons during the head-on quenching of a laminar methane flame”. *Combustion and Flame*, 108(3), pages 327–348. ISSN 00102180. doi:10.1016/S0010-2180(96)00144-7.

Popp, P., Smooke, M. and Baum, M. (1996) “Heterogeneous/homogeneous reaction and transport coupling during flame-wall interaction”. *Symposium (International) on Combustion*, 26(2), pages 2693–2700. ISSN 00820784. doi:10.1016/S0082-0784(96)80105-6.

Prandtl, L. (1925) “Bericht über Untersuchungen zur ausgebildeten Turbulenz”. *ZAMM - Journal of Applied Mathematics and Mechanics / Zeitschrift für Angewandte Mathematik und Mechanik*, 5(2), pages 136–139. doi:10.1002/zamm.19250050212.

Ranjan, R., Ebi, D.F. and Clemens, N.T. (2019) “Role of inertial forces in flame-flow interaction during premixed swirl flame flashback”. *Proceedings of the Combustion Institute*, 37(4), pages 5155–5162. ISSN 15407489. doi:10.1016/j.proci.2018.09.010.

Rao, G.N. (1964) “The law of the wall in a thick axisymmetric turbulent boundary layer”. *Journal of Applied Mechanics, Transactions ASME*, 34(1), pages 237–238. ISSN 15289036. doi:10.1115/1.3607642.

Reid, R.O. and Wilson, B.W. (1963) “Boundary flow along a circular cylinder”. *Journal of the Hydraulics Division*, 89(21).

Richards, G., McMillian, M., Gemmen, R., Rogers, W. and Cully, S. (2001) “Issues for low-emission, fuel-flexible power systems”. *Progress in Energy and Combustion Science*, 27(2), pages 141–169. ISSN 0360-1285. doi:10.1016/S0360-1285(00)00019-8.

Ruetsch, G.R., Vervisch, L. and Liñán, A. (1995) “Effects of heat release on triple flames”. *Physics of Fluids*, 7(6), pages 1447–1454. ISSN 10706631. doi:10.1063/1.868531.

Sandberg, R.D. (2007) “Governing equations for a new compressible Navier-Stokes solver in general cylindrical coordinates”.

Saric, W.S. (1994) “Görtler Vortices”. *Annual Review of Fluid Mechanics*, 26(1), pages 379–409. ISSN 0066-4189. doi:10.1146/annurev.fl.26.010194.002115.

Sellmann, J., Lai, J., Kempf, A.M. and Chakraborty, N. (2017) “Flame surface density based modelling of head-on quenching of turbulent premixed flames”. *Proceedings of the Combustion Institute*, 36(2), pages 1817–1825. ISSN 15407489. doi:10.1016/j.proci.2016.07.114.

Shin, J.O., Dalziel, S.B. and Linden, P.F. (2004) “Gravity currents produced by lock exchange”. *Journal of Fluid Mechanics*, 521, pages 1–34. ISSN 00221120. doi:10.1017/S002211200400165X.

Simpson, E.J. (1982) “Gravity currenty in the laboratory, atmosphere, and ocean.” *Annual Review of Fluid Mechanics*, 14(1), pages 213–234. ISSN 00664189. doi:10.1146/annurev.fl.14.010182.001241.

Smith, C.R. and Metzler, S.P. (1983) “The characteristics of low-speed streaks in the near wall region of a turbulent boundary layer”. *J. Fluid Mech.*, 129(C), pages 27–54. ISSN 0022-1120, 1469-7645. doi:10.1017/S0022112083000634.

Taamallah, S., Vogiatzaki, K., Alzahrani, F.M., Mokheimer, E.M.A., Habib, M.A. and Ghoniem, A.F. (2015) “Fuel flexibility, stability and emissions in premixed hydrogen-rich gas turbine combustion: Technology, fundamentals, and numerical simulations”. *Applied Energy*, 154, pages 1020–1047. ISSN 03062619. doi:10.1016/j.apenergy.2015.04.044.

Thibaut, D. and Candel, S. (1998) “Numerical study of unsteady turbulent premixed combustion: Application to flashback simulation”. *Combustion and Flame*, 113(1-2), pages 53–65. ISSN 00102180. doi:10.1016/S0010-2180(97)00196-X.

Tsai, C.H. (2008) “The Asymmetric Behavior of Steady Laminar Flame Propagation in Ducts”. *Combustion Science and Technology*, 180(3), pages 533–545. ISSN 0010-2202. doi:10.1080/00102200701807177.

Valiev, D., Gruber, A., Law, C.K. and Chen, J.H. (2015) “Numerical study of interaction between Darrieus-Landau instability and spatially periodic shear flow”. pages 2–7.

von Karman, T. (1930) “Mechanische Ahnlichkeitund Turbulenz”. In “Proc. Third Int. Congr. Applied Mechanics”, pages 85–105.

Von Kármán, T. (1940) “The engineer grapples with nonlinear problems”. *Bulletin of the American Mathematical Society*, 46(8), pages 615–683. ISSN 02730979. doi:10.1090/S0002-9904-1940-07266-0.

Wallace, J.M. (2016) “Quadrant Analysis in Turbulence Research: History and Evolution”. *Annual Review of Fluid Mechanics*, 48(1), pages 131–158. ISSN 00664189. doi:10.1146/annurev-fluid-122414-034550.

Xia, Z., Shi, Y. and Chen, S. (2016) “Direct numerical simulation of turbulent channel flow with spanwise rotation”. *Journal of Fluid Mechanics*, 788, pages 42–56. ISSN 14697645. doi:10.1017/jfm.2015.717.

Yoo, C.S. (2019) private communication.

Zhao, P., Wang, L. and Chakraborty, N. (2018) “Strain rate and flame orientation statistics in the near-wall region for turbulent flame-wall interaction”. *Combustion Theory and Modelling*, 22(5), pages 921–938. ISSN 17413559. doi:10.1080/13647830.2018.1465598.

Zhao, P., Wang, L. and Chakraborty, N. (2019) “Vectorial structure of the near-wall premixed flame”. *Physical Review Fluids*, 4(6). ISSN 2469990X. doi:10.1103/PhysRevFluids.4.063203.